NMR and Gas Sorption Studies of Structure-Transport Relationships in Porous Media

Shiko, Elenica

Award date:
2013

Awarding institution:
University of Bath

NMR and Gas Sorption Studies of Structure-Transport Relationships in Porous Media

Elenica Shiko

A thesis submitted for the degree of Doctor of Philosophy

University of Bath

Department of Chemical Engineering

March 2013

-To my family-

Preface

The work presented in this thesis is believed to be original except for the parts carried out in collaboration with others.

The silica sample, denoted as S1, was a commercially available catalyst support. The casein and Lutrol templated silicas studied in Chapter 6 were synthesised by Mr. Paulo Malheiro at the Dept. of Pharmacy and Biomedical Sciences, Strathclyde University under the supervision of Dr. Christopher van der Waal. Mr. Malheiro conducted and analysed the data obtained from the drug release profiles and the STEM, TEM, FTIR, HPLC and the CD techniques.

All the *in-vivo* studies performed on the mice brain and the *in-vitro* cell studies, presented in Chapter 7, were performed and analysed by Dr. Neil Barua, at the University of Bristol's Functional Neurosurgery research group.

List of Publications

1. Shiko, E., Edler, K.J., Lowe, J.P. and Rigby, S.P., 2012. Probing the impact of advanced melting and advanced adsorption phenomena on the accuracy of pore size distributions from cryoporometry and adsorption using NMR relaxometry and diffusometry. *Journal of Colloid and Interface Science*, 385 (1), pp. 183-192

2. Shiko, E., Edler, K.J., Lowe, J.P. and Rigby, S.P., 2013. Probing hysteresis during sorption of cyclohexane within mesoporous silica using NMR cryoporometry and relaxometry. *Journal of Colloid and Interface Science,* 398, pp.168-75

List of presentations

1. Shiko, E., Edler, K.J., Lowe, J.P. and Rigby, S.P. Investigation of co-operative effects in vapour adsorption and solid melting within mesoporous solids using T_2 NMR relaxometry and cryodiffusometry. *M4 Colloids Symposium, Cardiff ,July 2011.*

2. Shiko, E., Edler, K.J., Lowe, J.P. and Rigby, S.P. NMR relaxometry and diffusometry studies of pore - pore cooperative effects in melting cryoporometry of adsorbed phases. *Diffusion fundamentals IV, Troy, NY, August, 2011*

Acknowledgements

There are a few people I want to acknowledge as without them the completion of this thesis would have been hard. Firstly, my family, Spyros (*Σπύρος*), Valentina (*Βαλεντίνα*) and Evelina (*Εβελίνα*), who have been always encouraging me to study and absorb as much knowledge as possible. I am very sorry I wasn't able to visit you very often during my PhD, but I am sure you understand it was for a good purpose.

Secondly, I want to thank Sean Rigby, who was my first supervisor at the start of my PhD. Although he left Bath, he continued to critically guide and consult me throughout all my work. Sean, I enjoyed very much working with you and thanks for letting me "play pool" with research ideas (as you like saying), because this gave me the opportunity to explore different areas. I feel also very grateful to Marianne Ellis who took over as my first supervisor when Sean moved away. Marianne, was extremely helpful with everything I needed and she sorted out all the paperwork in a very organised manner.

I also want to thank Karen Edler, my co-supervisor, for improving my background in chemistry and introducing me to the 'scattering world'. Her enthusiasm for science influenced me a lot. Next goes John Lowe, my other co-supervisor and our favourite NMR spectroscopist in Bath. John provided me with all the NMR time I needed to complete more than a half of my thesis and it was a great person to talk to. I owe so much John but there is not enough space here to give you the glowing praise you deserve!

I am also very happy to have collaborated with Chris van der Waals and his research group, and Neil Barua as they made a part of my work more exotic and they helped me look at science from a different angle.

Heartfelt thanks to my boyfriend, George (*Γιώργος*), for encouraging me to study abroad and for his psychological support, calming influence and patience sent across the borders. Moreover, a big thank you to all the members of Rigby and Edler groups in Bath who made me enjoy my time in the UK; especially Iain (who had an answer to all my questions, although he was told to wait until I find it first), Navin (for being good at listening to me), Joyce (for providing me with coffee during my overnight experiments) and Ilaria (for her kindness and care). Last but not least, many thanks to the technical and support staff in both the Dept. of Chemical Engineering and Chemistry who arranged all the background work for me and smoothened all the technical problems raised.

Summary

The work in this thesis is focused on testing the accuracy of the gas sorption and NMR cryoporometry characterization techniques to estimate the key pore descriptors which affect the activity of porous materials used as catalyst supports and drug delivery systems. Both techniques, though, assume independent pores, neglecting advanced adsorption and melting phenomena that can specifically skew the pore size distribution and subsequently lead to inaccurate predictions of catalytic or therapeutic efficiency of the porous system. Firstly, the independent domain theory for both processes was studied by breaking down the pore-filling process of a mesoporous catalyst support, into steps. The system was partially saturated with water or cyclohexane at different pressures, via adsorption and desorption, followed by a cryoporometry experiment at each saturation fraction. Moreover, scanning curves and loops, together with PFG NMR and relaxometry were employed to ascertain the spatial arrangement of the liquid ganglia at each partial saturation and for certain molten fractions. It was shown that the configuration of the liquid condensates varied with position around the hysteresis loop, deviating from the single pore hysteresis mechanism for both adsorbates. Advanced melting of water was associated with a percolation-type transition in the connectivity of the ganglia, which could be curtailed to some extent by sample fragmentation. Also, some pores filled via advanced adsorption at lower pressures. On the contrary, advanced melting of cyclohexane arose from the liquid bridging the pore cross-sections of the partially filled pores. Secondly, an integrated nitrogen-water-nitrogen experiment was employed to test the source of sorption hysteresis and to compare the extent of advanced adsorption phenomena for nitrogen and water sorption, by isolating a subset of pores. It was found that the Kelvin-Cohan equations and the DFT algorithm overestimate the width of the sorption hysteresis in independent pores of the catalyst support studied in this work. Moreover, the adsorption mechanism of nitrogen differs to that of water, and advanced adsorption of nitrogen is less severe than that of water. Thirdly, cryodiffusometry and gas sorption techniques were used to estimate the pore space descriptors (surface area, pore size, tortuosity, porosity) of two different types of mesoporous silicas, candidates for drug delivery. The structure-transport relationships in these materials were investigated to interpret the drug release profiles obtained for release studies carried out in simulated gastrointestinal fluids. It was found that the release rate was mainly controlled by the size of the silica particles and the silica solubility itself in the environment present. Also, different synthesis routes were tested to optimize the drug loaded PLGA nanoparticles, for convection-enhanced drug delivery into the brain. Various model and real hydrophobic and hydrophilic drugs were tested. *In-vitro* and *in-vivo* studies showed that the dialysis method led to production of particles with the desirable characteristics, which were successfully distributed in the mice brain. The sensitivity of the cryoporometry melting, gas sorption and imaging techniques was found inadequate to resolve the inner structure of the polymer matrix. Last, the experimental time for the cryodiffusometry experiments in this work was long due to the high recycle delay times required to maximise the signal to noise ratio. It is though found that high delay times are unnecessary when BBP-LED pulse sequence is used, even when the fluid is imbibed in a mesoporous systems.

Contents

		Page
	Preface	iii
	List of publications	iii
	List of presentations	iii
	Acknowledgements	iv
	Summary	v
	List of Tables	xi
	List of Figures	xiii
	Abbreviations	xxi
	Nomenclature	xxii
	Introduction	xxvi
Chapter 1	**An introduction to gas sorption characterization technique**	1
1.1	Introduction	1
1.2	The adsorption mechanism	3
1.3	The adsorption isotherms	4
1.4	Assessment of microporosity	5
	1.4.1 Micropore surface area determination 1.4.2 Micropore volume 1.4.3 Pore size distribution	
1.5	Assessment of mesoporosity	9
	1.5.1 Mesopore surface area measurements 1.5.2 Pore volume 1.5.3 Pore size distribution	
1.6	Fractals	13
1.7	Hysteresis	15
1.8	Advanced adsorption	21
1.9	Independent domain theory and gas sorption scanning curves	23
1.10	Summary	28
Chapter 2	**Introduction to Nuclear Magnetic Resonance characterization techniques**	30
2.1	Introduction	30
2.2	Background theory	30
2.3	T_1 and T_2 relaxometry NMR	33
	2.3.1 T_1 relaxation 2.3.2 T_2 relaxation	
2.4	Pulse field gradient NMR	37
2.5	Magnetisation recovery in a PFG NMR experiment	42
2.6	Cryoporometry NMR	44
2.7	Freeze-thaw hysteresis in cryoporometry NMR	47
2.8	Defining cryoporometry NMR scanning curves and advanced melting mechanism	49

2.9	Summary	55
Chapter 3	**Probing the impact of cooperative phenomena on the accuracy of pore size distribution derived from cryoporometry NMR and gas sorption techniques**	56
3.1	Introduction	56
3.2	Previous studies	59
3.3	Experimental procedure and methodology	63
3.4	Water adsorption	64
3.5	NMR cryoporometry	65
3.6	T_2 relaxometry	67
3.7	NMR diffusometry	68
3.8	Nitrogen sorption	70
3.9	Results	70
	3.9.1 Water adsorption 3.9.2 NMR cryoporometry boundary melting curves. T_2 relaxometry and diffusometry studies 3.9.3 NMR cryoporometry scanning curves for the whole and the fragmented samples 3.9.4 NMR cryoporometry scanning loops for the whole pellet and the fragmented samples. Relaxometry studies 3.9.5 Further diffusion and relaxation studies. Comparing adsorption/desorption to the melting/freezing mechanisms 3.9.6 Pore size distributions	
3.10	Discussion	88
	3.10.1 Advanced phenomena studies on whole pellet S1 samples 3.10.2 Advanced phenomena studies after fragmentation of S1 sample 3. 10.3 Comparing advanced melting to advanced adsorption, and pore blocking in freezing to pore blocking in vapour desorption	
3.11	Conclusions	101
Chapter 4	**Probing hysteresis during sorption of cyclohexane within mesoporous silica using NMR cryoporometry and relaxometry**	103
4.1	Introduction	103
4.2	Previous studies	104
4.3	Experimental procedure and methodology	106
	4.3.1 Cyclohexane sorption 4.3.2 NMR cryoporometry 4.3.3 NMR relaxometry	
4.4	Results	109
	4.4.1 Cyclohexane sorption 4.4.2 NMR cryoporometry	
4.5	Discussion	115
4.6	Conclusions	120

Chapter 5	**Testing single pore hysteresis for S1 material via an integrated N_2-H_2O-N_2 sorption experiment**	121
5.1	Introduction	121
5.2	Previous studies	122
5.3	Experimental procedure	125
5.4	Data analysis	126
	5.4.1 Pore volume 5.4.2 Change in the incremental nitrogen volume 5.4.3 Fractal analysis	
5.5	Results and discussion	128
5.6	Conclusions	136
Chapter 6	**Release of cyclosporin-A from casein and Lutrol templated porous silica particles**	138
6.1	Introduction	138
6.2	Synthesis and application of mesoporous silica particles as drug delivery systems	139
6.3	Lutrol and casein templates	143
6.4	Cyclosporin-A	146
6.5	Drug release data analysis	148
6.6	Materials	153
6.7	Experimental procedures and characterization methods	153
	6.7.1 Synthesis of casein and Lutrol templated silicas 6.7.2 Simulated gastrointestinal fluids 6.7.3 Cyclosporin-A loading 6.7.4 Determination of loading efficiency of CsA and *in-vitro* release studies 6.7.5 SEM and TEM imaging 6.7.6 Nitrogen sorption 6.7.7 NMR cryoporometry 6.7.8 PFG NMR 6.7.9 Small Angle X-ray scattering (SAXS)	
6.8	Results	159
	6.8.1 Particle size and morphology of silica materials 6.8.2 Nitrogen sorption and NMR cryoporometry studies PFG NMR 6.8.3 Small angle X-ray scattering (SAXS) 6.8.4 CsA loading and *in-vitro* drug release studies	
6.9	Discussion	17
6.10	Conclusion	179
Chapter 7	**Synthesis and characterization of poly(lactic-*co*-glycolide) nanoparticles for convection-enhanced drug delivery into the brain**	181
7.1	Introduction	181
7.2	Background theory to poly(lactic-*co*-glycolic acid) polymer and synthesis methods for nanoparticles	182

7.3	Drug delivery to the central nervous system and recent studies	188
7.4	Materials	192
7.5	Experimental procedures	195
	7.5.1 O/W emulsion-solvent evaporation: Use of probe sonicator	
	7.5 .2 O/W emulsion-solvent evaporation: Use of cell disrupter	
	7.5.3 Emulsion-solvent diffusion	
	7.5.4 Dialysis method	
	7.5.5 Simple mixing	
	7.5.6 Nanoprecipitation	
	7.5.7 *In-vitro* analysis of glioma cell uptake of nanospheres	
	7.5.8 *In-vivo* CED in the brain parenchyma	
7.6	Nanoparticle characterization methods	202
	7.6.1 Electron microscopy	
	7.6.2 Dynamic and electrophoretic light scattering	
	7.6.3 Fluorescent and spectrometry techniques	
	7.6.4 Gas sorption studies	
7.7	Results. Drug free nanoparticles	208
	7.7.1 Morphology of drug-free nanoparticles	
	7.7.2 Size and charge of drug-free nanoparticles	
	7.7.3 Nitrogen and krypton sorption studies for pore characterization of nanoparticles	
	7.7.4 NMR cryporometry studies for pore characterization of nanoparticles	
7.8	Discussion. Drug free nanoparticles	218
	7.8.1 Effect of synthesis method on particle size and morphology	
	7.8.2 Charge of nanoparticles	
	7.8.3 Pore characterization of nanoparticles synthesized via dialysis method	
7.9	Results. Drug loaded nanoparticles	228
	7.9.1 Size and surface charge of nanoparticles	
	7.9.2 Encapsulation efficiencies	
	7.9.3 *In-vitro* TFMU and NR release studies	
7.10	Discussion. Drug loaded nanoparticles	234
	7.10.1 Size and charge of nanoparticles	
	7.10.2 Drug encapsulation efficiencies and release profiles	
7.11	Results. *In-vitro* and *in-vivo* studies	240
	7.11.1 *In-vitro* analysis of glioma cell uptake of drug loaded nanoparticles and cytotoxicity studies	
	7.11.2 *In-vivo* CED studies of drug loaded nanoparticles	
7.12	Discussion. *In-vitro* and *in-vivo* studies	246
7.13	Conclusions	249
Chapter 8	**Reducing the time of PFG diffusion NMR experiments**	250
8.1	Introduction	250
8.2	Literature review	250
8.3	Experimental procedure and methodology	253

8.4 Results and discussion 257
8.5 Conclusions 260
Chapter 9 Conclusions and proposed future work 262
9.1 Conclusions 262
9.1.1 Probing cooperative effects in water vapour sorption and
9.1.2 NMR cryoporometry
9.1.3 Probing the cyclohexane sorption hysteresis
9.1.4 Testing independent (single) pore theory and the cause of hysteresis via an integrated N_2-H_2O-N_2 experiment
9.1.5 Structure-transport studies for interpretation of CsA release profiles
9.1.6 Optimization of PLGA nanoparticles for convection-enhanced drug delivery into the brain
9.1.7 Reducing the experimental time of a PFG NMR experiment
9.2 Proposed future work 269
9.2.1 Comparing the influence of the meniscus geometry and surface chemistry for nitrogen condensation via an integrated N_2-H_2O-N_2 experiment
9.2.2 Studying the effect of pore connectivity into water and nitrogen sorption via an integrated N_2-H_2O-N_2 experiment
9.2.3 Probing the location of CsA in the pores of Lutrol and casein templated silicas
9.2.4 Synthesis of PLGA NPs for MRI
Appendices 274
Bibliography 291

List of Tables

1.1 Terms and definitions of porous materials by the IUPAC (Sing et al., 1985) 2

3.1 Results of the 2-component fit to the T_2 data obtained at various positions around the scanning loops of the whole pellet 2, shown in Figure 3.7 using equation 3.1 78

3.2 Results of the 2-component fit to the T_2 data obtained at various positions around the scanning loops of the fragmented sample, shown in Figures 3.8 and 3.9 using equation 3.2 81

3.3 Results of PFG NMR experiments, and 1- and 2-component fits to the T_2 data, obtained at some points on the boundary melting curves, obtained at different condensate saturations from adsorption. Notes: [a] 1-component fit, [b] 2-component fit gives same mean as 1-component. The values in bold and italics on this table are compared to those in Table 3.4 82

3.4 Results of PFG NMR experiments, and 1- and 2-component fits to the T_2 data, obtained at some points on the boundary freezing curves, obtained at different condensate saturations from desorption process. Notes: [a] 1-component fit, [b] 2-component fit gives the same mean as the 1-component fit. The values in bold and italics on this table are compared to those in Table 3.3 83

4.1 T_2 relaxation times obtained by fitting a two-component model to the relaxometry data obtained at the top of the scanning loops (where there was a very similar molten fraction of ~0.18 for all curves) shown in Figure 4.4 for various different ultimate saturation levels on the adsorption isotherm. The error in the fraction of the slow and the fast component varies between 0.01-0.06 ms 114

4.2 T_2 relaxation times measured at the end of the boundary melting curves, shown in Figure 4.4, for various different ultimate saturation levels on the adsorption isotherm.[d]: the error is ±0.38 ms. All the other errors in the fraction of the slow and the fast component vary between 0-0.06 ms 114

4.3 T_2 relaxation times measured at the end of the boundary melting curves, shown in Figure 4.5, for various different ultimate saturation levels on the desorption isotherm. The error for the slow and fast component fractions varies between 0.01-0.1 115

5.1 Pore volumes and surface area occupied with adsorbates pre and post partial saturation with water 129

5.2 Change in the fractal dimension before and after water adsorption calculated by equation 5.4, at P/P_0=~0.14-0.77. The error values correspond to the standard error from regression for data fitting in Excel 135

6.1 Porosity and surface area measurements of casein and Lutrol templated silicas 162

6.2 Tortuosities and rms displacement values of heptane within casein and Lutrol templated silicas for Δ=0.1 s and δ=0.0015 s. The error is found as described in Section A2.1, Appendix 164

6.3 Parameters predicted by LDF (k_2) and Weibull (k_3, b) models. The number in bold is to show that its value is quasi-similar to the one predicted from Model III, Table 6.4 171

6.4 Time constants for Lutrol and casein templated silicas, calculated from $k=15D_{intra}/r^2$, where D_{intra} was estimated from equations 6.9 and 6.11 (Model I), equations 6.11, 6.12 and 6.14 (Model II), equations 6.10, 6.12 and 6.13 (Model III), equations 6.10, 6.12 and 6.15 (Model IV). The number in bold is to show that its value is quasi-similar to the one found from the fit of Weibull model into the GF release profiles, Table 6.3 172

7.1 Summary of PLGA NP formulations, using acid (RG504H) and ester ended (RG504) polymer 194

7.2 Summary of experimental conditions used to investigate the effect of initial water content on PLGA NP size and morphology, using dialysis method 195

7.3 PLGA-PEG nanoparticles formulations.[a] PLGA-PEG was synthesized according to (Cheng et al., 2007). Stepwise description is provided in Section A5.1, Appendix 195

7.4 Comparative analysis of NP size and charge synthesized from ester and acid ended PLGA polymer via dialysis, at 0% v/v initial water content. Effect of solubility and interaction parameters between polymer-solvent and solvent-water on the particle size and charge 213

7.5 NP size and charge synthesized by simple mixing (MeCN) and nanoprecipitation (Acetone) in the presence of lipid or PVA/PLL mixture, respectively. [a]: size of NPs as visualized via TEM 214

7.6 BET constant and surface area values estimated from gas adsorption and geometrically 215

7.7 Mean (hydrodynamic) radius and zeta potential of NPs loaded with hydrophobic agents 226

7.8 Mean size and zeta potential of NPs loaded with hydrophilic agents as synthesized via dialysis method. [a]: refers to PLGA:NEP ratio 227

7.9 Mean size and charge of NPs loaded with hydrophilic agents as synthesized via simple mixing and nanoprecipitation methods. Bold font is used to emphasize (the only) positively charged NPs formulated. [a]: there was no PVA or PLL used for this formulation 228

7.10 Theoretical drug loading (TDL) and encapsulation efficiency (EE) of hydrophobic drugs for different NP formulations. IE[a]: insufficient encapsulation as determined from LC-UV-MS and *in-vitro* cell citotoxycity studies 229

7.11 Theoretical drug loading and encapsulation efficiency of hydrophilic drugs 230

for different NP formulations. IE[a]: insufficient encapsulation as determined from the *in-vivo* brain tissue studies (ELISA assay).

7.12 Fractions(%) of encapsulated, released and unreleased TFMU from NPs synthesized from ester-ended PLGA polymer and conjugated PLGA-PEG polymer. [a]: Total drug released(%)= 100x(mass of cum. Drug released)/(mass of encapsulated drug), [b]: Measured via UV-vis by dissolving the NPs in DMF at the end of the release studies, [c]: Drug loss(%) = 100-(total drug released + drug unreleased) 232

7.13 Summary of CED infusions into the rat brain. [a]: Number of rats euthanized at 0,1,2,3,4,5 and 6 h post infusion 242

8.1 T_1 relaxation values of the bulk liquids and when imbibed in the S1 pellet, measured at 298 K 256

9.1 Pore volume and surface area of the fragmented S1 pellet sample, pre and post partial saturation with water at water relative pressure of 0.91. The values in brackets correspond to the whole pellet sample, presented in Table 5.1 269

A4.1 Size of nanoparticles synthesized via dialysis, with and without loaded agent, after freeze drying 289

List of figures

1.1 The IUPAC main types of gas adsorption isotherms (Sing et al., 1985) 5

1.2 The IUPAC classification of hysteresis loops (Sing et al., 1985) 9

1.3 Schematic presentation of independent pore filling (top row) and advanced adsorption (bottom row) mechanisms. The continuous arrows show the direction of pore filling 22

1.4 Examples of adsorption and desorption scanning curves, crossing over or diverging at the lower and upper parts of a gas sorption isotherm. The arrows show the direction in the change of the pressure 24

1.5 Examples of adsorption and desorption scanning loops. The arrows show the direction in the change of the pressure 27

2.1 Distribution of protons, with spin quantum number of ½, between the high and low energy levels in the presence of a magnetic field 31

2.2 Schematic presentation of the magnetization vector, *M*, alignment before and after the application of the r.f. 90^o pulse, in the presence of a static magnetic field B_0 32

2.3 Pulse sequence for the inversion recovery, T_1, experiment 34

2.4 Typical CPMG pulse sequence for n repeats of the 180^o_y pulse 35

2.5 Schematic representation of the surface thin liquid (of thickness λ) within a pore, interacting with the bulk fluid molecules and the pore surface 36

2.6 Spin echo PFG NMR pulse sequence 38

2.7 BPP-LED pulse sequence. The empty and grey filled lines placed on the pulse field gradients row, represent the applied magnetic and small field (crusher) gradients, respectively 40

2.8	Magnetization recovery towards the equilibrium state for different multiples of T_1 relaxation times	43
2.9	Typical freeze-thaw hysteresis (continuous line) for a mesoporous sample obtained via cryoporometry NMR. Bulk supercooling and melting are also shown (dotted line). Pore melting (bottom schematic) commences via the cylindrical-type menisci from the liquid-like layer (dark grey). Pore freezing (top schematic) is nucleated by the frozen front (light grey) propagating the molten phase via hemispherical menisci. Detailed explanation of the schematic diagram is provided in the text above	48
2.10	Schematic presentation of cryoporometry NMR freeze-thaw hysteresis curves (continues line), shown in Figure 2.9, along with a crossing freezing (A→B) and crossing melting (B→A) scanning curves, a converging freezing curve (A→C) and a converging melting curve (B→E). The scanning curves are shown in dotted lines. The arrows show the direction of freezing or melting	51
2.11	Schematic presentation of cryoporometry NMR freeze-thaw hysteresis curves (continuous line), shown in Figure 2.9, along with freezing (A→A'→A) and melting (B→B→B) scanning loops. The arrows show the direction of freezing or melting	52
2.12	Schematic presentation for pores (P1, P2) melting independently by size (top row), for P2 melting via advanced melting at the same temperature, T1, as P1, by the hemispherical meniscus (dashed line) developed on the small P1 pore mouth (middle row), and melting initiated from the liquid-like layer on a dead end pore, P2 (bottom row). The arrows show the mechanism of pore melting for each pore	53
3.1	Schematic representation of the experimental set up for the equilibrium water sorption above NaOH solutions at 294 K and for the NMR experiments for the a) whole and b) fragmented samples	65
3.2	Normalized water isotherms for a sample of 30 whole pellets obtained at 21^{o}C. The water uptake was measured gravimetrically. The arrows show the direction of the water sorption process shows a close-up view of the steep parts of the melting curves for saturation at P/P_0=0.91 and 0.92	70
3.3	NMR cryoporometry melting curves for the adsorbed phase in a single pellet sample (pellet 1) at P/P_0=0.81, 0.84, 0.91, 0.92, 0.93, 0.94 and 1.0 of water vapour. The inset shows a close-up view of the steep parts of the melting curves for saturation at P/P_0=0.91 and 0.92	71
3.4	Variation of NMR spin-spin relaxation time (T_2) and unrestricted diffusion tortuosity for the adsorbed phase, obtained at the top of the melting curves (all at 273 K), with relative pressure of water vapour used to obtain the data in Figure 3.3 (pellet 1). The errors in the T_2 values are smaller than the size of the symbols	72
3.5	Freezing scanning curves for whole pellet 2 saturated at P/P_0=0.92 and 1.0 via equilibrium adsorption and via desorption at P/P_0=0.86 within their freezing and melting boundary curves. The arrows show the direction of the change in temperature	75
3.6	Freezing scanning curves for a fragmented sample saturated at P/P_0=0.92	76

	and 1.0 via equilibrium adsorption and via desorption at P/P_0=0.85 within their freezing and melting boundary curves. The arrows are shown to guide the eye	
3.7	Scanning loops for a single whole pellet saturated at P/P_0=0.92 and 1.0 via equilibrium adsorption within their freezing and melting boundary curves	77
3.8	Scanning loops for the fragmented sample saturated at P/P_0=0.92, 0.93 and 1.0 via equilibrium adsorption within their freezing and melting boundary curves. The bottom of each loop terminates at the same molten fraction	79
3.9	Scanning loops for the fragmented sample saturated at P/P_0 =0.93 and 1.0 via equilibrium adsorption within their freezing and melting boundary curves. The bottom of both loops terminates at the same temperature	80
3.10	Normalized T_2 relaxation values of pellet 2 and the fragmented sample measured at the end of the boundary melting curve for saturations at different relative pressures. Error bars for the whole pellet 2 are smaller than the size of the symbols. All the T_2 measured values are normalized to the T_2 value of the completely molten samples (fragmented or whole pellet), saturated at P/P_0=1.0	84
3.11	Normalized T_2 relaxation values of pellet 2 and the fragmented sample saturated at P/P_0=1.0, measured along the boundary melting curve, at molten fractions equivalent to the adsorbed volume fraction after partial saturation at different relative pressures. All the T_2 measured values are normalized to the T_2 value of the completely molten samples (fragmented or whole pellet), saturated at P/P_0= 1.0	86
3.12	Variation of unrestricted diffusion tortuosity for the adsorbed phase, obtained at the top of the melting curves (all at 273 K), with relative pressure of water vapour for the whole pellet 2 and fragmented sample	87
3.13	PSDs derived from the melting curves of the whole pellet 1 saturated at P/P_0=0.91 and 1.0, and the fragmented sample saturated at P/P_0=1.0 calculated via Gibbs-Thomson equation. PSD derived from nitrogen adsorption using the BJH algorithm is also included	88
4.1	Cyclohexane sorption isotherm for a batch of S1 pellets measured gravimetrically at 294 K via equilibrium adsorption above different concentrations of cyclohexane/mineral oil mixtures	109
4.2	Cyclohexane sorption isotherm for a batch of S1 pellets measured via a vapour analyser (IGA) including an adsorption and desorption scanning curves initiated from partially filled systems. The lines shown are to guide the eye. The arrows show the direction of the change in pressure	110
4.3	Boundary melting and freezing curves for a fully saturated sample of batch S1. Also shown are a reversible freezing scanning loop and a freezing scanning curve originating from different molten fractions on the melting boundary curve, along with a melting scanning curve and a reversible melting scanning loop originating from the boundary freezing curve. The arrows show the direction of the change in temperature. The lines are shown to guide the eye	111
4.4	Boundary melting and freezing curves for a fully saturated sample of	112

batch S1. Attached to the boundary melting curve for the fully saturated sample is a freezing-melting scanning loop originating at low (0.186) molten fraction. Also shown are the boundary melting curves obtained for partially saturated samples after equilibrium adsorption of cyclohexane at different partial pressures to give ultimate fractional saturations of 0.194, 0.268, 0.351, and 0.356. Individual freezing-melting scanning loops, starting from each of these boundary melting curves, were also obtained that originated at molten fractions of 0.183, 0.183, 0.185, and 0.184, respectively. The lines shown are to guide the eye

4.5 Boundary melting and freezing curves for a fully saturated sample of batch S1. Also shown are boundary melting curves obtained for partially saturated samples obtained by equilibrium desorption of cyclohexane to different partial pressures to give ultimate fractional saturations of 0.242, 0.343 and 0.416. Individual freezing-melting scanning loops originating from molten fractions of 0.182, 0.182, and 0.185, on the boundary melting curves with fractional saturation between 0.343-1.0, are also included. The inset shows a close-up of the boundary melting curves and scanning loops for partially saturated samples. The lines shown are to guide the eye 113

4.6 Schematic diagram depicting the different melting mechanisms described in the text for a set of pores with different sizes (P1, P2, P3), at a low and higher partial saturation. The dark grey represents liquid, light grey represents ice and the grey texture on the background represents the silica solid walls. The arrows show the direction of the direction in melting 116

5.1 Nitrogen sorption isotherms pre and post partial saturation with water of the whole pellet S1 material. The arrows are shown to guide the eye 129

5.2 Nitrogen sorption isotherm post water adsorption adjusted upwards by a volume of 110 cm^3(STP)/g. The nitrogen sorption isotherm pre water saturation is also included 130

5.3 Nitrogen sorption isotherm post water adsorption adjusted upwards by a volume of 380 cm^3(STP)/g. The nitrogen sorption isotherm pre water saturation is also included 131

5.4 Plots of adsorption and desorption curves of nitrogen in S1, post partial saturation with water. All the relative pressures in adsorption has been raised to a power of 1.8 132

5.5 Plot of the adsorbed amount of nitrogen in an empty fragmented S1 sample, where the relative pressures in the adsorption curve are raised into a power of 1.65. The inset shows the nitrogen sorption isotherm 133

5.6 Derived nitrogen sorption isotherm for the pores occupied by water 134

6.1 Synthesis steps of template-mediated mesoporous materials (Soler-Illia et al., 2003) 139

6.2 Molecular structure of CsA. Re-drawn from Zijlstra *et al.* (2007) 146

6.3 SEM (a, b) and TEM (c) images of a casein templated silica particle showing the particle morphology and its internal porous structure, respectively. The histogram (d) shows the particle size distribution obtained from DLS measurements (SD error bars: ±1% volume) 159

6.4	SEM (a) and TEM (b) images of a Lutrol templated silica particles showing the particle morphology and its internal porous structure, respectively. The histogram (c) shows the particle size distribution obtained by DLS (SD error bars: ±1% volume)	160
6.5	Nitrogen adsorption isotherms for casein and Lutrol templated silicas	161
6.6	a) Micropore and b) mesopore size distribution of casein and Lutrol templated silicas calculated from HK and BJH algorithms, respectively	161
6.7	Cryoporometry hysteresis loops obtained from freeze-thawing of water imbibed in the casein and Lutrol templated silicas. Molten fraction of 1 corresponds to the total pore volume. The inset shows the pore size distribution, as a change of the molten fraction with the pore diameter, where the diameter is calculated via the Gibbs-Thomson equation from the boundary melting curves of the silicas	163
6.8	Diffraction peaks of the casein and Lutrol templated silica powders. Casein scattering intensity has been shifted on the y-axis by a multiple of 12. The values displayed on the graph, show the mean q value of each diffraction peak	165
6.9	Drug release profile of CsA from casein and Lutrol templated silicas in simulated intestinal fluid. Solubility of the encapsulated CsA is compared with that of the free CsA. Error bars show the SD error for release studies performed in triplicate	167
6.10	Drug release profile of CsA from casein and Lutrol templated silicas in gastric fluid. Solubility of the encapsulated CsA is compared with that of the free CsA. Error bars show the SD error for release studies performed in triplicate	168
6.11	Drug release profile models fitted into the raw data of CsA released from Lutrol templated silicas in intestinal fluid using Higuchi (equation 6.2), Model 2 (equation 6.5), LDF (equation 6.6), and Weibull (equation 6.7) models	169
6.12	Drug release profile models fitted into the raw data of CsA released from casein templated silicas in intestinal fluid, using Higuchi (equation 6.2), Model 2 (equation 6.5), LDF (equation 6.6), and Weibull (equation 6.7) models	169
6.13	Drug release profile models fitted to the raw data of CsA released from Lutrol templated silicas in gastric fluid. Using Higuchi (equation 6.2), Model 2 (equation 6.5), LDF (equation 6.6), and Weibull (equation 6.7) models	170
6.14	Drug release profile models fitted to the raw data of CsA released from casein templated silicas in gastric fluid using Higuchi (equation 6.2), Model 2 (equation 6.5), LDF (equation 6.6), and Weibull (equation 6.7) models	170
7.1	Chemical structures of poly(lactic acid) (left) and poly(glycolic acid) (right)	182
7.2	a) Hydrolytic and b) autocatalytic degradation of PLGA co-polymer	182
7.3	Blood – Brain Barrier and Blood-Cerebral Spinal Fluid Barrier (re-drawn from (Zhang and Miller, 2005))	187
7.4	Molecular structure of drugs encapsulated in the PLGA NPs	192
7.5	Molecular structure of stabilizers used for NP synthesis	192

7.6	RG504/DMSO mixture within the dialysis tubes, dialysed against water. Left bottle: mixture at the beginning of dialysis (t=0 min). Right bottle: mixture after ~2 days of dialysis showing the emulsion formed	197
7.7	SEM images of PLGA spheres synthesized via o/w emulsion-solvent evaporation (probe sonicator) method from a) acid-ended (RG504H) and b) ester-ended (RG504) PLGA polymer	207
7.8	PLGA nanoparticles prepared from a) 100% DMSO and 0% H_2O, b) 20% DMSO and 80% H_2O, c) 100% DMF and 0% H_2O, d) 80% DMF and 20% H_2O, e) 20% DMF and 80% H_2O, f) and g) 100% MeCN and 0% H_2O, h) 80% MeCN and 20% H_2O, k) 20% MeCN and 80% H_2O v/v, and dialyzed against H_2O	209
7.9	Snapshot image from a re-constructed 3D volume texture rotating movie of a single PLGA NP synthesized via dialysis, from ester-ended PLGA polymer in DMSO, using tomo-TEM	210
7.10	Snapshot images taken from a re-constructed movie of a single PLGA NP synthesized via dialysis, from ester-ended PLGA polymer in DMSO, using tomo-TEM. Each image represents a slice (inner structure) of the NP at two different positions, perpendicular to the carbon grid	210
7.11	STEM image of a single RG504 nanoparticle synthesized via dialysis in 0.05 %w/v PVA/DMSO mixture. The black dots are gold nanoparticles coating the carbon grid	211
7.12	STEM image at a) 0^o and b) 70^o tilted angle of a single RG504/mPEG-DPSE nanoparticle synthesized by simple mixing and c) intensity profile measured at the region shown by the blue rectangle on the sphere	212
7.13	NMR cryoporometry melting curves of water in the PLGA NPs after 2 and 4 days of immersion in water. The molten fraction is normalized to the total volume of water melting at 272.8 K after 2 days of immersion in water	216
7.14	Cumulative TFMU release profile from different NP formulations in PBS (pH 7.4, 38^oC) over time. The inset graph shows a burst release of TFMU within the first 4 h	233
7.15	Brightfield, fluorescence and merged images of glioma cells incubated with RG504/NR nanoparticles (synthesized via dialysis in DMSO) at 2 h (a, b, c) and 48 h (d, e, f). Magnified image of boxed area in d: Brightfield, fluorescence and merged images (g, h, i)	240
7.16	Brightfield, fluorescence and merged images of glioma cells incubated with TFMU loaded PLGA-PEG nanoparticles (synthesized via nanoprecipitation) (a, b, c), Rhodamine loaded RG504/mPEG-DSPE (synthesized via simple mixing) (d, e, f) and Nile red loaded RG504/mPEG-DSPE (synthesized via simple mixing) (g, h, i), at 24 h post incubation	241
7.17	CED of 1 mg/ml unencapsulated Nile red into the striatum of rat brain. The images show a) the site of injection and b) the Nile red distribution around it	243
7.18	CED of 0.5 mg/ml Nile red loaded RG504 nanoparticles (synthesized via dialysis in DMSO). Brightfield (a) and fluorescence images at different magnifications (b,c,d) 1 h post infusion	243

7.19	CED of 0.5 mg/ml Nile red loaded RG504 nanoparticles (synthesized via dialysis in DMSO). Brightfield (a) and fluorescence images at different magnifications (b,c,d) 24 h post infusion	244
7.20	Volumes of distribution (Vd) following CED of NR and RG504/NR NPs (synthesized via dialysis in DMSO)	245
7.21	Ratio of volume of distribution /volume of infusion (Vd/Vi) following CED of NR and RG504/NR NPs (synthesized via dialysis in DMSO)	245
8.1	BPP-LED pulse sequence. The empty and grey filled lines placed on the pulse field gradients row, represent the applied magnetic gradients and the small field (crusher) gradients, respectively	252
8.2	Experimental set-up for the T_1 and PFG NMR measurements performed on the saturated whole S1 pellet	253
8.3	Modified inversion recovery pulse sequence. A gradient pulse is introduced after the 180^o pulse to destroy any transverse magnetization created	255
8.4	Absolute diffusion coefficients of the bulk liquids, measured at 298 K. The error bars included in the figure are smaller than the symbols. The lines are shown to guide the eye	257
8.5	Relative diffusion coefficients of the bulk liquids found by dividing the absolute diffusion coefficients by the diffusion coefficients value measured for t_r/T_1=5, for each respective bulk liquid. The error bars are included. The lines shown are to guide the eye	257
8.6	Absolute diffusion coefficients of the imbibed liquids within a S1 pellet, measured at 298 K. The error bars are included in the figure. The lines shown are to guide the eye	258
8.7	Relative diffusion coefficients of the imbibed liquids in the S1 pellet found by dividing the absolute diffusion coefficients with the diffusion coefficients value measured for t_r/T_1=5, for each respective imbibed liquid. The error bars are included in the figure. The lines shown are to guide the eye	258
9.1	Nitrogen adsorption and desorption isotherms of the fragmented S1 sample pre-water saturation, along with the adsorption isotherm post-water saturation. The arrows show the direction in the change of the pressure	270
A1.1	Log-attenuation plot of data from a T_2 relaxation experiment conducted on the 100% molten fraction of the single S1 pellet, at 273 K. The sample was saturated at P/P_0=0.84, 294 K. The solid line shows the fit to equation 3.1	273
A1.2	Log-attenuation plot of data from a PFG experiment (Δ=0.15 s and δ=0.002 s) performed for pellet 1. The sample was partially saturated at P/P_0=0.84 and the diffusion value was measured 273 K when the sample was completely molten. The raw data (diamonds) are fitted to equation 2.10	274
A4.1	Representation of Bragg's diffraction of two X-ray beams, from two parallel plans of a crystal lattice	277
A4.2	CsA standard calibration curve obtained by HPLC	279
A4.3	Far-UV CD spectra of sodium casein in media with a) pH 7 and b) pH 2	280

and pH 2.5. The ellipticities are expressed in (deg cm^2 d/mol)
A4.4 FTIR spectra of a) Lutrol (F127) and b) sodium casein templated silicas 282
A4.5 FTIR spectra of a) purchased and b) re-crystallized CsA recovered from absolute ethanol dissolution 283
A5.1 ^1H NMR (300MHz) spectra for NH_2-PEG-CH_3 and PLGA-COOH polymers and conjugated PLGA-PEG copolymer 285
A5.2 Nitrogen sorption isotherm (77.3 K) of PLGA NPs synthesized via dialysis method in DMSO. The high nitrogen uptake above P/P_0=0.96 corresponds to the interparticle nitrogen condensation 286
A5.3 Krypton adsorption isotherm (77.3 K) for PLGA NPs synthesized via dialysis method in DMSO 286
A5.4 Calibration curves for a) 70 kDa and b) 150 kDa FITC-Dextran in ultrapure water measured fluorimetrically (wavelength excitation: 495nm, emission: 505nm) 287
A5.5 Calibration curve of TFMU dissolved in DMF measured via UV-vis spectroscopy at 337 nm absorbance wavelength 288
A5.6 Calibration curve of Nile Red dissolved in DMSO measured via UV-vis spectroscopy at 553 nm absorbance wavelength 288

Abbreviations

Acronym	Definition
5-FU	5-Fluororacil
AcSF	Artificial spinal fluid
ADL	Actual drug loading
ASAP	Adsorption surface area porosimeter
BPP-LED	Bipolar pulse longitudinal eddy current delay
CED	Convection enhanced delivery
CO_2	Carbon dioxide
CPG	Controlled pore glass
CsA	Cyclosporine-A
DCM	Dichloromethane
DFT	Density functional theory
DLS	Diffraction light scattering
DMF	Dimethyl formamide

DMSO	Dimethylsulfoxide
DSPE	Distearoyl-sn-glycero-3 phosphoethanolamine
EE	Encapsulation efficiency
ELISA	Enzyme-linked immunosorbent *assay*
EtOH	Ethanol
FID	Free induction decay
FITC-Dextran	Fluorescein isothiocyanate dextran
FTIR	Fourier transform infrared spectroscopy
GCMC	Grand canonical Monte Carlo
H_2O	Water
HPLC	High-performance liquid chromatography
IF	Stimulated intestinal fluid
IG	Stimulated gastric
IUPAC	International Union of Pure and Applied Chemistry
Kr	Krypton
MeCN	Acetonitrile
MeOH	Methanol
MS	Mass spectrometer
N_2	Nitrogen
NEP	Neprilysin
NMR	Nuclear magnetic resonance
NP	Nanoparticle
NR	Nile red
PBS	Phosphate buffered saline
PEG	Polyethyleneglycol
PFG	Pulsed field gradient
PLGA	Poly lactic-co-glycolide)
PLL	Poly-L-Lysine hydrobromide
PVA	Polyvynil-acohol
r.f.	Radiofrequency pulse
Rdh	Rhodamine B
RG504	Ester-ended PLGA polymer
RG504H	Acid-ended PLGA polymer
rms	Root mean square
SD	Standard deviation

SAXS	Small angle light scattering
SE	Spin echo pulse sequence
STE	Stimulated echo pulse sequence
STEM	Scanning transmission electron microscopy
STP	Standard temperature and pressure (273.15 K and 1 atm)
TDL	Theoretical drug loading
TEM	Transmission electron microscopy
TFMU	4-(trifluoromethyl)-umbelliferone
Tomo-TEM	TEM tomography

Nomenclature

Symbol	Definition	Unit
A	External surface area of the drug carrier	m^2
B_0	Static magnetic field	T
B_1	Time-dependant magnetic field	T
C	BET constant	-
C_m	Drug content per drug carrier unit volume	g/cm^3
C_s	Drug solubility	g/ml
d	Mean size of the mesopores (Chapter 6)	nm
D	Fractal dimension of the surface	-
D_0	Unrestricted diffusion coefficient in the pores	m^2/s
$d1$	Time delay between the pulses	ms
D_b	Diffusion coefficient in the bulk (liquid) phase	m^2/s
D_B	Free bulk diffusion of the drug	m^2/s
D_{eff}	Effective diffusivity	m^2/s
D_{intra}	Drug diffusivity within the particle (Chapter 6)	m^2/s
D_{PFG}	Diffusion coefficient from a PFG experiment	m^2/s
FID	Free induction decay signal	-
g	Pulse field gradient	T/m
G	Magnetic field gradient vector	T/m
G_z	Magnetic field gradient vector in the z-direction	T/m

h	Planck's constant	6.626×10^{-34} Js
I	Nuclear spin quantum number	-
I	NMR signal intensity	-
I_0	NMR reference signal intensity	-
k, k_1, k_2, k_3	Kinetic time constants	1/s
k_B	Boltzman constant	1.38×10^{-23} $m^2/(kgKs^2)$
k_{GT}	Gibbs-Thomson constant	nmK
M	Net magnetization vector	J/T
M_0	Magnetization at time zero	J/T
m_a	Mass of the phase adsorbed	g
m_s	Mass of the dry sample	g
MW	Molecular weight	g/mol
M_z	Net magnetization vector at certain recovery fraction	J/T
n	Number of the adsorbed phase layers	-
n	Specific amount of gas adsorbed	mol/g
N_A	Avogadro's constant	6.023×10^{23} 1/mol
P	Equilibrium pressure	Atm
P/P_0	Relative pressure	-
Q_t	Amount of drug released with time	g
R	Universal gas constant	8.315 J/mol/K
r	Particle size	nm
r_d	Radius of the drug	m
r_p	Pore radius	nm
S/V	Surface-to-volume ratio	m^2/m^3
S_{BET}	BET surface area	m^2/g
S_L	Langmuir surface area	m^2/g
T	Temperature	K
t	Time	h
t	Multilayer thickness	nm
t	Liquid-like layer thickness	nm
T_1	Longitudinal relaxation	ms
T_2	Spin-spin or transverse relaxation	ms
T_{2av}	Average transverse relaxation time	ms
T_{2B}	Transverse relaxation time constant for the bulk	ms

T_{2S}	Transverse relaxation time constant for the surface	ms
taq	Signal acquisition time	ms
T^f_2	Transverse relaxation time for the fast component	ms
T_g	Glass transition temperature	K
T_m	Bulk melting temperature	K
tr	Repetition time (total recycle delay time)	ms
T^S_2	Transverse relaxation time for the slow components component	ms
V	Volume of gas adsorbed	cm^3 (STP)
V	Pore volume (NMR)	m^3
V_0	Pore volume (Gurvitch)	cm^3/g
Vd	Volume of distribution	mm^3
Vi	Volume of infusion	µl
V_m	Monolayer volume	cm^3/g
V_M	Molar volume at 77.3 K	cm^3/mol
V_n	Molar volume at STP	cm^3/mol
Vp	Micropore volume	cm^3/g
x	Pore size	nm
x,y,z	Axis	-
ΔG	Change in Gibbs free energy	J/mol
ΔS	Change in the molar entropy	J/mol
ΔE	Difference between the high and low energy levels	
ΔH	Change in the molar enthalpy	J/mol
ΔTf	Freezing point depression	K
ΔTm	Melting point depression	K

Greek letters	**Definition**	**Unit**
γ	Surface tension	N/m
γ	Gyromagnetic ratio	Rad/T/s
γ_{sl}	Surface tension between the liquid and the solid	N/m
Δ	NMR diffusion time	s

δ	NMR diffusion length	s
$\Delta\delta_{ps}$	Solubility parameter difference between the polymer and the solvent	$MPa^{1/2}$
$\Delta\delta_{sw}$	Solubility parameter difference between the solvent and the water	$MPa^{1/2}$
ε_p	Porosity	-
ϑ	Contact angle between the adsorbate and adsorbent	Degrees
λ	Thickness of the surface-affected layer for relaxation	nm
λ	Ratio between the radius of the drug (or solute) molecule to the radius of the pore	-
μ	Dynamic viscosity of the drug	mPa s
ν	Frequency of NMR radiation	Hz
π	Number	3.14
ρ	Density	g/cm^3
σ	Molecular cross-sectional area of the adsorbate	nm^2
σ_m	Thickness of the monolayer	nm
σ_{sl}	Surface energy of the crystal-liquid interface	N/m
τ	Delay time between the pulses	s
τ_0	Correction time	s
τ_p	Tortuosity	-
χ_{ps}	Polymer-solvent interaction parameter	-
χ_{sw}	Solvent-water interaction parameter	-

Introduction

1. Characterization of porous materials

Porous materials have a broad application ranging across industrial areas such as catalysis, health-care, ceramics and construction. Particularly in catalysis, robust microporous and mesoporous solids supports exhibiting a high surface area and porosity are needed to support heterogeneous catalysts. The chemical reaction occurs on these sites of the porous support, thus it is crucial for both the reactants and the products to be able to diffuse towards and away from these active sites in order to facilitate high activity and prevent catalyst deactivation. When this process is diffusion-limited a high concentration of reactants does not reach the active sites located within the centre of the particles, especially when their diffusion is hindered by narrow pores towards the particle's exterior. When the process is reaction-limited, the reactants are more free to distribute throughout the porous matrix, and the concentration of the reactive sites needs to be high to improve the efficiency of the catalyst. Therefore, it is necessary to evaluate the pore structure of the catalyst in order to understand and improve its performance. One of the key descriptors of the void space is the pore size distribution conventionally estimated by gas sorption or more recently using the NMR cryoporometry technique. Although, much effort has been made to improve the sensitivity and accuracy of these techniques, the processes involved in sorption and thermoporometry are not completely understood, thus the calculation of pore sizes is subject to inaccuracies. Both macroscopic and microscopic approaches have been suggested to describe the mechanism of these processes, such as those that give rise to hysteresis. However, it has not yet been decided which pore characterization technique and data analysis algorithm is best able to probe the width of the pore size distribution in a porous system. In gas sorption the adsorption branch of the hysteresis loop is recommended by the International Union of Pure and Applied Chemistry (IUPAC) to be converted into pore size distribution, usually via the Barrett-Joyner-Halienda (BJH) or the density functional theory (DFT) algorithms. In NMR cryoporometry, the melting curve is used for the estimation of pore sizes via the Gibbs-Thomson equation. However, both of these approaches to characterization do not account for cooperative phenomena, which are

said to arise when the key physical process probing the void space structure involves interactions between the pores of differenent characteristic dimension. These cooperative effects include advanced adsorption and advanced melting which can skew the apparent pore size distribution. It is therefore essential to evaluate the extent of these cooperative effects in order to measure the pore size distribution with the requisite accuracy to account for the activity of a porous material.

Similar types of porous materials, that are used as catalyst supports, can also be used as drug delivery systems to improve the therapeutic efficiency of the free drug molecules, particularly those which cannot be administered efficiently to the target areas due to biological barriers or unfavourable conditions of the local environment. For example, highly hydrophobic drugs exhibit low bioavailability, and thence, increasing their dissolution in a controlled and sustained manner is critical. By loading the drug molecules into particles, higher drug dosage can be delivered to the site of interest, and with minimal side effects. Silica and polymer based porous particles are currently being used as drug carriers due to their easily tailored pore structure and their biocompatibility. The drug encapsulation efficiency and the drug release rate are controlled by the pore structure, the particle morphology and the environment present. Therefore it is necessary to use accurate pore characterization and imaging techniques to completely survey the drug delivery system, and subsequently understand its performance.

In the case of drug encapsulation into biodegradable polymer systems, the release rates are also controlled by the movement of the polymer segments in the matrix (swelling, shrinking) when water penetrates through these systems, and their rate of degradation or erosion. Although many polymer systems, such as particles, films or foams, have been synthesised for drug delivery, only a few of them are currently available in the market because their release mechanism is not thoroughly understood. Thus, is it important to improve the sensitivity of current characterization techniques to gain a better insight into the interior space of these systems. Of specific relevance to their work described in this thesis is the use of biodegradable and biocompatible polymer particles as potential carriers of therapeutic agents for the treatment of diseases occurring in the central nervous system. For this application, convection-enhanced drug delivery (CED) is

suggested as a sophisticated method to deliver these nanoparticles directly into the target area by avoiding restrictions otherwise imposed by the blood-brain barrier, or their rapid clearance from the circulatory system. However, optimization of the nanoparticles with respect to their size and encapsulation efficiency for CED studies has not yet been done and needs to be investigated. Moreover, these systems have a low glass transition, or melting point temperature, and also the nature and the degree of intermolecular interactions between these polymers and different gases are not known. Hence, pore characterization using the gas sorption technique is difficult. NMR cryoporometry is, thus, suggested as an alternative technique to overcome these difficulties, although this method is still under development and its applicability to probe the void space of different polymer structures needs to be further tested.

Other NMR techniques, such as pulse field gradient (PFG) NMR are also used to probe the pore connectivity of porous matrixes, and thence the effective diffusivity of diffusing molecules therein. However, this method often requires long experimental times, which could possibly be reduced if more sophisticated pulse sequences were used.

2. Thesis structure

This thesis will focus on the issues raised above and it is divided into nine chapters as follows:

Chapter 1: This chapter introduces the reader into the fundamentals of gas sorption and the void space descriptors that can be obtained from this technique. Emphasis will be given to the errors induced when converting a sorption isotherm into a pore size due to cooperative effects which are ignored. A literature background is provided describing the recent advances to develop the method by firstly detecting the source of the errors and then by improving the (gas sorption) method.

Chapter 2: This chapter will provide the reader with the background theory to NMR characterization techniques, namely NMR cryoporometry, PFG NMR and NMR

relaxometry. Then the cooperative effects in NMR cryoporometry will be discussed and compared to those in gas sorption.

Chapter 3: This experimental chapter uses a combination of gas sorption and NMR techniques to probe advanced melting and advanced adsorption of water in a mesoporous silica support, with an ink-bottle pore shape. Cryoporomety scanning curves and loops are adopted to aid to their understanding of advanced phenomena. Moreover, pore blocking effects in desorption and freezing are detected and discussed.

Chapter 4: This experimental chapter studies the sorption and cryoporometry melting and freezing mechanisms of cyclohexane, which has weak interactions with the silica surface hence, it is susceptible to different advanced phenomena to those observed for water. The results obtained are used to further interpret the cause of hysteresis and, a pore filling and melting mechanism will be proposed. Scanning curves and loops are used to provide more information about these processes.

Chapter 5: This chapter uses an integrated nitrogen-water-nitrogen experiment to probe the extent of advanced phenomena for water and nitrogen and to compare their adsorption mechanism in a mesoporous catalyst support.

Chapter 6: This work is part of a collaboration with the University of Strathclyde. Two porous silicas were synthesised by using two different templates. They were then used as drug delivery carriers to improve the dissolution of a highly hydrophobic protein in the gastrointestinal area. The aim of the work was the characterization of the porous silicas , using the characterization techniques discussed in the previous chapters, for the investigation of structure-transport relationships developed in these materials, able to control the drug release rates.

Chapter 7: This work is part of a collaboration with the University of Bristol and it presents different synthesis methods for the optimization of drug loaded PLGA nanoparticles for CED studies. Moreover, pore characterization techniques are used to investigate the inner core of the nanoparticles, able to influence the drug delivery rates.

Chapter 8: This part investigates the possibility of reducing the experimental time of PFG NMR experiments, one of the main techniques used to study the porous materials, by maintaining the signal-to-noise ratio high.

Chapter 9: This chapter provides a summary of the main findings discussed in the previous chapters and suggests possibilities for future work.

Chapter 1
An introduction to gas sorption characterization technique

1.1 Introduction

Gas sorption is a characterization technique which provides information about the surface area, the pore size distribution, the pore connectivity, and the pore volume of porous materials, which are widely used in catalysis and pharmaceutics. Although improvements have been introduced to the method to better understand the sorption mechanism and the origin of hysteresis, critical for accurate data interpretation, the method still relies on auxiliary assumptions which need further investigation about their validity.

The main purpose of this chapter is firstly to introduce the reader into the fundamentals of gas sorption and the origin of hysteresis, and secondly to illustrate the drawbacks of this characterization technique specifically for calculating the pore size distribution. The most common algorithms used for estimation of pore sizes in industry assume the pores are independent of one another and neglect the possibility of any pore-pore interactions during gas adsorption. The reader is thus introduced to the 'advanced adsorption' mechanism, during which a filled pore enhances the filling of an adjoined empty pore at a lower pressure. Moreover, an introduction to sorption scanning curves is provided, as a test to examine the 'independent domain theory' and the extent of cooperative phenomena occurring in gas sorption.

Some of the terms used for pore characterization in this work are stated in Table 1.1 and they are defined by IUPAC (Sing et al., 1985).

Term	Definition
Porous Solid	Solid with cavities or channels which have a greater depth than width
Open Pore	Cavity of channel with access to the surface of the particle
Interconnected Pore	Pore which communicates with other pores
Closed Pore	Cavity not connected to the surface
Void	Space between particles
Pore Size	Pore width – minimum dimension
Micropore	Pore of internal width less than 2 nm
Mesopore	Pore of internal width between 2 and 50 nm
Macropore	Pore of internal width greater than 50 nm
Pore Volume	Volume of pores determined by stated method
Porosity	Ratio of pore volume to apparent volume of particle or granule
Surface Area	Extent of total surface area as determined by given method under stated conditions
Specific Surface Area	Surface area per unit mass of powder, area determined under stated conditions
External Surface Area	Area of surface outside pores
Internal Surface Area	Area of pore wall
Tortuosity	The path available for diffusion through a porous bed in relation to the shortest distance across

Table 1.1 Terms and definitions of porous materials by the IUPAC (Sing et al., 1985)

1.2 The adsorption mechanism

When a porous solid is exposed to a gas at a certain pressure and temperature, the gas is adsorbed onto the surface until equilibrium is reached. Adsorption is brought about by the interactions between the solid and the gas molecules and can be divided into two categories, chemical adsorption and physical adsorption, depending on the strength between the adsorbed species (adsorbate) and the porous solid (adsorbent). The former process involves the formation of irreversible chemical bonds between the gas and the surface and requires high heats of adsorption (Rouquerol et al., 1999). The latter process is completely reversible and is driven by weak dispersion and dipole-dipole forces (also called London or van der Waals forces) which are associated with low heats of adsorption. For physical adsorption, when a gas molecule approaches the adsorbent surface, the electron cloud of the gas molecules overlaps with that of the solid surface, thus increasing the interaction potential at short distances. As the interactions between the gas and the surface are greater than those exhibited between the gas molecules, the gas molecules reside on the surface, forming a statistical monolayer. At very low relative pressures the more energetic sites are those to be covered first, such as narrow pores, or spaces between horizontal and vertical edges of surface steps where the gas molecules can interact with the surface atoms in two planes. As the pressure increases the surface will be filled up with more gas molecules which are progressively attracted by the previously formed layer, via van der Waal forces. This type of surface coverage is known as multilayer adsorption (Gregg and Sing, 1982).

For the physical adsorption process to take place, the change in the Gibbs' free energy, ΔG, must be negative and the overall process exothermic, shown by the following equation:

$$\Delta \mathrm{H} = \Delta G + T\Delta S \qquad (1.1)$$

where ΔS is the change in the entropy of the system (negative), ΔH is the change in the heats of adsorption and T is the temperature (Gregg and Sing, 1982).

All the adsorption studies performed in this work are driven by a physical adsorption process, thus an interpretation of the chemical adsorption process will not be discussed.

1.3 The adsorption isotherm

The specific amount of gas adsorbed, *n* (volume of gas adsorbed per gram of solid), is controlled by the equilibrium pressure, *P*, temperature, *T*, and the gas-solid system. This is expressed by equation:

$$n = f(P, T, system) \tag{1.2}$$

Assuming that the gas sorption process is isothermal, then the amount adsorbed is solely dependant on the pressure and the following expression can be instead used:

$$n = f(P) \tag{1.3}$$

When gas sorption takes place below the critical temperature of the adsorbate, then the equation above becomes:

$$n = f(P / P_0) \tag{1.4}$$

where P_0 is the saturation pressure of the gas at temperature *T*.

As discussed earlier at low pressures the smaller pores fill before the larger ones. A plot of the amount adsorbed against the relative pressure produces a sorption isotherm. The shape of the isotherm provides information about the type of the pores (shape, size, structure ordering), and the pore filling and emptying mechanism. The IUPAC recognizes six main types of isotherms, shown in Figure 1.1. The reversible *Type I* isotherm is generally characteristic of a microporous material. The micropores are filled with gas at low relative pressures and as it approaches P/P_0=1.0, the isotherm plateaus showing that all the pores are completely saturated with gas. The reversible *Type II* isotherm, is typical of a non-porous or a macroporous system, where once a statistical monolayer coverage (point B) is formed, a multilayer develops; its thickness increases progressively with pressure until P/P_0=1.0, without plateauing. *Type III* isotherm is indicative of weak adsorbent-adsorbate interactions preventing gas deposition on the surface. Isotherms of

Type IV are characteristic of mesoporous materials. After the multilayer adsorption regime, the gas condenses within the pores and a sharp increase in the gas uptake is observed. All the pores are completely saturated before P/P_0=1.0. By reversing the pressure, gas desorption takes place at lower pressures than adsorption, creating a hysteresis between the adsorption and desorption processes. *Type V* isotherm illustrates the pore filling and emptying mechanism in a mesoporous solid where weak adsorbent-adsorbate interactions exist. The *Type VI* isotherm is associated with layer-by-layer adsorption on a highly uniform surface but it belongs to a relatively rare case. The porous systems studied in this work exhibit a *Type I* or *Type IV* isotherm.

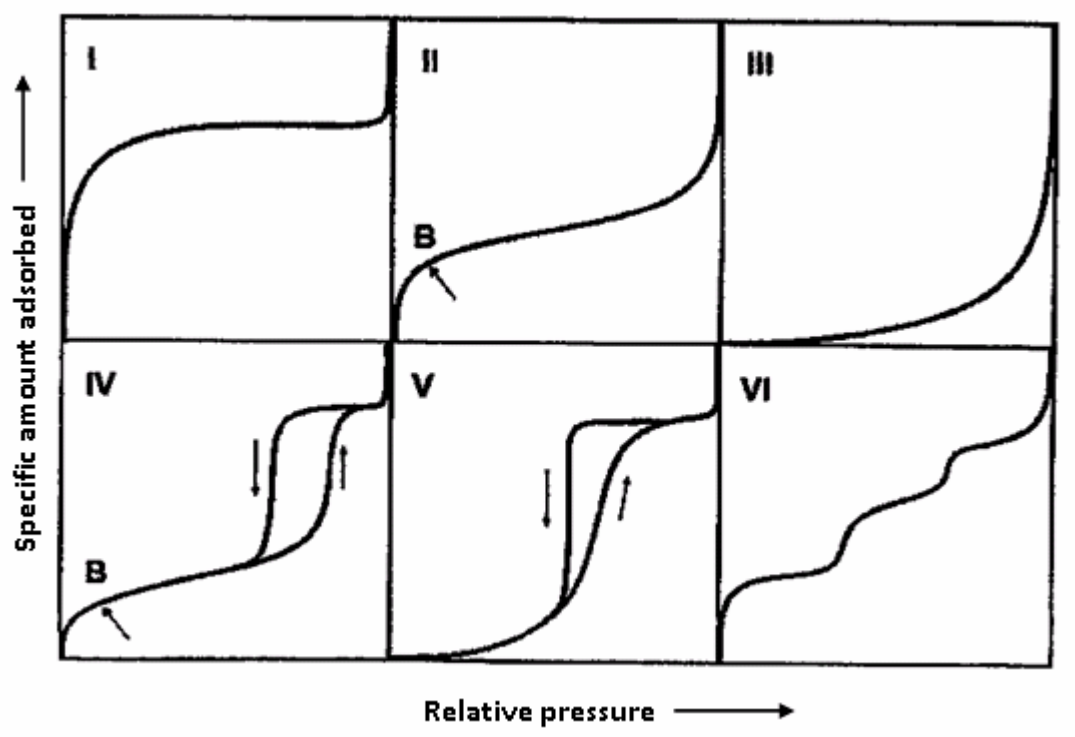

Figure 1.1 The IUPAC main types of gas adsorption isotherms (Sing et al., 1985)

1.4 Assessment of microporosity

Gas adsorption on the micropore walls occurs at very low pressures due to enhanced adsorption energy, resulting from strong interactions between the gas molecules and the pore surface. There exist two different micropore filling mechanisms. The first one occurs

below relative pressures of 0.01, where individual gas molecules access the very narrow micropores to form a monolayer. The second one appears between relative pressures of 0.01 and 0.2 in wider pores and is a cooperative process involving additional interactions between the gas molecules themselves, leading to formation of more layers. It is possible for some materials to have mesopores in addition to micropores. In this case, a *Type IV* isotherm is expected to be seen, where the hysteresis loop verifies the presence of mesopores, and the high volume adsorbed at low pressures indicates the existence of micropores.

1.4.1 Micropore surface area determination

Micropore surface area is estimated using Langmuir equation, under the assumptions that monolayer adsorption has taken place at a constant heat of adsorption with coverage. This is expressed as follows:

$$\frac{P}{V} = \frac{1}{V_m b} + \frac{P}{V_m} \tag{1.5}$$

where V is the volume adsorbed at the equilibrium pressure, P, V_m is the monolayer capacity and b is the adsorption constant indicative of the interaction strength between the adsorbate and adsorbent. A plot of P/V versus P yields a straight line with a slope A and an intercept B which allows the estimation of V_m and b, as follows:

$$V_m = \frac{1}{A} \tag{1.6}$$

$$b = \frac{1}{V_m B} \tag{1.7}$$

The Langmuir specific surface area, S_L, is then determined by the expression:

$$S_L = V_m N_A \sigma \tag{1.8}$$

Where N_A is the Avogadro constant (6.023×10^{23} 1/mol) and σ is the molecular cross-sectional area of the adsorbate. The value of σ depends on the temperature and

the adsorbent surface. Nitrogen adsorption is considered to be the most suitable adsorbate for surface area determinations as it is an inert gas which forms a close-packed monolayer at 77.3 K, with $\sigma(N_2)$=0.162 nm^2, although it may vary ~20% between different adsorbents. Arbitrary adjustments of the σ value have to be done for other adsorbates, in order to bring the estimated surface area into agreement with the value found from nitrogen adsorption. In some cases, ie for Krypton, the cross-sectional area calculated might differ appreciably from that of the closed-packed monolayer, depending on the density of the solid surface (Sing et al., 1985).

1.4.2 Micropore volume

The capacity of the micropores in a porous solid can be expressed in terms of micropore volume, V_p. Methods such as the t-plot, α_s-plot, Hovarth-Kavazoe (HK), density functional theory (DFT) and Dubinin-Radushkevich (DR) can be used for the determination of the micropore volume.

The *t*-plot method is more often adopted to estimate the micropore capacity in solids which exhibit additional mesoporosity. In this method, the multilayer thickness of a given porous solid is compared to that of a non-porous reference material, with similar surface chemistry. The multilayer thickness, *t,* of the reference material is estimated by the following relationship:

$$t = \frac{V}{V_m}\sigma_m \tag{1.9}$$

where V is the amount of gas adsorbed, σ_m is the thickness of the monolayer and V_m is the monolayer capacity. The thickness of a monolayer of nitrogen at 77.3 K is 3.45 Å (Lowell et al., 2004). The amount of gas adsorbed is then plotted versus the thickness. Horizontal departures from the straight line imply the existence of micropores, whereas more vertical plots reveal the presence of mesopores. The intercept obtained from extrapolation on the positive ordinate corresponds to the micropore volume.

For nitrogen adsorption at 77.3 K on surfaces which contain oxygen sites, Harkins and Jura, (1945) derived the following relationship to calculate the multilayer thickness:

$$t = \left[\frac{13.99}{0.034 - \log(P / P_0)} \right]^{0.5} \qquad (1.10)$$

This *t*-plot method is used in Chapter 6 to measure the micropore volume in the silicas.

1.4.3 Pore size distribution

The size of the micropores is usually estimated by applying the HK or, the semi-empirical methods in the low pressure regime. The HK model is based on a quasi-thermodynamic approach, where micropores of a certain size fill at a certain pressure characteristic of the adsorbent-adsorbate interaction energy (Lowell et al., 2004; Rouquerol, 1999). The method was initially proposed for the evaluation of micropores in carbon molecular sieves via nitrogen adsorption, but it was then extended to cylindrical-type geometry pores by Saito and Foley, 1995. There are some drawbacks accompanying the HK model, as it assumes that a) the confined fluid behaves similarly to the bulk fluid, b) it ignores the local density change of the fluid in close proximity with the walls and c) it requires calibration of the interaction energy parameters using known materials, which may not be valid for all the porous materials. To overcome the averaged bulk properties and the change in the local density, the DFT method was proposed but this method again requires calibration of the interaction energy between the gas molecules and the surface, using specific ordered materials of known surface chemistry. HK method will be employed to estimate the size of the micropores in the silica materials studied in Chapter 6 via nitrogen adsorption. This is because for nitrogen adsorption in silicon oxide based materials, the interaction parameters are found to be similar to those of nitrogen on carbon surfaces, thereby the size of the micropores can be accurately calculated (Storck et al., 1998; Saito and Foley, 1995).

1.5 Assessment of mesoporosity

Gas sorption in a mesoporous solid produces a *Type IV* isotherm, where the initial part of the isotherm follows the shape of the *Type II* isotherm but at higher pressures the volume adsorbed is much higher, and the isotherm swings upwards. This abrupt change in the volume adsorbed is due to capillary condensation in the mesopores. At low pressures, monolayer and multilayer adsorption of a vapour phase takes place but as the pressure increases there comes a point where the pores fill with a liquid-like phase separated by the vapour phase via menisci. Capillary condensation is necessary for the appearance of hysteresis in a gas sorption, in which case the pores empty at lower pressures than those that they filled.

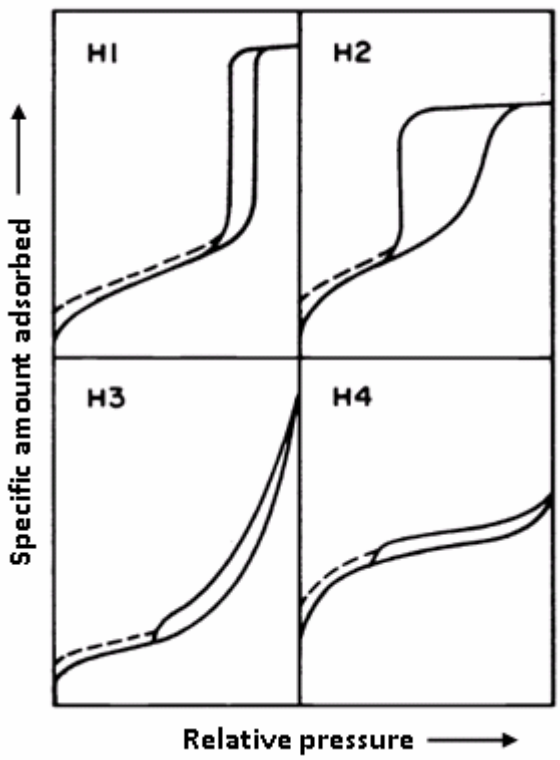

Figure 1.2 The IUPAC classification of hysteresis loops (Sing et al., 1985)

The shape of the hysteresis loop provides information about the pore structures. Figure 1.2 shows the four types of hysteresis loops classified by IUPAC. Type H1 loops are associated with ordered mesoporous materials, exhibiting a narrow pore size distribution of well defined cylindrical pores, such as those in MCM-41 and SBA-15 systems. H2 type

hysteresis is characteristic of disordered material, such as Vycor, which have a broad pore size distribution and pore shape. H3 and H4 loops are both indicative of slit-like pore geometry but H4 type loop has a higher micropore volume. H3 and H4 hysteresis loops will not be seen in this thesis.

1.5.1 Mesopore surface area measurements

The most commonly used method for estimation of the surface area in mesoporous solids, is the method proposed by Brunauer, Emmett and Teller (BET), which extends the Langmuir single-layer adsorption adsorption to infinite adsorbed layers (Brunauer, 1938). The BET method assumes that the pore surface is flat and energetically homogeneous, so that all the adsorption sites are equivalent. Moreover, it is assumed that there are no lateral interactions between the adsorbed molecules, and the heat of adsorption is the same as the latent heat of vaporisation for all the layers above the first.

The BET equation is applied on the multilayer region, in the relative pressures range that gives the best fit for equation 1.11, with a positive C constant. Usually this is between P/P_0=0.05 and 0.3 to avoid the influence of the high adsorption potentials developed in any micropores present and to obtain the best fitting, which gives a positive C constant. The BET expression is given by:

$$\frac{1}{V(1-P/P_0)} = \frac{1}{V_m C} + \frac{C-1}{V_m C}\left(\frac{P}{P_0}\right) \qquad (1.11)$$

where V is the volume of the gas adsorbed at a relative pressure P/P_0, C is the BET constant and V_m is the monolayer capacity. The BET constant C is related exponentially to the heat of adsorption on the first monolayer and it is indicative of the magnitude of adsorbate-adsorbent interactions. When strong interactions are favoured, C is ~100 whereas for weak interactions, C is <20.

A plot of $(P/P_0)/[V(1- P/P_0)]$ versus P/P_0 yields a straight line where V_m and C can be determined from the slope and the intercept of the curve. The BET (specific) surface area, S_{BET}, is then calculated via the expression:

$$S_{BET} = V_m N_A \sigma \tag{1.12}$$

The mass of the solid required for an adsorption experiment should have a surface area of (at least) 20 m^2, such that adsorption on the sample is large compared to the 'dead space' correction (space around the particles, occupied by non-adsorbed gas). However, when the porous solids have a low specific surface area (i.e. <5 m^2/g) and their amount is limited, adsobates with relatively low vapour pressure, such as krypton (Kr) or xenon (Xe) at 77.3 K are used to minimise the 'dead space' correction. Chapter 7 will present krypton adsorption studies performed to measure the low surface area of polymer nanoparticles synthesised for drug delivery into the brain. As previously stated in Section 1.4 the evaluation of the surface area becomes complicated because the cross-sectional area, σ, varies between solids. For example, σ(Kr)=0.17-0.23 nm^2 and σ(Xe)=0.17-0.27 nm^2 (Sing et al., 1985). It is generally accepted, though, that it remains nearly constant for nitrogen at 77.3 K and surface areas estimated via nitrogen adsorption are more accurate. Hence it was necessary, the surface area of the polymer nanoparticles obtained from krypton adsorption to be compared to that found from nitrogen adsorption.

1.5.2 Pore volume

The amount of gas adsorbed until a certain pore filling is converted to pore volume usually via the Gurvitsch rule as follows:

$$V_0 = \frac{V}{22414} V_M \tag{1.13}$$

where V_0 is the pore volume corresponding to an amount of gas adsorbed, V (at STP), with a molar volume V_M. For example, for nitrogen adsorption at 77.3 K, V_M is 34.68 cm^3/mol.

The total pore volume is calculated at complete saturation conditions. The presence of micropores in addition to the mesopores, though, will contribute to the total pore volume estimated. In order to differentiate these pore volumes from one another the *t*-plot analysis can be adopted to estimate the micropore volume separately, as discussed in Section 4.2.

1.5.3 Pore size distribution

In the capillary condensation regime, according to the Cohan model, the pores fill progressively with a liquid-like phase via cylindrical type menisci initiated from the pore walls, whereas during the evaporation process, the liquid phase evaporates from the hemispherical menisci developed in contact with the vapour phase. The relative pressure where these processes occur can be related to the pore size via Kelvin equation as follows:

$$\ln\left(\frac{P}{P_0}\right) = -\frac{a\gamma V_M \cos\theta}{RTr_p} \tag{1.14}$$

where r_p is the pore radius, γ is the surface tension of the liquid, V_M is the molar volume of the adsorbate, ϑ is the contact angle between the adsorbate and adsorbent, T is the temperature and R is the universal gas constant. The variant α is a geometry parameter and depends on the pore shape; for open cylindrical pores at both ends, α = 1, and for dead end pores, or desorption, α = 2.

Before capillary condensation commences multilayer adsorption takes place and the adsorbed layer developed has to be taken into account for pore size measurements.

Therefore, equation 1.14 is modified into the following expression to account for the multilayer thickness:

$$\ln\left(\frac{P}{P_0}\right) = -\frac{a\gamma V_M \cos\theta}{RT(r_p - t)} \tag{1.15}$$

where t is the thickness of the multilayer. The contact angle ϑ ranges from 0^o to 180^o, and it is assumed to be 0^o when the adsorbate wets the surface perfectly, although it is unrealistic on a molecular level. Hence the above equation is simplified to:

$$\ln\left(\frac{P}{P_0}\right) = -\frac{a\gamma V_M}{RT(r_p - t)} \tag{1.16}$$

The multilayer thickness of the adsorbed phase on silica surfaces is estimated via equation 1.10, assuming that the film covers the pore surface uniformly. The Kelvin equation and the film thickness are included as part of an algorithm developed by Barrett, Joyner and Halenda (BJH) to produce the pore size distribution at the capillary condensation region (Barrett et al., 1951). The BJH analysis is the most common method used in industry for estimation of pore sizes, although care should be taken as it follows the assumptions made for Kelvin equation, which may not be valid for all the porous material. The validity of Kelvin equation will be discussed in the next sections of this chapter and it will be experimentally tested in Chapters 3, 4, and 5.

1.6 Fractals

Fractals are structures that posses self-similarity when inspected at different length-scales and can be potentially a method to model complex geometries such as the rough surface of a porous material. The total surface area measured of a fractal pore surface is analogous to the resolution of analysis and it is expressed by the following power law:

$$\textit{Surface area} \propto \textit{(resolution of analysis)}^D \tag{1.17}$$

where *D* is the surface fractal dimension and for smooth surface is 2, whereas for a rough surface is 3. The spatial scale resolution of the analysis is usually the cross-sectional area of the adsorbed molecules used for the gas sorption studies. Thus the value of the total surface obtained may vary with the molecular size of the adsorbate used. This is because smaller molecules can enter small concavities, where big molecules (ie hydrocarbons) may not have access into. Moreover, the mechanism of adsorption is dependant on the gas-liquid-solid interactions, thus for materials with heterogeneous surface chemistry some molecules can adsorb locally and not uniformly into the pore surface. Based on these, the fractal approach can be adopted to study the change in the surface roughness after this surface has been modified, i.e. from the presence of a preadsorbed phase.

The fractal BET theory and the Frankel, Halsey and Hill (FHH) theory are commonly used to estimate the fractal dimension assuming multilayer adsorption. The BET method describes how the surface available for adsorption decreases with the number of adsorbed layers. In the FHH method, it is the thickness of the multilayer which acts as the varying ruler size to measure the surface roughness and the fractal dimension is measured using the adsorption isotherm of only one adsorbate. At the very low pressures in the monolayer regime, gas adsorption is controlled by the van der Waal forces and the FHH model is expressed as follows:

$$\ln\left(\frac{V}{V_m}\right) = c + \left(\frac{D-3}{3}\right)\left[\ln\left(\ln\left(\frac{P_0}{P}\right)\right)\right] \tag{1.18}$$

where V is the adsorbed volume of gas at different pressures, V_m is the volume of one adsorbed monolayer, c is a constant and D is the fractal dimension (Ismail and Pfeifer, 1994). A plot of $\ln V$ with $\ln(\ln(P_0/P))$, yields a straight line and D can be found from the slope gradient, $S=(D-3)/3$.

As the number of layers, n_L, increases with pressure, the surface tension will govern gas adsorption on the multilayer regime and the FHH fractal dimension is calculated as follows:

$$\ln\left(\frac{V}{V_m}\right) = c + (D-3)\left[\ln\left(\ln\left(\frac{P_0}{P}\right)\right)\right] \quad (1.19)$$

The number of layers is then calculated by:

$$n_L = \left(\frac{V}{V_m}\right)^{1/(3-D)} \quad (1.20)$$

In order to distinguish whether the van der Waal forces or the surface tension is the prevailing mechanism in adsorption, then the following test must be done:

$$X = 1 + 3S \quad (1.21)$$

where *S* is found by equation 1.18. If *X*>0, then the surface tension is negligible and equation 1.18 is used for fractal analysis. However, when *X*<0, equation 1.19 is used.

FHH fractal analysis in the upper part of the multilayer regime was used to investigate the surface roughness of a mesoporous catalyst support, before and after partially saturating this system with water. The results are presented in Chapter 5.

1.7 Hysteresis

The Kelvin equation assumes that the system is at equilibrium, thus the pore size can be estimated at varying pressures. It is though necessary to distinguish which branch of the hysteresis loop (adsorption or desorption) is at true equilibrium for the Kelvin equation to be applied. This requires an understanding of the origin of the hysteresis loop and has been described by theories based on the macroscopic level or statistical mechanics and will be now discussed.

The interpretation of the hysteresis loop based on thermodynamic fundamentals applied from the macroscopic level to the microscopic pore level, is termed as the 'classical approach' to hysteresis. This approach assumes that phase transitions in the pores are the same as those developed in a macroscopic level, and the parameters describing this

change (i.e. surface tension in Kelvin equation), receive the values of the homogenous bulk liquid or homogeneous bulk gas. Zsigmondy (1911, cited in Rouquerol et al., 1999) proposed that hysteresis occurs due to different contact angles developed in adsorption and desorption processes. Zsigmondy suggested that since adsorption commences from the pore walls, any impurities present on the pore surface will increase the adsorbate-adsorbent contact angle above 0^o but these impurities will then be displaced at higher pore filling and the adsorbate will wet the surface. In desorption though, the adsorbate completely wets the surface, thus the contact angle is 0^o. Therefore, Zsigmondy proposed that desorption is the equilibrium process, implying that the desorption branch must be used for pore size calculations. However, this interpretation is incorrect because by removing the impurities before gas adsorption, the adsorption and desorption branches must overlap, but this is not the case.

McBain (1935) and Kraemer (1931, cited in Rouquerol et al., 1999) introduced the theory of pore blocking in the desorption process due to pore structural effects. McBain suggested that in an 'ink-bottle' pore model, where an open neck is connected to a bigger dead end pore, condensation initially occurs at the dead end wall, thus filling the big pore. This pressure though exceeds that required for the small neck to fill, therefore the neck fills automatically at the same pressure as the big pore. In desorption, the liquid phase in the big pore is not in contact with the gas phase, thereby this pore empties once the pressure is reduced enough for the small neck to empty first. Based on this theory, Brunauer (1945) concluded that since the liquid is not in equilibrium with its vapour during the desorption process, adsorption must be considered as the equilibrium process.

Foster (1932), Cohan (1944), de Boer (1958) and Findenegg *et al.* (1944) described the presence of hysteresis in terms of a different meniscus shape developed in adsorption and desorption processes. Foster suggested that when there are no dead end pores in the system, condensation in the pores is 'delayed'. In the open pores condensation occurs from the multilayer developed on the pore walls. As the pressure is altered, the multilayer thickness increases, and there becomes a point where the layers from the opposite walls bridge, thus forming a hemispherical shape meniscus which propagates

through the pore. However, desorption is not delayed as there exist hemispherical menisci on both open ends of the pore. Foster then concluded that desorption is the equilibrium process. Cohan (1938) further developed this pore filling and emptying mechanism proposed by Foster. Cohan specified that the open pores will fill via a cylindrical or 'sleeve' type meniscus from the pore walls but they will empty via a hemispherical type meniscus as predicted by Kelvin equation for α=2. This difference in the pore geometry between adsorption and desorption is according to Cohan (1938) the reason for hysteresis. If these are the only mechanisms involved and the pore radius is much bigger than the multilayer thickness, then Kelvin equation for adsorption and desorption is expressed as follows:

$$\ln\left(\frac{P}{P_0}\right)_{ads} = -\frac{\gamma V_M \cos\theta_1}{RTr_p} \tag{1.22}$$

$$\ln\left(\frac{P}{P_0}\right)_{des} = -\frac{2\gamma V_M \cos\theta_2}{RTr_p} \tag{1.23}$$

Where $\vartheta 1$ and $\vartheta 2$ is the adsorbate-adsorbent contact angle in adsorption and desorption, respectively. By dividing the above equations, then the following relationship is obtained:

$$\left(\frac{P}{P_0}\right)_{des} = \left(\frac{P}{P_0}\right)_{ads}^{2\frac{\cos\theta_2}{\cos\theta_1}} \tag{1.24}$$

When $\vartheta 1=\vartheta 2=180^{o}$ then the Kelvin-Cohan relationship is derived and the above relationship is simplified to:

$$\left(\frac{P}{P_0}\right)_{des} = \left(\frac{P}{P_0}\right)_{ads}^{2} \tag{1.25}$$

The Kelvin-Cohan equation suggests that for independent pores filling and emptying the desorption branch can be predicted simply by squaring the relative pressures in adsorption. Thereby, the pore size can be calculated by either the adsorption or desorption branch.

Saam and Cole (1975), suggested that hysteresis in a cylindrical pore occurs due to different regimes of stability, metastability and instability on the multilayer film. According to Saam and Cole, the multilayer is stabilized by the van der Waals forces between the adsorbed film and the surface, but capillary forces between the film curvature and the vapour phase are responsible for gas condensation. The critical thickness at which the multilayer becomes metastable and the pore fills with condensate depends on the attractive adsorbate-surface interaction, the difference in the coexisting liquid and vapour bulk densities, and the surface tension. However, as evaporation takes places at lower pressures, the thickness of the multilayer is smaller. Therefore, this discrepancy in the film thickness between adsorption and desorption is the cause of the hysteresis. Findenegg *et al*. (1994) experimentally studied the Saam-Cole theory for adsorption in mesoporous Controlled-Pore Glass (CPG) material and found that it is qualitatively valid only, as it overestimates the width of the metastable region of the film. In this case, it is expected that $\vartheta_2 \neq \vartheta_1$ and the power value of equation 1.23 will be less than 2. Moreover, another approach to hysteresis was given by Broekhoff and de Boer which is a refined model to Cohan theory. The authors proposed that capillary condensation occurs due to a lack of stability of the adsorbed layer, and its thickness depends on both the pore radius and the pressure (Broekhof.Jc and de Boer, 1968a). Desorption on the other hand, starts from a stabilized capillary condensed liquid in the pores and this process is influenced by the adsorption forces from the pore walls (Broekhof.Jc and de Boer, 1968b). The curvature of the meniscus is then dependant on the distance from the walls and the pressure, thereby, its shape deviates from the well defined hemispherical one, as previously proposed by Cohan. Hence, both the different geometries of the menisci the film metastabilities are the causes of hysteresis.

The macroscopic approach though, might not be always true in a pore level or sometimes it is not clear which form of Kelvin equation (hemispherical or cylindrical meniscus) has to be applied. For example Neimark and Ravikovitch (2001) found that the Broekhoff and de Boer model was invalid for pore sizes below 7 nm and the Kelvin equation was inaccurate for pores as large as 20 nm in MCM-41 materials. Thus the statistical mechanics approach has been developed to bridge the gap. This approach studies the phase transitions in the pores taking into account the fluid density fluctuations and the gas-liquid-surface

interactions in close proximity with the surface, along with the pore geometry. The main methods include the DFT, Monte Carlo simulations and Molecular Dynamics and they will be now discussed.

In the DFT method, it is assumed that the pores are open, non-connected and the confined fluid is in thermodynamic equilibrium with the bulk fluid at a given temperature (Ball and Evans, 1989). The fluid in the bulk is homogeneous and has a constant density distribution whereas the confined fluid is subject to adsorption forces close to the pore walls, thus the density distribution is a function of the distance from the pore walls, as the pressure varies. The DFT treatment is adopted to determine the density profile of the confined adsorbate (at a given T) by minimising the grand free energy potential in the system, which is the difference between the intrinsic free energy potential of the adsorbed phase (developed from the gas-liquid-pore surface interactions), to the external energy potential of the bulk fluid. All the intermolecular interaction parameters are calibrated using standard materials with known surface chemistry. The simulated sorption isotherm is then generated from the surface excess number of molecules adsorbed per unit area, as a function of pressure (at a given T). Only one of the isotherm branches though, corresponds to an equilibrium phase transition. This is when the grand free energy potential of the gas and liquid phases are equal. The other branch is then indicative of a metastable phase transition which occurs at the limit of stability of the adsorbed film, and it is termed as 'spinodal spontaneous transition'. Ball and Evans (1989) used DFT to simulate xenon sorption isotherms for Vycor, by modelling the adsorbent as a system consisting of independent or interconnected pores. The simulated and experimental isotherms overlapped when the system was considered to be a set of interconnected pores, suggesting that the DFT model is inaccurate when the sorption process is controlled by pore network effects. To avoid pore connectivity effects, Neimark and co-workers studied gas sorption in MCM-41 materials, which are though to consist of independent cylindrical pores. These authors found that DFT can describe equilibrium phase transitions in MCM-41 materials with a pore size of 2-4.5 nm (Ravikovitch et al., 1995; Ravikovitch et al., 1998; Neimark et al., 1998) and above 5 nm (Neimark et al., 2000; Neimark and Ravikovitch, 2000; Ravikovitch and Neimark, 2001). It was shown that equilibrium transition occurred during the desorption process and

spinodal transition occurred during the capillary condensation process. Kelvin-Cohan equation applied on the desorption branch, is only valid for pore sizes above 20 nm and the relative pressures in the desorption branch are a power of 1.8 of the relative pressures in the adsorption branch (Neimark and Ravikovitch, 2001). However, Kruk *et al* (1997) found that by applying the BJH model in the nitrogen adsorption curve of MCM-41 samples (pore size of 2-6.5 nm) for a hemispherical type meniscus, and by adding an increment into the pore radius (i.e. 0.3 nm) then the PSD derived is in agreement to that predicted by the NLDFT model. This shows that Kelvin equation can be still applied in the small pores, but a modification is required.

Monte Carlo simulations (MCS) have been utilized to study whether the desorption process is controlled by pore blocking or cavitation effects. As firstly described by McBain (1935) pore blocking occurs when a big pore, located next to a small neck, is not in contact with the gas phase and will only empty once the pressure is reduced enough for the small to empty first. Pore emptying via cavitation effects occurs when the pressure is as such to create regions in the pores with low and high density. For very low densities, a gas bubble is nucleated and the pore empties via the hemispherical menisci developed at the gas-liquid interface. If the desorption process is prone to cavitation effects, then this branch should not be used to collect information about the size of the necks. Monte Carlo simulations have shown that for high pore body to neck size ratios, desorption is controlled by pore blocking, whereas at lower body to neck size ratios cavitation is enhanced (Libby and Monson, 2004; Thommes et al., 2006). In disordered porous materials, such as Vycor, cavitation is favoured and it is controlled by the high surface-liquid interaction strengths and the pore size (Woo et al., 2004). This means that the pore size distribution derived from the desorption branch for various adsorbates and temperatures, should be the same if pore blocking (and no cavitation) only occurs (Thommes et al., 2006). Coasne *et al*. (2006) used MCS to study the effect of surface roughness for the argon filling/emptying mechanism on MCM-41 materials as density configurations close to the pore walls will differ between smooth and rough surfaces. The authors found that when the pores modelled a smooth surface, condensation in the pores occurs in a discontinuous step via a jump from the gas to the liquid state. On the contrary, when the surface was rough small voids were formed due to this roughness,

behaving like small pores where gas condensation occurred first and then acted as a nucleation seed for more gas adsorption. The heterogeneity in the surface roughness and chemistry are not taken into account by the DFT method. Hence, it is expected that the DFT treatment will not generate accurate gas sorption isotherms for porous materials with functionalized or rough surfaces, such as catalysts and drug delivery systems. Moreover, studies have shown that SBA-15 materials do not have perfectly shaped 2D-hexagonal cylindrical pores, but they exhibit regions with irregular cross sections and undulates (Esparza et al., 2004; Tompsett et al., 2005). Hence, they should not be used as model systems to describe adsorption and desorption processes in cylindrical pores. Efforts have been made to statistically reconstruct irregular mesoporous systems, such as CPG, by incorporating topological and morphological properties in the pore model (Pellenq and Levitz, 2001). However, these properties are considered to be uniform in the material, which could not be the case for real systems. For example the S1 mesoporous catalyst support studied in Chapters 3, 4, 5 and 8 is found to have macroscopic heterogeneities with long-range, spatial correlations in pore sizes (Hollewand and Gladden, 1995b).

Despite all the advances made to interpret the adsorption and desorption processes by adopting macroscopic and simulation methods, it is recommended by IUPAC that the adsorption branch should be used for pore size measurements as the desorption branch is prone to pore blocking effects. The BJH algorithm, explained above, is then used to produce the pore size distribution values.

1.8 Advanced adsorption

All the sorption mechanisms described above, proposed to interpret the hysteresis, assume that the pores are independent of one another, and there are no pore-pore interactions. However, it has been shown that cooperative effects occur during the adsorption process and this mechanism is termed as ‘advanced adsorption’ or ‘advanced condensation’ (Esparza et al., 2004; Coasne et al., 2005). A schematic presentation of the

independent pore filling and advanced adsorption mechanism is shown in Figure 1.3. For independent pore filling, initially a multilayer is formed on the pore walls at pressure P0. Then the small pore fills at pressure P1 via the cylindrical type menisci from the pore walls. The bigger pore next to the small pore fills at pressure P2>P1 via the cylindrical type menisci too. In the case of advanced adsorption, the small pore fills at pressure P1, via the cylindrical type menisci but the hemispherical meniscus developed on the edge of the pore, enhances adsorption in the bigger pore at pressure P1. If the radius of the small pore is greater or equal to half of the big pore radius, then the pressure for condensation in the big pore via hemispherical meniscus is exceeded by the time the small pore is filled at pressure P1. This practically means that when advanced adsorption occurs, a pore with a size *2r* will fill at the same pressure as a pore with size *r*, thus the calculated pore size distribution via Kelvin equation can have an error as big as 100 %.

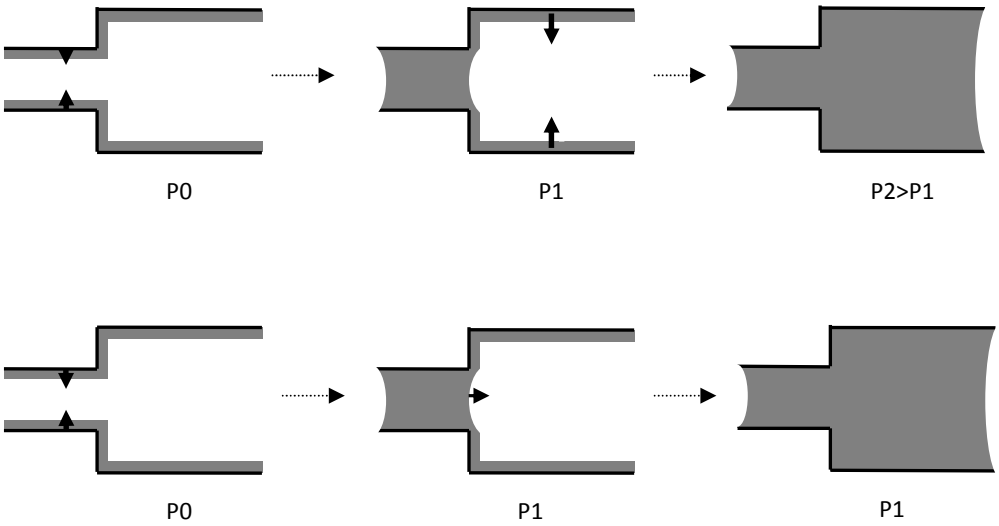

Figure 1.3 Schematic presentation of independent pore filling (top row) and advanced adsorption (bottom row) mechanisms. The continuous arrows show the direction of pore filling

Bruschi *et al.* (2010) studied the capillary condensation mechanism in nanoporous anodic aluminium oxides via molecular simulation studies. The authors used a model of non-interconnected pores with geometrical inhomogeneities along the pore axis. It was found that capillary condensation was driven by the smallest size pore/neck and actually for a pore neck to body size ratio equal to 2:3, both the pore body and the neck filled at the same pressure. This is true only when the pore body fills via advanced condensation mechanism. Hitchcock *et al.* (2010) utilized Magnetic Resonance Imaging (MRI) technique

to study water adsorption on an amorphous catalyst support. The authors found that the largest pores in the material, filled at the same time as the smaller pores by long-range cooperative adsorption effects. Moreover, DFT studies have shown that the critical ratio between the size of two neighbouring pores, where advanced condensation can occur, is also dependant on the adsorbate-adsorbent interaction strength (Rigby and Chigada 2009).

It is important to understand which is the geometry of the meniscus initiating condensation in the pores before applying Kelvin equation, as the discrepancy between the pore sizes calculated for cylindrical or hemispherical menisci, is a factor of 2 if the wrong meniscus is assumed to exist. Moreover, if the contact angles between the gas-liquid-solid interfaces in adsorption differ to those in desorption as proposed ($\vartheta_2 \neq \vartheta_1$) by Saam and Cole (1975), then it is expected that the relative pressure in desorption will be the relative pressures in adsorption raised into other than 2 power. The DFT method shows that this is a power of 1.8 for MCM-41 materials (Neimark and Ravikovitch, 2001), it is expected to vary for real samples with a different surface chemistry as the adsorbate-adsorbent interaction parameters might not be the same as those measured from standard samples. Also, a high surface roughness induces localized adsorption in the concavities, nucleating further adsorption into these sites possible to initiate advanced adsorption (Coasne et al., 2006).

1.9 Independent domain theory and gas sorption scanning curves

The concepts of independent domain theory of sorption hysteresis were introduced by Everett and coworkers (Everett, 1955; Everett, 1954; Everett and Whitton, 1952). The theory assumes that a porous network is an assemblage of independent pores which fill and empty independently of one another. Each pore domain fills at one step at a higher pressure than it empties, without multilayer adsorption taking place. This type of hysteresis recognized at a single pore level, is though to be representative of all the pores in the system and ignores pore-pore interaction effects.

Gas sorption scanning curves are curves obtained by reversing the pressure at a certain fraction of pore filling. A curve initiated part way up the adsorption boundary curve, in the capillary condensation region, is termed as 'desorption scanning curve'. A curve initiated part way up the desorption boundary curve is termed as 'adsorption scanning curve'. It is though that if a scanning curve crosses directly between the boundary sorption curves, then the pores behave like independent, but if it converges at the upper or lower closure point of the sorption isotherm, then the pores are prone to cooperative effects in adsorption or desorption. Figure 1.4 shows examples of adsorption and desorption scanning curves in a mesoporous material. The scanning curve between points A and C represents a diverging desorption scanning curve whereas the scanning curve between points B and E is a diverging adsorption scanning curve. The scanning curve passing through points A to B (or from B to A) is termed a crossing desorption (or adsorption) scanning curve.

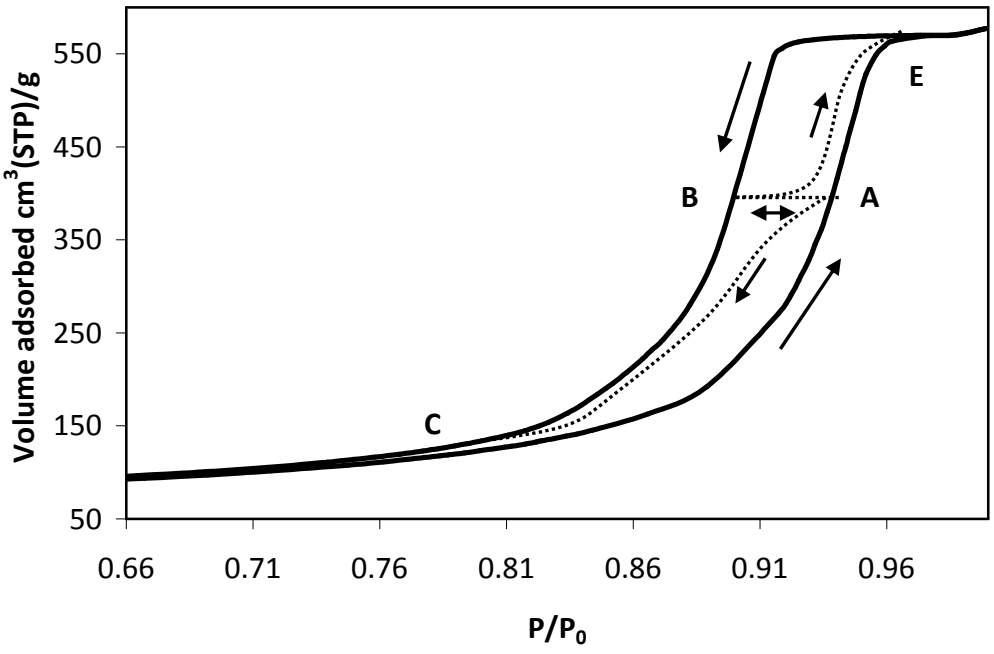

Figure 1.4 Examples of adsorption and desorption scanning curves, crossing over or diverging at the lower and upper parts of a gas sorption isotherm. The arrows show the direction in the change of the pressures

According to Everett's independent domain theory, in a network consisting of a small, a medium and a big pore, acting independently, if the pressure is reversed after the small

and the medium pores are filled (point A), then these two pores will empty at the same pressure (point B) as if desorption was initiated from a completely saturated network (point E). In a similar way, if the small and the medium pores have emptied after partial desorption has taken place (point B), these pores will fill with condensate at the same pressure (point A) that would fill if adsorption was initiated from an empty system (point C). Morishige (2009) observed desorption crossing scanning curves for CPG porous material which the author attributed to independent pore emptying, although it consists of highly interconnected and disordered pores. On the contrary, Tompsett *et al*. (2005) showed that desorption crossing scanning curves for MCM-41 materials, can be also obtained due to pore blocking effects. This means that when the filled big pores are located between filled smaller pores, these big pores will only empty once the pressure of the small necks is decreased enough. Thus, it is possible that the scanning curve crosses into the desorption boundary curve rather converging at the bottom closure point of the hysteresis. Crossing adsorption scanning curves showing an early increase in the adsorption volume, but that eventually meet part way up the boundary adsorption curve are found for MCM-41 and ink-bottle shaped pores. Esparza *et al.* (2004) and Hitchcock (2011) interpreted this as a combination of advanced adsorption filling some set of pores via the hemispherical menisci initiated from already filled neighbouring pores, and independent pore filling into the rest of them. Ravikovitch and Neimark (2002a) employed the DFT method to show that for FDU-1 silicas, which have an ink-bottle pore geometry, desorption crossing scanning curves are also observed due to pore blocking effect. The blocked pores eventually empty spontaneously via cavitation when the pressure is reduced enough. Monte Carlo simulations were adopted by Puibasset (2008) to study the sorption hysteresis in a collection of disordered, non-interconnected tubular pores to mimic the pore structure of MCM-41. The author found that the pores behaved like independent when statistical homogeneity existed within and between the pores. When the heterogeneity within and between the pores increased, the scanning curves diverged (Puibasset, 2009).

Tompsett *et al.* (2005) also found that when the size of the pores in the MCM-41 increased from 2.55 to 5.1 nm, the scanning curves changed from crossing to converging. The authors explained this in terms of variation in filling/emptying mechanism of pores

with different dimensions due to different adsorbate-adsorbent interaction strengths (higher for smaller pores and lower for the bigger pores). On the contrary, Coasne *et al.* (2005) proposed that converging scanning curves in the big pores are due to the presence of more undulates and constrictions as compared to the small pores. These undulates cause pore blocking in desorption and can initiate advanced condensation in adsorption. This was in agreement with the interpretation provided by Kruk *et al.* (200b) who further suggested that the presence of some micropores in the pore walls can provide some degree of interconnectivity between the cylindrical mesopores in the MCM-41, thereby the pores do not empty according to the independent domain theory. Moreover Coasne *et al.* (2005) pointed out that scanning curves indicative of non-independent pores can additionally be explained by a variation in the pore film thickness during the adsorption process which is absent during the desorption. Multilayer adsorption is not taken into account in Everett's theory, but it is highly possible to affect the shape of the scanning curves for small pore to film thickness ratios. Grossman and Ortega (2005) found that pores in SBA-15 samples do not empty independently of one another as converging desorption scanning curves were found. The authors though questioned pore blocking effects caused by intrawall pores, and instead attributed this to the state of the neighbouring filled pores and hence the history of the whole system, which goes through metastable states during desorption. In a later study Grossman and Ortega (2008a) showed that diverging desorption scanning curves are a common feature of both interconnected and non-interconnected pores, and they invoked elastic deformation in the porous silica matrix on the adsorption-desorption cycle (Grosman and Ortega, 2008).

Mixed scanning curves, where the adsorption scanning curve converges and the desorption scanning curve crosses over, were found for argon sorption in MCM-41 (Tompsett et al., 2005). This was explained due to pore network effects, for example if the system consists of small pores on the shell and bigger pores in the core of the sample. When the pressure is reversed the filled small pores provide constrictions to the big pores hence prohibiting them from emptying, but adsorption in the big pores is not restricted by the small pores.

Adsorption scanning loops are more complex scanning curves. Examples of adsorption and desorption scanning loops are shown in Figure 1.5. The desorption scanning loop (A→A'→A) is obtained by reversing the pressure from point A until point A' to obtain a desorption scanning curve, but the pressure is then increased again before the desorption scanning curve reaches the boundary desorption curve. The adsorption scanning loop (B→B'→B) is obtained by reversing the pressure from point B until point B' to obtain an adsorption scanning curve and then the pressure is reversed back, before it joins the boundary adsorption curve. If the adsorption and desorption scanning loops have the same shape and size when spanning the same pressure range and they superimpose by translocation or rotation, they are then termed as 'congruent'. In this case the pores are considered to fill and empty independently.

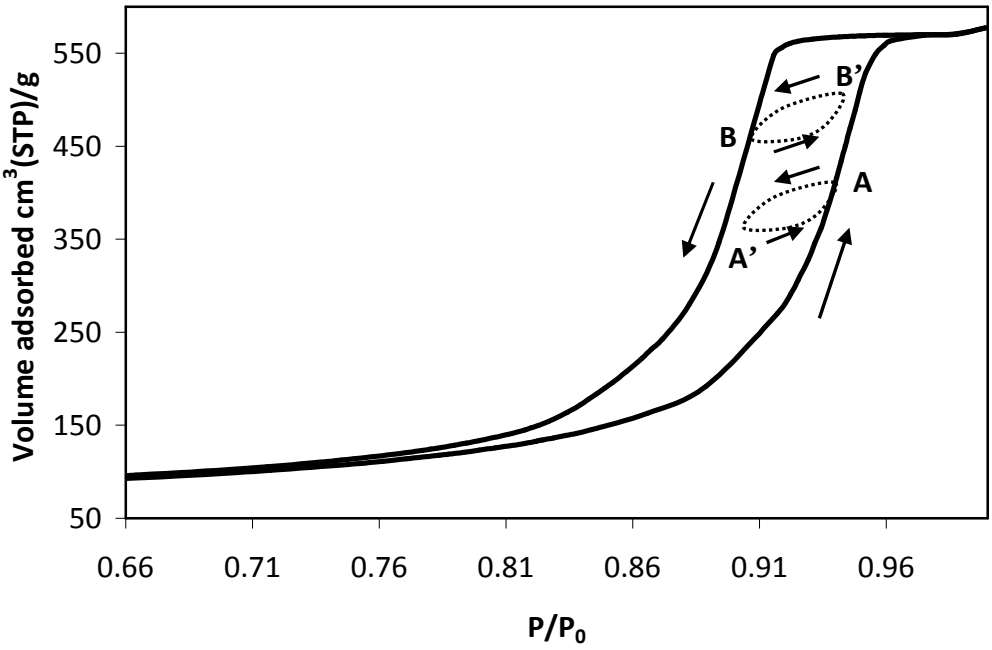

Figure 1.5 Examples of adsorption and desorption scanning loops. The arrows show the direction of the change in the pressure

Grossman and Ortega (2005) performed scanning loops to test independent domain theory for nitrogen adsorption in SBA-15 samples. The authors found that the scanning loops were not congruent, so they concluded that the pores were not filling and

emptying independently. Coasne *et al.* (2005) predicted desorption scanning loops in a pore model consisting of an assembly of independent pores, with a cylindrical regular structure. The authors found that these loops must be reversible and horizontal, i.e. the desorption and adsorption branches of the loop overlap. For another pore model consisting of cylindrical pores, with constrictions and cavities, the predicted scanning loops were neither congruent, nor reversible, reflecting non-independent pore filling mechanism. Hitchcock (2011), though, found that for ink-bottle shaped pores, hysteresis in the scanning loops can be purged if it extends over a narrow pressure range. This was explained as adsorption and desorption taking place via a retreating hemispherical meniscus. Hence, reversible scanning loops are not a concrete evidence of independent pores.

1.10 Summary

This Chapter initially introduced the reader into the basic concepts of gas sorption. Moreover, the relationships used to determine surface area and pore size distribution measurements in this thesis were mentioned. The origin of hysteresis was discussed by providing dominant theories developed the last 100 years. Equilibrium and spinodal sorption processes were also discussed as it is necessary to know which mechanism takes place before selecting the appropriate algorithm for pore size measurements. Moreover, the reader was introduced to the independent domain theory proposed by Everett and the use of scanning curves as a tool to investigate this theory. It was shown that both interconnected and non-interconnected pores are prone to cooperative effects in adsorption and desorption, such as advanced adsorption and pore blocking. IUPAC recommends the adsorption curve for pore size measurements, and the most common algorithm used in industry is the BJH model. The advanced adsorption mechanism is though neglected, leading to incorrect pore size measurements.

Chapters 3 and 4 will provide evidence that advanced adsorption takes place in ink-bottled pores and its degree varies according to the pore connectivity and the adsorbate. Assumption following the Kelvin-Cohan equation and the DFT model to measure the pore

size will be also questioned in Chapter 5. Moreover, the sensitivity of gas sorption technique to probe the real probe size distribution will be compared to the NMR cryoporometry technique. Scanning curves and loops will be mainly used in the NMR cryoporometry studies, to probe co-operative effects in freezing and melting. However, as the concepts of scanning curves in cryoporometry were introduced based on the Everett's independent domain theory in gas sorption, it was necessary to provide a background theory on the gas sorption scanning curves in this chapter first. Finally, it will be shown that neither the gas sorption, nor the NMR cryoporometry technique is sensitive to measure the size of the voids in polymer nanoparticles.

Chapter 2
Introduction to Nuclear Magnetic Resonance characterization techniques

2.1 Introduction

Nuclear magnetic resonance (NMR) spectroscopy is a characterization technique, which in principle studies the behaviour of charged particles (nuclei), in the presence of a magnetic field. The environment of specific nuclei is deduced from information obtained about these nuclei. This, along with the progress seen in the NMR pulse sequences adopted, gave rise to the application of this technique for more sophisticated investigations, such as for characterization of porous materials. In this work, NMR is primarily used to characterize porous systems, but a small section of work has been carried out for the analysis of chemical compounds synthesized (Chapter 7). Proton, (^{1}H) liquid-state NMR has been utilised through out all this work, and this chapter will introduce the reader to the fundamentals of NMR spectroscopy and the basic concepts of the NMR techniques.

2.2 Background theory

Nuclear magnetic resonance (NMR) spectroscopy is a technique that studies the magnetic properties of certain nuclei in order to elucidate the physical and chemical properties of the molecules, or the environment in which they are present. It has been widely applied in different fields such as chemistry, physics, biology and medical science, where information about the structure, dynamics and reactions rates need to be obtained. Nuclei with odd atomic or mass numbers are thought to have a 'spin', which is characterized by a nuclear spin quantum number, I, being a multiple of ½. It is the magnetic properties of the atomic nuclei that form the basis of NMR spectroscopy (Bloch et al., 1946; Purcell, 1946). The nuclei, or more precisely its associated magnetic moment, can obtain $2I+1$ possible orientations which are degenerate in energy in the absence of a magnetic field, but align themselves relative to the field, B_0, applied either

in a parallel or anti-parallel direction. This is known as their equilibrium state. For example, the hydrogen nuclei have a spin quantum number of ½ and can obtain either a +½or a -½ spin state direction.

The nuclei obtain the lowest energy when they are parallel to the magnetic field, giving this state a slightly higher excess of spin population, as compared to the higher energy state. A schematic diagram of the spins split between the two energy levels, after the magnetic field is applied, is provided in Figure 2.1. The difference between the high and low energy levels, ΔE, can be expressed as:

$$\Delta E = h\nu \tag{2.1}$$

where h corresponds to Planck's constant and ν is the frequency of radiation associated with the transition between these energy states (Claridge, 2009). When an external radiofrequency (r.f.) pulse is applied, the nuclei absorb a photon and are excited to a higher energy level. For this transition to occur, it is necessary that the photon has exactly the same frequency as the one required to match the energy gap, known as the Larmor procession frequency (Atkins and de Paula, 2010). This occurs at the frequency $\nu = \gamma B_0/2\pi$ and therefore, the following expression must be held for the nuclei to resonate:

$$\Delta E = h\nu = h\gamma B_0/2\pi \tag{2.2}$$

where γ is the gyromagnetic ratio.

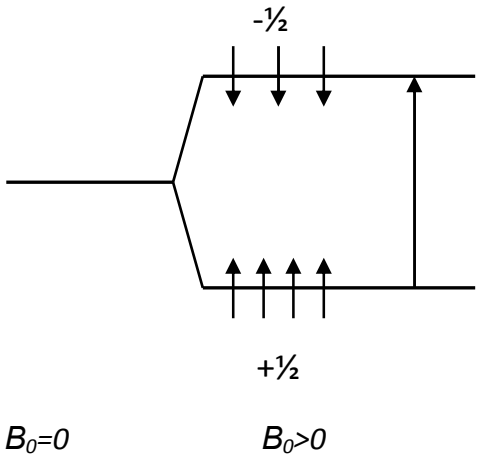

Figure 2.1 Distribution of protons, with spin quantum number of ½, between the high and low energy levels in the presence of a magnetic field

The NMR spectrometer used for this project employs a static field strength of 9.4 T which for a gyromagnetic ratio of 2.675×10^{8} 1/Ts, yields a 400.13 MHz frequency for ^{1}H nuclei. The static magnetic field B_0 is applied along the +z-axis of a set of Cartesian co-ordinates. This means that the excess of nuclei present at the lower energy state, will produce a bulk magnetisation vector *M* along the +z direction, as a result of the sum of each excess individual magnetic moment in this state (Claridge, 2009).

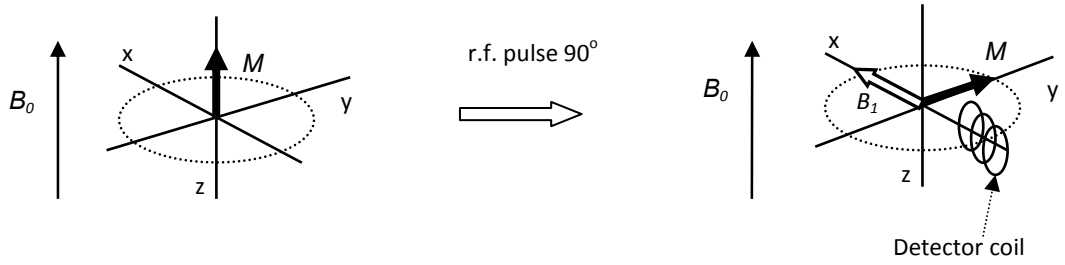

Figure 2.2 Schematic presentation of the magnetization vector, *M*, alignment before and after the application of the r.f. 90° pulse, in the presence of a static magnetic field B_0

The r.f. pulse, also known as a time-dependant magnetic field and denoted as B_1, is transmitted via a coil surrounding the sample on the x-axis direction, which oscillates the spins at their Larmor frequency, thereby causing transitions between the energy levels. Its efficiency depends on the strength of the r.f. pulse and its length. Application of a B_1 (r.f.) field actually rotates the bulk magnetization vector M around the x-axis. Application of a 90° or 180° pulse flips the magnetization vector onto the y- or -z-axis, respectively. This is seen in Figure 2.2. The stronger the r.f. pulse, the quicker the magnetization is tipped towards these directions. Once the r.f. field is turned off, the resultant magnetization vector rotates about the magnetic filed B_0, sweeping out a cone with a constant angle and in a motion called Larmor procession.

After switching off the r.f. radiation, the rotating bulk magnetisation vector *M* also starts recovering towards the +z-axis, until it reaches the equilibrium initial state for reasons that will be discussed below, termed as relaxation. During this precession of the magnetization vector, a weak oscillating voltage is produced in the coil and these electrical signals are detected. The plot of the decaying signal intensity with time is

known as Free Induction Decay (FID). This is then Fourier transformed into a frequency domain, called NMR spectrum, its intensity being proportional to the magnetization *M* (Gunther, 1995).

2.3 T_1 and T_2 relaxometry NMR

As discussed earlier, application of an r.f. pulse with a tilting angle of 90^o will result in the alignment of the magnetic moment *M* along the x-y plane. The spins will then process about the z-axis at their Larmor frequency. However each spin will experience different magnetization due to magnetic field inhomogenities. Some spins that experience a greater magnetisation will creep ahead, whereas others that experience a smaller field will lag behind resulting in a fanning-out of the bulk magnetization *ve*ctors, thereby in the shrinkage of the vector *M*. This kind of relaxation is referred as spin-spin or translational relaxation (T_2). In the latter case, where the magnetic moment *M* is on the x-y plane, the spins will loose their energy to their surroundings (the lattice) and the vector *M* will return to the equilibrium state, on the +z direction. This process is known as spin-lattice or longitudinal (T_1) relaxation and is always slower or equal to T_2 relaxation (ie, $T_1 \geq T_2$) (Claridge, 2009).

2.3.1 *T_1 relaxation*

The longitudinal T_1 relaxation time constant is measured via the inversion recovery experiment. Initially, a 180^o pulse tilts the magnetization vector *M* from the +z-axis direction into the on the –z direction. As the energy is transferred into the lattice, with time, the magnetization vector starts decaying towards the z-axis. However, this signal can not be recorded as the detector coil is placed on the x-y plane. Therefore after a delay time, τ, a 90^o pulse is applied, which flips the vector to the x-y plane. The system is left to relax back to the +z-axis and the FID signal is recorded. The intensity of this FID is therefore proportional to the signal present in the z direction immediately after the decay τ. A schematic diagram of this pulse sequence is given in Figure 2.3.

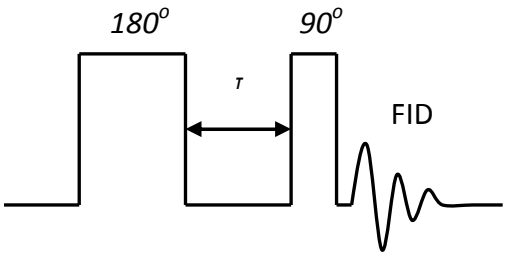

Figure 2.3 Pulse sequence for the inversion recovery, T_1, experiment

The variation in the magnetization in the z-axis with time $M(\tau)$, assuming a uniform magnetic field, follows the first-order differential equation (Keeler, 2005):

$$\frac{dM(\tau)}{dt} = -\frac{M(\tau) - M_0}{T_1} \tag{2.3}$$

where M_0 is the magnetization vector at equilibrium. This equation is integrated into:

$$\ln\left[\frac{M(\tau) - M_0}{M(0) - M_0}\right] = -\frac{\tau}{T_1} \tag{2.4}$$

where $M(0)$ is the magnetization at time zero. A more simple version of equation 2.4 is the following equation:

$$M(\tau) = M_0\left[1 - B\exp\left(-\frac{\tau}{T_1}\right)\right] \tag{2.5}$$

Thus, a series of experiments can be run for different time intervals, τ, and an exponential curve described by equation 2.5 can be fitted to the spectra obtained. The higher the values of τ, the more the signal would decay (Keeler, 2005). The constant B is equal to 2, assuming that $M(0) = -M_0$, as all the magnetization is initially inverted into the -z direction after a perfect 180^0 pulse (Figure 2.3).

2.3.2 T_2 relaxation

The translational relaxation on the x-y plane occurs due to the magnetic inhomogeneities in the magnetic field, which cause some spins to process at different rates, not having the Larmor frequency. The spin echo pulse sequence is used to remove these

inhomogeneities. Here a 90^{o}_{x} pulse is initially applied and the spins are flipped from the z-axis onto the y-axis where they are allowed to relax for a delay time τ. Experiencing the defects on the magnetic field, the spins start to de-phase. In order to re-phase them, another 180^{o}_{y} pulse is applied about the y-axis, thereby the slowly rotating individual vectors will exchange their position with the fast rotating ones. The system is left to relax for time τ and the FID is then recorded. As the spins will follow the same path as before, they are bound to meet and produce a refocused magnetization vector. This pulse sequence is known as spin echo (SE) (Claridge, 2009).

The magnitude of the spin echo is a function of τ and for a homogenous system, obeys the following expression:

$$M(2\tau) = M_0 \exp\left(\frac{-2\tau}{T_2}\right) \tag{2.6}$$

where M_0 is the magnetization at time zero (Keeler, 2005).

By repeating the 180^{o}_{y} pulse, the overall experimental time (2τ, 4τ, etc) increases and the signal intensity decreases, as shown in Figure 2.4. This type of sequence is called Carr-Purcell-Meiboom-Gill pulse train (CPMG) and will be used to measure the T_2 relaxation times of the liquids studied.

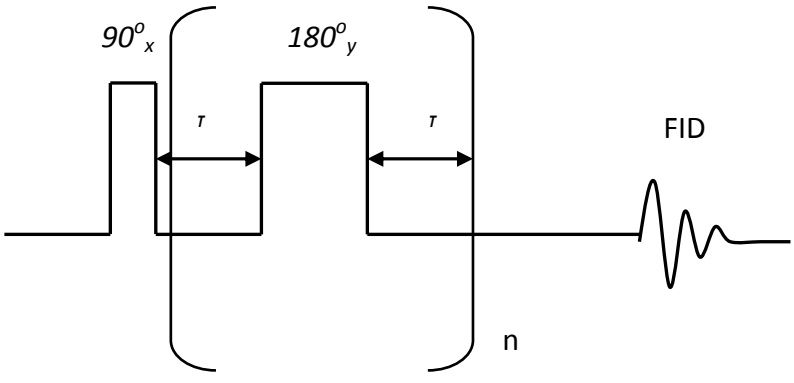

Figure 2.4 Typical CPMG pulse sequence for n repeats of the 180^{o}_{y} pulse

Typically one type of nuclei is examined per spectrum which provides information about the number of chemical environments that the nucleus is in and the ratio of nuclei in each environment. The nucleus examined in this work is hydrogen contained in the water, cyclohexane or heptane molecule, present either in the solid (frozen state) or liquid phase. Solids exhibit a short T_2 relaxation time, of the order of several microseconds, while liquids experience larger relaxation times, of the order of milliseconds to seconds. Thus, by choosing a time delay τ for the detector coil, shorter than the liquid T_2 relaxation time but higher than the T_2 of the solid, the signal intensity detected will correspond to the liquid phase only (relaxation in the solid phase will have already occurred, so it will not be detected).

In this work, the liquid will be either confined in porous materials or around them. T_2 relaxation within the pores is faster than that in the bulk external liquid. This is because the molecules present on a thin layer of liquid on the pore wall, are in fast exchange with the pore walls and the fluid molecules in the middle of the pore (bulk molecules). A schematic presentation of this is given in Figure 2.5. Within the timescale of a typical NMR experiment, the root mean square displacement of the nuclei is of a micron order, which is bigger than the pore size of the materials studied, as they pore size is within the nanometer range (<30 nm). This subsequently leads to a rapid and multiple exchange between the molecules on the pore surface layer and those in the middle of the pores.

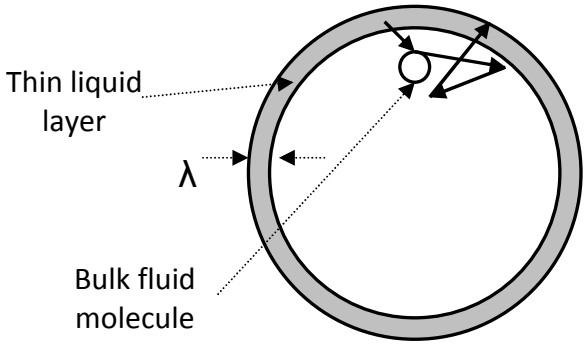

Figure 2.5 Schematic representation of the surface thin liquid (of thickness λ) within a pore, interacting with the bulk fluid molecules and the pore surface

The T_2 relaxation value measured is a mean value between the relaxations of the thin layer and the liquid in the remaining pore volume. The following expression describes this averaged T_2 relaxation (Brownstein and Tarr, 1977):

$$\frac{1}{T_2} = (1 - \lambda \frac{S}{V}) \frac{1}{T_{2B}} + \lambda \frac{S}{V} \frac{1}{T_{2S}} \tag{2.7}$$

where the T_{2S} and T_{2B} refer to the relaxation on the pore surface layer and bulk fluid in the middle of the pore, respectively, λ is the thickness of the surface-affected layer, and S/V is the surface area to volume ratio of the pore. In general $T_{2B} >> T_{2S}$ and thus S/V is given, approximately, by:

$$\frac{S}{V} = \frac{T_{2S}}{\lambda} \frac{1}{T_2} \tag{2.8}$$

For example, for a completely saturated cylindrical pore, S/V would be equal to $2/r$, where r is the radius. Therefore, T_2 is then proportional to the pore size; the higher the T_2 value the bigger the pore size. Relaxation times can be measured in the range of 1 μs to 2 s leading to a size range of 1 to 30 μm, which actually denotes the limits for pore size measurements (Claridge, 2009). The T_2 relaxation decay is monoexponential (equation 2.6) when the liquid molecules are homogenously distributed, and thus they all experience the same exchange interactions. For more heterogeneous systems, equation 2.6 becomes biexponential and its form will be provided in each chapter separately, according to the environment present.

2.4 Pulse field gradient NMR

All of the molecules of a fluid undergo Brownian motion which represents a random and continuous movement of the molecules driven by the thermal energy of the system. Pulsed field gradient (PFG) NMR can provide diffusion measurements based on the self diffusion that the molecules experience. This method relies upon the application of time and spatial dependant pulsed field gradients, G, (in addition to the static magnetic field

B_0) to encode the physical location a molecule in a fluid and study its diffusion in the direction in which the gradients are applied. In this work the gradients are applied in the z direction and consequently, the resonance frequency will vary with the magnetic field strength, B_0, the nuclear spin position, z, and the gradient strength in the z direction, G_z, according to the expression:

$$\nu(z) = \frac{\gamma B_0}{2\pi} + \frac{\gamma z G_z}{2\pi} \tag{2.9}$$

There are different types of PFG NMR pulse sequences. The simplest one is the spin echo PFG (PGSE), depicted in Figure 2.6, for a pulse of length δ and diffusion time Δ between the gradients (Stejskal and Tanner, 1965). This sequence is used under the condition that T_2 relaxation is not much faster than T_1 relaxation. The first gradient causes an offset to the spins phase, dependant on the spin position along the applied field. After a time Δ, the second gradient is applied to re-phase the spins. If the molecules have diffused during that time course, they will experience a different local field. Therefore the signal will be only partially refocused and its signal attenuation will depend on the distance the nuclei diffused during the time Δ.

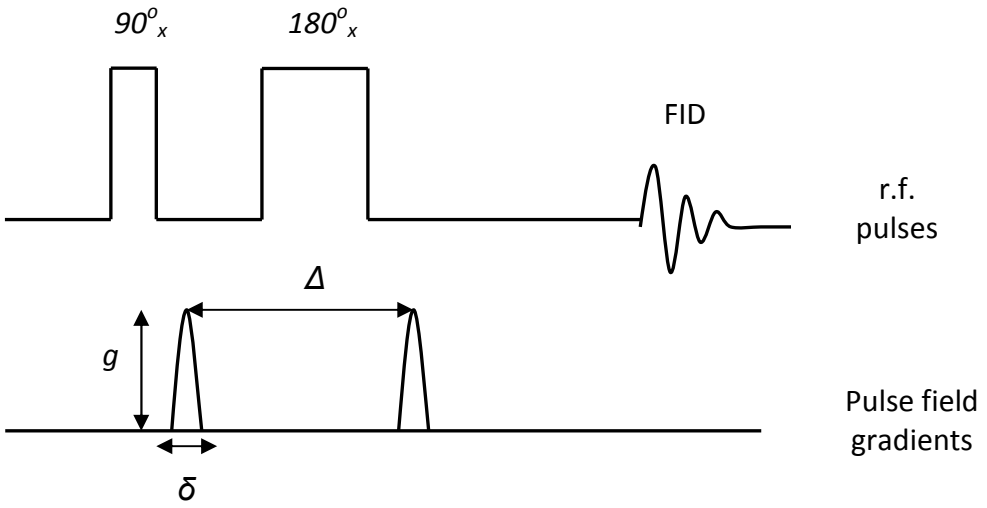

Figure 2.6 Spin echo PFG NMR pulse sequence

PGSE experiments are severely affected by significant transverse relaxation process in the x-y plane, where the net magnetization is lost during the time Δ. This means that

when diffusion is slow, the use of long Δ, can lead to low signals. In most cases $T_2 << T_1$. This issue is therefore resolved by application of the stimulated echo sequence (PFG-STE). Here the 180^{o}_{x} pulse is replaced by two 90^{o}_{x} pulses. After the second 90^{o} r.f. pulse the magnetization vector is tilted to the z direction, where there is no T_2 relaxation but instead, there is only T_1 relaxation, which is much slower than T_2. After a time Δ, the magnetization is rotated back into the x-y plane via the third 90^{o} r.f. pulse, where it is then recorded. The amount of signal attenuation for a certain diffusion length and gradient strength, depends on the distance the molecules diffused during the time Δ.

In this work, a more advanced version of the PFG-STE sequence is used, called a bipolar pulse longitudinal eddy current delay (BPP-LED). A schematic presentation of this is given in Figure 2.7. Here, each magnetic field is replaced by two gradients, separated by a 180^{o}_{y} pulse. The gradients are of equal but opposite magnitude and each of them is half the duration ($\delta/2$) to those used in the PFG-STE. Their combined effect is the equivalent to the single gradient in the PGSE sequence. However, because the gradients are of equal but opposite sign, the eddy currents that they create-which generate undesired transient field inhomogeneities and therefore can result impairing the signal-are cancelled out. Furthermore, rather than acquire the FID immediately after the final gradient, as in the PFG-STE sequence, a pair of 90^{o} pulses are employed before acquisition, separated by a short delay T_e, during which the magnetization is stored longitudinally (z-axis) and any further eddy currents can decay. Finally, two small field gradients are applied to remove any unwanted residual magnetization remaining in the x-y plane at positions in the pulse sequence where all the magnetization should all be along the z-axis. The overall effect of this pulse program is to reduce to the phase cycling required to improve the spectrum line shape.

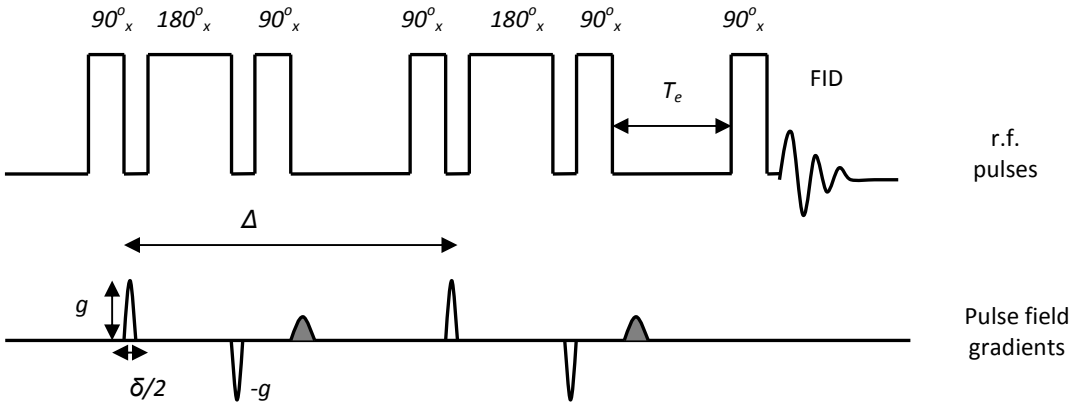

Figure 2.7 BPP-LED pulse sequence. The empty and grey filled lines placed on the pulse field gradients row, represent the applied magnetic and small field (crusher) gradients, respectively

The observed signal intensity, *I*, at the end of a PFG experiment is related to the diffusion that the nuclei undergo within the observed diffusion time *Δ*. The signal attenuation is expressed as follows (Stejskal and Tanner, 1965; Claridge, 2009):

$$I = I_0 \exp\left(- D_{PFG} \gamma^2 \delta^2 g^2 \left(\Delta - \frac{\delta}{3} - \frac{\tau_0}{2} \right) \right) \qquad (2.10)$$

where I_0 is the reference intensity, in the absence of gradient fields, and τ_0 is correction time for the phasing and de-phasing between bipolar gradients (Kerssebaum, 2002). By plotting the equation 2.10 in a form of $ln(I/I_0)$ versus $\zeta=(-\gamma^2 g^2 \delta^2 (\Delta-\delta/3-\tau/2))$ a straight line is obtained, where its slope is the diffusion coefficient required. For a heterogeneous system, though, where the molecules experience different magnetic fields, and as such significantly different local diffusivity, equation 2.10 becomes multi-exponential. In this work, both mono-exponential and bi-exponential logarithmic attenuations were observed, for the materials studied, and the type of the equation used, will be specified in each chapter.

In a porous material, the diffusion coefficient of the imbibed liquid is an average between the individual diffusion coefficients experienced by all the spins. This means that D_{PFG} has a spin density contribution, which is proportional to the voidage space, ε, and is related

to the effective diffusivity, D_{eff} by the following expression (Hollewand and Gladden, 1995a):

$$D_{PFG} = \frac{D_{eff}}{\varepsilon_p} \tag{2.11}$$

This allows the estimation of the tortuosity, τ_p, of the material as follows:

$$\tau_p = \frac{D_b}{D_{PFG}} \tag{2.12}$$

where, D_b is the diffusion coefficient of the molecules in the bulk liquid, experiencing free diffusivity, at the same temperature as the measured D_{PFG}. These equations are valid only when $\delta << \Delta$. Moreover, to account for the transverse and longitudinal relaxation of the magnetization vector, occurring in the x-y plane and z direction, respectively, it must be selected $\delta << T_2$ and $\Delta << T_1$.

In the PFG experiments, it is assumed that the molecules diffusivity is isotropic, i.e. it is similar for all x,y,z directions. Hence, even though the molecules displacement over time in the 3D system is zero, their mean square displacement in a single direction $<r^2_{rms}>$, during a diffusion time Δ, is non-zero and it can be calculated from Einstein equation:

$$< r^2_{rms} > = 6 D_{PFG} \Delta \tag{2.13}$$

In a porous material, diffusivity can be free, restricted or partially restricted. When the $<r^2_{rms}>$ increases linearly with diffusion time, than the molecules experience a free diffusivity. This is true for the molecules in a bulk liquid, or for confined liquid studied in very short time scales. However, in the long-range diffusion regime, restrictions are induced into the mobility of the imbibed liquid from interaction with the pore walls, or its exchange with different phases present (ice, liquid, vapour), or the connectivity of the adsorbed phase is limited (such as in the case of partially saturated systems). Therefore PFG NMR is a technique that can provide information about pore topology and spatial distribution of the adsorbed phase.

Mitra *et al.* (1993) have shown that for a partially restricted diffusivity, the measured diffusion coefficient is related to the unrestricted diffusivity, D_0, by the following equation:

$$D(\Delta) = D_0 - \frac{4D_0^{3/2}\Delta^{1/2}S}{9\pi^{1/2}V} \qquad (2.14)$$

where *S*/V is the external surface area-to-volume ratio of the liquid boundary layer. A straight line fit of PFG NMR data for the measured diffusivity against $\Delta^{1/2}$ yields an intercept equal to the unrestricted matrix diffusion coefficient D_0. This value can then be used to estimate the reciprocal tortuosity via equation 2.12. The equations used for the calculation of the diffusivity and tortuosity will be specified in the chapters when necessary.

2.5 Magnetisation recovery in a PFG NMR experiment

Longitudinal relaxation (T_1) determines the time that must be left between two successive experiments in order to allow complete recovery of the magnetization vector *M* from the x-y plane into its equilibrium state, on the +z direction. This is important for the PFG experiments where gradient pulses are introduced into the pulse sequence and spins de-phasing is enhanced, leaving possible 'spin residuals' on the x-y plane after FID acquisition.

Assuming that at the end of the signal acquisition in one experiment, the magnetization in the z-axis is zero, $M(0)=0$, and the magnetization vector needs a time τ to return to a fraction *f* of its complete equilibrium ($f=1$), then we can say that $M(\tau)=fM_z$, where M_z is the amplitude of the magnetization vector at fraction *f*. Then, following equation 2.4, it can be written (Keeler, 2005) that:

$$\ln\left[\frac{fM_z - M_z}{-M_z}\right] = -\frac{\tau}{T_1} \qquad (2.15)$$

which is simplified to:

$$\tau = -T_1 \ln(1 - f) \tag{2.16}$$

This means that for 99% of the magnetization to return to equilibrium, before the next pulse sequence is applied, the system must have a delay time of *d1*=4.6xT_1. It must be noted that the total delay time between the experiments, includes also the FID acquisition time, t_{aq}, as longitudinal relaxation continues during the FID. This total time is called repetition time, $t_r=t_{aq}+d1$. An illustration of how the spin recovery changes with multiples of relaxation time T_1 (characteristic of the total relaxation delay time) is presented in Figure 2.8.

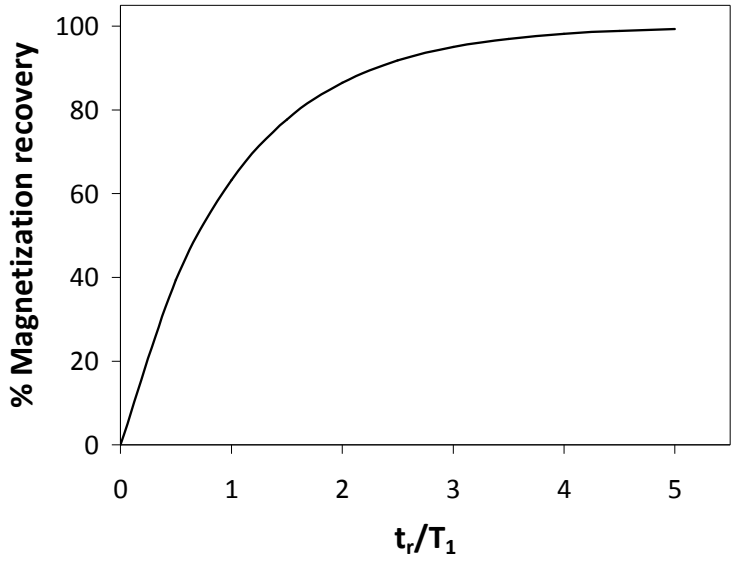

Figure 2.8 Magnetization recovery towards the equilibrium state for different multiples of T_1 relaxation times

T_1 relaxation, though, varies with the type of molecules and the environment present, as described in Section 2.3.1. Subsequently, diffusion measurements would require different delay times, specific to the system studied, that can increase the experimental times dramatically. Moreover, 'spin residuals' on the x-y plane are more prominent when simple pulse sequences, such as PGSE, are used, but are expected to reduce by application of more sophisticated pulse sequences such as BPP-LED PFG NMR.

2.6 Cryoporometry NMR

The basic fundamentals of cryoporometry were set by Thomson and Gibbs (Thomson, 1871; Thomson, 1888; Gibbs, 1928, cited at Mitchell et al., 2008a). The authors reported that the melting point of a small crystal is lower than its bulk, and its size is inversely proportional to the temperature. This is because the increase in the free energy of the surface area to volume ratio of the crystals becomes significant. Later, Jackson and McKenna (1990) and Mitchell *et al.* (1998a) used this relationship to describe the melting point depression, ΔT_m, of frozen phases confined in porous materials using the expression:

$$\Delta T_m = T_m - T_m(x) = \frac{4\sigma_{sl} T_m}{x \Delta H_f \rho_s} \cos(\theta) \tag{2.17}$$

where σ_{sl} is the surface tension at the crystal-liquid interface, T_m is the bulk melting point while $T_m(x)$ is the melting point of the crystals inside the pores, x is the diameter of the crystals, ΔH_f is the bulk enthalpy of fusion (heat of melting) per g of material, ρ_s is the density of the crystal, and ϑ is the contact angle between the crystal and the pore wall. It is also assumed that most adsorbates will have weak interactions with the adsorbent surfaces, ensuring that the pore dimension is the parameter defining the melting point depression (Mitchell et al., 2008a). Moreover, it is assumed that ϑ is 180^o which means that the crystal is not in contact with the pore wall (Jackson and McKenna, 1990), and equation 2.17 takes the form of:

$$\Delta T_m = T_m - T_m(x) = \frac{4\sigma_{sl} T_m}{x \Delta H_f \rho_s} \tag{2.18}$$

This assumption can be correct, as it is found that there is liquid-like layer on the pore walls that never freezes (Schmidt et al., 1995; Schreiber et al., 2001; Overloop and Vangerven, 1993). Equation 2.18 is known as Gibbs-Thomson equation and a simplified version of it, is given by the expression:

$$\Delta T_m = T_m - T_m(x) = \frac{k_{GT}}{x} \tag{2.19}$$

where k_{GT} is referred as Gibbs-Thomson constant and it is measured empirically. The k_{GT} constant is characteristic of the imbibed liquid and the pore wall, via the contact angle, and sets limits to the pore size measured. This is because the imbibed liquid might not completely wet the pores during adsorption (i.e. because of their different hydrophilic nature), therefore some pores will remain empty leading to an incorrect PSD calculation. Moreover, surface chemical heterogeneity, such as in the case of coked catalysts or other grafted groups (Dosseh et al., 2003), changes the wetting efficiency of the liquid along the pore surface, due to variation of the contact angle between the pore wall surface and the liquid. Hence, liquid-solid phase transitions will not be solely controlled by the pore size, but also by the surface chemistry, assumed to be homogenous in a cryoporometry NMR experiment.

The Gibbs-Thomson constant is empirically derived by plotting the ΔT_m versus $1/x$. Following equation 2.19, the gradient of the slope, gives the k_{GT} (Strange et al., 1993). However, this requires estimation of the pore size by an independent method, such as gas adsorption. The latter method though, relies on a set of auxiliary assumptions made about the Kelvin equation, and it is prone to cooperative phenomena (Esparza et al., 2004; Casanova et al., 2007) leading to an incorrect PSD. This error is then transferred from the gas adsorption to the cryoporometry NMR experiment, which in fact is influenced by its own cooperative phenomena during melting (Hitchcock et al., 2011) as it will discussed in Section 2.8. Moreover, a non-linear relationship between the melting point depression and the inverse pore size was observed by Hansen *et al.* (1997) who attributed this behaviour to the fact that the heat of fusion and the surface tension change with temperature. A corrected version of equation 2.19 was later proposed, which accounts for the unfrozen layer on the pore wall, likely to induce errors in the calculation of small pore sizes (Hansen et al., 1996a; Schreiber et al., 2001):

$$\Delta \mathrm{T}_m = T_m - T_m(x) = \frac{k_{GT}}{x - 2t} \tag{2.20}$$

where t is the thickness of the liquid-like layer on the pore wall. Perkins (2009) suggested a more accurate method for the calculation of k_{GT} constant, specific to the sample and

the probe liquid used. In this work, a mesoporous sol-gel silica (S1) pellet sample was initially fragmented to remove co-operative effects (such as pore blocking during cryoporometry freezing). The freezing curve obtained from cryoporometry NMR was directly compared to the intrusion curve from mercury porosimetry (Perkins, 2009). The Gibbs-Thomson parameter and the liquid-like layer of water were found to be 26 nmK and 0.4 nm, respectively.

Different pore liquids have been used for porous characterization, such as water (Webber et al., 2001), benzene (Aksnes et al., 2001b), octamethylcyclotetrasiloxane (Vargas-Florencia et al., 2007), cyclohexane (Dore et al., 2004), acetonitrile (Aksnes et al., 2001a) and nitrobenzene (Kondrashova et al., 2010). Liquids with high k_{GT} constants are used to probe big pore sizes, as deduced from equation 2.19. Vargas and Florencia, (2007) used octamethylcyclotetrasiloxane to measure pores sizes up to a micrometer range within CPG samples.

The basic idea of NMR cryoporometry is to detect the change in the phase transitions of a liquid confined into a porous material, with temperature variation, using NMR. The method relies on the fact that molecules present in different phases have different mobility, thereby relaxation times. Using a solution state NMR, as done in this work, the liquid phase will be detectable but the solid one will not be observed as its relaxation time is short. Some bulk liquids, such as cyclohexane, change their structure upon melting from crystalline to disordered plastic phase and then to liquid. Hence, it is possible that in a porous material, both the plastic and the bulk phase co-exist, requiring great care during conversion of the detected volume into a PSD, as strictly the molten liquid phase must be used for this calculation. In an NMR experiments the solid-liquid transition is detected upon increasing/decreasing the temperature, by applying a spin-echo type pulse sequence. This means that the magnetization vector (or signal intensity) is T_2-weighted. The crystalline and plastic phase have a faster T_2 relaxation time, compared to the liquid, thus, the former phases can be suppressed by choosing a high delay time between the 90^o and 180^o pulses (Figure 2.4, for n=1), allowing only the molten liquid phase to be distinguished. In order to convert the variation of the molten phase volume with temperature, into a PSD, though, the correct k_{GT} constant must be

selected. For this Webber (2000) firstly employed equation 20 to calculate the Gibbs-Thomson constant for cyclohexane, at a particular echo time (2τ). Then the author repeated the experiments at other echo times, and plotted all the k_{GT} constants obtained versus the echo times. This way the author produced an expression where the k_{GT} constant is an exponential function of 2τ (Webber, 2000). However, this method again relies on the accuracy of the PSD calculations derived from the gas adsorption studies, thus, it is subject to errors.

2.7 Freeze-thaw hysteresis in cryoporometry NMR

In a cryoporometry NMR experiment freezing and melting of the imbibed liquid occurs at different temperatures, referred to as freeze-thaw hysteresis. Different theories have been proposed to interpret this difference by Petrov and Furo (2009) based on the fact that the liquid within the pores is trapped in a metastable state, where phase transitions occur once the activation energy barrier, separating these states, is overcome. There are two reasons for metastabilities occurring during freezing. Firstly, the molten phase is not in contact with a frozen phase, which would act as nucleation site to initiate pore freezing. Therefore, the confined liquid has to be supercooled, or to freeze via homogeneous nucleation at lower temperatures than the equilibrium freezing temperature. Secondly, freezing can be seeded by frozen sites in contact with the molten ones (heterogeneous nucleation process), but the ice front propagation is hindered by confinement constrictions, such as pore necks. In this case, the temperature has to be lowered enough to promote freezing of the pore necks first, following the Gibbs-Thomson equation. This mechanism is analogous to pore blocking effects in gas desorption. However, melting is seeded by the liquid-like layer on the pore walls, which is always in contact with the frozen remaining phase. Another reason for the freeze-thaw hysteresis is the different geometry of the menisci commencing the two mechanisms. Melting process occurs via a sleeve-type meniscus and progresses radially (similarly to gas adsorption), whereas freezing occurs via a hemispherical-type meniscus and continues in an axial direction along the pore (analogous to gas desorption). Figure 2.9 presents a typical freeze-thaw hysteresis of water confined in a mesoporous sol-gel silica

material along with the bulk freezing and melting curves. The whole system goes initially through supercooling until both the bulk and pore water freeze spontaneously at ~264 K. The temperature is then increased and pore melting commences via a sleeve-type meniscus from the liquid-like layer. If the temperature is inversed before the bulk water melting temperature (273 K), pore freezing commences via the propagation of the freezing front, into the molten phase via a hemispherical type menisci, originating from the frozen bulk.

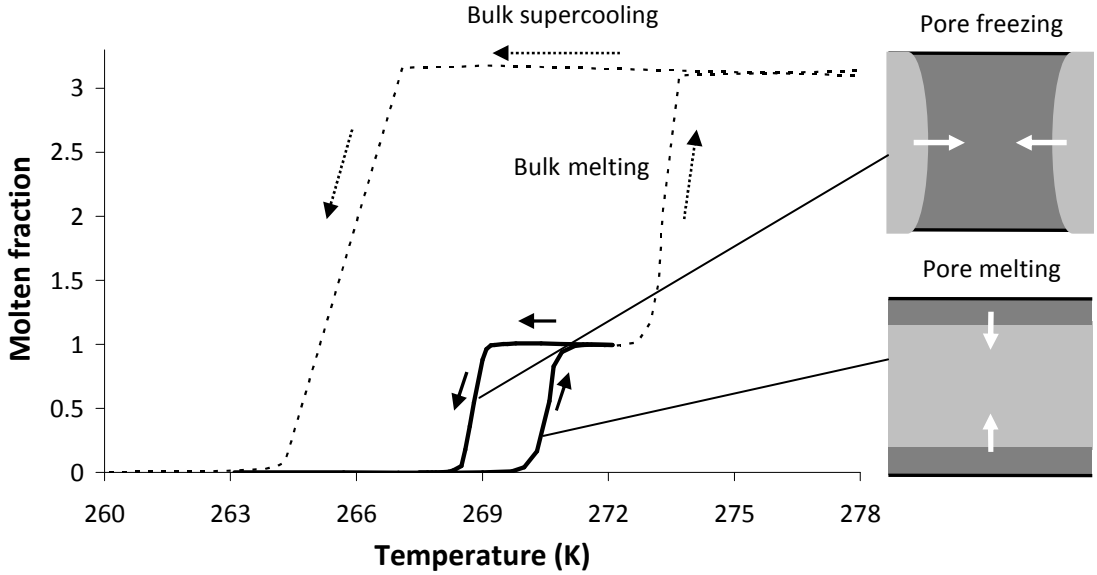

Figure 2.9 Typical freeze-thaw hysteresis (continuous line) for a mesoporous sample obtained via cryoporometry NMR. Bulk supercooling and melting are also shown (dotted line). Pore melting (bottom schematic) commences via the cylindrical-type menisci from the liquid-like layer (dark grey). Pore freezing (top schematic) is nucleated by the frozen front (light grey) propagating the molten phase via hemispherical menisci. Detailed explanation of the schematic diagram is provided in the text above

It has been demonstrated that the freezing point depression, ΔT_f, depends on the surface-to-volume ratio, *S/V*, whereas the melting point depression, ΔT_m, is determined by the curvature of the pore surface, *dS/dV*, (Petrov and Furo, 2009; Vargas-Florencia et al., 2008) as follows:

$$\Delta T_f \cong -k_c \frac{S}{V} \qquad (2.21)$$

$$\Delta T_m \cong -k_c \frac{dS}{dV} \qquad (2.22)$$

where $k_c=V_M \sigma_{sl} T_m/\Delta H$. Combining equations 2.21 and 2.22 and using the Steiner formula, the freezing point depression is related to the melting point depression via the expression:

$$\frac{\Delta T_m}{\Delta T_f} = 2\kappa \frac{V}{S} \tag{2.23}$$

where κ is the integral mean curvature of the pore surface, and the expression describes the single pore hysteresis in cryoporometry. Equation 2.23 can provide information about the pore geometry. For example, in the case of a cylindrical-type pore, the following relationship (Petrov and Furo, 2009) is derived:

$$\frac{\Delta T_m}{\Delta T_f} = \frac{1}{2} \tag{2.24}$$

which suggest that the freezing and the melting point depressions differ by a factor of two. Perkins *et al.* (2008) compared the freezing and melting cryoporometry curves for a water saturated, whole pellet S1 material, which has an ink-bottle type geometry. The authors found that $\Delta T_m/\Delta T_f \neq ½$ which they attributed to pore blocking effects in freezing. However, particle fragmentation lead to a ratio of ½. This was because some of the pore blocking effects during pore freezing were curtailed.

2.8 Defining cryoporometry NMR scanning curves and advanced melting mechanism

The sections above described the pore freezing and melting mechanism for single pore hysteresis. This part will introduce the reader into advanced melting phenomena occurring during cryoporometry pore melting, likely to induce errors in the calculation of pore size distributions as derived from the Gibbs-Thomson equation. Moreover, an introduction to cryoporometry scanning curves and scanning loops will be provided, as

they will be utilized in Chapters 2 and 3 to test the independent pore theory in the cryoporometry NMR freeze-thaw processes.

Scanning curves are extensively used in gas sorption experiments as a tool to investigate the 'independent domain theory' of sorption hysteresis. The basic concepts of independent pore theory have been already provided in Section 1.9, thus a summary will be now provided. This theory assumes that adjacent pore domains behave like autonomous entities, which fill and empty at well-defined pressures independently of their connectivity, as firstly suggested by Everett and Smith (1954). There are two types of scanning curves referred to as desorption and adsorption scanning curves. The former is obtained by decreasing the pressure at any partial filling of the pores, within the capillary condensation region of the adsorption boundary curve. The latter is obtained after increasing the pressure, initiated from a partial pore filling on the desorption boundary curve. Everett and Smith (1954) assumed that pores of a certain size will fill at a specific higher pressure than that required for them to empty, ignoring the multilayer adsorption process. This means that the sorption scanning curves ought to cross over between the boundary sorption curves, once the pressure is reversed (Ravikovitch and Neimark, 2002b; Morishige, 2009). However, experimental and simulation results have shown that it is possible for the scanning curves to converge, and thereby to meet the top and the bottom closure points of the hysteresis curve (Coasne et al., 2005, Rojas et al., 2002, Esparza et al., 2004). Moreover, mixed scanning curves, where one of the scanning curves converges and the other one crosses over, were found from Monte Carlo simulations studies (Puibasset, 2009) and argon sorption in MCM-41 (Tompsett et al., 2005). Independent domain theory can also be tested using scanning loops. To obtain the desorption (or adsorption) scanning loop, the pressure in the adsorption (or desorption) boundary curve is lowered (or increased) from a particular pore filling and it is again increased (or decreased), to meet the boundary curve (Grosman and Ortega, 2005; Hitchcock, 2011). If the adsorption and desorption scanning loops, that span over the same pressure range, have the same size and shape, then they are termed as 'congruent' and the system is believed to be composed of independent pores.

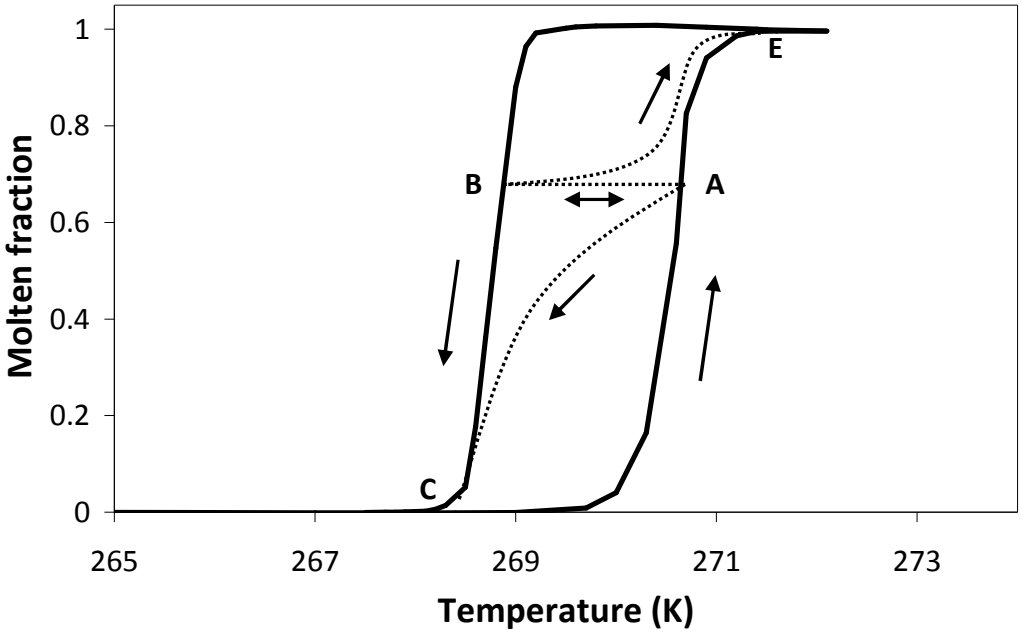

Figure 2.10 Schematic presentation of cryoporometry NMR freeze-thaw hysteresis curves (continues line), shown in Figure 2.9, along with a crossing freezing (A→B) and crossing melting (B→A) scanning curves, a converging freezing curve (A→C) and a converging melting curve (B→E). The scanning curves are shown in dotted lines. The arrows show the direction of freezing or melting

Cryoporometry NMR can be also adopted to test independent pore theory, as pore melting and freezing processes are thought to be analogous to adsorption and desorption processes (Jackson and McKenna, 1990; Schreiber et al., 2001). Figure 2.10 shows some scanning curves within the boundary freeze-thaw hysteresis curves, of a mesoporous material. Here the freezing scanning curve is initiated from a partially molten fraction on the boundary melting curve (point A) by decreasing the temperature, whereas the melting scanning curve commences from a partially molten fraction on the boundary freezing curve (point B), by increasing the temperature. Similarly to gas sorption, it is expected that the scanning curves initiated from partially molten fractions will cross over between the boundary curves (A→B or B→A) if the pores were freezing and melting depending only on the temperature, irrespective of the interaction with the neighbouring pores. However, if co-operative phenomena during freezing and melting were to occur, then converging freezing (A→C) and melting (B→E) scanning curves would be obtained.

Moreover, it is possible to obtain cryoporometry scanning loops by reversing the temperature within the freeze-thaw hysteresis region, and a comparison between their shape and size over the same temperature range, can provide information about the validity of independent pore theory. In addition to this, scanning curves and loops can be used to study the configuration of the molten/frozen phase at different molten fractions and the freeze-thaw mechanism up to/from the fractions studied. A freezing (A→A'→A) and a melting (B→B'→B) scanning loop is shown in Figure 2.11.

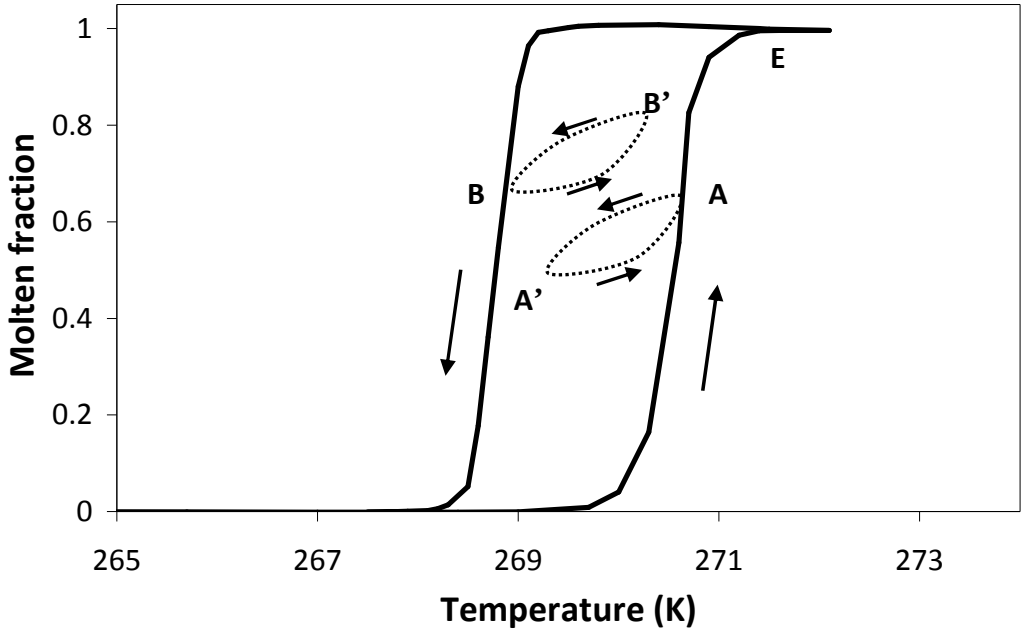

Figure 2.11 Schematic presentation of cryoporometry NMR freeze-thaw hysteresis curves (continuous line), shown in Figure 2.9, along with freezing (A→A'→A) and melting (B→B'→B) scanning loops. The arrows show the direction of freezing or melting

In Sections 2.6 and 2.7, it was discussed that the freezing mechanism is prone to pore blocking effects, as the ice front propagation, via a hemispherical meniscus, is delayed by narrow necks that require a lower temperature to freeze. Moreover, it was mentioned that melting commences from the liquid-like layer via a cylindrical meniscus (Petrov and Furo, 2009). It is though possible that once a critical pore size is reached, then the hemispherical meniscus of the molten phase can initiate melting of an adjoining pore. This effect is called advanced melting and it is analogous to advanced condensation in gas adsorption (de Boer, 1958). Figure 2.12 shows a schematic representation of independent and advanced melting mechanisms for a set of adjoined pores, P1 and P2. If

the pores melt only according to their size, then the small pore P1 will melt at temperature T1 and the big pore P2 will melt at a higher temperature, T2 (Figure 2.12, top row). Both pores melt via the cylindrical menisci from the pore walls. However, if advanced melting occurs (Figure 2.12, middle row), then P1 will melt via the cylindrical menisci, but, once the hemispherical meniscus is formed, it will enhance immediate melting of pore P2 at the same temperature, T1. Melting can additionally be initiated from dead end pores (Figure 2.12, bottom row), via the liquid-like layer at the end of the pore. Both mechanisms lead to melting of bigger pores at lower temperatures, contrary to the melting point depression predicted by Gibbs-Thomson equation and consequently to a narrowing of the temperature width over which pores melting occurs. This leads to an underestimation of the pore size distribution because incorrect meniscus geometry, by a factor of 2, is assumed to initiate melting in some pores.

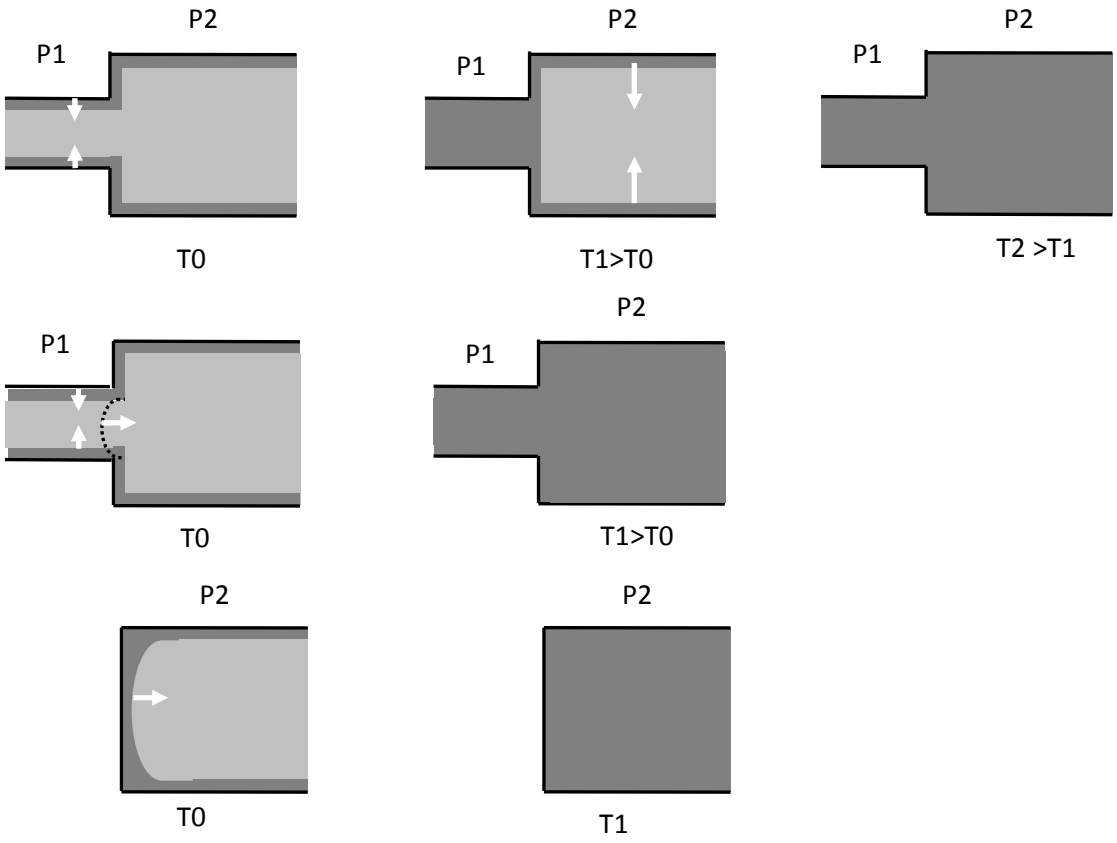

Figure 2.12 Schematic presentation for pores (P1, P2) melting independently by size (top row), for P2 melting via advanced melting at the same temperature, T1, as P1, by the hemispherical meniscus (dashed line) developed on the small P1 pore mouth (middle row), and melting initiated from the liquid-like layer on a dead end pore, P2 (bottom row). The arrows show the mechanism of pore melting for each pore

Previous studies have shown an immediate melting upon increasing the temperature from a partially molten fraction on the boundary freezing curve, or within a scanning loop for different samples (Kondrashova et al., 2010; Hitchcock et al., 2011; Petrov and Furo, 2011a). Kondrashova *et al.* (2010), who used nitrobenzene confined in Vycor glasses (poorly interconnected and disordered pore structure), demonstrated that this was caused by the presence of some dead end pores in Vycor, but the overall melting process was a single pore property. Petrov and Furo (2011a) on the contrary, attributed the early melting of water in Vycor, to the presence of the liquid segments on the liquid-ice interfaces along the pore channels that will act as nucleation sites to accelerate melting of the solid phases next to them, at lower temperatures. Hitchcock *et al.* (2011), performed cryoporometry experiments in a water saturated sol-gel sample (S1), with a well connected pore structure. Hitchcock et al. firstly referred to this phenomenon as 'advanced melting', speculating it to be equivalent to the advanced condensation mechanism in gas sorption. Hitchcock *et al.* explained this in terms of hemispherical meniscus geometry developed at the liquid-solid interface, between a small and a bigger pore, able to enhance melting of both pores in one step. The authors also pointed out that advanced melting in a well connected pore system is more severe than that in a poorly connected system. Indeed, advanced melting was curtailed by particle fragmentation (Hitchcock et al., 2011). Petrov and Furo (2011a) compared the melting scanning curves and loops for water confined in Vycor to water imbibed in CPG glasses. CPG glasses have an ordered and well connected pore structure, thus, they would have had greater potentials for advanced melting to occur. However, melting scanning curves for CPG were less steep than Vycor glasses. These authors interpreted this as a slower exchange between the solid-liquid phases (Petrov and Furo, 2011a). Freezing initiated from the boundary melting curve or within the scanning loops, was found to be controlled by percolation effects and pore topology (Kondrashova et al., 2010; Hitchcock et al., 2011; Petrov and Furo, 2011a).

2.9 Summary

This chapter firstly introduced the reader into the basic principles of NMR spectroscopy. Then a background theory to the T_1, T_2, PFG and cryoporometry NMR experiments was provided, and will be used in this work, mainly for characterization of porous materials. A more detailed literature review on co-operative phenomena in cryoporometry NMR will be provided in the experimental chapters, according to the purpose of study. Moreover, some equations introduced in this chapter will be presented again in the following chapters for clarity.

Chapter 3

Probing the impact of cooperative phenomena on the accuracy of pore size distribution derived from cryoporometry NMR and gas sorption techniques

3.1 Introduction

The pore size distribution (PSD) is a key descriptor for characterising the void space of a porous solid, such as a heterogeneous catalyst (Rouquerol, 1999). The PSD can be the main factor determining important features of porous solids, such as the overall activity, or coking-resistance, of a heterogeneous catalyst. Hence, it is important to obtain an accurate determination of the PSD. A number of different techniques, such as gas adsorption, mercury porosimetry, NMR cryoporometry, DSC thermoporometry and NMR relaxometry can be used to determine pore size information. Each of these techniques depends on a different physical process, and relies upon a different theory, and accompanying set of auxiliary assumptions, with which to transform raw experimental characterisation data into a PSD.

For a porous solid the PSD can be obtained from the nitrogen adsorption isotherm using an algorithm, such as the BJH model which is widely adopted in industry (Barrett et al., 1951). This algorithm makes the assumption that pores of different sizes are thermodynamically independent. This is equivalent to treating the individual 'pores' within an irregular, interconnected void space as if they were located within a hypothetical parallel pore bundle. Even assuming it is possible to obtain a physically meaningful definition of a 'single pore' within an irregular, interconnected void space, this assumption neglects the possibility of interactions between neighbouring pores, or even over much larger length-scales. Alternative methods, such as non-local density functional theory (NLDFT) (Neimark and Ravikovitch, 2001), improve on the pore-scale physics of the phase transition in a single pore but subsequent calculations of pore size

distributions still make the same assumptions regarding thermodynamically independent pores as with the BJH method.

From considerations of basic adsorption theory, involving the Kelvin equation, it is possible to deduce that cooperative pore-pore interaction phenomena will occur during adsorption (de Boer, 1958). It is proposed that, for a through (open in both sides) ink-bottle pore geometry, if the radius of the two shielding pore necks is greater than half that of the intermediate pore body then all will fill at the same pressure. In this case, the pressure required is equivalent to that given by the Cohan equation (Cohan, 1938) for a cylindrical meniscus in the pore neck. This is because once condensate has filled the pore neck, filling of the pore body may then proceed via ingress of the, now hemispherical, meniscus from the end of the pore neck. If the pore neck radius is over half that of the pore body, then the pressure for condensation within the pore body, for a hemispherical meniscus, is exceeded by the pressure required to condense in the neck with a cylindrical meniscus. This process is known as the 'advanced adsorption' or 'advanced condensation' effect (Esparza et al., 2004). Grand canonical Monte-Carlo (GCMC) simulations (Coasne et al., 2007) of argon adsorption in model, unconnected pores possessing corrugations have confirmed the aformentioned general picture as originally proposed by de Boer (de Boer, 1958). Mean-field density functional theory (MFDFT) simulations of adsorption, in disordered models for silica aerogels, have shown that an initially localized condensation event can trigger further collective condensation in neighbouring cavities, such that the independent pore model is completely inappropriate for these materials (Detcheverry et al., 2004). In gas desorption, the condensate empties via a hemispherical meniscus, at the liquid-vapour interface. However, when big pores are shielded from small necks, desorption is delayed until these necks are emptied, thus the PSD derived from gas desorption is not accurate. If cylindrical pores were filling and emptying independently, as proposed by the 'single pore' theory, then the relative pressure during desorption would be a power of two of the relative pressure in adsorption. Hitchcock (2011), showed that they are correlated by a power of 1.85.

In cryoporometry the melting process for the solid is initiated from the existing molten phase, such as the liquid-like layer that is retained at the pore wall even when that in the centre of the pore is frozen. However, it is possible that if a small radius cylindrical pore is attached to a larger radius cylindrical pore at one end, in a funnel-like arrangement, then, once the smaller pore melts via its cylindrical sleeve meniscus, a hemispherical meniscus will be formed at one end of the larger pore. If the larger pore radius is smaller than the critical size for melting via a hemispherical meniscus at the current temperature, then the larger pore will also melt at the same temperature as the smaller pore. Hitchcock *et al.* (2011) have shown that such advanced melting effects can lead to a dramatic skew towards smaller pores in PSDs for mesoporous sol-gel silicas, determined from cryoporometry melting curves. Cryoporometry freezing follows a similar geometrical mechanism, known as heterogeneous nucleation. Here pore freezing is nucleated by the frozen external bulk layer which penetrates the molten phase via a hemispherical meniscus, but is prone to pore blocking effects, caused by the small necks. If cylindrical pores were freezing and melting independently, as proposed by the 'single pore' theory, then the freezing point depression would differ from the melting point depression by a factor of two. This relationship is not true for the whole pellet sample S1, as shown by Perkins *et al.* (2008).

In this chapter cryoporometry and water vapour sorption are combined to study the onset of advanced melting effects in a sample partially-saturated with different volumes of condensate, in turn, by pre-equilibration at different vapour pressures of the adsorbate. NMR relaxometry and diffusometry have been used to independently study the size and connectivity of adsorbed liquid ganglia at different molten fractions. These studies will enable the critical pores governing the advanced processes to be identified, and the likely errors in PSDs arising from advanced effects to be quantified. Moreover, the freezing mechanism of the partially saturated samples will be studied and discussed in terms of pore blocking and supercooling effects. The role of pore connectivity in cooperative phenomena occurring during melting/freezing and adsorption/desorption processes will be further elucidated by sample fragmentation and scanning loops initiated from partially molten fractions on the boundary melting curves of the samples.

3.2 Previous studies

The filling of mesoporous silica materials with water has been studied previously using cryoporometry, T_2 relaxation and PFG NMR techniques, but, usually, only using each technique individually, or in concert with just one other method, and not using all three simultaneously. In early work, Allen *et al.* (1998) studied the filling processes of water and cyclohexane in porous silica using NMR relaxometry and cryoporometry, and interpreted their data in terms of a 'puddle pore-filling model', whereby condensed liquid initially collects in particular concavities within the void space. These authors only considered growth in puddle size and geometry, and not the manner of that growth. More recently, Troyer *et al.* (2005) have interpreted similar datasets in terms of a so-called 'plug model' of pore-filling. Farrher *et al.* (2007) have used MRI without pre-conditioning and magnetization grid rotating frame imaging (MAGROFI) to study the spatial distribution of liquid within partially saturated silica samples. Their MRI studies demonstrated a heterogeneous spatial distribution of liquid on macroscopic length-scales. Naumov *et al.* (2008) have studied the spatial arrangement of condensate within the void space, on the adsorption and desorption branches of the hysteresis loop region of the isotherm, for cyclohexane sorption in Vycor porous glass. They found that the diffusivity differed between the boundary adsorption and desorption branches of the hysteresis loop at the same degree of pore-filling. In addition they also found that the spatial arrangement of condensate at the same saturation level differed for scanning loops, when compared with the boundary curves. These results suggested that the spatial arrangement of condensate within pores was dependent upon the adsorption-desorption history of the sample.

Partially saturated KIT-5 systems, with a pore size of ~10-19 nm and ink-bottle shape, were studied by Morrishige *et al.* (2007) via DSC. The authors found that by decreasing saturation and the pore size, both freezing and melting point depression increases. This was because, when the molten pore bodies are isolated from the frozen menisci by necks smaller than 4 nm, or when the systems are partially saturated and the molten pores are surrounded by empty pores, then they will freeze spontaneously close to the homogenous nucleation temperature of bulk water between 230-240 K (Morishige et al.,

2007). The authors thus concluded that freezing is a percolation controlled process, highly dependant on the neck size, whereas melting is controlled only by the cavity size. Bogdan *et al.* (1998) found that water adsorption (from 1-4 nominal statistical monolayers) on a layer of fumed silica particles with a low number of silanol groups, occurs in clusters which will merge and form a population of droplets with a wide size distribution, as opposed to the fully hydroxylated surfaces, where adsorption occurs in monolayers. They suggested that the small droplets will require a lower temperature to freeze due to the lower probability of the density and configuration fluctuations favouring freezing of small size water droplets as reported by Pruppacher (1995). This will appear as a "tailing" towards low temperatures, for a DSC peak, whereas the asymmetric and wide DSC peak invokes the presence of droplets with a wide size distribution (Bogdan et al., 1998). DSC studies on the freeze/thaw mechanism of water confined in regularly structured materials, such as MCM-41 and SBA-15, of sizes 2.9-3.7 nm and 4.4-11.7 nm respectively, and at different saturations levels were conducted by Schreiber *et al*. (2001). These authors found that the melting point depression was sensitive to the pore size (i.e. decreased when the cavity size increased), but was only slightly dependant on the pore filling (only a small shift to higher temperatures was observed when saturation increased). On the contrary, freezing was more sensitive to probe the different states of the condensed phase in the partially saturated samples. For example in these systems, when the temperature is decreased the completely filled pores freeze first, followed by the liquid bridges and then the thick water layers on the pore walls (Schreiber et al., 2001). Morishige and Iwsaki (2003) found that melting in partially saturated SBA-15 (pore size ~7.8 nm) was independent of pore filling but freezing differed according to the state of the condensed phase. These studies (Morishige et al., 2007; Morishige and Iwasaki, 2003; Schreiber et al., 2001) suggest that the freezing is more sensitive to detect the different states of the condensed phase in the pores, but it is prone to pore blocking and supercooling effects, thus the boundary freezing curve in a cryoporometry experiment must not be used to calculate PSDs. Moreover, melting occured over a narrow temperature range, depending only slightly on the pore filling, due to the narrow PSD of these ordered materials. Hence, studies of cooperative effects within model porous solids with controlled pore size and geometry, achieved either by templating (such as SBA-15 or MCM-41) or electrochemically-etching

(such as alumina or silicon membranes), are of limited value in understanding the extent of the cooperative effects in more commonly used catalyst support materials, such as γ-alumina or sol-gel silica pellets, because of the limited size, and reduced complexity, of the controlled unit cell within the model materials. In a later study, Liu *et al.* (2010) studied the freeze/thaw mechanism of water in partially saturated Vycor and completely saturated samples with regular (MCM-41, SBA-15) and irregular (Vycor, sol-gel silica, Develosil) pore structure. The authors found that freezing is associated with the radius of curvature for high pore fillings but remains constant for low pore fillings. On the contrary, melting is more sensitive to the geometrical structure of pores, as a different correlation between the melting temperature and the surface-to-volume ratio was obtained for regular and irregular pores. Moreover, Liu *et al.* found that the melting temperature for Vycor saturated via adsorption is lower than that saturated via desorption, attributing this behaviour to the water redistribution in the pores during the collective freezing processes. However, these authors ignored the effect of the different spatial arrangement of the condensate in the pores and the size of the pores filled, on the freezing mechanism, at each saturation level. They also invoke water distribution in strong and weaker adsorption sites, to interpret the broad melting DSC peak patterns observed, not taking into account the size of the pores filled and their connectivity.

Pore size distributions though are critical descriptors used to aid the understanding of the performance, and design, of porous heterogeneous catalysts, and it is important to know their limitations. The only way to establish the extent and importance of the cooperative effects, particularly those of longer range, within amorphous materials is to study them directly. Hence, it is necessary to be able to isolate the individual stages in the inception, growth and pervasion of cooperative processes within complex pore networks using highly sophisticated characterisation techniques. Therefore, in this work, it is proposed to study the progressive adsorption of water vapour within a mesoporous sol-gel silica, denoted as S1, using NMR cryoporometry, NMR relaxometry and NMR diffusometry at different relative pressures. Further, the particular material selected for this study possesses highly pronounced, macroscopic correlations in the spatial distribution of pore size (Rigby and Gladden, 1996; Hollewand and Gladden, 1995b), which makes it appropriate for studies of long-range effects, well beyond the unit-cell

size of templated or etched model materials. MRI studies show that there are macroscopic heterogeneities in the spatial distribution of pore size in the S1 material (Rigby and Gladden, 1996; Hollewand and Gladden, 1995b), capable of inducing pore blocking in freezing and advanced melting, analogous to pore blocking in desorption and advanced adsorption in gas sorption, respectively. Perkins *et al.* (2008) showed that by fragmenting the S1 material, it is possible that pore shielding effects in freezing can be reduced. Hitchcock (2011) used scanning curves on the same material to further show that particle fragmentation also decreased advanced melting phenomena.

Cryoporometry scanning curves and loops, initiated from partially molten phase were previously reported by Kondrashova *et al.* (2010). The authors demonstrated that pore melting of nitrobenzene imbibed in Vycor, occurs independently, in the radial direction. However, they attribute the immediate melting upon increasing the temperature from the partially molten fractions on the boundary freezing curve, to melting initiated via the hemispherical meniscus offered by the liquid-like layer on some dead end pore walls. Hitchcock *et al.* (2011) showed that hysterisis in the cryoporometry scanning loops for water imbibied in S1 material, can be purged over small temperature ranges, indicative of axial freezing and melting mechanisms, and as such advanced melting process. They further showed that although a ratio of two between the melting and freezing point depression on the arms of the scanning loops, indicative of single pore hysterisis, does not exist, pore blocking during freezing and advanced melting during melting can lead to identical connectivity and pore sizes of the molten phase. Petrov and Furó (2011) used NMR cryoporometry scanning curves and loops and T_2 relaxometry, to ascertain the interconnectivity of the porous structure on well and poorly connected sol-gel materials (CPG and Vycor, respectively). The authors found that for CPG, at equal molten fractions, there exists similar interconnectivity between the frozen pores, no matter if it reached there via freezing or melting. On the contrary, for Vycor, spatial distribution of frozen pores changes upon freezing and melting due to topological restrictions during freezing, and the fast exchange between the frozen and molten phases. Here the molten menisci are able to initiate melting in the neighbouring frozen pores.

In this work cryoporometry, T_2 relaxation and PFG NMR techniques will all be used to study each stage in the progressive equilibrium adsorption and desorption of water vapour within a mesoporous silica pellet (denoted as S1) , with an explicit aim to detect and study advanced phenomena during water vapour sorption and freeze/thaw mechanisms. In particular, the nature of the pore-filling process will be followed to determine how and when the advanced phenomena arise. In addition, cryoporometry scanning loops will be used to assess the reversibility of the melting process, and the connectivity of the condensed phase following vapour sorption at different relative pressures. A partially saturated fragmented sample will be also studied to elucidate the advanced phenomena for pore filling/emptying and melting/freezing mechanisms, operating during vapour sorption and liquid/solid phase transitions, respectively, when pore connectivity is diminished.

3.3 Experimental procedure and methodology

The material studied in this work was a batch of commercially-available sol-gel silica spheres, denoted S1, of diameter ~2-3 mm. The batch average BET specific surface area is ~200 m^2/g, and the batch average specific pore volume estimated from the sample studied in this work is ~0.80-0.92 cm^3/g, as there are some differences between individual pellets due to intra-batch variability. This material has been extensively characterised by Rigby and co-workers, including calculation of pore size distributions obtained from gas sorption, mercury porosimetry and NMR cryoporometry (Rigby et al., 2008; Hitchcock et al., 2011). Sodium hydroxide (NaOH) (99.99% trace metals basis) was purchased from Fluka. Prior to the adsorption experiments, the samples were pre-soaked in ultra pure water, and then the bulk and physisorbed moisture was removed by degassing for 2 h at 363 K, followed by 10 h at 393 K. These conditions were chosen to avoid any partial dehydroxylation of the silica surface, since only water physisorption is required.

3.4 Water adsorption

In order to obtain relative pressures of water vapour of 0.81-1.0 (capillary condensation region), the sol-gel pellets were suspended above NaOH solutions of different concentrations (Perry and Green, 1997). The samples were then left to equilibrate for 5-7 days at 294 K, over a 'large' solution reservoir, in order to permit the assumption that the concentration of NaOH remains constant throughout the adsorption process. The points of the water isotherm were obtained by gravimetrically measuring the water uptake of thirty similarly sized pellets, at each relative pressure.

For the NMR experiments, a given sample, consisting of a single pellet, was prepared identically to as described above, and then was quickly transferred to an NMR tube (Figure 3.1a). The experimental set-up and procedures were as described below. Single pellet samples were weighed before and after the experiments, to check that no significant liquid evaporation occurred during the experiment and the course of transfer into the NMR tube. Sets of cryoporometry experiments were performed at different saturation levels for the same single pellet sample. For the NMR experiments, two different single pellet samples from the same batch were used.

Pellet 1 was used to generate cryoporometry melting curves, T_2 and tortuosity values for fully molten samples saturated via adsorption at each relative pressure in the range between 0.81-0.94. Pellet 2 was also partially saturated via the same procedure between P/P_0=0.84-1.0. This sample was then used to generate both freezing and melting boundary curves, T_2 and tortuosity values for fully molten sample, after equilibrium adsorption with water vapour at P/P_0=0.84-1.0 and equilibrium desorption at P/P_0=0.86. For the fully saturated pellet 2, further T_2 and tortuosity values were obtained along its boundary melting curve, at molten fractions equal to the volume of the adsorbed phase for the partially saturated samples. Moreover, freezing and melting boundary curves were obtained for the case of pellet 2 partially saturated via equilibrium desorption at P/P_0=0.86. Scanning loops and scanning curves were performed for pellet 2 saturated via adsorption at P/P_0=0.92 and 1.0, but only a scanning curve was performed for this sample after equilibrium desorption *at* P/P_0=0.86.

Whole dry S1 pellets, from the same batch as above, were fragmented using a pestle and mortar. Their particle size was determined using a microscope and they were found in the range of 5-40 μm. Then, 5 mg of this sample were placed within a plastic pipette tip and was partially saturated above NaOH solutions at the range of P/P_0=0.83-1.0 via equilibrium adsorption and at P/P_0=0.85-0.86 via equilibrium desorption. The same NMR experiments as for pellet 2 were performed for this fragmented sample. A schematic representation of the experimental set up is provided in Figure 3.1b.

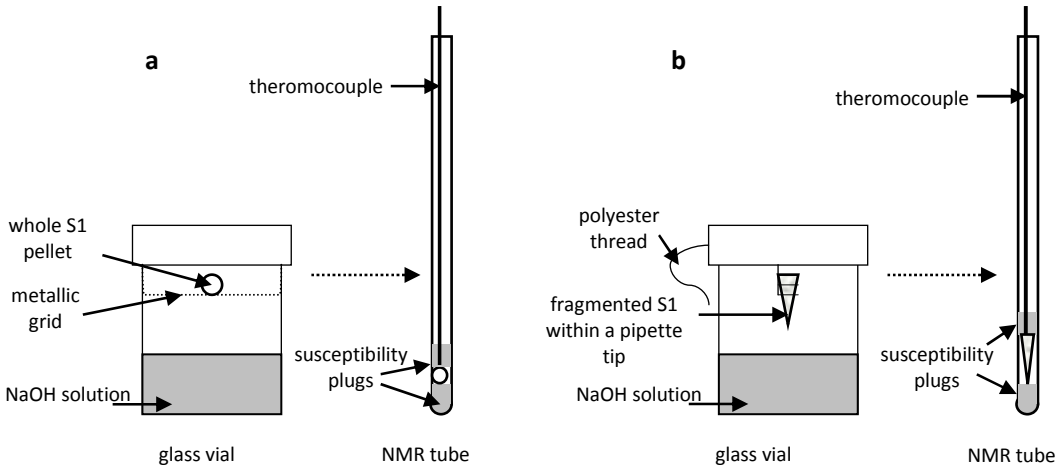

Figure 3.1 Schematic representation of the experimental set up for the equilibrium water sorption above NaOH solutions at 294 K and for the NMR experiments for the a) whole and b) fragmented samples

3.5 NMR cryoporometry

All NMR experiments were carried out on a Bruker Avance 400 MHz spectrometer with a static field strength of 9.4 T, yielding a resonance frequency of 400.13 MHz for ^{1}H nucleus. The temperature control unit within the probe uses a controlled flow of cool nitrogen gas evolved from liquid nitrogen, in combination with a heating element below the sample in the gas flow stream. Temperature control was achieved using a Bruker BVT3200 temperature control unit, able to measure and maintain the probe temperature within ±0.1 K within the range of 123–423 K. The chosen pulse sequence was a simple spin-echo sequence, a more basic form of the Carr–Purcell Meiboom–Gill (CPMG)

sequence (Fukushima and Roeder, 1981). The choice of the simple spin echo pulse sequence was made according to literature (Khokhlov et al., 2008, Strange et al., 1993) as it accounts for small magnetic field inhomogeneities that are present within the sample, therefore enhancing the quality of the signal obtained. A CPMG sequence was not used due to the hardware limitation not permitting the delay time between the successive 180° pulses to be less than 1.2 ms, while the echo time (2τ) had to be kept at 2 ms to suppress the signal from the liquid like layer on the pore surface.

A single saturated pellet, or the fragmented sample within the pipette tip, was placed within a 5 mm NMR tube, between two susceptibility plugs to reduce the water evaporation from the pores (Figures 3.1a and b) and to hold the sample in the middle of the active region of the radiofrequency coil. A thermocouple was used to measure the real temperature of the sample and it was placed on to the top of the pellet, via a hole in the centre of the top susceptibility plug. The thermocouple calibration was previously described by Hitchcock (2011). The sample was frozen down to 225 K, and then the temperature was increased stepwise. At each step, it was then allowed 15 min to reach equilibrium and a series of proton spin-echo spectra was taken for each saturation, at each temperature. This time proved to be sufficient for the system to complete any phase transition at each temperature change. All the molten fractions are normalized to the 100% molten fraction at the top of the pellet or the fragmented sample melting curve for the 100% saturated sample (at P/P_0=1.0). It was noticed that for samples saturated below P/P_0=0.81, the free induction decay (FID) was inadequate to be recorded due to the fast relaxation of the water molecules in close proximity with the pore walls; hence, all the samples used for the cryoporometry experiments were saturated at higher relative pressures. As there is no bulk liquid on the surface of the pellet, the total FID at ~273 K corresponds only to the total water adsorbed within the pores. Application of a suitable correction of the results for the Curie law was found to make no significant difference.

The pore size distribution from cryoporometry boundary melting curves for pellet 2 and the fragmented sample were calculated via Gibbs-Thomson equation 2.19. However, cryoporometry is an indirect pore size characterisation technique, since to obtain

absolute pore sizes, it requires a calibration of the Gibbs-Thomson parameter against pore size measures from another technique that may encounter other cooperative phenomena. Hence, we have used the cumulative PSD as a function of the reduced pore radius (r/r_{ref}). For this, firstly the cumulative PSD was plotted for each melting curve and a point of inflexion, r_{ref}, was found for each of them. The pore size was then divided by r_{ref}.

3.6 T_2 relaxometry

NMR relaxometry is used to probe the adsorbed ganglia sizes. For the relaxometry experiments, the samples were prepared as described in Section 3.2 and T_2 relaxation was measured, using a CPMG sequence. T_2 relaxation is calculated according to the expression:

$$I = I_0 \exp(-t / T_2) \tag{3.1}$$

where t is the echo time and I is the FID signal intensity. For more heterogeneous samples a two-component relaxation model was used:

$$I = I_0 [a \exp(-t / T^f_2) + (1-a) \exp(-t / T^S_2)] \tag{3.2}$$

where T^f_2 and T^S_2 are the relaxation times for the fast and slow components, with fractions a and $(1-a)$, respectively.

As discussed in Section 2.3 the value of T_2 may be converted to a surface area to volume ratio by the adoption of a relaxation model. For a liquid imbibed within a confined space, the relaxation rate is enhanced. This is due to the particular thin layer of liquid in close proximity to an interface being affected by its presence, thereby increasing the relaxation rate. There is also diffusional exchange between the surface-affected layer and the remainder (bulk) of the liquid. In the case, as here, where the liquid ganglia are several orders of magnitude smaller than the rms displacement of the probe water molecules during the course of the experiment, the ‘‘two-fraction fast exchange model’’ of

Brownstein and Tarr can be used (Brownstein and Tarr, 1977). The measured value of T_2 is then expressed by equation 2.7.

For pellet 1 of S1, relaxation time measurements were performed at the 100% molten fraction, for each relative pressure, at ~273 K. For pellet 2 and the fragmented sample, relaxation time measurements were obtained at various positions around the scanning loops, and the boundary freezing and melting curves. The time between 180° pulses in the CPMG sequence, for all relaxation experiments, was 1.2 ms. It was found that the single component model (equation 3.1) gave a good fit to data for fully molten samples, while the greater heterogeneity of the partially molten samples required a fit to the two-component relaxation model (equation 3.2).

3.7 NMR diffusometry

All PFG-NMR experiments were carried out using the NMR system described above. The pulse sequence used was a stimulated echo with bipolar longitudinal eddy current delay (BPLED) developed by (Wu et al., 1995). The values of δ and τ were 0.002 and 0.0001 s, respectively, and the diffusion times, Δ, used, were 0.05, 0.1, 0.15 and 0.2 s. For each diffusion experiment, 10 data points were taken at increasing gradient strengths between 0.674 and 33.143 G/cm, and each point was obtained with 16 scans. The apparent diffusion coefficients were measured at ~273 K, corresponding to the completely molten state for all samples and at lower temperatures for the partially molten state when they are fully saturated. Their values were calculated from the signal attenuation observed during the experiment. To account for any temperature dependency of the apparent diffusion coefficient between the experiments, a calibration curve of bulk water was used based upon literature data (Holz et al., 2000) and determined by Perkins (2009).

Pulsed field gradient (PFG) NMR can be used to determine the effective diffusion coefficient of a molecule within a sample calculated according to equation 2.10. In the experiments considered in this work, diffusion is occurring within the molten, adsorbed

ganglia of water, as any bulk water will be frozen. Adsorbed ganglia may be complex in geometry and topology, and extend beyond a single pore. At the very shortest diffusion times, the diffusing molecule is free to explore the localised ganglia topology, and will henceforth be referred to as unrestricted diffusion (though, of course, it will still be confined due to local pore walls and menisci). At slightly longer diffusion times, the motion of the molecule within each ganglion may become restricted by collision with the outer, boundary perimeter (i.e. edge) of the ganglion formed by the vapour-liquid meniscus and/or solid walls of the pore, and, therefore, the measured effective diffusion coefficient is indicative of the overall 'cavity size' of the confining ganglion. At the longest diffusion times, if the ganglia are all isolated, all molecular motion will become completely restricted, or, if the ganglia are interconnected, the molecule may find (a potentially narrow exit and) leave the cavity formed by the proximity of various nearby pore walls and menisci, and begin to probe the wider interconnected ganglia network. In this case the measured diffusion coefficient is indicative of the overall tortuosity of the continuous, adsorbed phase. In between these limits, it is likely that there will be a combination of restricted and unrestricted diffusion. For diffusion within the adsorbed phase, the tortuosity of the ganglia network may be obtained using equation 2.12.

In this work, the self-diffusion of molten phase (water) will be studied within the ganglia of adsorbed phase. The root mean square (rms) displacements of the water molecules during the PFG NMR experiments will typically be smaller than the overall spatial extent of particular ganglia, but diffusion times will be employed such that a fraction of the diffusing molecules sense the outer perimeter at the edge of a ganglion. Hence, following the suggestion of Gjerdåker *et al.* the short time diffusion model of Mitra *et al.* will be applied to the PFG NMR. Mitra *et al.* have shown that a perturbation expansion of the measured diffusivity will deviate from the macroscopically unrestricted intra-ganglion diffusion coefficient, thus equation 2.14 can be applied for the estimation of the unrestricted diffusivity (or reciprocal tortuosity) within the liquid ganglia. The PFG experiments conducted in this thesis require a substantial amount of time (~2 hr for a set of PFG experiments at Δ=0.05-0.2 s), as based on the literature the delay time between the pulses has to be $5xT_1$ to ensure complete magnetization recovery into the z-axis. Chapter 9 will show that this time can be reduced ~5 times.

3.8 Nitrogen sorption

Nitrogen adsorption studies were performed using a Micrometric Accelerated Surface Area and Porosimetry (ASAP) 2010 apparatus, at 77.35 K. Initially the whole pellet sample of ~0.14 g was degassed as described in Section 3.3 and the adsorption isotherm was obtained at the relative pressure range between 0.003-0.99, with 45 s equilibration time. Again the cumulative PSD was plotted against r/r_{ref}, where r_{ref} is the point of inflexion in the cumulative PSD calculated from the BJH model for cylindrical type pores using the adsorption curve.

3.9 Results

3.9.1 Water adsorption

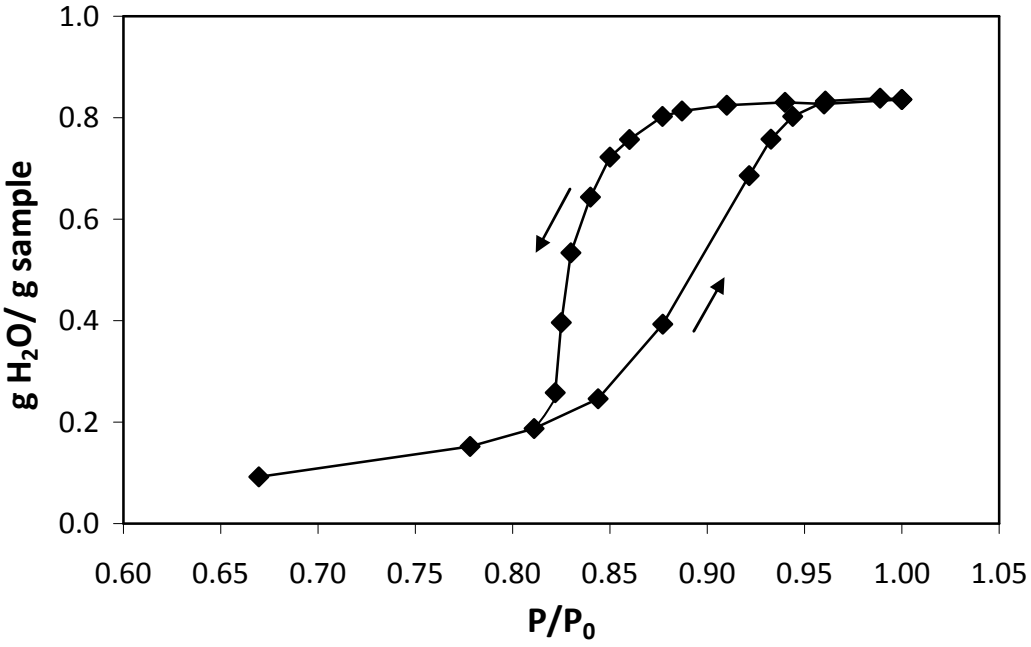

Figure 3.2 Normalized water isotherms for a sample of 30 whole pellets obtained at 21°C. The water uptake was measured gravimetrically. The arrows show the direction of the water sorption process

Figure 3.2 shows the equilibrium water sorption isotherms obtained gravimetrically for a sample of 30 pellets from batch S1 used in this work. The shape of the hysteresis loop is Type H2, which is similar to that generally obtained for nitrogen adsorption in

disordered, mesoporous solids (Rouquerol, 1999). In Chapter 5 it will be shown that nitrogen sorption isotherm for this material is more Type H1.

3.9.2 NMR cryoporometry boundary melting curves. T_2 relaxometry and diffusometry studies

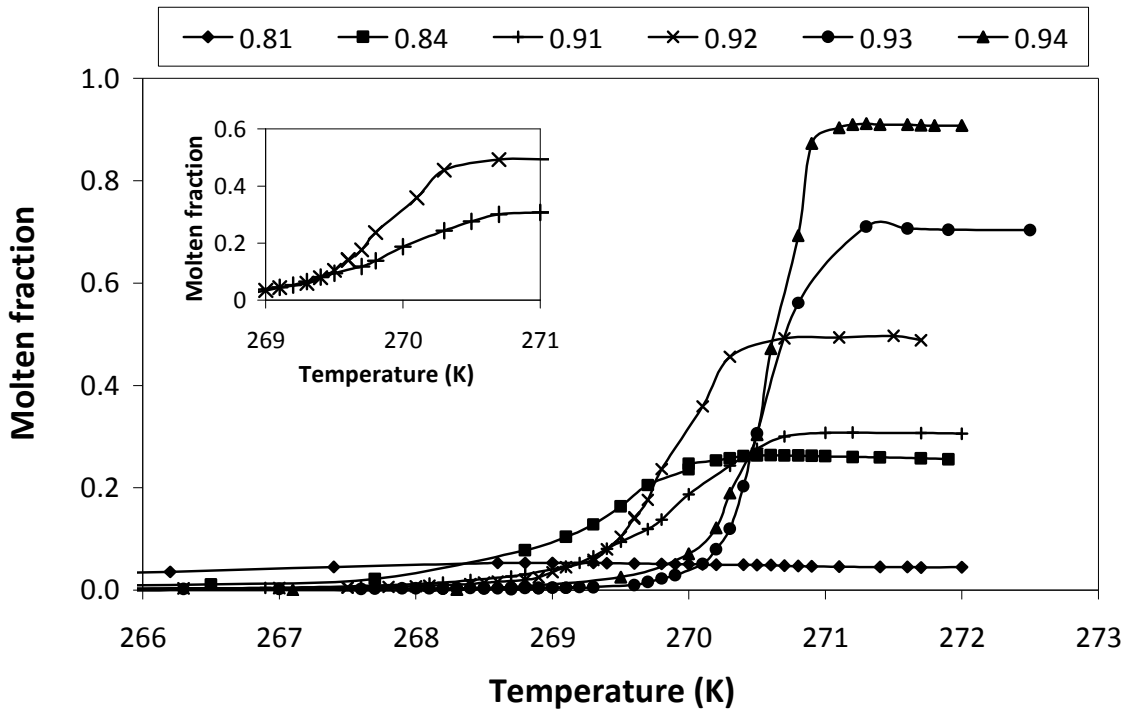

Figure 3.3 NMR cryoporometry melting curves for the adsorbed phase in a single pellet sample (pellet 1) at P/P_0=0.81, 0.84, 0.91, 0.92, 0.93, 0.94 and 1.0 of water vapour. The inset shows a close-up view of the steep parts of the melting curves for saturation at P/P_0=0.91 and 0.92

Figure 3.3 shows the boundary melting curves obtained for the adsorbed phase within a single pellet sample, denoted pellet 1, at various different relative pressures of water vapour in the range 0.81-0.94. The molten volume fractions, at different relative pressures, are measured relative to the total pore volume of this pellet, and, thus, the ultimate molten volume fractions achieved for experiments below total saturation are less than unity. It can be seen that, with increasing relative pressure, the melting curves move to higher temperatures and the steps up in intensity become more abrupt (i.e. spread over a smaller temperature range). In particular, it is noted that the melting curves for relative pressures of 0.91 and 0.92 generally overlay each other up to

~269.5 K, after which they diverge. The 0.92 relative pressure curve rises more abruptly than that for the 0.91 relative pressure curve, as highlighted in the inset in Figure 3.3. However, it is noted that the 0.91 relative pressure curve shows a significantly larger increase in signal intensity over the higher temperature range ~270.3-270.7 K than the P/P_0=0.92 curve, despite the larger overall final intensity of the latter.

Figure 3.4 shows the variation in T_2 of the adsorbed phase with relative pressure (humidity) for the same pellet sample as used to obtain the data in Figure 3.3 (pellet 1). It can be seen that after an initial rise up to a relative pressure of 0.84, the T_2 value stays roughly constant until a relative pressure of 0.92, when it begins to rise steeply. All the data from the relaxation experiments for fully molten samples exhibited mono-exponential log-attenuation behaviour, suggesting that extensive diffusional averaging of the size of the liquid ganglia, arising at each pressure, was occurring. Figure A1.1, in the Appendix shows an example of the log-attenuation plot, fitted to the raw relaxation data, obtained for pellet 1 at low saturation (P/P_0=0.84).

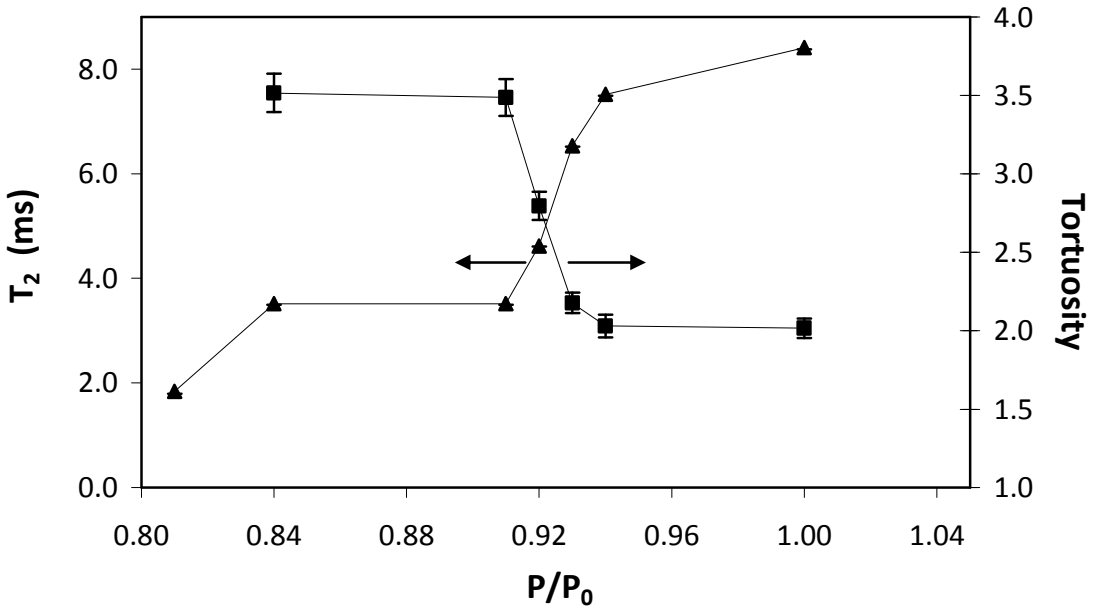

Figure 3.4 Variation of NMR spin-spin relaxation time (T_2) and unrestricted diffusion tortuosity for the adsorbed phase, obtained at the top of the melting curves (all at 273 K), with relative pressure of water vapour used to obtain the data in Figure 3.3 (pellet 1). The errors in the T_2 values are smaller than the size of the symbols

The raw log-attenuation data were obtained for diffusion within the molten phase at the top of the melting curve (where any bulk liquid in the thin external film would still have been frozen if any had existed) for pellet 1. These data were fitted to a monoexponential model according to equation 2.10, and were found to give rise to good fits with respect to the small standard and fitting errors observed. For each relative humidity, the set of values of diffusivity thus obtained at different diffusion times, were then fitted to the model for partially restricted diffusion (D_0) as given by equation 2.14. These data all gave rise to good fits to the partially restricted diffusion model. The limiting values of the apparent tortuosity for unrestricted (but confined) diffusion were then obtained using the value of bulk (free) diffusivity appropriate to the relevant temperature. The rms displacements calculated from the unrestricted diffusivity are consistent with liquid-phase only mass transport, as there was no indication of diffusion apparently occurring faster than for bulk liquid. Figure 3.4 also shows the variation of unrestricted diffusion tortuosity with relative humidity (pressure) for the same pellet sample used to obtain the data in Figure 3.3 (pellet 1). It can be seen that the tortuosity is roughly constant until a relative pressure of 0.91, and thereafter it declines rapidly with increasing relative pressure.

During the PFG experiments it is likely that there was negligible exchange between the vapour and liquid phases within the pores, even at the very low saturation levels where a larger fraction of the void space was occupied by vapour. This is because, as shown in the typical data-set for a sample saturated at relative pressure of 0.84 given in Figure A1.2, Appendix, a mono-exponential fit (equation 2.10) to the log-attenuation data was found to be sufficient, which would have been unlikely if significant exchange was occurring between the liquid and vapour phases. Moreover, when there is an exchange between the liquid and vapour phases, the diffusivity observed would be significantly higher than that of the bulk pure liquid itself (Crank, 1975). This means that the tortuosity estimated via equation 2.12 would be lower than one. However, this is not the case as seen from Figure 3.4, where for the partially saturated systems had a tortuosity higher than two.

3.9.3 NMR cryoporometry scanning curves for the whole and the fragmented samples

The whole pellet 2 was used to obtain a closer insight into the melting and freezing mechanism of partially saturated samples, when they are saturated via equilibrium adsorption and desorption. Both boundary freezing and melting curves for pellet 2 for adsorption at P/P_0=0.92 and desorption at P/P_0=0.86 are presented in Figure 3.5. From Figure 3.5 it can be seen that the boundary melting curve, for the sample equilibrated at P/P_0=1.0, begins to rise at a significantly lower temperature, and rises more steeply, than that for the same sample equilibrated at P/P_0=0.92 and P/P_0=0.86. This is in good agreement with the results presented in Figure 3.3 for pellet 1. However, some interbatch variability between pellet 1 and 2 regarding the pore connectivity would possibly induce a different distribution in the adsorbed water ganglia and therefore pore water melting. Moreover, it is shown that for the partially saturated samples, the presence of an external bulk layer is not necessary to initiate pore freezing upon reversing the temperature at the end of the boundary melting curves. Indeed the imbibed pore water in the partially saturated system starts freezing at 269 K, which is slightly lower than the temperature where the 100% saturated system begins to freeze (~269.2 K). However, complete pore freezing for the 100% saturated sample is achieved at 268.3 K, whereas the partially saturated ones show an abrupt freezing until 268.8 K and then the pores freeze over a wide temperature range in a form of a “tail”, until they all freeze at ~265 K.

Scanning curves initiated from partially molten fractions along the boundary melting curve are also included in Figure 3.5. It is seen that upon reversing the temperature freezing commences immediately for all samples. The scanning curve of the partially saturated sample via adsorption at P/P_0=0.92, though, crosses over the boundary freezing curve at 267.9 K, in contrast to the fully saturated sample at P/P_0=1.0 (even though the scanning curves commence from the same molten fraction of ~0.51), and the one saturated via desorption at P/P_0=0.86 which meet the boundary curve on the closure point of the hysteresis. This shows that different pathways of freezing are followed for each sample.

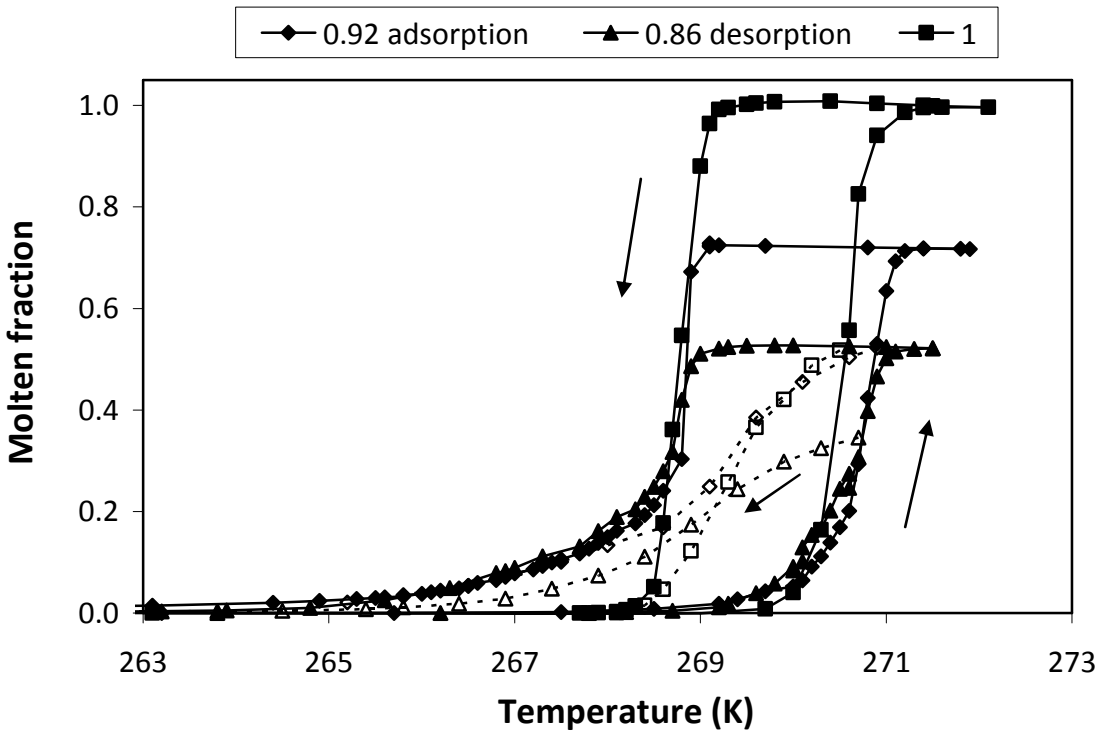

Figure 3.5 Freezing scanning curves for whole pellet 2 saturated at P/P_0=0.92 and 1.0 via equilibrium adsorption and via desorption at P/P_0=0.86 within their freezing and melting boundary curves. The arrows show the direction of the change in temperature

Boundary melting and freezing curves were also obtained for the fragmented sample saturated via adsorption at P/P_0=0.92 and 1.0, and via desorption at P/P_0=0.85, and the results are presented in Figure 3.6. The boundary melting curves for the samples saturated via adsorption show that pore melting starts at the same temperature, 266 K, but it is steeper for the fully saturated sample. The sample saturated via desorption generated a melting curve where the pores started melting at higher temperature (267 K) although the volume of the adsorbed phase was lower than that of the samples saturated via adsorption. This shows that some of the small pores filled with water at P/P_0=0.92 and 1.0 have emptied after desorption at P/P_0=0.85, and as such a higher temperature is required to initiate melting of the remaining bigger filled pores. Moreover Figure 3.6 shows that pores start freezing at higher temperature for the fully saturated sample (269.8 K), in contrast to the partially saturated samples at P/P_0=0.92 and 0.85 where freezing starts at 269 K and 268.5 K, respectively. For all these samples freezing extend over a wide temperature range, exhibiting a long "tail" similar to that observed for the whole partially saturated pellet 2, shown in Figure 3.5, although the pores of the

100 % saturated fragmented sample eventually all freeze at only slightly higher temperature (261.3 K) than the partially saturated ones. Furthermore, all the freezing scanning curves meet the closure point of their respective hysteresis (Figure 3.6).

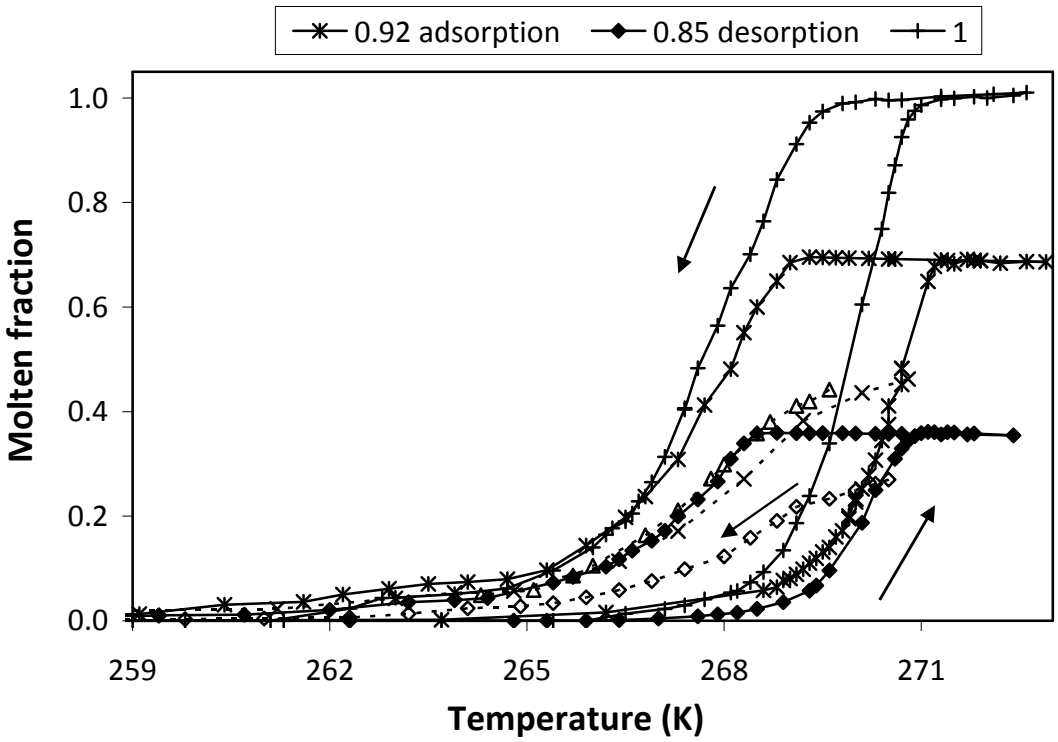

Figure 3.6 Freezing scanning curves for a fragmented sample saturated at P/P_0=0.92 and 1.0 via equilibrium adsorption and via desorption at P/P_0=0.85 within their freezing and melting boundary curves. The arrows are shown to guide the eye.

3.9.4 NMR cryoporometry scanning loops for the whole pellet and the fragmented samples. Relaxometry studies

Figure 3.7 shows a set of scanning loops, for pellet 2, following equilibration with water vapour at P/P_0=0.92 and 1.0. For both saturation levels, the scanning loops have the same starting point, which is ~51% of the total pore volume in the molten state. For the sample equilibrated at a relative pressure of unity, two scanning loops are shown, namely one which ends at the same temperature as the loop for the sample equilibrated at P/P_0=0.92 (wide loop), and one ending at the same molten fraction as the loop for the sample equilibrated at P/P_0=0.92 (small loop). It is also noted that, while the freezing

(upper) arm of the scanning loops for the sample equilibrated at P/P_0=1.0, more or less overlay the upper arm of the scanning loop for the sample equilibrated at P/P_0=0.92 for the range of temperatures ~270.5-269.5 K, they drop below it at lower temperatures. Hence, a larger volume of pores is frozen over the same drop in temperature for the sample equilibrated at a higher relative pressure. Also, from Figure 3.7, it can be seen that the melting arms of the scanning loops for the sample equilibrated at P/P_0=1.0 begin to rise at a lower temperature than the corresponding boundary melting curve. However, an early rise is not so evident in the melting arm of the scanning loop for the sample equilibrated at P/P_0=0.92, where the lower temperature section is much flatter.

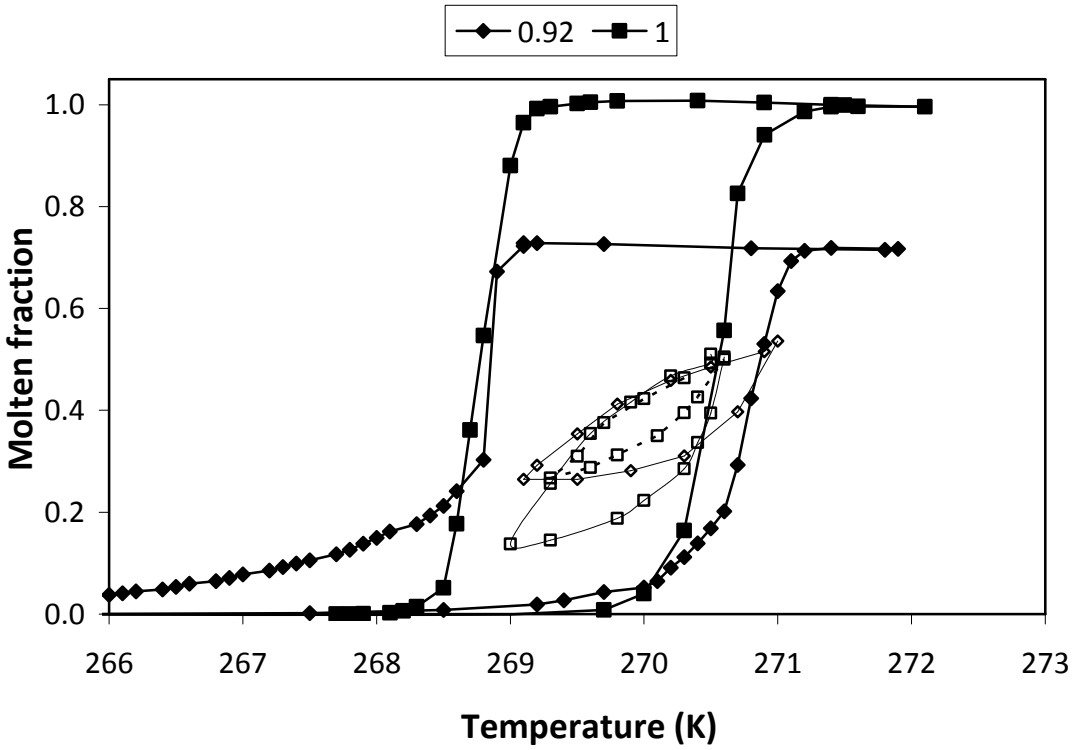

Figure 3.7 Scanning loops for a single whole pellet saturated at P/P_0=0.92 and 1.0 via equilibrium adsorption within their freezing and melting boundary curves

Studies of the variation in T_2 values with temperature, along the flat plateau at the top of the boundary freezing curve for a fully saturated sample, suggest that there is insignificant temperature dependence of T_2 values (±0.12 ms maximum error) over the narrow temperature range of interest between the boundary curves. Table 3.1 shows the

results of fitting a two-component relaxation time model (equation 3.2) to the relaxometry data obtained at different positions around the scanning loops for pellet 2, shown in Figure 3.7. It is noted that the average T_2 value at the top of the scanning loop, for the sample equilibrated at P/P_0=0.92, is higher than that at the top of the scanning loop for the sample equilibrated at P/P_0=1.0. Also, the average T_2 value at the bottom of the scanning loop, for the sample equilibrated at P/P_0=0.92, is higher than that corresponding to the same temperature (within experimental error) at the bottom of the scanning loop for the sample equilibrated at P/P_0=1.0 but equal to that corresponding to the same molten fraction.

P/P_0	Loop position	T^f_2 (ms)	α	T^S_2 (ms)	1-α	T_{2ave} (ms)
0.92	Top	4.7	0.85	2.20	0.15	4.30 ± 0.30
1.0	Top	5.5	0.45	2.10	0.55	3.60 ± 0.10
0.92	Bottom	2.9	0.54	1.06	0.46	2.10 ± 0.10
1.0	Bottom (equal temperature to 0.92 loop)	1.7	0.46	0.50	0.54	1.06 ± 0.01
1.0	Bottom (equal molten fraction to 0.92 loop)	3.0	0.42	1.40	0.58	2.1 ± 0.10

Table 3.1 Results of the 2-component fit to the T_2 data obtained at various positions around the scanning loops of the whole pellet 2, shown in Figure 3.7 using equation 3.2

Scanning loops, initiated from the same molten fraction of ~0.46, were also obtained for the fragmented sample at P/P_0=0.92, 0.93 and 1.0 in order to study the variation in the melting and freezing processes for freezing initiated from partially molten states, and the variation in the water ganglia connectivity, for less adjacent molten pores in proximity with frozen ones (as compared to the whole pellet 2). Figure 3.8 shows that freezing starts immediately upon reversing the temperature contrary to the boundary freezing

curve over the same temperature range. The freezing (upper) arm of the loops, for samples saturated at P/P_0=0.93 and 1.0 overlap along the same temperature range and the same rate of freezing (ie change in the molten fraction with temperature change) is observed for the sample saturated at the lower relative pressure of 0.92. The melting branch of the loops is nearly flattened until 268.8 K, for all the samples, similar to the boundary melting curves, but becomes steeper as saturation increases, even though the bottom of the loops correspond to the same molten fraction, and as such pore volumes.

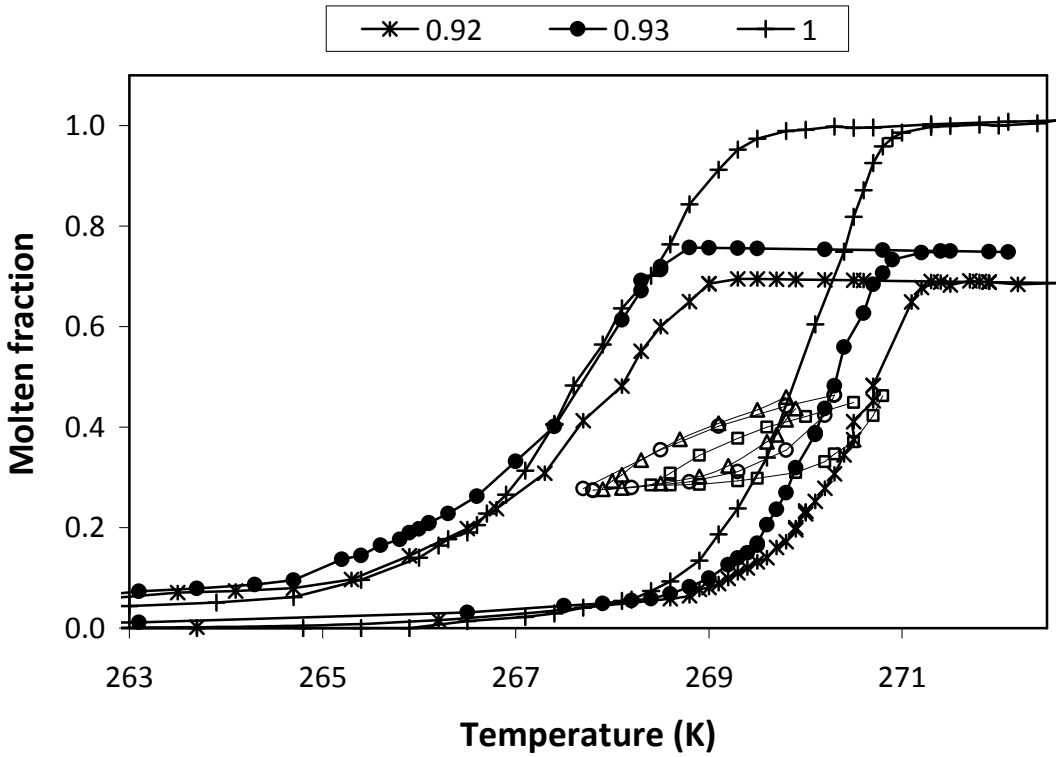

Figure 3.8 Scanning loops for the fragmented sample saturated at P/P_0=0.92, 0.93 and 1.0 via equilibrium adsorption within their freezing and melting boundary curves. The bottom of each loop terminates at the same molten fraction

Figure 3.9 compares the scanning loop of sample saturated at P/P_0=1.0 with the sample saturated at P/P_0=0.93 for freezing terminating at the same temperature on the loops, and as such, at the same pore size. It is seen that further freezing led to a slightly lower molten fraction and only a small change in the steepness of the melting branch of the loop which corresponds to the sample saturated at P/P_0=1.0.

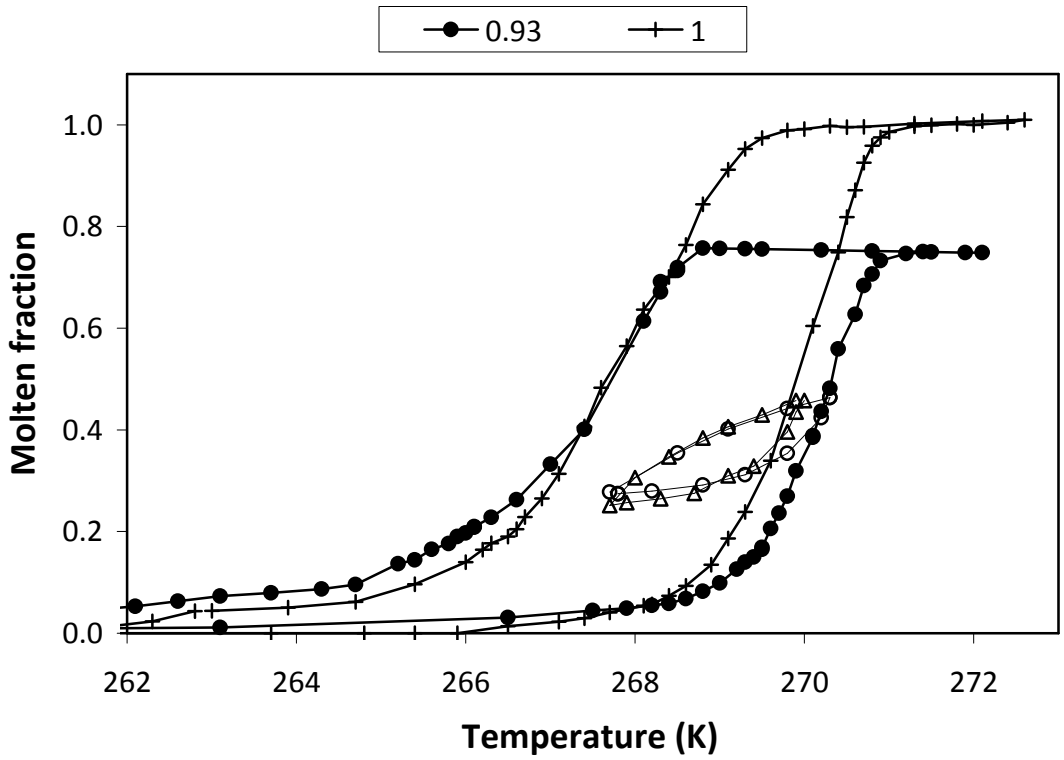

Figure 3.9 Scanning loops for the fragmented sample saturated at P/P_0=0.93 and 1.0 via equilibrium adsorption within their freezing and melting boundary curves. The bottom of both loops terminates at the same temperature

T_2 relaxation measurements at the top of the loops for the fragmented sample, Table 3.2, show that bigger pores are melted at the same molten fraction, but at a lower temperature, in the 100% saturated sample compared to the lower saturated one at P/P_0=0.93. Also, slightly bigger pores remain molten (on average) at the bottom of the loop for the sample saturated at P/P_0=1.0, at the same molten fraction or temperature, as the partially saturated sample at P/P_0=0.93.

P/P_0	Loop position	T^f_2 (ms)	α	T^S_2 (ms)	1-α	T_{2ave} (ms)
0.93	Top	2.02	0.60	6.73	0.40	3.90±0.10
1.0	Top	1.78	0.50	6.66	0.50	4.21±0.15
0.93	Bottom	1.56	0.66	6.69	0.34	3.28±0.09
1.0	Bottom (equal temperature to 0.93	1.50	0.58	6.84	0.42	3.74±0.11
1.0	Bottom (equal molten fraction to 0.93 loop)	1.43	0.59	6.57	0.41	3.56±0.10

Table 3.2 Results of the 2-component fit to the T_2 data obtained at various positions around the scanning loops of the fragmented sample, shown in Figures 3.8 and 3.9 using equation 3.2

3.9.5 Further diffusion and relaxation studies. Comparing adsorption/desorption to the melting/freezing mechanisms

Similar ganglia connectivity and pore size, between a partially melted 100% saturated sample (on the boundary melting curve) and a fully molten partially saturated sample, at equal fractions would be indicative of similar melting and adsorption mechanisms, up to the volume fractions studied.

Table 3.3 shows the values of tortuosity and T_2 relaxation values obtained from PFG NMR experiments conducted on pellet 2 when fully molten, following equilibration at P/P_0=0.92 and P/P_0=1.0, and when partially molten (on the boundary molting curve), following equilibration at P/P_0=1.0, where the overall molten volume is the same as when fully molten following equilibration at P/P_0=0.92. It can be seen that tortuosity and T_2 relaxation are higher for the sample with the lower saturation level when it is fully molten, compared to the partially molten, fully saturated sample at the same (or higher) molten fraction. This indicates a better connectivity of water ganglia in the partially molten state in the completely saturated sample, located in smaller pores than those filled at P/P_0=0.92. From Tables 3.1 and 3.3, it can be seen that, while the T_2 value at the top of the scanning loop for whole pellet 2, for the sample equilibrated at P/P_0=0.92, is higher than that at the top of the scanning loop for the sample equilibrated at P/P_0=1.0,

when the molten fraction increases to 0.72, the T_2 value for the sample equilibrated at P/P_0=1.0 becomes higher than that at the top of the scanning loop for the sample equilibrated at P/P_0=0.92, despite still corresponding to a lower melting temperature. If T_2 was solely dependant on the temperature, then T_2 values measured at the lower temperatures, would be smaller than those at higher temperatures, hence the opposite behaviour to what is found, would have been observed.

Sample	P/P_0	Molten fraction	Tortuosity	T_2 (ms)
Whole pellet	0.92	0.72	2.25±0.07	7.6±0.20[a]
	1.0	0.72	1.86±0.06	4.6±0.10[a,b]
	1.0	1.0	1.82±0.05	9.95±0.02[a]
Fragmented	0.92	0.69	*1.91±0.09*	7.2±0.10[a]
	0.93	0.75	2.04±0.06	7.4±0.20
	1	0.69	**2.1±0.07**	6.0±0.20[a,b]
	1	0.75	2.08±0.07	6.5±0.10
	1	1	2.0±0.06	9.2±0.10[a]

Table 3.3 Results of PFG NMR experiments, and 1- and 2-component fits to the T_2 data, obtained at some points on the boundary melting curves, obtained at different condensate saturations from adsorption. Notes: [a] 1-component fit, [b] 2-component fit gives same mean as 1-component. The values in bold and italics on this table are compared to those in Table 3.4

Table 3.3 also shows that tortuosity for the partially filled fragmented sample saturated at P/P_0=0.92 is smaller than that of the partially molten sample saturated at P/P_0=1.0, at equal volume fractions (0.69). However as saturation increases to P/P_0=0.93 and the adsorbed phase is increased to a fraction of 0.75, tortuosity increases and its value becomes similar to that of the partially molten sample saturated at P/P_0=1.0, at equal molten fraction. T_2 relaxation data for those samples proves that melting of a larger volume of smaller pores is favoured until 0.75 molten fraction of the sample saturated at P/P_0=1.0 as compared to the partially filled ones. However, T_2 relaxation at 0.75 molten fraction of the sample equilibrated at P/P_0=1.0 was higher than the T_2 value measured at

the top of the scanning loop of the sample saturated at P/P_0=0.93 (Table 3.2), despite the fact that the former was measured at a lower temperature than the latter (Figure 3.8).

Sample	P/P_0	Molten fraction	Tortuosity	T_2 (ms)
Whole pellet	0.86	0.52	2.45 ± 0.08	6.45 ± 0.10[a]
	1.0	0.52	1.80 ± 0.07	7.50 ± 0.40[a,b]
Fragmented	0.86	0.69	*2.09 ± 0.07*	7.70 ± 0.50[a]
	1.0	0.69	**2.05 ± 0.06**	7.40 ± 0.20[a,b]

Table 3.4 Results of PFG NMR experiments, and 1- and 2-component fits to the T_2 data, obtained at some points on the boundary freezing curves, obtained at different condensate saturations from desorption process. Notes: [a] 1-component fit, [b] 2-component fit gives the same mean as the 1-component fit. The values in bold and italics on this table are compared to those in Table 3.3

In order to compare the process of pore water freezing during NMR cryoporometry, to that of pore emptying during water vapour desorption, tortuosity and T_2 relaxation were measured along the freezing boundary curve of the sample saturated at P/P_0=1.0, at molten fraction equal to the volume of the condensed phase of the sample saturation via desorption at P/P_0=0.86. The tortuosity and the T_2 value of the latter were measured at the end of its boundary melting curve. The results are presented in Table 3.4 for both the whole pellet 2 and the fragmented sample. It is seen that much bigger pores remain unfrozen within the whole pellet 2 saturated at P/P_0=1.0, at 0.52 molten fraction during freezing (T_2=7.5±0.4 ms), as compared to the pores that remain filled with water during desorption at P/P_0=0.86 (T_2=6.45±0.1 ms). Moreover, the connectivity of the water ganglia within the pellet, as denoted by the tortuosity value, is higher when the same molten fraction is achieved by freezing for the sample saturated at P/P_0=1.0 (τ_p=1.8±0.07) than that achieved via desorption at P/P_0=0.86 (τ_p=2.45±0.08). On the contrary, for the fragmented sample only slightly smaller pores remain molten during freezing of the sample saturated at P/P_0=1.0 (T_2=7.4±0.2 ms), as compared to those that remain filled with water after desorption at P/P_0=0.86. The tortuosity though, for both the partially frozen and partially filled fragmented samples are equal (within

experimental error), showing that the connectivity of the water ganglia during freezing and the adsorbed phase (in desorption) are similar in the fragmented sample.

Tables 3.3 and 3.4 (tortuosity values in italics), show that the connectivity of molten water in both the boundary melting and freezing curve, at equal molten fractions (0.69), are similar for the fragmented sample saturated at P/P_0=1.0. Moreover, when water adsorption at P/P_0=0.92 and desorption at P/P_0=0.86 led to equivalent volumes of adsorbed phase (0.69), the pore connectivity was slightly higher on adsorption (tortuosity values in bold), and pores filled are smaller.

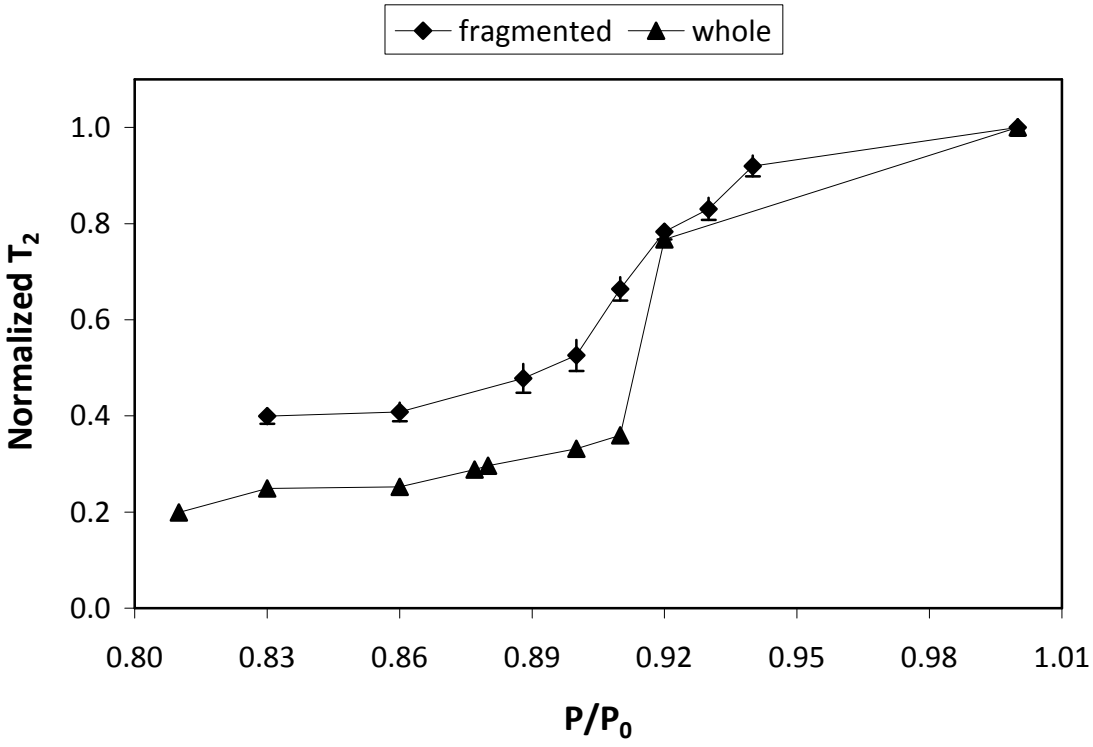

Figure 3.10 Normalized T_2 relaxation values of pellet 2 and the fragmented sample measured at the end of the boundary melting curve for saturations at different relative pressures. Error bars for the whole pellet 2 are smaller than the size of the symbols. All the T_2 measured values are normalized to the T_2 value of the completely molten samples (fragmented or whole pellet), saturated at P/P_0=1.0

The T_2 relaxation values measured at the end of the boundary melting curve for pellet 2, after water adsorption at the relative pressure range of 0.81-1.0, are compared to those

of the fragmented sample, saturated via adsorption on the relative pressure range of 0.83-1.0. Figure 3.10 shows the normalized T_2 values, found by dividing each T_2 value measured with the T_2 of the completely molten sample, saturated at P/P_0=1.0 . It is seen that the fragmented sample shows a more gradual increase on the T_2 over the whole relative pressure range, as compared to the whole pellet 2 sample, which shows a gradual increase between P/P_0=0.81-0.91, but an abrupt increase thereafter between the relative pressures of 0.91 and 0.92, showing that a big fraction of big pores is filled at P/P_0=0.91 in the whole pellet 2. Moreover, the normalized T_2 values of the fragmented sample are higher (at least) until P/P_0=0.92 implying that the pores (on average) filled with water during adsorption in the fragmented sample, are bigger than those in the whole pellet 2 at the same pressures.

Figure 3.11 shows the T_2 values of the fragmented and whole pellet 2 samples, measured at different molten fractions along the boundary melting curve, when the samples are saturated at P/P_0=1.0. Each of these molten fractions is equal to the adsorbed volume fraction when these systems are partially saturated at different relative pressures. For example, a molten fraction of 0.72 in the boundary melting curve for the sample saturated at P/P_0=1.0, corresponds to an adsorbed volume fraction of 0.72 when the system was partially saturated at P/P0=0.92. Therefore the x-axis in Figure 3.11 is labelled as 'equivalent P/P_0' (a virtual variable), to show that each of the relative pressures correspond to an equivalent molten fraction in the boundary melting curve when the sample is completely saturated. By plotting the normalized T_2 values measured at different molten fractions versus the equivalent P/P_0 (rather than the molten fraction itself) provides ease of comparison between Figures 3.9 and 3.10. For example, one can compare the size of the pores filled with condensate via adsorption to those molten via cryoporometry melting, when equivalent adsorbed/molten fractions are occupying the void space.

The results in Figure 3.11 show that the size of the molten pores are roughly similar for both the fragmented and the whole pellet 2 sample until the molten fraction is equal to the volume of the adsorbed phase in the P/P_0=0.90 saturated sample (0.22 molten fraction). An abrupt increase in the T_2, similar to that seen in Figure 3.9, is observed in

the whole pellet sample for melting fractions between 0.31-0.72, equal to the adsorbed volumes between P/P_0=0.91-0.92. At a molten fraction of 0.72 the T_2 value of the whole pellet 2 has already jumped into a higher value to that of the fragmented sample, which follows a smoother increase along the melting curve.

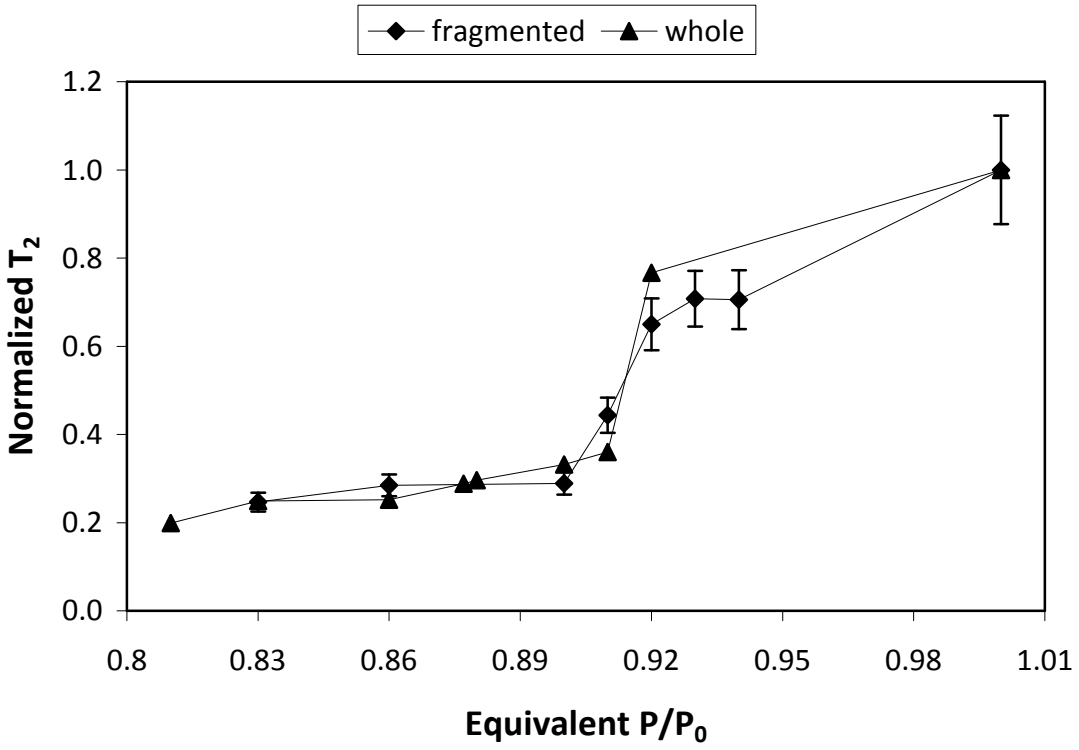

Figure 3.11 Normalized T_2 relaxation values of pellet 2 and the fragmented sample saturated at P/P_0=1.0, measured along the boundary melting curve, at molten fractions equivalent to the adsorbed volume fraction after partial saturation at different relative pressures. All the T_2 measured values are normalized to the T_2 value of the completely molten samples (fragmented or whole pellet), saturated at P/P_0= 1.0

Figure 3.12 compares the tortuosity values between the whole pellet 2 and the fragmented samples, for fully molten partially saturated samples. It is seen that while the tortuosity of the whole pellet decreases gradually up to P/P_0=0.91, it then follows an abrupt decrease until P/P_0=0.92, and a smoother one for higher relative pressures. This is consistent with the results found for pellet 1, presented in Figure 3.4. The fragmented sample has a quasi constant tortuosity until P/P_0=0.91 followed by a small drop at P/P_0=0.92, but it remains constant at higher pressures. Moreover, the tortuosity of the fragmented sample is lower than that of the whole pellet over the whole range of

pressures measured, showing that the (average) connectivity of the adsorbed phase in the fragmented sample, at each corresponding relative pressure, is higher than that of the whole pellet 2.

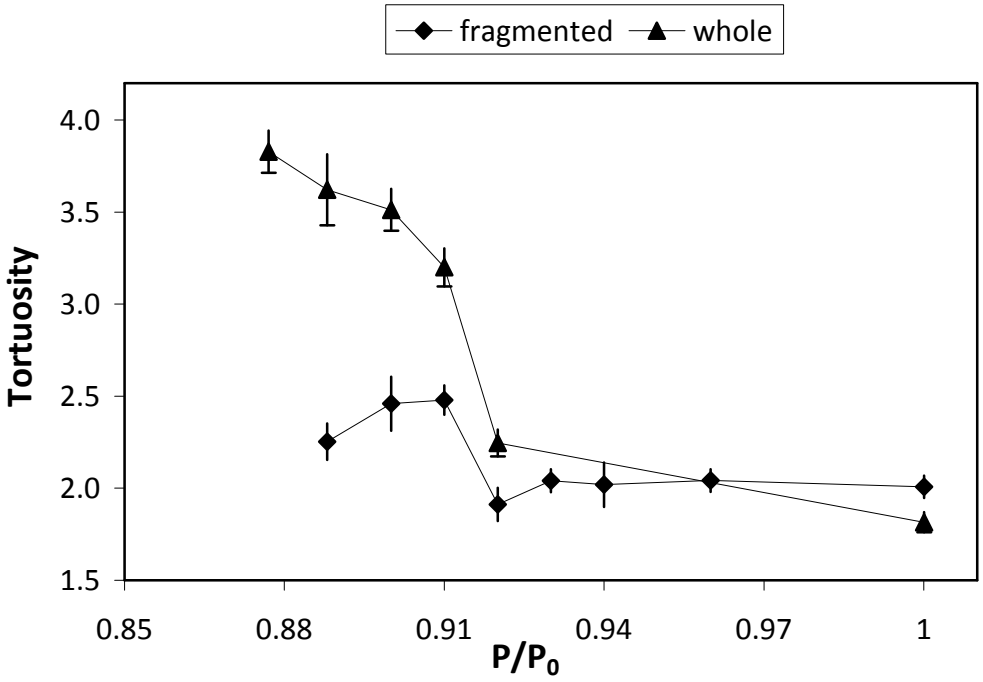

Figure 3.12 Variation of unrestricted diffusion tortuosity for the adsorbed phase, obtained at the top of the melting curves (all at 273 K), with relative pressure of water vapour for the whole pellet 2 and fragmented sample

3.9.6 Pore size distributions

The PSDs derived from the boundary melting curves were compared to that obtained from nitrogen adsorption using the BJH algorithm and the results are shown in Figure 3.13. From Figure 3.13, it can be seen that the cryoporometry PSD of the partially saturated sample (P/P_0=0.91) is wider than that for the fully saturated sample, as the former expands between the reduced pore radius of 0.4-1.5, whereas the latter has a width between 0.6-1.2. On a similar way, a comparison of the PSD obtained from cryoporometry for a fully saturated sample, and that from gas adsorption, shows clearly that cryoporometry underestimates the width of the PSD and, thus, that advanced melting and advanced adsorption are not completely analogous in complex materials. The PSD for the fragmented sample from cryoporometry is also included and shows the

increase in the width of the PSD. This further suggests that advanced adsorption can be curtailed if the pore connectivity is reduced.

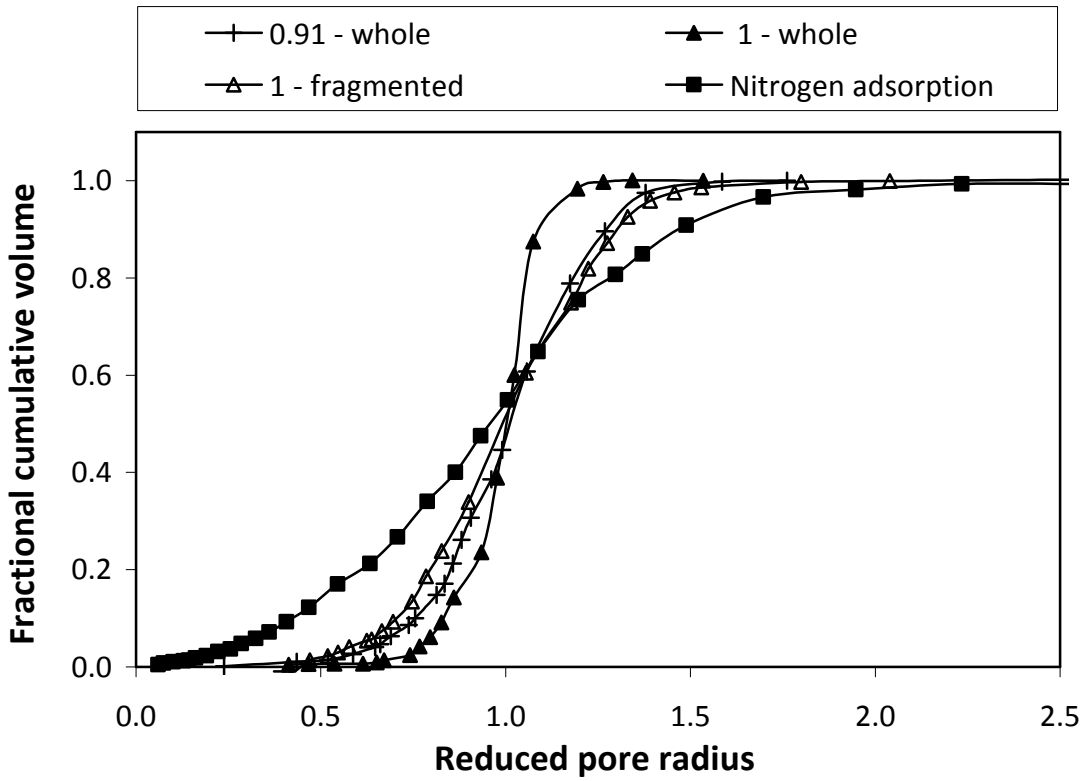

Figure 3.13 PSDs derived from the melting curves of the whole pellet 1 saturated at P/P_0=0.91 and 1.0, and the fragmented sample saturated at P/P_0=1.0 calculated via Gibbs-Thomson equation. PSD derived from nitrogen adsorption for the whole pellets, using the BJH algorithm is also included

3.10 Discussion

3.10.1 Advanced phenomena studies on whole pellet S1 samples

Advanced melting occurs when the molten phase occupying a small pore immediately adjoins the frozen phase in a larger pore. The effect is thus facilitated by increased inter-connectivity of the occupied void space, since then more pores would have increased numbers of neighbours also filled with condensate that might potentially aid their own melting. Hence, a pore network with a lower pore connectivity will have less potential connections via which advanced melting could occur. Steadily increasing the liquid saturation level towards complete pore-filling will progressively fill pores within the network, thereby also progressively improving the level of pore interconnections within

the network. Hence, it would be expected that the opportunities for advanced melting would increase with increased pore filling. This procedure also allows the study of the importance of the various individual pores to the overall connectivity of the network in the fully saturated state. If a critical pore becomes filled at a given relative pressure then the connectivity of the adsorbed ganglia will rise significantly. In a fully saturated sample, it is these critical pores that will also permit the rapid transmission of the advancing meniscus as the melting front percolates the network following a temperature increase. Hence, the study of the partially saturated samples allows the identification of these critical pore sizes that greatly impact the advanced melting process in the fully saturated sample. It is these critical pore sizes that would feature prominently in a cryoporometry PSD.

The PFG NMR data for pellet 1, Figure 3.4, suggest that there is a relatively rapid decline in tortuosity of the adsorbed phase between P/P_0=0.91-0.92. Decreasing tortuosity is associated with increased inter-connectivity of the diffusing phase, since it facilitates easier diffusion. Hence, the PFG NMR data suggests that the large increase in the adsorbed phase interconnectivity, which would be necessary to facilitate advanced melting, did occur when the melting curves indicated that the influence of advanced melting had increased. The abrupt increase in phase connectivity, observed after P/P_0=0.91, is akin to the similar sharp transition generally observed during the formation of the sample-spanning cluster at the onset of percolation of the vapour phase during gas desorption. For pellet 2, the tortuosity for the fully molten sample was 2.25±0.07 and 1.82±0.05, when the sample had been equilibrated at P/P_0=0.92 and 1.0, respectively. Higher tortuosities are generally associated with lower connectivities. Hence, the interconnectivity of the adsorbed phase is probably higher at higher relative pressure, as might be expected. A higher interconnectivity of condensed phase at P/P_0=1.0 is also consistent with the differences observed in the form of the scanning loops when pellet 2 had been equilibrated at P/P_0=1.0, compared with that at P/P_0=0.92. A higher connectivity of the condensed phase would better facilitate initiation of advanced melting, from the molten remnant, on the melting arm. Higher interconnectivity would also lead to less shielding during invasion percolation of the freezing front, and thus more pores freezing, on the freezing arm of the scanning loops. The higher T_2 value at

the lower temperature end of the freezing arm of the P/P_0=0.92 loop, compared with the equivalent location for the P/P_0=1.0 loop ending at the same temperature, suggested that some larger pores remain shielded in the former, despite the same neck sizes potentially being frozen.

The melting curve data for pellet 1 for P/P_0=0.91 and 0.92 are consistent with the onset, between these relative pressures, of significant advanced melting at the point where they diverge (~269.5 K) as seen from Figure 3.4. The steeper shape of the upper part of the melting curve for the sample saturated at P/P_0=0.91, compared to that saturated at P/P_0=0.92, suggests that the larger pores, melting between ~270.3-270.7 K, occupied by condensate at the lower pressure, are, apparently, no longer occupied at the higher pressure. The range of this discrepancy greatly exceeds the size of the estimated, potential error in the temperature measurement of 0.1 K. Since this lack of occupation at higher pressure seems unlikely (as higher pressures tend to increase occupancy of larger pores by condensate, not reduce it), the alternative interpretation is that the steep deviation upwards, at ~269.5 K, in the melting curve for the sample saturated at P/P_0=0.92, from that saturated at P/P_0=0.91, represents the onset of a significant advanced melting effect. This would mean that pores melting at a lower temperature than ~270.3 K, for saturation at P/P_0=0.92, have also facilitated the lower temperature melting of those pores that originally melted between ~270.3-270.7 K for saturation at P/P_0=0.91. Since this effect only arose once the relative pressure had increased from 0.91 to 0.92, leading to an increase in ultimate fractional saturation from ~0.3 to ~0.5, this would suggest that some of the pores filling between those pressures enabled the advanced melting to occur.

For pellet 2, the melting curves for P/P_0=0.92 and 1.0 (Figure 3.5) bear a similar relationship to each other, in terms of overall form and relative position, as the melting curves for P/P_0=0.91 and 0.92 do for pellet 1. In each case, the higher relative pressure melting curve deviates from the lower relative pressure curve at a low molten fraction, and then rises steeply on the lower temperature side of the lower relative pressure curve. For pellet 2, the change in molten fraction in the range 270.7-271.2 K is much less for the higher relative pressure curve. As with the analogous result for pellet 1, this

discrepancy has arisen because advanced melting has meant that some of the pores that previously melted in this higher temperature range, at lower relative pressure, have, at higher relative pressure, melted at lower temperatures despite their large size. There was an increase in the T_2 values, occurring between molten fractions of 0.51 and 0.72 on the boundary melting curve obtained at P/P_0=1.0, to beyond the T_2 value for a molten fraction of 0.51 on the P/P_0=0.92 curve (Table 3.2). This increase in the T_2 values, occurring despite the corresponding melting temperature not also, concomitantly, increasing beyond that point for the P/P_0=0.92 curve, suggested significant advanced melting was occurring on the P/P_0=1.0 curve between molten fractions of 0.51 and 0.72. The difference, between pellet 1 and pellet 2, in the relative pressure range over which boundary melting curves have a similar form must reflect differences in the spatial disposition of adsorbed phase, at the same relative pressure, between these samples. As mentioned above, a more interconnected adsorbed phase would better facilitate opportunities for advanced melting. Hence, advanced melting effects are a definitive probe for the development of interconnectivity of adsorbed phase for a given sample. Moreover, the difference found in the connectivity of the water ganglia and the pore size at a molten fraction of 0.72, between the sample saturated at P/P_0=1.0 and that the sample saturated at P/P_0=0.92, further indicates that the mechanism of water melting in cryoporometry differs to that in water adsorption.

The above findings enable an assessment to be made of which particular pores facilitate the advanced melting of which other pores, and thus the likely inaccuracies in the final cryoporometry PSD over a given pore size range. The pore size distribution for S1 can be determined from the melting curve using a value of 26 nm K for the group of physical constants in the relationship between melting point depression and pore core size (Mitchell et al., 2008b). This value was assumed since advanced melting occurs via a hemispherical meniscus. It was assumed that the thickness of the pore surface layer left as unfrozen liquid-like phase was 0.4 nm (Schreiber et al., 2001). Using these parameters this would suggest that particular advanced melting identified for pellet 1 in Figure 3.3, would mean that at least 37 % of the pores in the range 9.9-11.4 nm would be missed using NMR cryoporometry. This missing pore volume would be attributed to smaller pore sizes in the range 7.9-9.9 nm. For pellet 2, the advanced melting seen in Figure 3.5 would

lead 26 % of the total pore volume that actually consists of pores in the size range 11.4-14.1 nm being falsely attributed to pores in the size range 9.1-11.4 nm, if the boundary melting curve for the fully saturated sample were used to derive the PSD.

The cryoporometry, relaxometry and diffusometry data obtained here can also shed light on the pore-filling mechanism for S1 sol-gel silica. Previous work, using solid-state ^{1}H NMR, has suggested two different pore-filling mechanisms for water adsorption in silica-based materials (Grünberg et al., 2004; Vyalikh et al., 2007). Pore filling in SBA-15 and controlled pore glass (CPG) involved, after initial coverage of the surface, a radial growth in the surface film towards the pore axis. However, for MCM-41, the proposed mechanism involved initial wetting of the surface, then a coexistence of filled pores, or pore segments, with wetted pores, or pore segments, and then further filling occured as a growth of the filled pores involving an axial filling of the pores. Grünberg et al., (2004) suggested that the observed difference in pore-filling mechanism arose because of the difference in pore sizes between SBA-15 and MCM-41. Further, as mentioned above, Troyer *et al.* (2005) proposed an alternative, 'plug-model', pore-filling mechanism, for water adsorption in silicas, distinct from the puddle-growth model of Allen *et al.* (1998). Troyer *et al.* suggested that adsorption began as an adsorbed film, that then grew into undulates, that then met to form a plug of liquid bridging the pore cross-section completely. The pore then filled by axial growth of this plug. These workers then used relaxometry data to study pore-filling in CPG.

The data obtained for pellet 1 of S1 can be considered in the light of this previous work. The gradual shift to higher temperature in the melting curves up to P/P_0=0.91 is consistent with a growth in the thickness of an adsorbed film, or the growth in size of adsorbed puddles. However, the steep increase in relaxation time of the adsorbed phase, between P/P_0=0.91-0.92, would be consistent with the onset of the meeting and merger of adsorbed films, or undulates, from opposite sides of a pore. This is because, if this merger were to occur, the characteristic size of the adsorbed phase, governing relaxation rate, would then jump from the film, or undulate, thickness, to the diameter of the pore, since the liquid molecules would suddenly then be able to traverse the pore diametrically, through a large zone of bulk-like phase, rather than around the walls in

closer proximity to the surface-affected layer. This change in freedom of motion might also be partly associated with the above observed decrease in the tortuosity of the adsorbed phase, as well as that originating from increased connectivity due to increased saturation. Once formed, the adsorbate plug could fill the pore radially, thereby giving rise to the hemispherical menisci that facilitate advanced melting and advanced adsorption.

However, the variation in the shape and position of the melting curves between relative pressures of 0.92 and 1.0, observed for pellets 1 and 2 suggests a difference in the pore-filling process between the two samples for the respective critical pores governing advanced melting. The shift to higher temperature of the 'lift-off' point (where the gradient increases steeply) of the melting curves for pellet 1, between relative pressures of 0.92 and 0.93, suggests that the critical neck of condensed phase that initiates melting at P/P_0=0.92 probably only occupies part of a pore cross-section. The shift in the position of the lift-off point is thus associated with the complete-filling by P/P_0=0.93, and thus a larger ice crystal size, for the critical pore. The subsequent changes in the shape of the melting curve for pellet 1, between relative pressures of 0.93 and 0.94, just represent the filling of more larger (than the existing critical neck size) pores connected to the original cluster of filled pores present at relative pressure of 0.93. However, for pellet 2, previously empty critical necks completely fill between P/P_0=0.92 and 1.0, leading to a large interconnected condensate network, and thus there is a shift in only the body of the boundary melting curve (and not the base) with increased relative pressure, and that shift is towards lower temperature.

The results shown in Figure 3.13 indicate, in general, advanced melting is more acute than advanced adsorption for the S1 material. However, the above data can also be used to gain insight into advanced adsorption processes. If adsorption was occurring without advanced adsorption and pores simply filled in order of increasing size, the melting curves for successive relative pressures would be expected to show the form seen for the boundary melting curves obtained at P/P_0=0.93 and 0.94 for pellet 1. As the relative pressure is increased, without advanced adsorption, only larger pores fill with condensate, and, thus, the melting curve for the higher relative pressure then only

deviates from the curve obtained at lower relative pressure towards the top of that curve, thereby simply reflecting the melting of the additional larger pores at higher temperature. However, if some smaller pores fill with condensate only at higher relative pressure than some larger pores, then there is the potential that the newly-filled smaller pores can act as a nucleation site for advanced melting that did not exist previously (at lower pressure). In that situation, the melting curve obtained at higher relative pressure would be expected to deviate from that obtained at lower relative pressure towards the lower end (at lower molten fraction) of that curve (in contrast to the scenario above without advanced adsorption), where the critical new small pore melts, and rise more steeply (over a narrower and lower temperature range) than that for lower relative pressure melting curve. This is what has been observed for the boundary melting curves obtained for pellet 2 equilibrated at P/P_0=0.92 and 1.0. Hence, this suggests that the larger pores, melting at temperatures ~271 K in the melting curve for P/P_0=0.92, fill at a lower pressure than the smaller pore that melts at ~270.2 K, in the curve obtained at P/P_0=1.0, that represents the critical size where the steep rise of the higher pressure melting curve starts.

From Figure 3.5 it is seen that freezing of the partially saturated pellet 2 occurs over a broad temperature range. As saturation increases though, freezing commences at a slightly higher temperature and the temperature width of the boundary freezing curve decreases. In particular, it is seen that pore freezing commences at ~269 K for the partially saturated samples at P/P_0=0.92 (via adsorption) and at P/P_0=0.86 (via desorption), and at 269.2 K for the sample saturated at P/P_0=1.0. Here it must be noted that the partially saturated samples are free from any bulk water layer, which would have provided nucleation sites to the molten pore water, to initiate freezing via heterogeneous nucleation, such as that in the sample saturated at P/P_0=1.0. These results suggest that freezing in the pellet 2, saturated below P/P_0=1.0, will be initiated due to supercooling effects when all the pores are molten. At low saturations, there are small pores completely filled with condensate, but some others will be partially filled with a thick film of water, or liquid bridges and undulates. When the water is supercooled, the bigger filled pores freeze first at higher temperatures (Pruppacher, 1995), which will provide nucleation sites to the smaller pores next to them. This is

obvious from the boundary freezing curves presented in Figure 3.5 for the whole pellet where at low saturations pore freezing occurs at lower temperatures than the completely filled one, and all the pores freeze within the narrow temperature range of 268.8-269 K. However, if the molten water is isolated from these frozen sites, or is hindered by narrow necks, further pore freezing will be delayed by percolation controlled penetration of the ice front and pore blocking, and as such it will freeze due to further supercooling at lower temperatures. Moreover, the freezing point depression increases for the liquid film and bridges, due to their different metastability relative to the frozen pore water, and the freezing temperature will be determined from the liquid thickness rather than the pore diameter (Schreiber et al., 2001). This is observed as a 'tail' over the temperature range of 265-268.8 K. These results are consistent with the DSC findings by Schreiber *et al.* (2001) for MCM-41 and SBA-15 materials which are partially saturated with water. However, it is also likely that some of the pores or narrow necks and layers (<4 nm), will freeze due to homogenous nucleation from the spontaneous occurrence of ice nuclei and growth as found by Morishige and co-workers in partially saturated SBA-15 and KIT samples (Morishige and Iwasaki, 2003; Morishige et al., 2007). When the samples were completely saturated, in the presence of an external bulk (frozen) layer, pore freezing commenced via heterogenous nucleation. Although initially freezing in pellet 2 was delayed by pore blocking effects, it then progressed within a narrow temperature range, due to the higher connectivity of the molten water ganglia with the frozen menisci. During desorption at P/P_0=0.86 (Figure 3.5), it is unlikely for water films to be present in the pores, as pores empty via the hemispherical menisci at the liquid-vapour interface. Therefore, the 'tail' observed, is due to supercooling of small isolated pores.

For both the partially and the completely saturated samples, pore freezing commences immediately upon reversing the temperature part way up the boundary melting curve, from the same molten volume. This is because the presence of freezing fronts from frozen pores adjacent to molten ones inhibited pore blocking and initiated pore freezing of the molten pores. Also, a higher volume of pores freeze over the same temperature range for the sample saturated at P/P_0=1.0 as compared to the one partially saturated at P/P_0=0.92. This is due to the better connectivity of the molten ganglia with the frozen pores in the higher saturated sample, which enhanced easier penetration of the freezing

fronts compared to the partially saturated one. The fact that the freezing scanning curve of the sample saturated via adsorption at P/P_0=0.92 crosses over the freezing boundary curve at 267.9 K is due to the presence of some small isolated pores (or very thick films), which required supercooling over the same temperatures range no matter if freezing occurred from a partially molten or a fully molten state. On the contrary, the freezing scanning curve of the sample saturated via desorption at P/P_0=0.86 converges, possibly due to the presence of some well connected pores which freeze by nucleation induced from the already frozen pores, and the absence of water layers and/or isolated pores that would have frozen via supercooling.

3.10.2 Advanced phenomena studies after fragmentation of S1 sample

Accurate pore size distributions are essential if they are to be used successfully in understanding phenomena such as relative catalyst activities. The above findings suggest that pore-size distributions obtained using the typical experimental methods (employing boundary curves alone, for whole samples), and usual analysis techniques, are likely to be inaccurate in the presence of advanced phenomena. As shown above, these phenomena can be detected using additional cryoporometry experiments run on partially saturated samples. Hence, it is recommended that these experiments are run in addition to the standard experiment. Alternatively, for those materials, such as S1 that are known, or suspected to have macroscopic heterogeneities in the spatial distribution of pore size (Rigby and Gladden, 1996; Hollewand and Gladden, 1995b), the presence of advanced phenomena can also be detected and removed (to some degree) by obtaining the pore size distribution for the fragmented sample.

Fragmentation of the sample and saturation at P/P_0=1.0 leads to pore melting over a wider temperature range, characteristic of wider pore size distribution. The melting curves of the fragmented sample saturated between P/P_0=0.93-1.0, Figure 3.8, deviate at 268.2 K and as saturation increases the melting curves become steeper. This suggests that only a part of advanced melting was curtailed by fragmentation and that there are still frozen pores, connected to already molten ones that would melt via hemispherical

menisci. Pores with a size of 5.4 nm (268.2 K), have initiated melting of larger pores filled after equilibration at the higher pressure of P/P_0=1.0. This is confirmed by the T_2 relaxation data, Table 3.2, where the T_2 values on the partially molten fractions of the fragmented sample saturated at P/P_0=1.0, are higher than the T_2 value at the top of the loop of the sample saturated at P/P_0=0.93, although the melting temperatures of the former is lower. It is possible that in the partially saturated sample at P/P_0=0.93, some of the pores that melted between fractions of 0.46 and 0.57 in the boundary melting curve, or/and new medium sized pores filled after the pressure is increased up to P/P_0=1.0, are now melting before the fraction of 0.46, on the boundary melting of the sample saturated at P/P_0=1.0, via advanced melting.

From Figure 3.8 it is observed that for melting initiated from the same molten volume at the bottom of the scanning loops, only a few small pores melt until ~268.5 K for saturations at P/P_0=0.93 and 1.0, similar to the molten pores on boundary melting curves for the same temperature range, but once pore melting commences it then progresses at a narrower temperature range as saturation increases. For lower saturation at P/P_0=0.92, rapid melting starts at the higher temperature of ~270.1 K. This suggests that small pores of sizes until 5.9 nm will initially melt independently for the higher saturations of P/P_0=0.93 and 1.0, but their free menisci enhance melting of bigger pores, well connected to them. On the contrary, at the lower saturation of P/P_0=0.92, where connectivity of the water ganglia is worse and fewer big pores are filled with condensate, advanced melting is curtailed until bigger size pores of ~13.8 nm melt, and an abrupt pore melting is thereafter seen. The higher T_2 value for the saturated sample at P/P_0=1.0, measured at the bottom of the scanning loop, at equal volume of molten phase as the partially saturated sample at P/P_0=0.93 (Table 3.2), shows that shielding of big pores by necks, is inhibited for the saturation at P/P_0=1.0 when the sample is partially frozen. These pores can provide bigger menisci and facilitate melting of neighbouring pores at lower temperatures upon reversing the temperature, for the sample saturated at P/P_0=1.0, compared to those saturated at P/P_0=0.92 and 0.93. The melting arm of the scanning loop, initiated from similar temperatures, Figure 3.9, is only slightly steeper for the saturated sample at P/P_0=1.0 as compared to the one saturated at P/P_0=0.93, due to bigger pores on the former (and thus meniscus size) that remained molten at the bottom

of the loop, as shown in Table 3.2, upon reversing the temperature. Moreover, the freezing arm of the loops either overlap over the same temperature range (for saturation at P/P_0=0.93 and 1.0), or have the same freezing rate over these temperatures (saturation at P/P_0=0.92, 0.93 and 1.0), showing that the freezing mechanism within similar sized pores is the same for all these saturations.

Figure 3.6 shows that sample fragmentation, saturated at P/P_0=1.0 permits initiation of pore freezing at higher temperatures. This is due to less pore shielding by the narrow necks that require lower temperatures to freeze. Thus, penetration of the ice front from the external water, into the molten phase was encouraged, similarly to the results shown by Perkins *et al.* (2008) for this material. MRI images of water vapour saturated S1 pellets (Hollewand and Gladden, 1995b) show a heterogeneous spatial distribution of the big and small pores, therefore particle fragmentation will lead to severing of pore connectivity between these pores. In the partially saturated samples, where the bulk frozen layer is absent, fragmentation is also expected to inhibit the progression of the freezing front towards the molten pores (apart from advanced melting). Therefore, supercooling will firstly initiate pore freezing of individual big pores that are completely filled, likewise in the whole pellet 2 described in Section 3.10.1. These pores will then nucleate freezing of smaller filled pores next to them only. However, if small pores of the same size are located in different particles, where there exist no bigger pores frozen next to them, or are isolated in the same particle by empty pores, then supercooling at lower temperatures is required for their freezing.

Pore freezing in both partially saturated samples, via adsorption and desorption, and the completely saturated samples, extends over a broad temperature range, that reaches 265 K for the partially filled sample, but increases up to 268.4 K for the 100% saturated sample, as seen from Figure 3.6. The abrupt decrease in the molten fraction, seen for the partially saturated whole pellet 2 in Figure 3.5, once pore freezing commenced, is not observed here. This is firstly because particle fragmentation disconnects the clusters of frozen pores to the molten ones, thereby frozen fronts in big pores can not initiate freezing of smaller pores, which were previously located next to them in the whole pellet sample. Moreover, there will be fewer big pores filled in the fragmented sample, as part

of advanced adsorption is curtailed. For the fragmented sample, the 'tail' is attributed to the freezing of small pores (and perhaps isolated) which required cooling until very low temperatures for both samples saturated via adsorption and desorption.

Fragmentation of the pellets and subsequently a reduction in the pore connectivity, during pore filling, caused water adsorption to occur over a slightly wider pore size range at the capillary condensation region, as seen by the T_2 relaxation measurements at the end of the boundary melting curves in Figure 3.10. Moreover, connectivity of the condensed phase in this sample remains constant until P/P_0=0.91, followed by a small increase at P/P_0=0.92 and again remains constant until P/P_0=1.0 as seen the tortuosity measurements presented in Figure 3.12. This is because initially the pores will fill like the plug model proposed above for the whole pellets, but then advanced adsorption is less severe than that in the whole pellet, and condensation in the pores expands over a wider pressure range. This means that advanced adsorption can only occur in very well connected pores, within the same fragmented particle

3.10.3 Comparing advanced melting to advanced adsorption, and pore blocking in freezing to pore blocking in vapour desorption

The whole pellet 2 sample, saturated at P/P_0=1.0 at a molten fraction of 0.72, exhibits a higher connectivity of the water ganglia but a smaller pore size, as compared to the adsorbed phase in the partially saturated sample at P/P_0=0.92 when it is fully molten, Table 3.1. This suggests that melting and adsorption mechanisms caused a different spatial distribution of the liquid water phase up to the volumes studied. As discussed in Section 3.10.1, advanced melting mechanism is more severe than advanced adsorption in whole pellets 1 and 2. Moreover, Table 3.4 shows that partial melting of the fragmented sample saturated at P/P_0=1.0 up to a fraction of 0.75, which is equal to the adsorbed phase in the partially saturated sample at P/P_0=0.93, leads to similar connectivity of the molten phase, but the size of the pores in the partially molten phase (at P/P_0=1.0) smaller than those in the fully molten phase (P/P_0=0.93). Again this indicates that sample fragmentation did not completely remove advanced adsorption at lower relative pressures (P/P_0=0.93) and therefore the two mechanisms are not equivalent up to those

pore volumes. However, Table 3.4 shows that sample fragmentation led to similar connectivity of the molten phase and sizes of molten pore, for the sample saturated via desorption at P/P_0=0.86 and the sample saturated at P/P_0=1.0 which was partially frozen until a molten fraction of 0.69 (Figure 3.6). For the whole pellet 2 it is shown that well connected big pores remain molten after freezing up to a fraction of 0.69, in contrast to the lower pore connectivity and size, caused after desorption at P/P_0=0.86. These indicate that particle fragmentation can lead to similar mechanisms of freezing and desorption once the pore blocking effects are removed but, advanced melting and advanced adsorption can not completely be curtailed. Moreover, they show that both advanced melting and advanced adsorption are more severe than pore blocking effects during freezing and desorption, even if the pore connectivity is reduced. This could be due to the geometry of the menisci that initiates and controls each mechanism. Both freezing and desorption are initiated and progress via hemispherical menisci only, commencing from the frozen bulk water and the water vapour, for the two mechanisms respectively. On the contrary, pore melting and adsorption are initiated via cylindrical menisci, but they progress via combined cylindrical and hemispherical menisci.

As shown from Figure 3.10, a large volume of big pores is filled between relative pressures of 0.91 and 0.92 in the whole pellet sample, causing an abrupt increase in the T_2 relaxation values measured at the end of boundary melting curves. This is indicative of advanced adsorption in the whole pellet 2, which is less pronounced in the fragmented sample. The pore filling of the latter is smoother and expands over regions with similar connectivity, as supported by the tortuosity data presented in Figure 3.12. Figure 3.11 shows a sudden increase in the amount of big pores melting at a molten fraction of 0.72, which is not observed for the fragmented sample and suggests that fragmentation curtailed (at least) some of the advanced melting phenomena.

Figure 3.13 shows the PSD derived from the cryoporometry melting curves, for a fully saturated S1 whole pellet 1 sample and the fragmented sample, for comparison. It can be seen that the pore size distribution for the fragmented sample is much wider than that for the whole sample, which is what would be expected if (at least some of) the effects of advanced phenomena had been removed by fragmentation because regions of larger

pores were no longer connected to those of smaller pores. Moreover, Figure 3.13 includes the PSD derived from the cryoporometry melting curve of the partially saturated pellet 1, which is again wider than the sample saturated at P/P_0=1.0, indicative of less advanced melting caused for adsorption in smaller and less connected pores. The wider PSD derived from nitrogen adsorption data than that estimated from cryoporometry melting on the whole pellet, signifies that fewer pores fill via hemispherical menisci during nitrogen adsorption as compared to those that melt via hemispherical menisci, n cryoporometry melting. This shows the higher sensitivity of the nitrogen adsorption technique to detect the difference between the pore sizes and subsequently to probe the real PSD of the whole pellets in S1 material.

3.11 Conclusions

In this Chapter, advanced phenomena occurring during water vapour sorption and water freeze/thawing in a mesoporous silica S1 material before and after fragmentation, are studied using NMR cryoporometry, T_2 relaxomentry and PFG NMR. It is found that as fractional saturation increases, the onset of particular advanced melting effects of the adsorbed phase can be discerned using NMR cryoporometry. For the whole pellet samples, NMR relaxometry and diffusometry data have also shown that the surface area to volume ratio, and the inter-connectivity of the condensed ganglia, decreased and increased, respectively, at the saturation levels associated with significant onset of advanced melting. Pore blocking during freezing and desorption were also detected. After particle fragmentation, these techniques showed that a large part of the advanced melting was curtailed and adsorption occurred over similarly connected pore clusters. Moreover, sample fragmentation led to less pore blocking during freezing, possibly similar to that in vapour desorption. It is thus supposed that the onset of advanced melting is associated with a percolation-type transition in the connectivity of the ganglia. The breakdown of the pore-filling process into steps, that can be monitored independently, enables the particular subsets of pores, and their relevant inter-connections, that control advanced melting to be discerned. On the contrary, pore freezing is governed by a percolation-controlled penetration of the freezing front via

heterogeneous nucleation, and additional supercooling effects for the partially saturated systems, which are more severe at low saturations. Therefore, a combination of these NMR techniques, allows the deduction of which sets of pore sizes are most likely to be either over-represented, or under-estimated, when calculating the PSD.

Chapter 4

Probing hysteresis during sorption of cyclohexane within mesoporous silica using NMR cryoporometry and relaxometry

4.1 Introduction

As previously mentioned in Chapter 1, in order to convert an isotherm, for a disordered porous material, into a PSD it is necessary to make particular assumptions about the filling or emptying mechanisms for the pores, within the chosen theoretical approach. The Barrett-Joyner-Halenda (BJH) algorithm (Barrett et al., 1951), requires the choice of either cylindrical-sleeve menisci, or hemispherical type menisci (Rouquerol, 1999), and the non-local density functional theory (NLDFT), requires the option of either spinodal or equilibrium processes to be assumed (Neimark and Ravikovitch, 2001). Both these techniques assume a thermodynamically independent pore filling mechanism, neglecting the possibility of co-operative adsorption effects, such as advanced condensation (Hitchcock et al., 2010). Mean-field density functional theory (MFDFT) simulations of adsorption on irregular pore structural models have suggested that condensation for disordered void spaces may even occur part way between the equilibrium and spinodal pressures (Kierlik et al., 2002). MFDFT simulations also suggest that the difference in pore sizes, between neighbouring pores, required before they behave thermodynamically independently is a function of the adsorbate-adsorbent interaction strength (Rigby and Chigada, 2009). Hence, the impact of using different adsorbates needs to be explored.

Chapter 3 showed that cooperative phenomena, likely to induce errors in the calculation of PSDs derived from water (vapour) sorption and cryoporometry melting can be probed by concomitantly applying NMR cryoporometry, T_2 relaxometry and PFG techniques, after step-wise equilibrium sorption at different relative pressures. Also in Chapter 3 cryoporometry scanning loops assessed the reversibility of the melting process, and the connectivity of the condensed phase of water at the relative pressures studied. However

this work was limited to the adsorption of water, which has significant dipole-dipole interactions with the hydroxylated silica surface. As mentioned above, the likely prevalence of advanced condensation effects is influenced by the strength of adsorbate-adsorbent interactions. Hence, there is a need to study experimentally the impact of varying intermolecular interactions on advanced adsorption processes.

In this chapter, NMR cryoporometry and T_2 relaxometry will be used to study the configuration of the cyclohexane condensate within the S1 sol-gel silica material, at different pore fillings in the adsorption and desorption isotherm. This will allow the interpretation of the cause of the sorption hysteresis, for varying amounts adsorbed. Cryoporometry scanning loops will be used to study the geometry of the menisci governing pore freezing and melting mechanisms, thereby the validity of the Gibbs-Thomson equation for different subsets of pores. Scanning curves, initiated from different partial fillings in the cyclohexane sorption isotherm, will be further performed to investigate the validity of the independent pore theory during cyclohexane vapour sorption.

4.2 Previous studies

NMR relaxation studies at different pore fillings were previously done by Strange and co-workers in order to detect the filling mechanisms of water and cyclohexane in mesoporous silicas (Allen et al., 1997; Strange et al., 1996). The authors found that water saturation commenced with the formation of a monolayer over the pore surfaces, and with puddles of a minimum size in the silica interstices, that grew in size and joined one another before complete pore filling. However, saturation with cyclohexane led to complete pore filling, rather than surface coating with liquid layers, with the smaller pores being filled before the larger ones as the filling fraction increased. Simina *et al.* (2011) found that for different filling fractions of water and cyclohexane in silica glass, there were more water molecules present on the surface layer in fast exchange with the remaining bulk-like molecules, as compared to cyclohexane, indicative of the different configuration of the solvents in the silica. This is because cyclohexane has non-specific

interactions with silica surfaces, in contrast to water which strongly adsorbs on the hydroxyl groups.

NMR cryoporometry has been utilized to study the phase transitions of cyclohexane imbibed in porous silicas with different nominal sizes, at temperatures well below the bulk phase transition from monoclinic crystal to plastic ice (187 K), and above the plastic to liquid transition temperature (279 K) (Booth and Strange, 1998). Aknes and Gjerdåker (1999) using T_2, T_1 and PFG NMR found that the plastic ice formed in the centre of the silica pores with a nominal size of 4-50 nm, is in fast exchange with the liquid-like layer, or glassy component, at the pore surface which never freezes, even below the ordered monoclinic to plastic phase transition temperature (187 K). Non-freezing cyclohexane within pores less than 4 nm, was also reported by Jackson and McKenna (1990). In a later study the authors were able to distinguish two more phases arising from the slow exchange between the well separated liquid states of cyclohexane confined in the mesopores and the small pores of CPG materials (Aksnes et al., 2004). Moreover they found that as the pore filling and the pore size increased, T_2 relaxation decreased due to higher contribution of the plastic phase formed. The liquid layer was approximately one molecular layer thick, i.e. 0.65 nm (Aksnes et al., 2005). Gizatullin and Pimenov, (2009) found that cyclohexane adsorption on a monolayer level, occurred in clusters which form different phases upon freezing, exhibiting different T_2 relaxation times.

In the above NMR studies, cyclohexane was always introduced to the silica by liquid imbibition or drying, rather than controlled pressure, vapour-phase adsorption/desorption. As many sorption studies have shown, the particular history of the pore-filling process can substantially impact the spatial arrangement of adsorbate for a given saturation state (Valiullin et al., 2009). Hence, it seems, that no previous work has been done to follow cyclohexane equilibrium adsorption and desorption using combined NMR cryoporometry and T_2 relaxometry. Also, given that previous work has indicated that the advanced melting phenomenon is more prevalent than the corresponding advanced adsorption phenomenon in disordered materials, then NMR cryoporometry can be used as a sensitive probe of the spatial arrangement of condensate and its changes with relative pressure.

4.3 Experimental procedure and methodology

The material studied in this work was an S1 pellet which was used for all the NMR studies. The batch average specific pore volume, estimated from the sample studied in this work, is ~0.70-0.97 cm^3/g. All of the sol-gel pellets used in this study are from the same batch, but there are some differences between individual pellets due to intra-batch variability.

4.3.1 Cyclohexane sorption

Cyclohexane sorption experiments were performed on a Hiden intelligent gravimetric analyser (IGA) using IGASwin software. The sample (15 pellets; 70 mg) was initially degassed and the adsorption isotherm was obtained at relative pressure range P/P_0=0.09-0.97, at 294 K. Desorption and adsorption scanning curves initiating from the boundary adsorption and desorption curves, respectively, then followed.

Equilibrium sorption experiments of partially saturated samples were performed by suspending another sample of ~29 sol-gel pellets (0.14 g) above cyclohexane/mineral oil solutions of different concentrations. The sample was well sealed and left to equilibrate for ~24 hours, at 294 K, above a 'large' solution reservoir to allow the assumption that the cyclohexane concentration remains constant throughout all the adsorption process. The points of the cyclohexane isotherm were obtained by measuring gravimetrically the cyclohexane uptake at different cyclohexane concentrations. No mineral oil adsorption can occur during this timescale due to the low vapour pressure of mineral oil at this temperature. This was further tested by suspending a batch of pellets above pure mineral oil for an even higher equilibration time (5 days), but no mineral oil adsorption occurred. The cyclohexane/mineral oil solution approach for measuring sorption isotherms was validated as follows. The relationship between the cyclohexane concentration in the mixture with mineral oil, and the relative pressure of cyclohexane produced above, was obtained by assuming that points on the adsorption isotherms produced on the IGA, and using cyclohexane/mineral oil solutions, with the same specific amount adsorbed, were equivalent. This calibrated relationship between cyclohexane

concentration and relative pressure was then tested by using it to directly compare the respective desorption isotherms, produced by the two methods, on a relative pressure scale. It was found that the calibrated relationship led to the superposition of the two desorption isotherms.

For the NMR experiments, a given sample, consisting of a single pellet (5.4 mg), was partially saturated identically to as described above, and it was then quickly transferred into an NMR tube. The mass of the partially saturated pellet was weighed before and after experiments to check that no significant cyclohexane evaporation occurred during the course of pellet transfer into the NMR tube. Severe kinetic limitations on desorption meant that the sample did not deviate from equilibrium saturation. All NMR experiments were performed on the same single pellet to avoid intra-batch variability effects. Cryoporometry boundary melting curves of partially saturated samples were thus generated and T_2 values were measured for fully molten samples for each saturation level. Also, scanning loops were performed at a particular molten fraction on the boundary melting curves (~0.18) for each saturation level and the T_2 relaxation time was measured at the top of each scanning loop. A thin layer of bulk cyclohexane was left on the 100% saturated sample and the sample was subject to supercooling and then pore melting and freezing. For this sample, scanning curves and scanning loops were also obtained at higher molten fractions on both boundary curves.

4.3.2 NMR cryoporometry

All NMR experiments were carried out on a Bruker Avance 400 MHz NMR spectrometer as described in Chapter 3. For the cryoporometry experiments, the echo time (2τ) was 16 ms to account for the plastic phase of cyclohexane formed below its bulk melting point (280 K) and the delay time for spin recovery was 13 s (~$5\times T_1$, where T_1 is the relaxation time of cyclohexane imbibed in the pellet).

A single saturated pellet was placed within a 5 mm NMR tube, between two susceptibility plugs to reduce cyclohexane evaporation from the pores. A thermocouple

passing through a hole at the centre of the top susceptibility plug was used to measure the real temperature of the sample. The sample was frozen down to 225 K, and then the temperature was increased stepwise. At each step, it was then allowed 15-18 min to reach thermal equilibrium and a spin-echo spectrum was then recorded. This time proved to be sufficient for the system to complete any phase transition at each temperature change.

4.3.3 T_2 relaxometry

NMR relaxometry will be used to probe adsorbed ganglia sizes. The intensity of the transverse magnetisation in NMR, I, decays, from an initial value of I_0, with a time constant known as the spin-spin relaxation time, denoted T_2, according to the expression.

$$I = I_0 \exp(-t / T_2) \tag{4.1}$$

where t is the time. For more heterogeneous samples a two-component relaxation model was used:

$$I = I_0 [a \exp(-t / T^f_2) + (1-a) \exp(-t / T^S_2)] \tag{4.2}$$

where T^f_2 and T^S_2 are the relaxation times for the fast and slow components, with fractions a and $(1-a)$, respectively.

For the relaxometry experiments, the samples were prepared as described above and T_2 relaxation was measured, using a CPMG sequence. The time between 180° pulses in the CPMG sequence, for all relaxation experiments, was 3.4 ms. This time is short enough to detect the plastic phase of cyclohexane (compared to 16 ms used to obtain the cryoporometry melting curves). The single component model (equation 4.1) gave a good fit to data for fully molten samples, while the greater heterogeneity of the partially molten samples along with the liquid and plastic phases formed, required a fit to the two-component relaxation model (equation 4.2). The slow and the fast components, of the two-component fit, are attributed to the liquid and the plastic phase present at each saturation level, respectively.

4.4 Results

4.4.1 Cyclohexane sorption

Cyclohexane sorption isotherms for a batch of S1 sample, at 294 K are presented in Figure 4.1. In Figure 4.1 the desorption isotherm seems not to join the adsorption isotherm at its bottom part, possibly due to temperature fluctuations over that range.

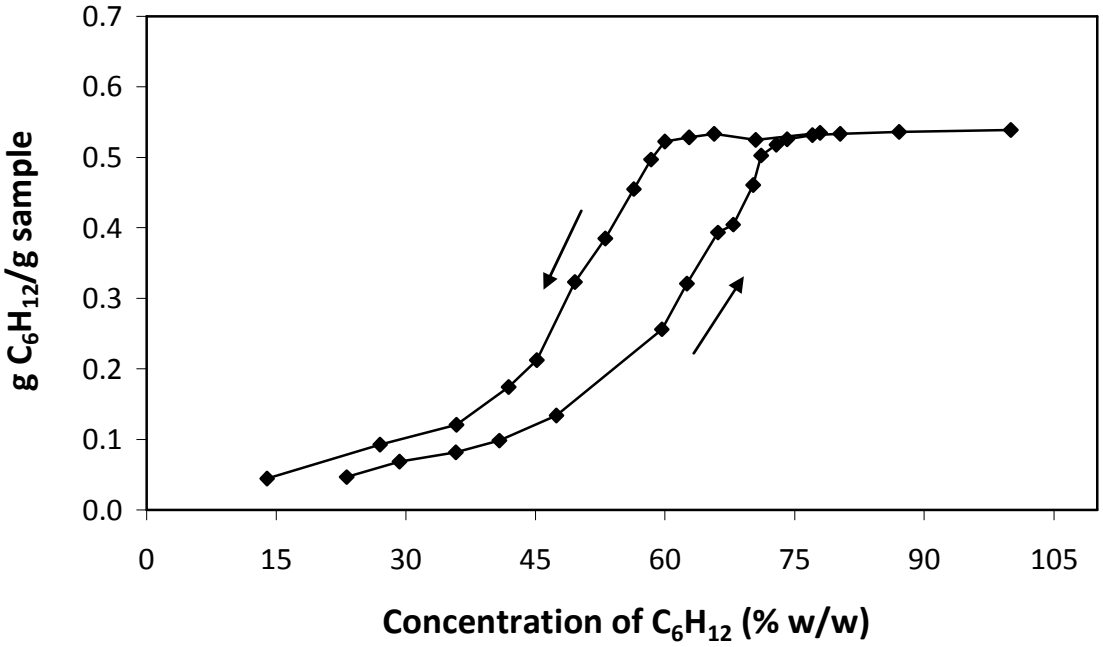

Figure 4.1 Cyclohexane sorption isotherm for a batch of S1 pellets measured gravimetrically at 294 K via equilibrium adsorption above different concentrations of cyclohexane/mineral oil mixtures

Figure 4.2 shows examples of adsorption and desorption scanning curves obtained upon reversing the pressure at partial fillings of 0.82 and 0.74 on the adsorption and desorption curves, respectively. It is noted that adsorption and desorption on the scanning curves commences immediately upon reversing the control variable, pressure, and the curves are of the converging type, since they head towards their respective hysteresis closure points.

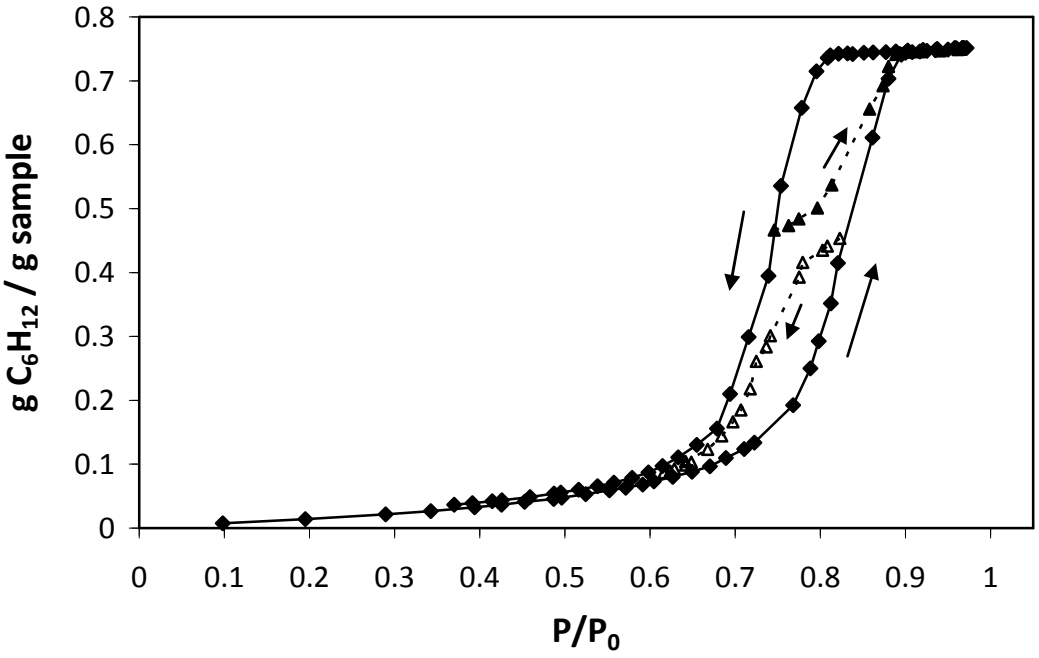

Figure 4.2 Cyclohexane sorption isotherm for a batch of S1 pellets measured via a vapour analyser (IGA) including an adsorption and desorption scanning curves initiated from partially filled systems. The lines shown are to guide the eye. The arrows show the direction of the change in pressure

4.4.2 NMR cryoporometry

The boundary freezing and melting curves, for a sample completely saturated with cyclohexane are shown in Figure 4.3. A melting scanning curve and a melting scanning loop originating from the boundary freezing curve when the molten fraction was 0.73 are also included in this figure. It can be seen that melting begins immediately upon reversing the control variable and starts before (at lower temperature) any significant melting starts on the boundary melting curve for the fully saturated sample. A freezing scanning loop originates from the same molten fraction (0.73) on the boundary melting curve. Both the freezing and melting scanning loops are reversible for all of their temperature range studied. Also shown is a freezing scanning curve, originating part way up the boundary melting curve. For the scanning curves, it can be seen that freezing starts immediately on reversing the direction of change of temperature, unlike the boundary freezing curve at the same temperature.

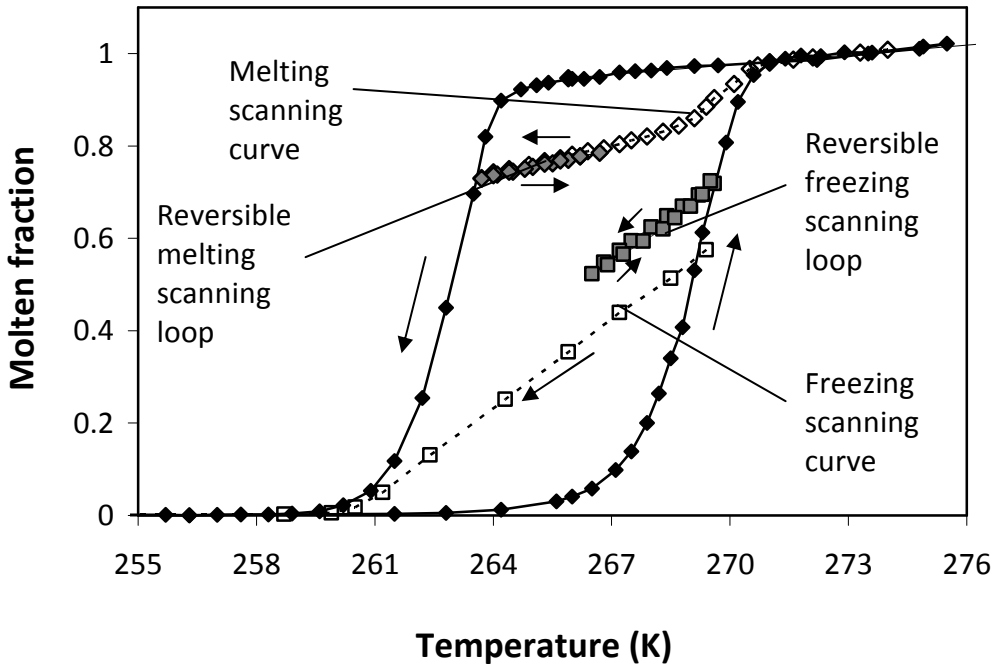

Figure 4.3 Boundary melting and freezing curves for a fully saturated sample of batch S1. Also shown are a reversible freezing scanning loop and a freezing scanning curve originating from different molten fractions on the melting boundary curve, along with a melting scanning curve and a reversible melting scanning loop originating from the boundary freezing curve. The arrows show the direction of the change in temperature. The lines are shown to guide the eye

Figure 4.4 shows the boundary melting curves and scanning loops for partially-saturated samples filled by equilibrium adsorption to different partial pressures. It can be seen that, as the saturation level is increased the boundary melting curves shift to higher temperature and become steeper. It can also be seen that all of the freezing scanning loops are reversible.

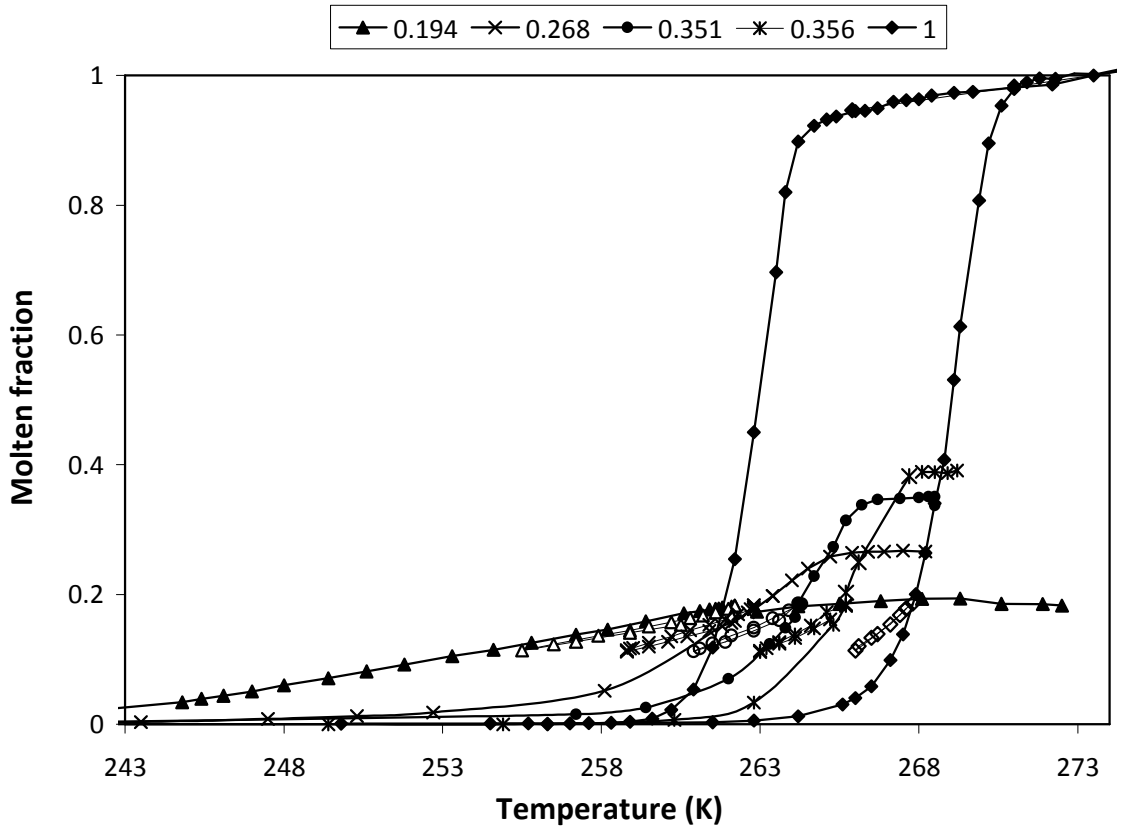

Figure 4.4 Boundary melting and freezing curves for a fully saturated sample of batch S1. Attached to the boundary melting curve for the fully saturated sample is a freezing-melting scanning loop originating at low (0.186) molten fraction. Also shown are the boundary melting curves obtained for partially saturated samples after equilibrium adsorption of cyclohexane at different partial pressures to give ultimate fractional saturations of 0.194, 0.268, 0.351, and 0.356. Individual freezing-melting scanning loops, starting from each of these boundary melting curves, were also obtained that originated at molten fractions of 0.183, 0.183, 0.185, and 0.184, respectively. The lines shown are to guide the eye

Figure 4.5 shows the boundary melting curves and scanning loops for different saturation levels obtained via equilibrium vapour desorption. To facilitate easier comparison with the corresponding adsorption data, these curves are shown against the backdrop of the same boundary melting and freezing curves for the fully saturated sample as shown in Figure 4.3. The inset in Figure 4.5 shows a close-up of the boundary curves obtained for ultimate saturation levels of 0.343 and 0.416. It can be seen that, in contrast to what occurs for the corresponding adsorption data over a similar saturation range in Figure 4.4, as the saturation level decreases, the bottom sections of the melting curves remain superimposed, rather than shifting to lower temperature with lower ultimate saturation. As the saturation level decreases the upper, higher temperature, portion of

the melting curve is simply lost. However, at lower saturations levels still the melting curve does shift to lower temperatures.

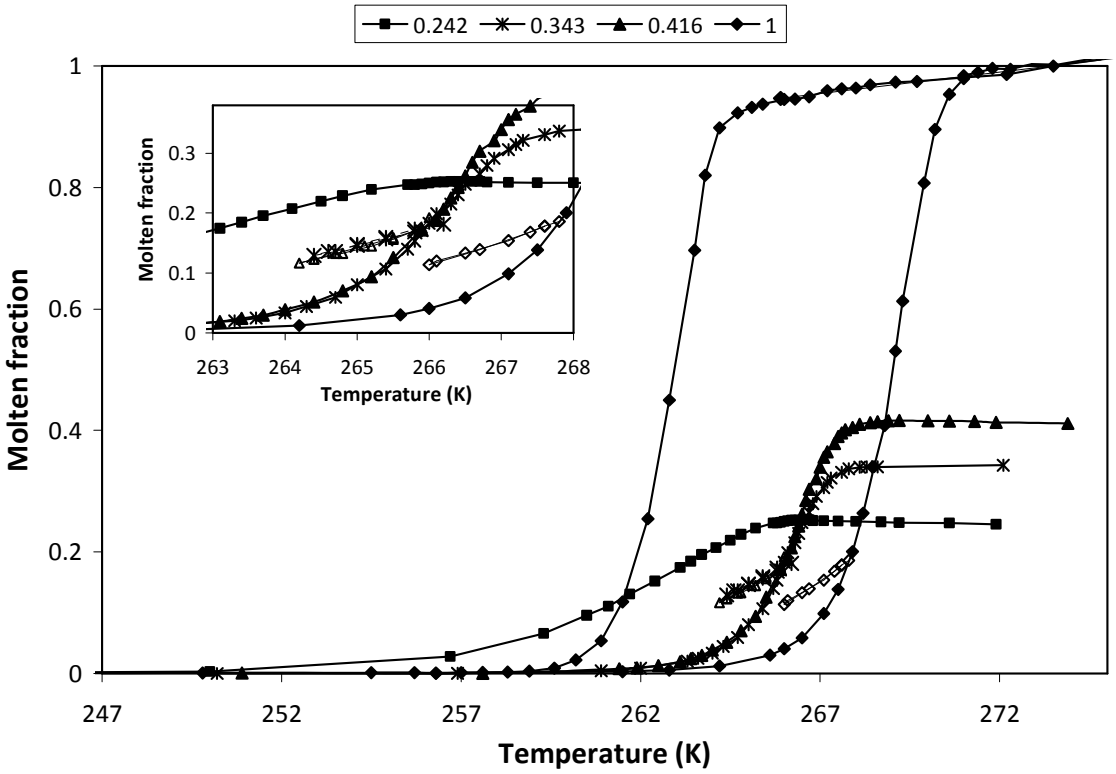

Figure 4.5 Boundary melting and freezing curves for a fully saturated sample of batch S1. Also shown are boundary melting curves obtained for partially saturated samples obtained by equilibrium desorption of cyclohexane to different partial pressures to give ultimate fractional saturations of 0.242, 0.343 and 0.416. Individual freezing-melting scanning loops originating from molten fractions of 0.182, 0.182, and 0.185, on the boundary melting curves with fractional saturation between 0.343-1.0, are also included. The inset shows a close-up of the boundary melting curves and scanning loops for partially saturated samples. The lines shown are to guide the eye

4.4.3 T_2 relaxometry

Table 4.1 shows the T_2 relaxation times obtained by fitting a two-component model to the relaxometry data obtained at the top of the scanning loops (where there was a very similar molten fraction of ~0.18 for all curves) shown in Figure 4.4 for various different ultimate saturation levels on the adsorption isotherm. It can be seen that the slow-component T_2 values declined with increased ultimate saturation level. The T_2 values of the fast component are ~7-8 ms, which is consistent with the value obtained at a similar temperature for the cyclohexane in the plastic ice phase by Booth and Strange (1998).

Fractional saturation	Molten fraction	T (K)	T_2^s (ms)	(1-a)	T_2^f (ms)	a	T_2^{av} (ms)
0.194	0.183	262.2	24.7±0.3	0.82	10.8±1.0	0.18	22.2±0.7
0.268	0.183	262.8	21.5±0.2	0.60	7.9±0.2	0.40	16.1±0.3
0.351	0.185	264.3	20.3±0.4	0.44	7.7±0.2	0.56	13.2±0.5
0.356	0.184	265.7	18.0±1.0	0.44	7.9±0.5	0.56	12.4±0.1

Table 4.1 T_2 relaxation times obtained by fitting a two-component model to the relaxometry data obtained at the top of the scanning loops (where there was a very similar molten fraction of ~0.18 for all curves) shown in Figure 4.4 for various different ultimate saturation levels on the adsorption isotherm. The error in the fraction of the slow and the fast component varies between 0.01-0.06 ms

Table 4.2 shows the T_2 relaxation times measured at the end of the boundary melting curves, shown in Figure 4.4, for various different ultimate saturation levels on the adsorption isotherm. It can be seen that the T_2 value for the slow component was constant, within experimental error, at ~36 ms for ultimate saturation values in the range ~0.26-0.37. However, the T_2 value increased to 74.8 ms for the completely saturated sample.

Fractional saturation	T (K)	T_2^s (ms)	(1-a)	T_2^f (ms)	a	T_2^{av} (ms)
0.194	272.5	43.3±6.5	0.82[d]	23.9±14.8	0.18[d]	40.0±20
0.268	268.2	35.8±0.9	0.8	18.1±2.1	0.19	32.5±2.4
0.351	268.5	35.0±0.2	0.93	9.8±1.4	0.07	33.2±0.4
0.356	269.2	36.6±0.4	0.91	10.5±2.1	0.09	34.2±0.8
1.0	272.5	74.8±0.2	0.98	10.6±1.8	0.02	73.2±0.2

Table 4.2 T_2 relaxation times measured at the end of the boundary melting curves, shown in Figure 4.4, for various different ultimate saturation levels on the adsorption isotherm.[d]: the error is ±0.38 ms. All the other errors in the fraction of the slow and the fast component vary between 0-0.06 ms

Table 4.3 shows the T_2 relaxation times measured, at approximately the same temperature as each other, at the end of the boundary melting curves, shown in Figure 4.5, for various ultimate saturation levels on the desorption isotherm. It can be seen that the T_2 values for the slow component decrease slightly with saturation. It is noted that while the spread (standard deviation/mean) in the T_2 values for the adsorption isotherm (in Table 4.2) is ~0.2, for those in Table 4.3 the spreads are ~0.5, and so there is a much wider distribution in T_2 values for the desorption isotherm.

Fractional saturation	T (K)	T_2^s (ms)	(1-a)	T_2^f (ms)	a	T_2^{av} (ms)
0.343	273.9	52.9±0.9	0.70	11.9±0.2	0.30	40.4±1.0
0.416	273.9	58.6±1.0	0.71	13.5±0.1	0.29	45.4±1.1

Table 4.3 T_2 relaxation times measured at the end of the boundary melting curves, shown in Figure 4.5, for various different ultimate saturation levels on the desorption isotherm. The error for the slow and fast component fractions varies between 0.01-0.1

4.4 Discussion

The pattern of change in the shape and position of the cryoporometry melting curves at different saturations obtained by adsorption is similar to that observed, for cyclohexane at different filling fractions and pore size in silicas, by Strange and co-workers (Strange et al., 1996; Strange et al., 1993; Allen et al., 1998). They attributed this behaviour to the growth in liquid puddle size with increasing saturation. However, it is noted that, assuming that the average liquid T_2 value for the fully saturated sample (73.2 ms) corresponds to the volume-weighted average pore size for sample S1 (having a modal pore radius of 7 nm) the liquid ganglion size corresponding to the liquid T_2 value for an ultimate saturation level of ~0.19 (40 ms) corresponds to a pore radius of ~4 nm, which is much larger than the smallest pore radius observed in S1 using mercury porosimetry. Hence, it seems likely that, for the liquid saturation levels considered here, condensation of cyclohexane in a given pore results in complete pore-filling. Thus an alternative

scenario, underlying the shapes of the melting curves, is proposed here. It is suggested that, at least in some part of the network, as the relative pressure is raised, cyclohexane condenses in progressively larger pores, as shown in Figure 4.6. Where a filled small pore (P1, low saturation) adjoins an empty larger pore, freezing of the liquid in the small pore would leave an ice wall, filling the cross-section of the end of the small pore at the join with the larger pore P2. Since molten cyclohexane should wet its own ice, it seems likely that a liquid film would spread from the surrounding walls of the unfilled larger pore to coat the ice wall at the end of the small pore P1. Previous work has also suggested that bulk ice is covered in a liquid-like film (Rosenberg, 2005; Doppenschmidt and Butt, 2000). This liquid film, bridging the complete pore cross-section between pore P1 and P2, could then act as a seed for initiating advanced melting of the small pore via a hemispherical meniscus. Hence, both freezing and melting would be expected to occur by piston-like movement of a liquid-ice front down the long axis of the pore. This is consistent with the reversible nature observed for the cryoporometry scanning loops for partially saturated samples where the pores are freezing and melting via a hemispherical meniscus.

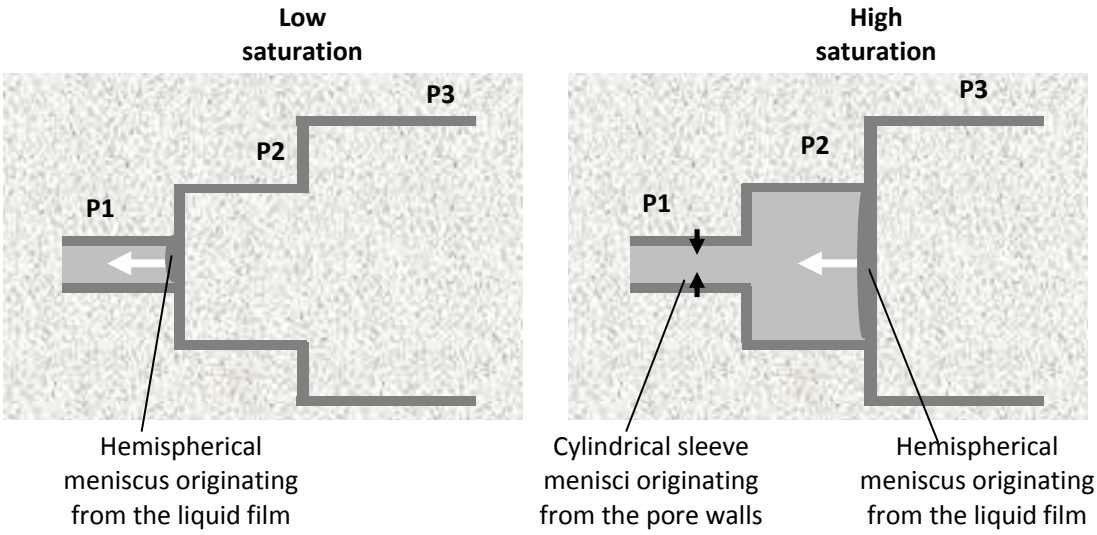

Figure 4.6 Schematic diagram depicting the different melting mechanisms described in the text for a set of pores with different sizes (P1, P2, P3), at a low and higher partial saturation. The dark grey represents liquid, light grey represents ice and the grey texture on the background represents the silica solid walls. The arrows show the direction of the direction in melting

As the equilibrium vapour pressure is raised the larger pore P2 adjoining the smaller pore P1 will also fill with condensate as presented in Figure 4.6 for the higher saturation set of

pores. If the temperature is lowered sufficiently to freeze both small and large pores then the liquid-like film across the pore cross-section, between P1 and P2, would now be situated at the far end of the larger pore, between P2 and P3. While the larger pore P2 would be able to initiate melting via the hemispherical meniscus at its terminus end, the small pore P1 would only now be able to initiate melting via the cylindrical sleeve-shaped meniscus at the pore wall. Hence, the temperature required to melt the smaller pore would increase, since it would only melt via its own cylindrical-sleeve meniscus, or following melting of the larger pore via a hemispherical meniscus. This would result in a shift towards higher temperatures for the composite melting curve. Therefore, melting via a hemispherical meniscus can be initiated from liquid bridging pore cross-sections for either partially saturated samples, as described above, or for fully saturated samples where melting is initiated in a partially frozen sample. This would suggest that boundary melting curves for partially saturated samples and melting scanning curves for fully saturated samples should potentially begin to rise over similar ranges of temperature. Indeed, this is what has been observed in Figures 4.3 and Figure 4.4 for batch S1.

It has been seen that the changes in shape and position of the cryoporometry melting curves, with varying saturation, for fluid saturation levels in the range ~0.34-0.42 are different depending upon whether the particular saturation level was obtained by equilibrium adsorption or desorption. This suggests that the spatial distribution of condensate is different between adsorption and desorption at these saturation levels. This finding is consistent with the presence of hysteresis, at these saturation levels, between the sorption isotherms shown in Figures 4.1 and 4.2. The particular form of the desorption melting curves is what would be expected if melting is initiated, as temperature is raised, strictly in the order of increasing pore size. This suggests that no ‘pore-blocking’ in melting, as described above for adsorption melting curves, is occurring. This would be the case if the remaining filled pores during desorption are more independent than the pores filled at the equivalent saturation level in adsorption, which may mean more spatial segregation between pores of different sizes, or the differences in size between adjacent pores exceeded the critical value for advanced melting to occur. It is noted that the spreads in T_2 values, measured at the end of the desorption melting curves, exceeded those of the corresponding adsorption melting curves. This suggests

that some desorption pore-blocking was occurring on the desorption branch. This is because, if pore-blocking is occurring on the desorption branch, then larger pores that should have desorbed remain filled with liquid, and, thus, the spread of filled pore sizes is artificially high. It thus seems likely that the blocked pores are much larger than their blocking pore necks. However, it is noted that, in contrast, as the fractional saturation level drops to ~0.25 on desorption, the boundary melting curve does shift to lower temperature. Indeed the form of the melting curves for a saturation level ~0.25 is very similar for both adsorption and desorption. This would suggest that the liquid spatial distribution on the adsorption and desorption isotherms becomes similar as the saturation drops to the lower level. Given that there is still hysteresis in the sorption isotherms at a saturation level of ~0.25, this may be due to single pore hysteresis. Condensation of liquid into a through, cylindrical pore neck, guarding a larger cylindrical pore body, would occur via a cylindrical-sleeve meniscus on adsorption and a hemispherical meniscus on desorption (or spinodal condensation and equilibrium desorption), leading to hysteresis in the sorption isotherms. However, the local liquid distribution detected by cryoporometry would be identical. Together, the above findings suggest that the pore sizes derived for at least ~8-17% of the porosity of S1 would be wrong if spinodal condensation (or a cyclindrical sleeve meniscus) was assumed for the adsorption branch.

As the ultimate adsorption saturation level decreases, the scanning loops starting at a molten fraction of 0.18 become closer in slope to the corresponding boundary curve suggesting that the melting-freezing process is becoming more dominated by reversible processes, and levels of shielding are declining. This would be consistent with the condensation at lower saturation levels of the sorption hysteresis loop being associated with independent, through necks. The reversibility of the melting scanning loop in Figure 4.3 and the freezing scanning loops, Figures 4.4 and 4.5, initiated from the partially molten fractions on the boundary curves, is attributed to the hemispherical menisci initiating both pore melting and freezing, independently of the thermal pathway followed. This differs to the water scanning loops, obtained for the same S1 material, when they are initiated from the boundary freezing and melting curve (Hitchcock et al., 2011).

The delay time parameters of the NMR relaxometry experiment are such that both the slow component, corresponding to the liquid phase, and the fast component corresponding to the plastic ice phase were detected. At around 268.5 K, at the end of the boundary melting curves for saturations in the range ~0.26-0.37 achieved by equilibrium adsorption, the T_2 values for the majority slow component were constant, within experimental error. This suggests that the average size of pores filling as the relative pressure is raised is not increasing. This would be consistent with the occurrence of advanced condensation such that there was not a simple monotonic relation between condensation pressure and pore size.

It was noted above that the T_2 values for the slow-relaxing component, obtained at the top of the scanning loops at a fractional saturation of ~0.18 on the boundary melting curves for adsorption, declined with increased saturation (and thence temperature). The fraction, in the two-component fit, attributed to this component also declined, despite the fact that the molten fraction was the same. It is suggested that these findings arise because the slow-relaxing component consists of liquid phase in exchange with plastic ice. As the total saturation level increases, the amount of plastic ice phase in contact with the constant molten fraction of ~0.18 will increase, leading to more exchange with the molten phase. As mentioned above the T_2 value for the isolated plastic ice phase is much less (~8 ms) than the isolated liquid, and thus exchange would lead to a reduction in the observed relaxation time. The self-diffusivity of cyclohexane in the plastic phase, at the melting point, is 1.9×10^{-13} m^2/s (Aksnes et al., 2004). Hence, the typical rms displacement during the characteristic time T_2 (of the slow component) is ~0.16 μm, which is much larger than the pore size. Thus it seems likely that exchange between plastic and molten phases is possible.

The hysteresis for cyclohexane sorption seen in Figures 4.1 and 4.2 is Type H1 (Rouquerol, 1999). The immediate reversibility of the desorption scanning curve, upon lowering the pressure, in contrast to the desorption boundary curve (over the same pressure range), suggests that pore blocking is initially curtailed and the pores empty via hemispherical menisci arising from the presence of empty neighbouring pores. However,

as the scanning curve meets the boundary curve at the hysteresis closure point, this suggests that not all pore blocking effects are removed. The immediate initiation of pore-filling, as shown by the adsorption scanning curve, is consistent with the form of the boundary adsorption curve, but, as the pressure increases, the scanning curve does not cross over to the boundary curve, implying that some pores are filling via an equilibrium process, and some via delayed condensation. Hence, gas sorption scanning curves alone are not enough to extract the information needed to determine an accurate PSD. Hence, the data from the NMR techniques described above are also required.

4.5 Conclusions

Cryoporometry melting curves have shown that, depending on the amount adsorbed, at corresponding positions on the adsorption and desorption branches of the cyclohexane sorption isotherm for a mesoporous silica, the configuration of the liquid condensate could be identical, or different. This implied that the particular local source of sorption hysteresis varied with position around the hysteresis loop. This work has thus shown that PSDs derived using conventional analysis methods, which presume a single mechanism for pore filling and hysteresis, are likely to have significant errors. Obtaining accurate PSDs for disordered porous materials requires more information than can be provided from just boundary adsorption and desorption isotherms, or sorption scanning curves. Advanced condensation also occurs in the adsorption of cyclohexane on silica.

Chapter 5
Testing single pore hysteresis for S1 material via an integrated N_2-H_2O-N_2 sorption experiment

5.1 Introduction

Chapter 2 gave an introduction to the single pore hysteresis mechanism and the models used to analyse the adsorption and desorption isotherms. It was suggested by Cohan (1938) that the gas and the fluid during gas sorption processes are in equilibrium, and that hysteresis is caused due to the different type geometry of the menisci filling (cylindrical) and emptying (hemispherical) the pores. Based on this, the BJH algorithm was developed to calculate the pore size distribution in adsorption and desorption. Other models describe the cause of hysteresis as the difference between the gas-liquid-surface interactions between the sorption processes, termed as spinodal sorption. DFT simulation models were then developed to interpret the hysteresis and were adopted to calculate the PSD.

In Chapters 3 and 4 it was shown that NMR cryoporometry and vapour sorption in S1 material, are prone to advanced melting and advanced adsorption phenomena which are different for water and cyclohexane. This means that S1 sample is not solely comprised of independent set of pores which both the BJH and DFT models assume to exist. Moreover, comparison between the PSD obtained from the cryoporometry melting curve of water and nitrogen adsorption, showed that nitrogen adsorption is a more sensitive technique to probe the PSD in a porous material with ink-bottle shaped pores, as compared to the cryoporometry melting. However, Hitchcock (2011) used scanning curves to show that for a whole pellet S1 material nitrogen adsorption is prone to advanced condensation phenomena too.

This chapter will further test the validity of independent (single) pore theory for water and nitrogen, utilizing an integrated N_2-H_2O-N_2 experiment, performed in a whole pellet S1 material. In previous studies integrated experiments, which involved saturation with a gas phase after another pre-adsorbed phase, such as mercury, were conducted to isolate pores and study them separately from the remaining void space (Rigby and Chigada, 2009; Hitchcock, 2011), or to modify the surface heterogeneity of the pores to probe its impact onto the gas sorption mechanism (Pfeifer et al., 1991). This is because the gas-liquid-surface interactions change after pre-adsorbed species. Thus, it would be of interest to know firstly, whether nitrogen adsorption is sensitive to pre-adsorbed water interfaces on the S1 sample, and secondly whether water has isolated sets of pores with a critical size that would have promoted advanced adsorption of nitrogen if the silica surface was dry. Moreover, an FHH fractal analysis will be adopted to detect the way water has condensed on the pore walls.

5.2 Previous studies

Integrated experiments involving nitrogen adsorption following mercury porosimetry, have been already adopted by others authors de-convolve the pores that enhanced advance adsorption and pore blocking of nitrogen in mesoporous silicas (Rigby and Chigada, 2009; Rigby et al., 2008; Rigby and Fletcher, 2004). The authors found that entrapment of mercury into the big pores turned the smaller adjacent pores into dead end pores, where advanced condensation of nitrogen can commence via the hemispherical menisci at the dead ends. Hitchcock (2011) further introduced sorption scanning curves after mercury porosimetry and found that, for an S1 pellet material, mercury remained entrapped into sets of pores that fill and empty like independent pores. The relative pressures for nitrogen desorption into the mercury entrapped pores were equivalent to the relative pressures for nitrogen adsorption to a power of 1.5. This was because nitrogen does not perfectly wet the surface of S1 (Hitchcock, 2011). This finding contradicts the sorption mechanism shown by Kelvin-Cohan relationship, equation 1.25, which assumes that the gas perfectly wets the surface and that cylindrical pores fill and empty via cylindrical and hemispherical menisci, respectively and this

geometrical difference of the menisci produces a power of 2. Moreover, it shows a lack on the accuracy of the DFT model to predict the correct interactions between the gas, surface and solid, for pores higher than 20 nm, as the power is found to be 1.8 by Neimark and Ravikovitch, (2001).

Mercury, though, was entrapped in some big pores of S1 which were shielded by smaller pores. However, subsets of pores can also be isolated and their filling mechanism can be studied by equilibrating the system with a vapour phase. For example, Giacobbe *et al*. (1972) studied the pore filling mechanism of argon on Vycor glasses after pre-adsorption of water at a multilayer level. It was found that capillary condensation of water in the pores occurred after adsorption of three statistical monolayers of water, although some micropores and necks had already filled at lower pressures. In addition to this, argon adsorption post water adsorption, occurred at lower relative pressures than that required for adsorpton on bare surface, but the authors did not explain this behaviour. If the pores were filling independently, via the same pore filling mechanism, irrespective of the adsorbate, then it would have been anticipated that argon adsorption would occur at a higher relative pressures regime, as the small pores/necks would have been already filled with water at lower pressures. Morishige and co-workers examined the cage-like structured of SBA-16 and KIT-5 using integrated gas sorption experiments following water adsorption, at different pore fillings (Morishige and Kanzaki, 2009; Morishige and Yoshida, 2010). These authors found that the volume of nitrogen and argon adsorbed in the large cavities reduced as the frozen water located in the narrow necks blocked the entrance to these gases. When the size of the necks increased via longer hydrothermal treatment of the materials, it was found that fewer void cavities remained unfilled with gas, as water adsorbed simultaneously in the necks and the large cavities. For all these materials, gas sorption following water adsorption, spanned over the same relative pressure as before water adsorption.

Changes in the surface chemical heterogeneity and roughness are also expected to affect the adsorption mechanism of various gases. This is because gas deposition at the early stages of adsorption is controlled by the interaction strength and the contact angle between the adsorbate and the surfaces, capable of driving a uniform layer-by-layer

adsorption or a more irregular one. Fractal analysis is utilized to detect these changes caused in the surface roughness. Pfeifer et al. measured the change in the surface area via nitrogen adsorption, post water and heptane adsorption at different surface coverage degrees, for Vycor, CPG and silica xerogel materials. They found that the decrease of the film area on a fractal surface is described by a power law of the increasing film volume, governed by the fractal dimension (Pfeifer et al., 1991). In a later study, Hua and Smith (1992) increased the surface hydrophobicity of these porous materials by silylation, at different fractions of alkylchlorosilane molecules and for a wide range of alkyl groups molecular weight. Fractal analysis showed that the alkylchlorosilane molecules were located in the big pores and that silylation smoothened the surface roughness of the silicas (Hua and Smith, 1992). Neimark *et al.* (1993) performed nitrogen sorption experiments to study the deposition of different amounts of polybutadiene polymer within LiChrospher Si 300 silica material. The authors found that the fractal dimension detected by nitrogen molecules, changed insignificantly with the amount of pre-loaded polymer, although the surface and the pore volume of the material decreased. They attributed this to the complete bulk filling of random sets of pores with polymer, rather then uniform surface coverage by the polymer, which would have changed its roughness. Thus, it seems that fractal analysis can be adopted to study the way water deposition occurs on the pore surface of the S1 material.

In summary, previous work has shown that both the Kelvin equation and the DFT algorithm overestimate the width of hysteresis in cylindrical pores, and that pore-pore interactions can lead to advanced adsorption phenomena. An integrated N_2-H_2O-N_2 experiment is utilised in this chapter to test the single pore hysteresis theory for ink-bottle shaped pores filled with water and the validity of the independent domain theory in these type of pores, when they are saturated with nitrogen and water. Fractal analysis is performed, to study the morphology of the adsorbed frozen water on the silica walls, as detected by nitrogen molecules after water adsorption.

5.3 Experimental procedure

The integrated N_2-H_2O-N_2 experiment was initially performed for the whole pellet sample of S1 material. For this ~0.14 g of S1 pellets were transferred in a gas sorption tube and the sample was degassed as described in Chapters 3 and 4. The nitrogen sorption isotherm, at 77 K, was then obtained using an ASAP 2020 apparatus. At the end of the experiment and following helium free-space analysis, the sample was degassed again, and it was partially saturated with water vapour via equilibrium adsorption, up to a water relative pressure of 0.913, at 294 K, as described in Section 3.3. This corresponds to a nitrogen relative pressure of 0.922 (Appendix, A3) and will be referred into all the sections below as partial saturation with water at a relative pressure of 0.922. The sample was left to equilibrate for 10 days above a NaOH solution, and it was then quickly transferred within a gas sorption tube (sealed with a seal frit to prevent water evaporation) and the mass of the sample was measured in a weigh balance. The adsorption/desorption isotherm for water obtained from equilibrium sorption experiments was presented earlier, in Figure 3.1. The mass of the adsorbed water was calculated from the difference between the mass of the partially saturated sample and that before water adsorption. The tube was connected to the ASAP 2020 apparatus and a Dewar filled with liquid nitrogen was manually raised to cool the system down to 77.3 K, for 20 min. This allowed the condensed water in the pores to freeze and behave like a solid phase before the system was evacuated for the next nitrogen sorption experiment to start. This ensured that no condensed water would be degassed prior to the gas sorption experiment. The equilibration time used for nitrogen sorption was 45 s, which was proved to be sufficient by Hitchcock (2011). The error in the volume adsorbed, for each pressure point is ±0.30 cm^3/g and it is calculated by ASAP 2020 apparatus. This sample was then fragmented to a particle size of 5-40 μm (measured in a microscope) and the nitrogen sorption isotherm was obtained.

5.4 Data analysis

5.4.1 Pore volume

The specific volume of nitrogen adsorbed was measured by the ASAP 2020 apparatus which uses units of cm^3/g at standard temperature and pressure (STP). However, the volume of water adsorbed is measured gravimetrically and has weight units (g). The Gurvitsch rule was used to convert nitrogen (1) and water data (2) into liquid volumes, V_0 (cm^3/g) as follows:

$$V_0 = \frac{V V_M}{V_n} \tag{5.1}$$

$$V_0 = \frac{m_a}{\rho} \frac{1}{m_s} \tag{5.2}$$

where V is the total volume of nitrogen adsorbed (STP), V_M is the molar volume of liquid nitrogen at 77.3 K (34.61 cm^3/mol), V_n is the molar volume of nitrogen gas at STP, (22,414 l/mol), m_a is the mass of water adsorbed, ρ is the water density at 294 K and m_s is the mass of the dry silica sample. It was assumed that the density of water in the pores remains constant (1 g/cm^3) after the partially saturated system was frozen at 77.3 K.

5.4.2 Change in the incremental nitrogen volume

The difference between the change in the incremental nitrogen volume adsorbed for two consecutive pressure points before water adsorption, and that after water adsorption, for the same set of pressure points, can be used to detect the location of adsorbed phases and this methodology was previously adopted by Rigby *et al.* (2008), for an integrated N_2-Hg-N_2 sorption experiment. By cumulatively adding the change in the incremental volumes of nitrogen obtained, a nitrogen isotherm can be produced, representative of the pores filled with water. If the gas sorption mechanism in cylindrical pores is driven only by the macroscopic characteristics such as the surface tension and pore geometry, then the pores would fill with nitrogen via cylindrical menisci and empty

via hemispherical menisci, and Kelvin-Cohan equation takes the following form (as discussed in Chapter 1):

$$\left(\frac{P}{P_0}\right)_{des} = \left(\frac{P}{P_0}\right)^2_{ads} \tag{5.3}$$

It was already shown by Hitchcock (2011) that the pores that entrapped mercury in a whole pellet S1 material would empty with nitrogen at relative pressures equal to a power of 1.5 of the relative pressures in adsorption, thus the pores filled with mercury would not fill and empty with nitrogen by the menisci geometries proposed by Kelvin-Cohan relationship, equation 5.3. These pores behave like independent cylindrical pores, as shown by the similar (parallel) shape of the adsorption and desorption curves, of H1 type isotherm, which fill and empty at a higher contact angle.

The error in the change of incremental volume of nitrogen is calculated as follows. It was assumed that capillary condensation for both nitrogen and water does not occur below a relative pressure of 0.71. Any difference between the incremental volumes adsorbed before and after water adsorption was attributed to noise. The standard deviation (SD) of the noise was then estimated for the changes in the volumes below a relative pressure of 0.71 as shown in Section A2.2, Appendix. Any fluctuations observed, below the double value of the SD, was attributed to noise.

5.4.3 Fractal analysis

The surface roughness of the S1 samples (whole and fragmented) before and after partial saturation with water was investigated via FHH fractal analysis in the multilayer region between P/P_0 =0.14-0.77, where the surface coverage is high and the surface tension between the liquid/gas interface is not negligible. This is described as follows:

$$\ln\left(\frac{V}{V_m}\right) = c + (D-3)\left[\ln\left(\ln\left(\frac{P_0}{P}\right)\right)\right] \tag{5.4}$$

where V is the adsorbed volume of nitrogen for different pressures at STP (cm^3/g), V_m is the volume of one adsorbed monolayer, c is a constant and D is the fractal dimension (Ismail and Pfeifer, 1994). A plot of $\ln V$ with $\ln(\ln(P_0/P))$, yields a straight line and D can be found from the gradient, (D-3), of the slope. An increase in the fractal dimension after partial saturation with water would indicate that the water adsorbed did not smoothened the bare silica surface, but in fact it was deposited in a disordered manner, along the pores.

5.5 Results and discussion

The sorption isotherms for nitrogen pre and post partial saturation with water are shown in Figure 5.1. It is seen that nitrogen hysteresis starts at a relative pressure of 0.758 before the sample is partially saturated with water and ends at a relative pressure of 0.975. However, after the system is partially filled with water, hysteresis starts at the higher relative pressure of 0.825, but ends at the same relative pressure as before (P/P_0=0.975). The shift to higher relative pressure post water adsorption is explained by the fact that water has filled the small pores where previously nitrogen would condense between the relative pressures of 0.758 and 0.825. As the sample is saturated under equilibrium adsorption with water up to P/P_0 =0.922, it would have been, however, expected that nitrogen condensation in the pores, post water adsorption, would start above a relative pressure of 0.922 if the pore filling mechanism for water at 294 K was the same as that of nitrogen at 77 K. In Chapter 3 it was shown from Figure 3.1 that the water sorption isotherm was of H2 type in contrast to the nitrogen sorption isotherm which is H1 type, Figure 5.1. This suggests that nitrogen filling and emptying mechanisms are those characteristic of independent cylindrical through pores, whereas water experiences more co-operative phenomena in adsorption and desorption, due to pore-pore interactions. Thus, water has filled different pores to those that nitrogen would fill, until the same relative pressure. Moreover, it can be the case where some pores are partially filled with water layers, that they now appear now as pores with a

smaller radius, therefore their filling with nitrogen occurs at lower relative pressures than 0.922.

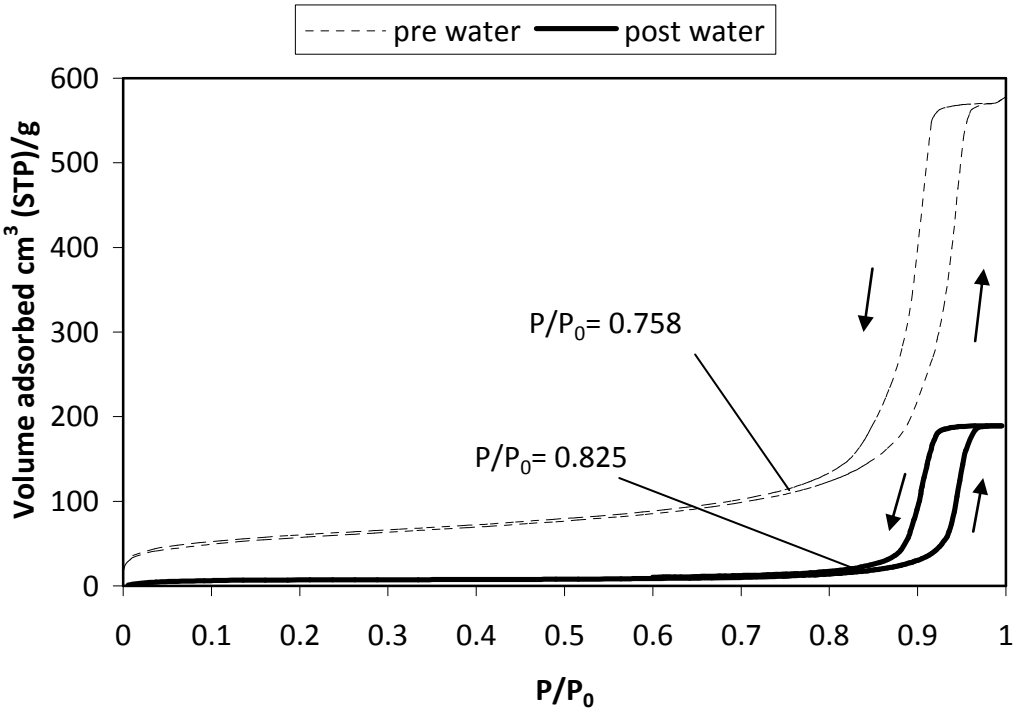

Figure 5.1 Nitrogen sorption isotherms pre and post partial saturation with water of the whole pellet S1 material. The arrows are shown to guide the eye

Measurements	**Adsorbate**	V_0 (cm^3/g)	S_{BET} (m^2/g)	C	V_m (cm^3(STP)/g)
Pre water	Nitrogen	0.89	199.2	216	46.3
Post water	Nitrogen	0.29	25.2	100.5	5.9
	Water	0.51	–	–	–

Table 5.1 Pore volumes and surface area occupied with adsorbates pre and post partial saturation with water

Table 5.1 presents the Gurvitsch pore volumes occupied by water and nitrogen, pre and post water adsorption. The available BET surface area for nitrogen adsorption is also

presented in Table 5.1. It is seen that water has filled a pore volume of 0.51 cm^3/g, nitrogen has filled a volume of 0.29 cm^3/g but there is a pore volume of 0.09 cm^3/g which remains empty after nitrogen adsorption in the partially saturated sample. This is possible if water is located on both sides of some empty pores, and after freezing it converts into solid state, thus blocking the access of nitrogen molecules into a pore volume of 0.09 cm^3/g.

It is also observed from Figure 5.1 and Table 5.1 that the amount of nitrogen adsorbed in the multilayer regime decreased. This is because the available surface for multilayer nitrogen adsorption is reduced after partial saturation with water. Figure 5.2 shows the nitrogen isotherms presented in Figure 5.1, but the isotherm following saturation with water is adjusted upwards by 110 cm^3(STP)/g, which is the difference between the adsorbed nitrogen volume in the multilayer region, before and after water adsorption. An overlap of the plots in the multilayer regime would mean that all the adsorbed water is located within the completely filled pores, and there do not exist partially saturated pores with water layers, where the nitrogen multilayer would start forming. However, as this is not observed, it must mean that nitrogen, post water adsorption, starts adsorbing on a surface where frozen water fractions are present in the form of puddles, thereby, the contact angle and the interactions between the nitrogen and silica surface have changed. Also, the BET constant of nitrogen, as seen from Table 5.1 has decreased following water adsorption, suggesting that (at least some of) the silica surface is covered by frozen water.

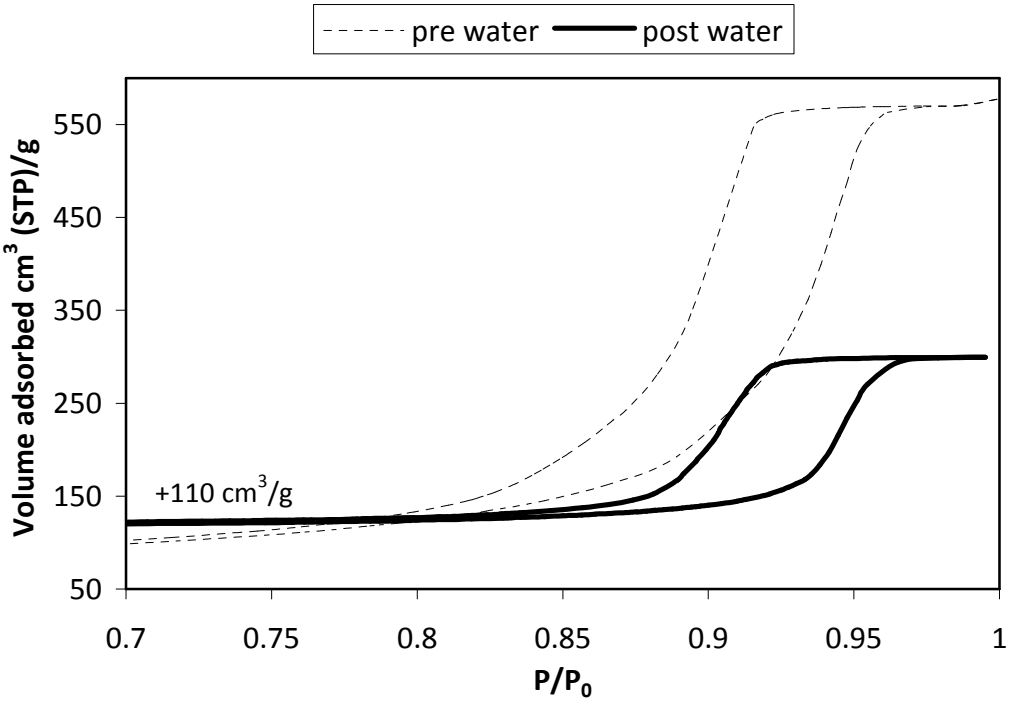

Figure 5.2 Nitrogen sorption isotherm post water adsorption adjusted upwards by a volume of 110 cm^3(STP)/g. The nitrogen sorption isotherm pre water saturation is also included

Moreover, it is seen from Figure 5.2 that the nitrogen isotherms do not overlap in the lower part of the hysteresis loop suggesting that the pores occupied with water fill and empty over the whole relative pressure range of the nitrogen capillary condensation regime. In Figure 5.3 the nitrogen isotherm in the partially filled system is adjusted upwards by 380 cm^3(STP)/g. This isotherm overlaps that obtained before water adsorption at the upper part, but diverge at lower pressures. This divergence means that the pores occupied by water would fill and empty at relative pressures below 0.952 and 0.913, respectively.

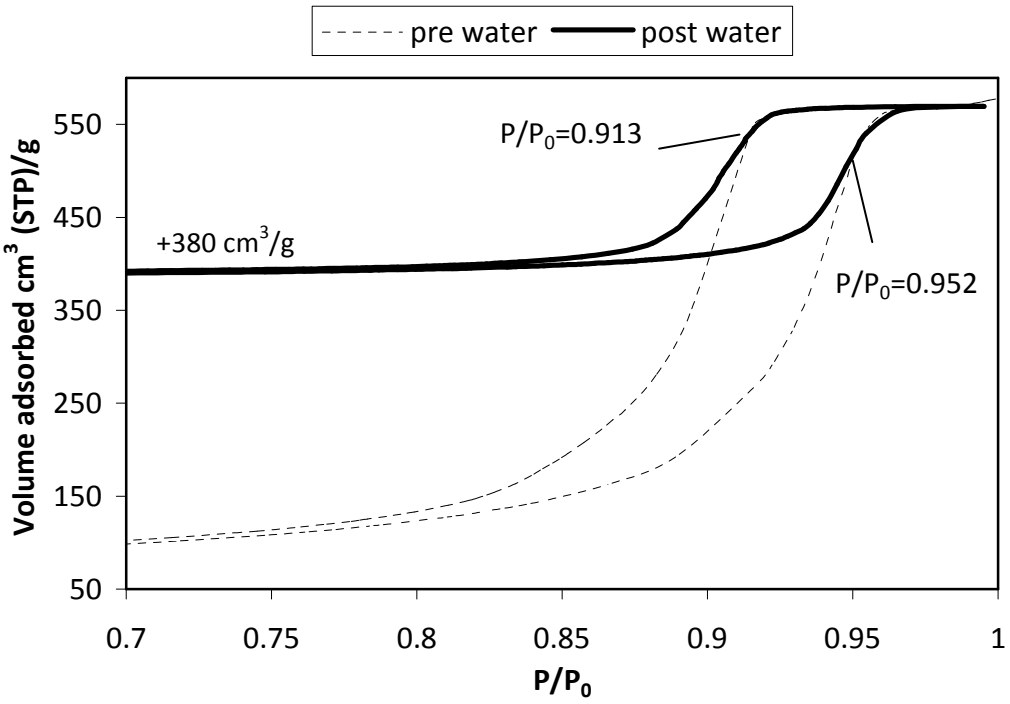

Figure 5.3 Nitrogen sorption isotherm post water adsorption adjusted upwards by a volume of 380 cm^3(STP)/g. The nitrogen sorption isotherm pre water saturation is also included

From Figures 5.1, 5.2 and 5.3, it is seen that the nitrogen isotherm in the partially saturated sample is H1 type, indicative of open cylindrical pores which fill and empty like independent pores. By raising all the relative pressures in the adsorption curve to a power of 1.8, as shown in Figure 5.4, the adsorption and desorption plots overlay. This power value is the same as the one predicted by the DFT model, previously adopted by Neimark and Ravikovitch (2001) for empty MCM-41 and SBA-18 samples.

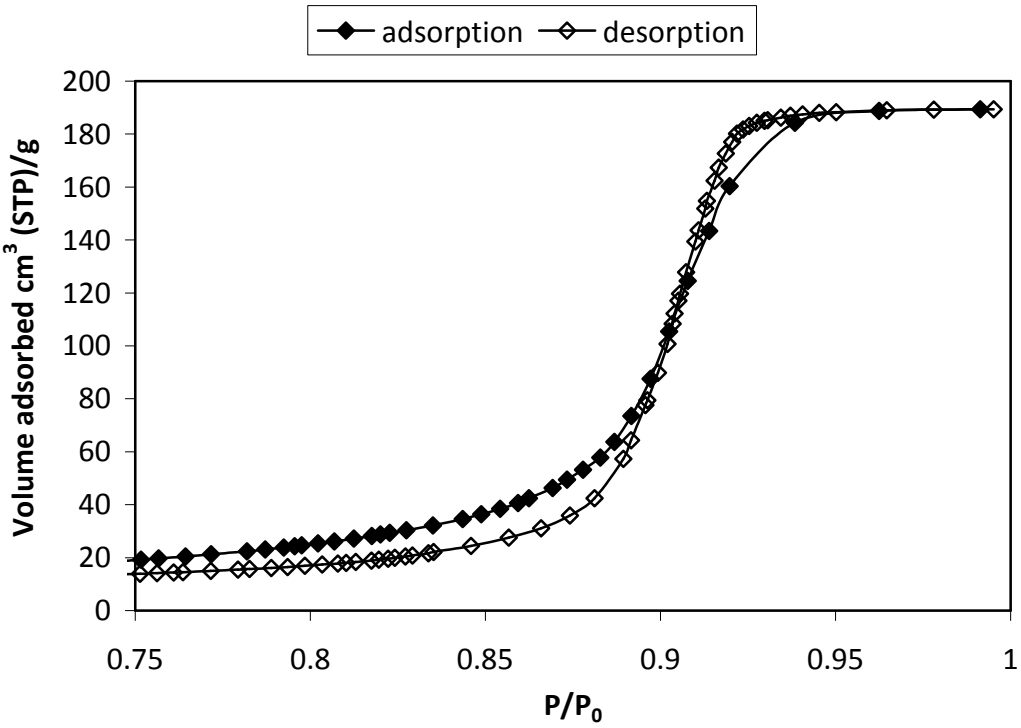

Figure 5.4 Plots of adsorption and desorption curves of nitrogen in S1, post partial saturation with water. All the relative pressures in adsorption has been raised to a power of 1.8

To study the wetting efficiency of nitrogen in a bare surface of S1 sample, and thereby the hysteresis width, the whole pellet sample was fragmented in order to curtail advanced adsorption and pore blocking effects in nitrogen sorption. Perkins *et al.* (2008) used a fragmented S1 sample to reduce pore blocking induced in cryoporometry NMR freezing and compared the menisci geometry initiating melting to that seeding freezing. Rigby *et al.* (2008) used a fragmented S1 sample to curtail pore shielding of mercury. Figure 5.5 shows the adsorption and desorption curves for nitrogen sorption when the whole pellets are fragmented, and all the relative pressures in adsorption are raised to a power of 1.65, which results in them overlaying the relative pressures in desorption. Hitchcock (2011) found that pores which entrapped mercury would fill with nitrogen independently and a power of 1.5 was required for the nitrogen sorption curves to overlay. These findings suggest that the DFT model overestimates the wetting efficiency of the adsorbed gases into the pore surface, and as such the width of the gas sorption hysteresis. The DFT model is an adsorption model developed to take into account the gas-gas, gas-liquid, gas-solid and liquid-solid interactions along with the pore geometry. The microscopic characteristics arising during gas sorption are included in the pore filling

and emptying mechanisms, as Kelvin-Cohan equations are only taking into account surface tension and the contact angle of the liquid with the pore walls, resulting in inaccuracies for pores smaller than 20 nm. However, these microscopic interactions adopted in the DFT model are calibrated by using reference porous materials with different interactions as well as by the pore geometry. It is thus possible that they are inconsistent with the interactions developed within an empty S1 material. The similarity in the isotherm width, shown by the power of 1.8, occurs when nitrogen is adsorbed on the partially saturated with water system. This proves that DFT applies only to a range of porous materials with specific miscroscopic and geometrical characteristics and must not be generalized to all the types of porous systems.

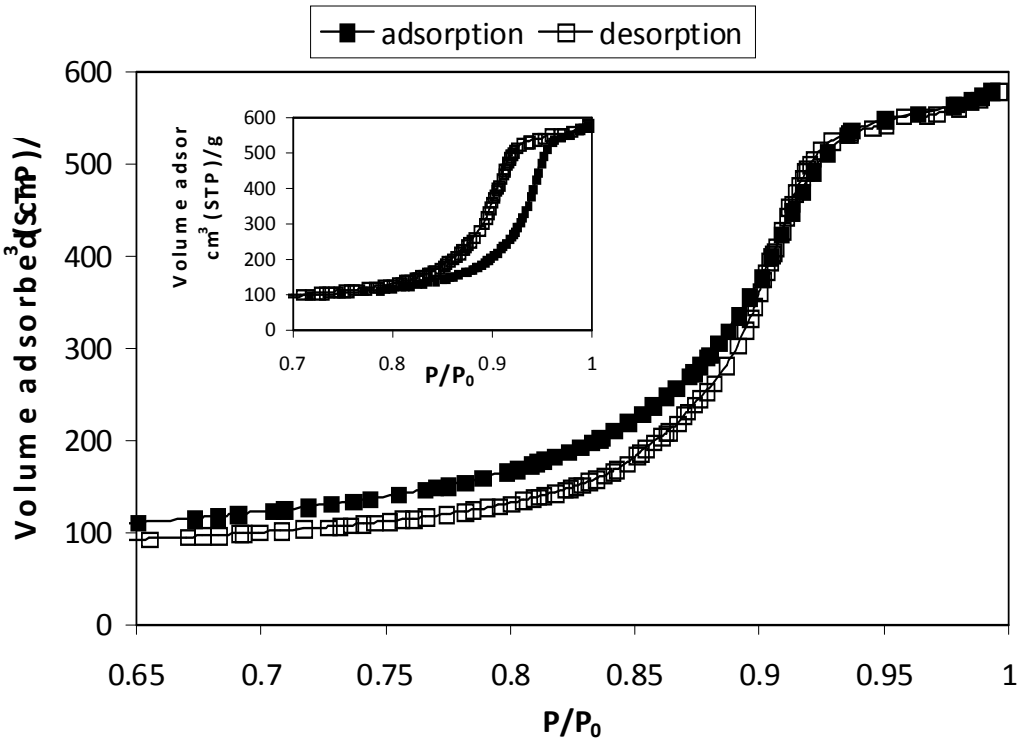

Figure 5.5 Plot of the adsorbed amount of nitrogen in an empty fragmented S1 sample, where the relative pressures in the adsorption curve are raised into a power of 1.65. The inset shows the nitrogen sorption isotherm

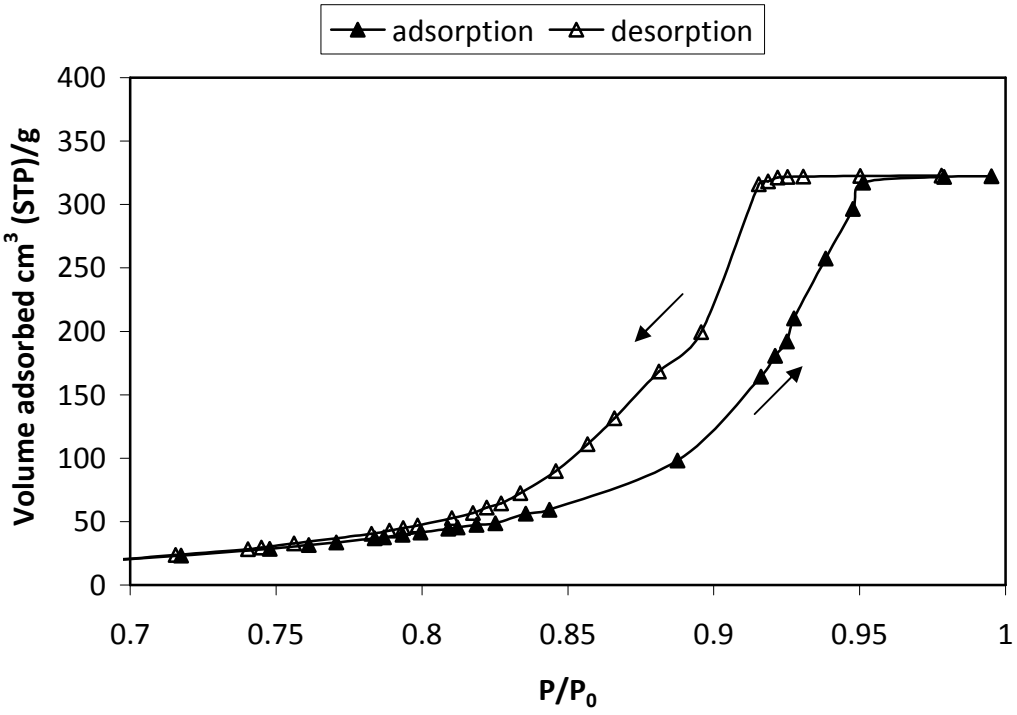

Figure 5.6 Derived nitrogen sorption isotherm for the pores occupied by water

By cumulatively adding the change in the incremental volumes adsorbed pre-water sorption and post-water adsorption, the gas sorption isotherm presented in Figure 5.6 for the pores that are filled with water, is then generated. From Figure 5.6 it is seen that water has filled pores over a relative pressure of 0.825-0.952. If equilibrium water adsorption occurred independently until the relative pressure of 0.922 and the water adsorption mechanism was similar to that of nitrogen, then the water filled pores would fill with nitrogen strictly at the range of P/P_0=0.758-0.922. Pore filling above P/P_0=0.922, is associated with water condensation in some bigger pores via advanced condensation. Nitrogen condensation at lower pressures than 0.922 post water adsorption means that water has not filled some small pores, where nitrogen has access into at the same relative pressures. These small pores will fill with water at higher relative pressures than 0.922, where water vapour adsorption was terminated. This is consistent with the findings in cryoporometry studies presented in Chapter 3, where advanced melting is some big pores was favoured when the previously empty smaller neighbouring pores filled at higher saturations. It was discussed that condensation into small pores at higher

pressures than those required if they were only filling by size, increased the water ganglia connectivity, and as such advanced melting.

Measurements	FHH fractal dimension, *D*±error
Pre water	2.63±0.003
Post water	2.81±0.011

Table 5.2 Change in the fractal dimension before and after water adsorption calculated by equation 5.4, at P/P_0~0.14-0.77. The error values correspond to the standard error from regression for data fitting in Excel

During gas sorption at low pore fillings, surface coverage is governed by the surface chemical heterogeneity and roughness whereas at higher fillings, surface tension plays the key role in flattening the liquid interface. Therefore, estimation of FHH fractal dimension before and after water adsorption provides information about the way water is deposited on the surface. The fractal dimensions measured pre and post water adsorption are presented in Table 5.2. It is seen that the surface roughness in the pores that are filled with nitrogen post partial saturation with water, increased beyond the error range. This indicates that water has not smoothened the silica surface by homogeneously covering it, as in this case the fractal dimension would decrease. Thus, the adsorbed nitrogen can experience different interfaces and as such the contact angle between gas-silica, gas-ice and gas-gas and gas-liquid differ to that of nitrogen adsorbing on the bare silica surface, before partial saturation with water.

5.6 Conclusions

In this chapter the integrated N_2-H_2O-N_2 experiment was used to study the validity of independent domain theory for water and nitrogen sorption. The water was introduced into the system by equilibrium adsorption. It was found that the nitrogen adsorption mechanism differs to that of water, in the way that less advanced condensation occurs

for nitrogen compared to that of water. Moreover it was shown that the DFT model and the Kelvin-Cohan equations overestimate the width of the nitrogen sorption isotherm in an S1 material, although the DFT model correctly predicts this width when the sample is partially saturated with water. This implies that the DFT model must not be generalized for all porous materials.

Chapter 6
Release of Cyclosporin-A from Casein and Lutrol Templated Porous Silica Particles

6.1 Introduction

The previous chapters gave initially an introduction to the fundamentals of gas sorption and NMR cryoporometry techniques, and then their sensitivity to probe the real PSD was investigated. For those studies, a well characterized, mesoporous, silica catalyst support, with an ink-bottle pore shape, was used as a model system to investigate the cooperative effects in gas adsorption and cryoporometry melting, likely to induce an error in the calculation of the PSD.

Porous materials are also used as drug delivery systems, thus an incorrect prediction of the pore size can lead to misinterpretation of the structure-transport relationships in these materials, and therefore their therapeutic activity. The objective of this chapter is to firstly characterize the porous structure of two different templated silicas, which were used as potential carriers of a poorly soluble drug in order to improve its solubility in the gastrointestinal area, and secondly to investigate how the pore structure characteristics and the particle morphology influence the dissolution rates of the drug in the environment present.

Highly ordered porous silica materials have been synthesised in the past from ionic and non-ionic surfactants, in both acidic and basic media, however, there is an extensive need for other non-toxic and cheap templating agents. The reader will be firstly introduced to a background literature review on the most common synthesis methods and the current templating agents used to produce porous silica particle, which are then used as drug carriers. The ability of a milk protein, sodium casein as a templating agent to obtain porous silica particles, is then studied as an alternative to the commonly used

non-ionic surfactant, Lutrol. Both the sodium casein and Lutrol templated silicas were synthesised under acidic conditions, and the porous particles formed were tested *in-vitro* as potential drug carriers of a highly hydrophobic protein, cyclosporin-A (CsA), with an aim to improve its poor solubility in the gastrointestinal area. Gas sorption, NMR cryoporometry, PFG NMR and SAXS characterization techniques were employed following SEM and TEM imaging, CD, FTIR and HPLC analysis. The dissolution profiles generated from the drug release studies will be fitted into the experimental CsA release profiles obtained, to investigate which parameters influence the release rate and to what extent.

The synthesis of silica particles, the *in-vitro* CsA loading and release profiles experiments, the FTIR, CD, DLS particle size measurements and SEM, TEM imaging techniques were conducted by Mr. Paulo Malheiro. Nitrogen gas sorption, NMR cryoporometry, PFG NMR and SAXS characterization techniques along with the diffusion model fittings were accomplished as part of this thesis work. The results were interpreted by both groups.

6.2 Synthesis and application of mesoporous silica particles as drug delivery systems

Over the past decade, ordered mesoporous silica materials gave been gaining increased interest for biomedical applications. Their size, morphology and porous structure can be tailored to achieve controlled and sustained drug release (Wang, 2009; Zeng et al., 2005) or increase solubility of drugs with low bioavailability (Van Speybroeck et al., 2009, Thomas et al., 2010). The synthesis of these periodic mesostructures is a template-directed process which involves the development of noncovalent bonds (hydrogen bonds, van de Waals forces) and electrocovalent bonds between the organic template and the inorganic silica precursors in aqueous media. A mesostructured hybrid is thus formed where the removal of the organic template leads to the formation of pores with surface areas reaching the order of 1000 m^2/g, Figure 6.1.

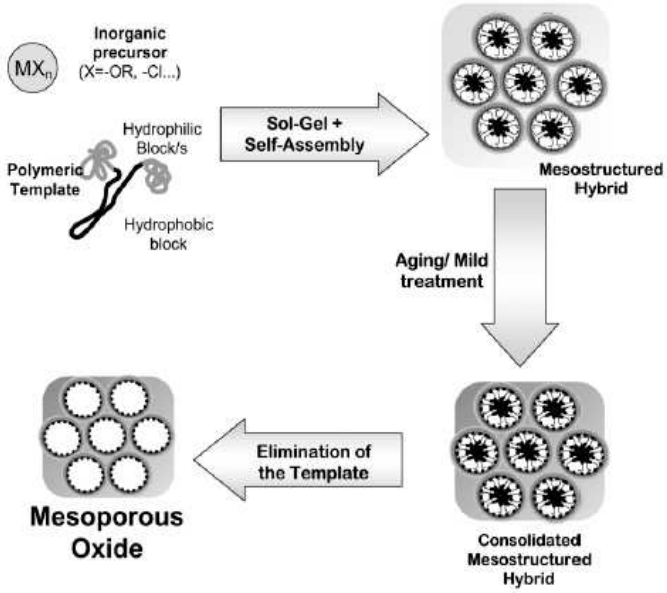

Figure 6.1 Synthesis steps of template-mediated mesoporous materials (Soler-Illia et al., 2003)

The organic template is a surfactant consisting of hydrophobic and hydrophilic groups capable to self-assemble in solvents, where one of these parts is insoluble, and form micellar systems. They are categorized as anionic, cationic, non-ionic and amphoteric according to their charge. The packing order of these micelles into spherical, cylinder, lamella, inverse cylinder or other geometrical structures is dependent on: the hydrophobic interactions between the organic groups, the molecular exchange between aggregates, the electronic repulsion between polar heads and the ratio between the polar head surface area to the hydrophobic volume (Israelachvili et al., 1976). Silica has a good compatibility and it is accepted as a "Generally Recognized As Safe" material by the FDA organization. Inhalation of crystalline silica causes silicosis and disorders associated with lung cancer, or heart and kidney diseases (Rice et al., 2001; W.H.O, 2000) dependant on the shape and the size of the particles (Mattson, 1994; Dufresne et al., 1998; Borm et al., 2011). However, small and smooth particles of silica have been already used in cosmetics and as a food additive. It exhibits an isoelectric point at ~pH 2, so for higher pH values conditions bears a negative charge, thus promoting electrostatic interactions with positively charged surfactants. The mostly used silica precursors are sodium silicate, tetraethoxysilane (TEOS) and tetramethoxysilane (TMOS). Beck et al. proposed two mechanisms, for high surfactant concentration, leading to the synthesis of silica porous structures, a) the liquid crystal phase initiated templating, where at high surfactant

concentration the surfactant interacts with the solvent resulting in ordered micelle formation, around which silica precursor condenses creating silica wall, and b) the silicon anion mediated templating route where the silica precursor coats the surfactant micelles in more dilute solutions, that then aggregates to form an ordered mesostructure (Beck et al., 1992). Firouzi *et al*. (1995) suggested a co-operative mechanism of formation, based on charge interactions between the species and it is valid for dilute surfactant systems too. Here, surfactant micelles and free molecules initially co-exist in dynamic equilibrium, but introduction of silica precursor leads to ion exchange between the silica oligomers and the surfactant, forming inorganic-organic aggregates, that can self-assemble and arrange in perhaps a different structure to the initial micellar one. Frasch *et al*. (2000) though reported that the charge effect is overemphasised due to the lack of organization in the system prior to precipitation. The authors suggested that perhaps the most critical step in the process is the formation of siliceous pre-polymers that coat the surfactant molecules leading to the micelle growth and then reorganization of the silica/micelle complexes into an ordered structure. More recently, a liquid-liquid phase separation mechanism of both the surfactant and precursor species into unordered liquid droplets is proposed. These droplets undergo an ordering transition due to the high concentration in the droplet, leading to the final organized mesostructure (Chan et al., 2001).

In any of these pathways, the surfactant is removed by calcination and a porous structure is consequently obtained. The pore size and structure, specific surface area and surface roughness, and the particle size, will therefore be controlled by the type of the organic template (charge, chain length, hydrophilicity) and the inorganic precursor (Sel et al., 2006; Yang and Edler, 2009) , the ratio between the template and the silica precursor (Bagshaw et al., 1995; Witoon et al., 2010), the pH of the hydrothermal solution (Hsu et al., 2006), its aging temperature and time (Ertan et al., 2009; Galarneau et al., 2001; Prouzet et al., 2009) and the method of template removal (washing or calcination). Zhao *et al.* synthesized highly ordered mesoporous silica materials and found that a small, an intermediate and a big PEO/PPO ratio in triblock copolymers leads to lamellar, hexagonal and cubic structure respectively. Moreover, in acidic conditions, silica precipitation occurs faster for weaker and higher concentration of acids (Zhao et al., 1998a). Ethanol or methanol biproducts produced from silica hydrolysis (i.e. from TEOS, TMOS) during

synthesis increase surfactant solubility in the water thus making their self-assembly more difficult leading to less ordered structures. Therefore sodium silicate is alternatively used to prevent alcohol production. Furthermore, silica materials synthesized from low molecular weight cationic surfactants at basic conditions (i.e. MCM-41) are less thermally stable than those formed from non-ionic surfactants at acidic conditions (i.e. SBA-15) due to formation of thinner walls in former case. The macroscopic shape of the material synthesized under the same conditions depends mainly on the stirring rate of the template-precursor mixture (Zhao et al., 1998b), but also on the presence of other small molecules (alcohols, amines, surfactant impurities) and salts, the pH of the environment and the monodispersity of the surfactant.

The aforementioned silica's unique properties, along with their easily functionalized surface, make them ideal candidates for drug delivery applications, where controlled release is required over a period of time. Their biodegradability depends on the particle size and the local fluid flow conditions (Finnie et al., 2009). Vellet-Regi *et al.* (2000) firstly introduced the application of MCM-41 mesoporous silica material as a drug release system of ibuprofen. The pores in this material are highly ordered and cylindrical, arranged in a 2D-hexagonal structure. Later on, SBA-15 with cylindrical 2D-hexagonal structured pores, thicker walls and micropores interconnecting adjacent mesopores was used for gentamicin and amoxicillin controlled delivery (Doadrio et al., 2004; Vallet-Regí et al., 2004). Further functionalizing of their porous surface provided controlled release rate and improved drug loading efficiencies of drugs (Manzano et al., 2008) and proteins (Yiu et al., 2001; Song et al., 2005). Encapsulation of poorly water soluble drugs within ordered mesoporous structures also increased their oral bioavailability (Mellaerts et al., 2008; Thomas et al., 2010). Drug loading efficiency within the silica particles is controlled by the pore size and pore volume, surface area and its roughness, the presence of functional groups and the particle size. These factors along with the release medium will also influence the drug release rate and its solubility. Qu *et al.* (2006) found that the loading efficiency of water-soluble Captopril in MCM-41 and SBA-15 particles was higher for higher S_{BET}. Its release rate was faster from bigger sized pores, smaller particles, and for dispersion in gastric fluid rather than intestine fluid. Similar results were found for ibuprofen release (Horcajada et al., 2004). Riikohen *et al.* (2009) found that ibuprofen

loaded MCM-41 particles contain a crystalline phase of drug outside the pores but a crystalline and disordered ibuprofen layer within the pores, which is thicker for the thermally carbonized surfaces compared to the hydrogen terminated ones. The size of the pores had no substantial effect on the size of this layer. Two physical states (crystalline, glassy) of adsorbed itraconazole in SBA-15 were observed by Mellaerts et al., (2007) after a critical drug loading and the concomitant presence of these phases led to slower drug release rates. Moreover, the increase in pore width after a certain value had no effect on the drug release kinetics implying that diffusion from small pores is retarded by the steric hindrance of guest molecules. Song *et al.* (2005) reported that unfolding of charged proteins can be hindered by the small pore size and the pH of the environment. However, the protein is able to orientate co-axially with the pore, hence being able to diffuse through the very narrow pores.

6.3 Lutrol and casein templates

The structural order of the pores in a porous material depends mostly on the way the templating agents, arrange themselves in the environment present, to form micelles. Therefore, it is necessary to understand what parameters control the self organization of the Lutrol and casein micelles and what are the interactions induced between the micelles, the silica precursor and any other groups present, from findings reported in the literature precedence.

Lutrol® F-127 (Polaxomer 407) is a non-ionic triblock copolymer consisting of a central hydrophobic polypropyleneoxide (PPO) block and two lateral hydrophilic polyethyleneoxide (PEO) blocks ($PEO_{106}PPO_{70}PEO_{106}$, MW=12,500 g/mol). It has been extensively used for synthesis of silica porous materials such as SBA-16 to obtain cubic structures, with a narrow pore size distribution and specific surface area reaching 740 m^2/g. In aqueous environment and above their critical micellar concentration (CMC) the PEO chains point towards the water whereas the PPO ones form the inner core of a micelle. In fact the PEO groups are responsible for the complimentary microporosity in the walls of silicon materials, whereas the PPO groups assemble to form the mesopores

(Kruk et al., 2000). Elevating the synthesis temperature, the hydrophibicity of the PEO groups increases, hence, there will be fewer interactions with the water molecules and their penetration into the silica framework will be limited. This is also expected to promote an increase in the pore size as the hydrophobic domain volumes will be increased. In an acidic environment silica precursor after hydrolysis gains a positive charge and the PEO chains are also able to interact with the hydronium H^+ ions. The interaction between the silica and the PEO is thus ascribed to strong H-bonding between them.

Caseins are proteins present in mammalian milk and represent 80% of its composition. There are three types of proteins, α_{S1}-, a_{S2}-, β- and κ-casein, with a molecular weight ranging between 20-25 kDa and a high net charge (Chakraborty and Basak, 2007). In the bovine sodium casein, they exist in a ratio of 4:1:3:0.7. Caseins exhibit a pI=4-5.8 and they gain an amphiphilic character from the hydrophilic N-terminal polar aminoacid groups and the C-terminal non-polar hydrophobic units. This amphiphilicity is responsible for their self assembly into micelles, resembling the classical surfactant micelles. By lowering the pH from 7 to 2.6, the net charge redistributes along the peptide chain, consequently changing the hydrophilicity of the molecule. It is thus important to understand the structure of the casein submicelles at different pH conditions because the way they are arranged will influence their templating properties.

In particular, β-casein peptides have an elongated conformation and have some degree of secondary structure. Portnaya *et al.* (2008) showed that at pH 2.6, it obtains an intermediate state between globular and random-coil structure, and above its CMC (1.8 mg/ml) it self-assembles to disk-like geometry micelles (~5.5 nm) with 6 monomers per micelle. On the contrary, at pH 7, the micelles are spherical and constitute of 20 monomers. β-caseins are highly temperature responsive and at neutral conditions an increase in the temperature leads to morphological change from flat disk to spherical, with a higher aggregation number (more monomers) (Moitzi et al., 2008; de Kruif and Grinberg, 2002). This change though is not observed at low pH suggesting that they do not exactly mimic the block-copolymer surfactant self-assembly. α_{S2}-caseins, form spherical micelles (3.7 nm) through a series of consecutive association steps (Snoeren et

al., 1980) whereas the shape of the a_{S1}-casein micelles is proposed to be either wormlike (Thurn et al., 1987) or spherical (Schmidt, 1970). κ-casein micelles have a bigger spherical size (~25 nm) consisting of 30 monomers (Vreeman et al., 1981) or, elliptic (5 nmx10.2 nm) (Ossowski et al., 2012).

It is important to distinguish the difference between milk casein micelles and α_{S1}-, a_{S2}-, β- and κ-casein micelles. Actually, the milk casein micelles are formed by aggregation and connection of α_{S1}-, a_{S2}-, β- and κ-casein micelles by calcium phosphate molecules (CP). Both α- and β-caseins are highly phosphorylated, so they get easily attached onto the CP present in the milk whereas κ-caseins are CP insensitive. There are different models proposed for the milk casein organization into micelles. One model presents micelles as spheres (100-120 nm) where the shell consists of hydrophilic κ-casein rich submicelles and the inner core has α- and β- casein closely packed submicelles (~7-9 nm) attached through a calcium phosphate molecule (Hansen et al., 1996b). These submicelles swell slightly at decreasing pH leading to an increase of their volume. Others utilized SEM imaging technique and showed that micelles are spherical but with tubular submicelles of ~10-20 nm, protruding from the bulk of the particle (Dalgleish et al., 2004). On the contrary, Holt describes the micelles as structures solely formed by crosslinking of calcium phosphate nanoclusters (NC) with α- and β-caseins, resulting in an extended 3D regular network, where the C-terminal region of κ-caseins protrudes like a hairy layer on the surface of the micelles (Holt et al., 1998). The NC core is ~2.3 nm and the peptide shell is ~4 nm, separated at an average distance of 18.6 nm. De Kruif further extended this model into NC co-consisting with denser protein regions (mini-clusters) with a total volume of 5 times higher than the NC. Mini-cluster are ~2 nm and formed by some entangled hydrophobic tails of caseins facing out of the clusters, separated by a distance of 6 nm (de Kruif et al., 2012). The dual binding model had also been suggested by Horne where α- and β-caseins obtain a train-loop-train and train-loop structure, respectively. Bonding between α- and β- and κ- caseins takes place in their hydrophobic regions while the phosphorylated groups of α- and β-caseins are attached via a CP molecule (Horne, 1998).

Milk micelle integrity in general is accomplished by an interplay of hydrogen bonds, hydrophobic and electrostatic interactions between the casein peptides and the CP. Acidification at pH=4.6 would lead to CP dissolution and consequently into micelle destabilization and caseins precipitation. This would mean that a mixture of α_{S1}-, a_{S2}-, β- and κ-caseins dispersed in acidic aqueous solution, in the absence of CP, would not regain the milk micellar structure. Instead each type of casein would form its own micelles, separated from one another. However, Liu and Guo showed that casein micelles can still be formed at pH 2-3 due to hydrophobic and H-bonding interactions between the α- and β- and κ- caseins molecules and their size can reach ~120 nm (Liu and Guo, 2008). Most recently, Post and co-workers showed that sodium casein solubility is high below and above pH 4.6, and the particle size is independent of pH (Post et al., 2012a; Post et al., 2012b).

Recently Shchipunov and Shipunova used caseins as a novel biocompatible templating agent to synthesize silica aerogels at pH above casein pI (Shchipunov and Shipunova, 2008). The nanocomposites consisted of crossed-linked clusters whose size decreased by increasing the pH. The cluster size was ~100 nm, thus the authors concluded that these must have been micelles, similarly arranged to those in the milk, covered with silica. To our knowledge, no (other) work has been reported on synthesis of casein-templated porous silica materials in acidic conditions, below the casein pI. Sodium casein solubilisation at pH 3-6, leads to formation of aggregates to a point that is unsuitable for templating purposes, thus pH 2-2.5 can be chosen (Liu and Guo, 2008). Also mild acids, such as acetic acid (CH_3COOH), have to be chosen to lower the pH in order to prevent precipitation of the protein. At this interval sodium casein is positively charged and is expected to interact with the negatively charged silica via electrostatic interactions. If casein has sufficient hydrophobic groups to exclude silica, they will aggregate together and try to reorganize forming the final mesostructure.

6.4 Cyclosporin-A

Cyclosporin-A (CsA, MW: 1202.61 g/mol), is a highly hydrophobic and nonpolar cyclic protein, with molecular dimensions 0.21 Å x 9 Å x 8 Å (The Protein Data Bank, processed

in HyperChem). It has a high immunosuppressive activity and it is mainly used to prevent organ rejection after transplantation or for several autoimmune diseases. The protein consists of 11 aminoacids; 7 are N-methylated and 4 are linked via intramolecular hydrogen bonding between an N-H group and a C=O group (Figure 6.2). The latter provides advanced stability to the molecule when present in a nonpolar solvent.

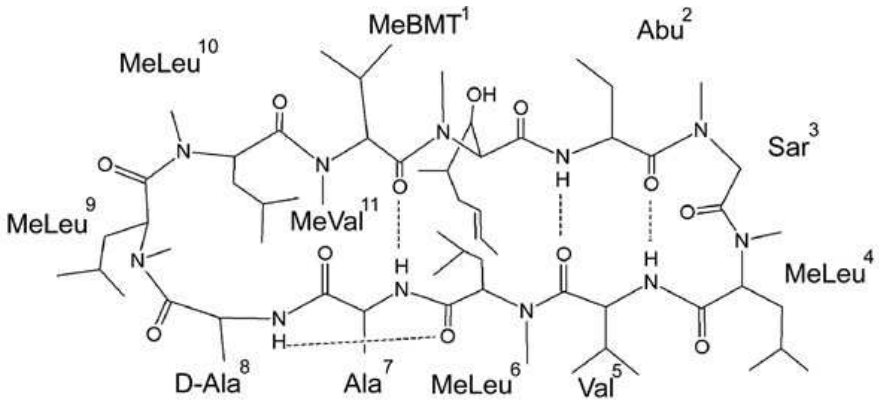

Figure 6.2 Molecular structure of CsA. Re-drawn from Zijlstra *et al.* (2007)

Oral administration of CsA is limited by its poor bioavailability in aqueous media (solubility 6.6-25.67 μg/ml) and its low permeability across the biological barriers including the gastrointestinal one. Also, variation of pH does not alter its solubility due to lack of ionisable sites within the molecule. Indeed, Ismailios *et al.* (1991) found its solubility to be similar in buffer solutions of pH 1.2 and 6.6, but it was inversely proportional to the temperature. Hydrophobic drugs can, however, increase their solubility in water by means of cosolvency, micellization and complexation. Introduction of water miscible cosolvents with small hydrocarbon regions reduces the polarity of the water and hence improve the solubility of nonpolar CsA. Incorporation of the drug into the core of surfactant micelles will also increase its solubility, initiated by hydrophobic interactions between the protein and the hydrophobic part of the surfactant. Moreover, recently cyclodextrins have recently been used as complexes for drug inclusion into their matrix. Ran *et al.* studied the aforementioned methods but none of these routes

increased the drug solubility. The authors suggested that CsA in water is potentially arranged in a unimolecular micelle with the methyl groups pointing towards the interior of the cyclic structure and the polar carboxyl groups along with the H-bonded ones face the water (i.e. the inverse to Figure 6.2 morphology) (Ran et al., 2001; El Tayar et al., 1993). However, the H-bonds between the amide and the carbonyl groups are quite metastable and interact stronger with water or ethanol molecules, providing the molecule with many slowly interconverting conformations (el Tayar et al., 1993). Other DDS systems for CsA transportation such as liposomes, microemulsions and polymer nanoparticles were used and reviewed by (Czogalla, 2009). Only very recently, Lodha et al. (2012) synthesized amorphous silica nanoparticles from zwitteronic surfactant SB3-12 for encapsulation of CsA. Although at pH 6.6 the CsA solubility increased from 8 to 85 %, the protein loading efficiency was only 15 %. Moreover, the authors observed a slow release which they attributed to the hindrance effects encountered by the protein, as its hydrodynamic radius was similar to the pore size of the silicas.

6.5 Drug release data analysis

From both a pharmaceutical and engineering point of view, the first step before designing a potential drug delivery system is to study and then predict, the release mechanism of the drug molecules from this system into the target area. In general, drug diffusivity is controlled by the morphological characteristics of the drug (pI, size, solubility, stability), the drug carrier (material, shape, size, porosity, stability) and the release medium (pH, enzymes, barriers). Different models have been already applied to determine the extent of contribution of those parameters into the release kinetics of the therapeutic agents from porous materials. Higuchi was the first to derive an equation describing the time dependant release of a drug from the surface of an ointment film, based on Fickian diffusion considering perfect sink conditions and a pseudo-steady state diffusion (Higuchi, 1963):

$$Q_t = (k_1 t)^{1/2} \tag{6.1}$$

An alternative approach to this equation was then used (Strømme et al., 2009) to take into account the porosity, ε_p, of the drug carrier:

$$\frac{Q_t}{A} = \left[D_{\text{int}ra} C_s (2C_m - C_s \varepsilon) t\right]^{1/2} \tag{6.2}$$

$$\varepsilon = \frac{V_0}{V_0 + 1/\rho_s} \tag{6.3}$$

where Q_t is the amount of drug released, A is the external surface area of the drug carrier, $k_1(C_s, C_m, D_{intra})$ is a release rate constant, D_{intra} is the drug diffusivity within the particle, C_s is the drug solubility within the aqueous phase, C_m is the drug content per drug carrier unit volume, V_0 (cm^3/g) is the total pore volume (cumulative pore volume from Horvath-Kawazoe method) and ρ_s is the solid density of the silica (2.2 g/cm^3).

Molecular diffusion through an isotropic porous sphere can also be determined from Fick's second law in radial coordinates described by:

$$\frac{Q_t}{Q_\infty} = 1 - \frac{6}{\pi^2} \sum_{n=1}^{\infty} \left(\frac{1}{n^2}\right) \exp\left(\frac{-D_{\text{int}ra} n^2 \pi^2 t}{r^2}\right)$$

(6.4)

which for drug release fractions of less than 0.4 is reduced to:

$$\frac{Q_t}{Q_\infty} = 6\left(\frac{D_{\text{int}ra} t}{\pi r^2}\right)^{1/2} - 3\frac{D_{\text{int}ra} t}{r^2} \tag{6.5}$$

For drug release fractions higher than 0.4, equation 6.4 becomes:

$$\frac{Q_t}{Q_\infty} = 1 - \exp(-k_2 t) \tag{6.6}$$

which is known also as the Linear Driving Force model (LDF) (Glueckauf, 1955; Glueckauf and Coates, 1947). Q_∞ is the total amount of the drug released after infinite time, r is the radius of the spherical drug carrier and k_2 is a release rate constant, equivalent to $15D_{intra}/r^2$ for a sphere.

Another empirically derived equation to describe drug release/dissolution profiles is the Weibull equation, simplified to equation:

$$\frac{Q_t}{Q_\infty} = 1 - \exp\left(-k_3 t^b\right) \tag{6.7}$$

Although parameters k_3 and b lack any physical meaning, it was found from Monte Carlo simulations that it can describe Fickian diffusion of drug release from both Euclidian and fractal spaces (Kosmidis et al., 2003). Parameter k_3 is a release rate constant and b defines the shape of the release curve, characteristic of the diffusion mechanism. For diffusion in Euclidian matrices, $0.69<b<0.75$, for diffusion in a fractal geometry or disordered structure, $b<0.69$ and for a combined diffusion in Euclidian space with contribution from another release mechanism, $b>0.75$ (Papadopoulou et al., 2006). As k_3 constant determines the release rate, it is likely to be controlled by the intraparticle diffusivity and the particle size, and be similarly expressed by $15D_{intra}/r^2$, likewise k_2. All the particles are assumed to be perfectly spherical (for modelling purposes), with even drug distribution across the matrix and isotropic drug diffusion. Drug release is assumed to be driven by the difference in the drug concentration within and outside the particles, and it is also pore diffusion controlled.

The free bulk diffusion, D_B, of a drug in a solute can be calculated from the Einstein-Stokes equation:

$$D_B = \frac{k_B T}{6\pi\mu r_d} \tag{6.8}$$

where k_B is the Boltzman constant, T is the temperature, μ is the dynamic viscosity of the drug within the solvent (μ_{CsA} = 0.93 mPa s, 293 K, aqueous solution) and r_d is the radius of the diffusing drug.

For drug diffusion within a porous matrix D_{intra} will deviate from that in a bulk liquid as the system's tortuosity, τ_p, has to be taken into account, hence the following equation is used:

$$\frac{D_{\text{int}ra}}{D_B} = \frac{\varepsilon_p}{\tau_p} \tag{6.9}$$

The τ_p can either be found by PFG NMR using equation 6.10 or from the empirical expression 6.11 (Veith et al., 2004), where D_{PFG} and D_b are the diffusion coefficients of the solute imbibed in the particles and in the bulk, respectively, due to Brownian motions.

$$\tau_p = \frac{D_b}{D_{PFG}} \tag{6.10}$$

$$\tau_p = \varepsilon_p + 1.5(1-\varepsilon_p) \tag{6.11}$$

However, when the ratio between the radius of the drug or solute molecule to the radius of the pore ($\lambda = r_d/r_p$) exceeds 0.1, then the diffusing molecules are subject to hindrance and friction resistance from the pore walls. Therefore, the D_{intra} is likely to decrease and the transportation of the molecules through the porous matrix will be retarded. To account for these effects, a restrictive factor $F(\lambda)$ is added to eq. (9) :

$$\frac{D_{\text{int}ra}}{D_B} = \frac{\varepsilon_p}{\tau_p} F(\lambda) \tag{6.12}$$

When adsorbed species (i.e. drugs) encounter steric hindrance in the pore mouth due to the accumulation of other drug molecules, i.e. when they are attached more strongly

onto the pore surface, then the diffusivity of the former will be retarded and the general following equation is used to account for this effect (Spry and Sawyer, 1975, cited in Mace and Wei, 1991):

$$F(\lambda) = (1-\lambda)^4 \tag{6.13}$$

For spherical diffusing molecules in cylindrical channels and for $0.1<F(\lambda)<0.5$, equation 6.14 (Karger and Ruthven, 1992) or equation 6.15 (Beck and Schultz, 1970) can be adopted:

$$F(\lambda) = (1-1.83\lambda + 4.18\lambda^2)\exp(-6.52\lambda) \tag{6.14}$$

$$F(\lambda) = (1-\lambda)^2(1-2.14\lambda + 2.09\lambda^2 - 0.95\lambda^5) \tag{6.15}$$

The radii of pores and diffusing species are calculated from gas sorption studies via BJH method and from equation 6.8, respectively. However, it must be noted that all the aforementioned models are not accounting for any physicochemical interactions of the diffusing species with the porous medium and the solute, which are likely to contribute into the drug release rate.

The aim of this work is to investigate the potential of sodium casein to be used as a templating agent for the synthesis of porous silica particles, at pH~2 and to compare their structure to Lutrol templated silicas, synthesized under the same experimental conditions. Particle size, morphology and porous structure will be characterized via SEM and TEM imaging, DLS, nitrogen gas sorption, NMR cryoporometry, PFG NMR and SAXS techniques. Furthermore the casein and Lutrol templated particles synthesized will be used for CsA encapsulation with an aim to increase CsA solubility in the simulated intestinal fluid (IF) and gastric fluid (GF).

The impact of silica morphology on the CsA release behaviour in IF and GF will be then investigated. For this, equations 6.2, 6.5, 6.6 and 6.7 will be firstly fitted into the

experimental release profile data, using Excel Solver, to obtain the experimental release constant. A combination of equations 6.9 and 6.11 (Model I), equations 6.11, 6.12 and 6.14 (Model II), equations 6.10, 6.12 and 6.13 (Model III), and equations 6.10, 6.12 and 6.15 (Model IV) will be then used to calculate the D_{intra}. The values obtained will be further used for the estimation of the theoretical release rate constants ($k=15D_{intra}/r^2$) and will be compared to the experimental ones. The ratio between the Lutrol and casein experimental release constants for each model, and in each release medium will be then compared to the ratio of the theoretically calculated ones.

6.6 Materials

Sodium silicate solution ('water glass', 17 % SiO_2), sodium casein (composition α_{S1}:a_{S2}:β:κ = 4:1:3:1), Cyclosporin-A (CsA), hydrochloric acid (HCl), sodium chloride (NaCl), sodium hydroxide (NaOH), heptane and dichloromethane (DCM) were purchased from Sigma-Aldrich. Lutrol® 127 was purchased from BASF, acetic acid from Reidel-de-Haën, sodium dodecyl sulphate (SDS), sodium taurocholate, L-α-Phosphatidylcholine (lecithin) and sodium phosphate from Fluka Biochemika and HPLC grade ethanol (EtOH) from Fisher Scientific.

6.7 Experimental procedures and characterization methods

6.7.1 Synthesis of casein and Lutrol templated silicas

The experiments described in this section were conducted by Mr. Paulo Malheiro. The mesoporous Lutrol templated silicas were synthesized as previously reported by (Kosuge et al., 2004a). For Lutrol templated silicas, 6 g of Lutrol were dissolved in 180 ml of HCl solution (2 M) under constant stirring at 298 K. 15.3 g of sodium silicate were dissolved in 45 ml deionised H_2O and this mixture was added dropwise into the polymer solution, under continuous stirring that was maintained for 24 h. The final solution had a pH 1. Precipitated silica particles were recovered, washed with deionised H_2O and calcined in the furnace at 873 K, for 8 h, for complete removal of the template. At the end of the

process, porous silica particles were obtained. The casein templated silicas were prepared in the same way except that HCl solution was replaced by acetic acid (2 M) solution. Casein was initially dissolved in this acid media (pH 2) under rigorous agitation speed, at 303 K. Addition of sodium silicate solution increased the pH to ~2.5.

6.7.2 Simulated gastrointestinal fluids

The experiments described in this section were conducted by Mr. Paulo Malheiro. The simulated intestinal fluid (IF) was prepared according to the patent developed by Dr. Jennifer Dressman of the J.W. Goethe University, Germany to simulate fasted state conditions. Firstly, a stock IF solution was prepared by dissolving 0.348 g of NaOH, 3.95 g of sodium phosphate and 6.19 g of NaCl in 1 l of deionised H_2O. Within 125 ml of this solution were subsequently added 0.825 g of sodium taurocholate and 2.95 ml of a solution containing 100 mg/ml lecithin in DCM. The resulting emulsion was placed in a rotary evaporator to remove the DCM and the remaining emulsion obtained was completed to a volume of 500 ml by adding stock IF solution.

The simulated gastric fluid (GF) was prepared by dissolving 1.25 g of SDS, 1g of NaCl and 3.5 ml of HCl in deionized H_2O to a total volume of 500 ml with vigorous stirring (British Pharmacopoeia 2004, A51). This fluid was then immediately used for the drug release studies.

6.7.3 Cyclosporin-A loading

The experiments involving CsA loading in the paticles and its release were conducted by Mr. Paulo Malheiro. Briefly, CsA solution (10 mg/ml) was firstly prepared by dissolving 20 mg of CsA in 2 ml of EtOH. 1 ml of this solution was added into 90 mg of silica particles (Lutrol or casein templated) placed in a glass vial. The system was capped and sealed with parafilm and was then placed in a platform shaker for 24 h providing a gentle stirring to allow CsA absorption into the silica. The vial was uncapped and the particles were left to air dry at 298 K under continuous stirring.

6.7.4 Determination of loading efficiency of CsA and *in-vitro* release studies

To determine the CsA loading efficiency, 5 mg of loaded silica particles were placed in a flask with 5 ml EtOH. The mixture was bath sonicated for 30 min and vigorously stirred under a vortex for 3 min. 1 ml of the resulting solution was collected and centrifuged at 14,000 rpm for 3 min and the supernatant was removed for High Performance Liquid Chromatography analysis (HPLC) analysis (refer to Appendix A2 for further information on the HPLC analysis system and the CsA calibration curve, Figure A4.2).

CsA release from Lutrol and casein templated silicas was studied in both IF and GF mediums at 298 K. For this 15 mg of drug loaded silicas were placed in an Eppendorf tube and filled with 1.5 ml of either IF or GF. These tubes were then placed in a rotating wheel under gentle stirring to ensure homogenization of the system. At certain time intervals, over 48 h of release studies, the samples were centrifuged at 7,000 rpm for 30 s and all the supernatant was collected and replaced with fresh medium. The collected medium was then centrifuged one more time to ensure the suspension was free of silica particles. 200 µl of this solution were removed and diluted with water to a total volume of 1 ml and used as such for HPLC analysis.

To compare the dissolution of free CsA to the CsA released after encapsulation into the mesoporous silica, a control study was additionally conducted by dissolving powdered CsA in both media, under the same experimental conditions. For this, 1.5 mg of CsA was placed in an Eppendorf tube which was then filled with 1.5 ml of intestinal or gastric fluid. The CsA was collected by centrifugation at a higher speed (14,000 rpm, 1 min) due to the low density of the bulk CsA powder. These samples were directly introduced into the HPLC without further dilution.

All samples were run in triplicate and the average value of these measurements was used to obtain the dissolution profiles. The SD error was estimated as described in Section A2.2, Appendix.

6.7.5 SEM and TEM imaging

SEM images of Lutrol and casein templated silicas were obtained by using a Company Quanta 200 F Field Emission Scanning Electron Microscope, with backscattered electron detection. These imaging experiments were conducted by Mr. Paulo Malheiro. The samples were gold plated and fixed into aluminium stubs before their placement on the microscope chamber. The TEM images of silica samples were obtained by using a Jeol JEM 2011 HRTEM Transmission Electron Microscope with a maximum accelerating voltage of 200 kV, and a GATAN CCD camera attached to it.

6.7.5 Particle size measurements

The particle size of silicas was measured by diffraction light scattering using a Malvern Mastersizer 2000 instrument. Three successive measurements were obtained for each sample and the average particle size is reported. The SD error in the average particle size value obtained was estimated as described in Section A2.2, Appendix.

6.7.6 Nitrogen sorption

Nitrogen sorption experiments were performed in a Micrometric Accelerated Surface Area and Porosimetry (ASAP) 2010 apparatus, 77.35 K. For this, 0.12-0.14 g of dry silica particles were degassed at 500 K for 2 h to remove any physisorbed species from the surface of the particles. The PSD of the mesopores was calculated from the adsorption curve by applying the BJH algorithm in the capillary condensation region assuming cylindrical pore type geometry. The PSD of the micropores was evaluated by the Horvath-Kawazoe (HK) algorithm for cylindrical pore geometry and their volume, V_p, was assessed by using t-plot analysis. Micropore surface area, S_L, was calculated from Langmuir equation.

6.7.7 NMR cryoporometry

NMR cryoporometry was used as an alternative method to measure the PSD of silicas. For this, ~20 mg of silica particles were placed within a plastic pipette tip which was then filled with water. The bottom and the top of the tip were sealed with Parafilm avoid water leakage and the tip was placed within an NMR tube (5 mm) between two susceptibility plugs. The system was left for ~2 d at room temperature, to allow water adsorption into the pores. A nonmagnetic thermocouple was used to measure the real temperature within the sample. The tube was then placed into the 400 MHz NMR machine and the sample was subjected to supercooling, pore melting and pore freezing to obtain the hysteris loop. The system was left to reach thermal equilibrium for 11 min at each temperature point and each spectrum was recorded with 4 scans. The PSD was calculated from the melting curve, using Gibbs-Thomson equation for cylindrical type meniscus geometry and k_{GT}=26 nmK.

6.7.8 PFG NMR

PFG diffusion NMR experiments were performed to determine the tortuosity, τ_p, of the silica particles following equation 6.10. The heptane molecules (or any other alkane) lack polar groups, hence there will only be weak dipole-dipole interactions with the silica surface and heptane diffusivity within the porous matrix is inherently dependant only on the pore connectivity. This means that it can provide a good estimation of the τ_p (D'Agostino et al., 2012). Also, heptane molecular size (diameter: 5.46 Å) (Doetsch et al., 1974) is similar to the molecular size of CsA assuming the protein retains a spherical geometry (diameter: 7.12 Å). This makes heptane an ideal candidate to further mimic protein restricted mobility facilitated by the low pore to molecular size ratio.

Initially, pure heptane was placed into a glass capillary tube with ~1.5 mm diameter and the top of the tube was sealed by heating it with a Bunsen burner to prevent any heptane evaporation during the time course of the experiment. The sample was then placed within a 5 mm NMR tube for PFG measurements. This experimental set up was also found as the most appropriate to eliminate convection effects arising from the

temperature difference along the NMR tube, to which PFG NMR is very sensitive. The diffusion experiments were carried out in a 400 MHz NMR, at 25°C. The diffusion time (Δ) was 0.1 s, the diffusion length (δ) was 1.5 ms and the relaxation delay time was 15 s (~5xT_1). For each diffusion experiment, 8 data points were taken at increasing gradient strengths between 0.674-33.143 G/cm, and each data point was obtained with 16 scans.

The silica samples were first dried in the furnace at 500 K for 2 h to ensure complete removal of any water molecules physisorbed on the silicas. Then, ~10 mg of silicas were placed in the capillary tube and the sample was filled with an excess amount of heptane. Similarly to the bulk heptane sample, the top of the tube was sealed and it was then left to equilibrate at room temperature for 1-8 d. The PFG experiments were performed every ~24 h to ensure that complete saturation of the sample was achieved. An average diffusivity value between the saturated samples was taken for the calculation of the root mean square displacement (r_{rms}) expressed by the Einstein equation:

$$r_{rms} = \sqrt{6D_{PFG}}\Delta \tag{6.16}$$

This is done to determine the distance the heptane molecules diffuse within the porous matrix. The bulk diffusion coefficient, D_b, was estimated via the monoexponential expression:

$$I = I_0 \exp(D_b \xi) \tag{6.17}$$

The diffusion coefficient in the pores, D_{PFG}, were calculated by fitting the data into the biexponential expression

$$I = I_0[x\exp(D_b\xi) + (1-x)\exp(D_{PFG}\xi) \tag{6.18}$$

where I_0 is the signal intensity with no field gradient applied γ is the gyromagnetic ratio, g is the field gradient strength, Δ is the diffusion time, τ is the correlation time between bipolar gradients, x is the fraction of bulk heptane and $\xi=\gamma^2\delta^2g^2(\Delta-\delta/3-\tau/2)$. This was due

to the presence of excess bulk heptane around the particles contributing onto the overall diffusivity of the liquid phase. The calculated D_b was used as a fixed value in the biexponential model to describe the diffusivity in the excess (bulk) heptane. The error in the diffusivity and tortuosity values were found as described in Section A2.1.

6.7.9 Small Angle X-ray scattering (SAXS)

Small Angle X-ray scattering measurements were performed to obtain information about the mesostructure of the silicas. A thin film of dry silica particles was placed between two pieces of sellotape®, held together by the two copper plates of the sample holder. The background arising from the sellotape® was then measured by exposing solely the sellotape® in the X-rays for the same amount of time as the silica samples, and it was subsequently subtracted from the scattering profile of the silica samples The experiments were conducted in an Anton Paar SAXSess small and wide angle X-ray scattering instrument with a measurable q range of 0.077 – 27.0 1/nm. A Pin-hole X-ray source operated at 40 kV and 50 mA was used. Collimation is achieved using a block collimator with 0.14 μm/cm flatness, where the X-ray flight path from the source to the detector is maintained in a chamber evacuated to below 5 mbar. The scattered profile is collected into a reusable image plate with 42.3 μm^2 pixels which is then read into cyclone reader via Optiquant software, and processed in a SAXSquant 1.01 program. A theoretical background on SAXS technique is provided in the Appendix, Section A4.1.

6.8 Results

6.8.1 Particle size and morphology of silica materials

Silica particles obtained using Lutrol and casein templating agents had different size, morphology and porous structure. Figure 6.3d shows that casein templated silicas had a bimodal particle size distribution with two distinct modal sizes at ~15 μm and 660 μm. For modelling purposes though, the average particle size will be used (653± 9 μm) from

the DLS measurements assuming monomodal distribution/fit. The external surface is very rough and consists of small silica clusters of ~300 nm, each of them exhibiting a disordered, highly microporous internal structure. Circular dichroism (CD) spectroscopy was further performed to study the secondary structure of casein and monitor its structural changes under the silica synthesis conditions. The results are presented in Figure A4.3, in the Appendix, and they show that casein structure changed from α-helix at pH 7 into a random coil at pH 2.

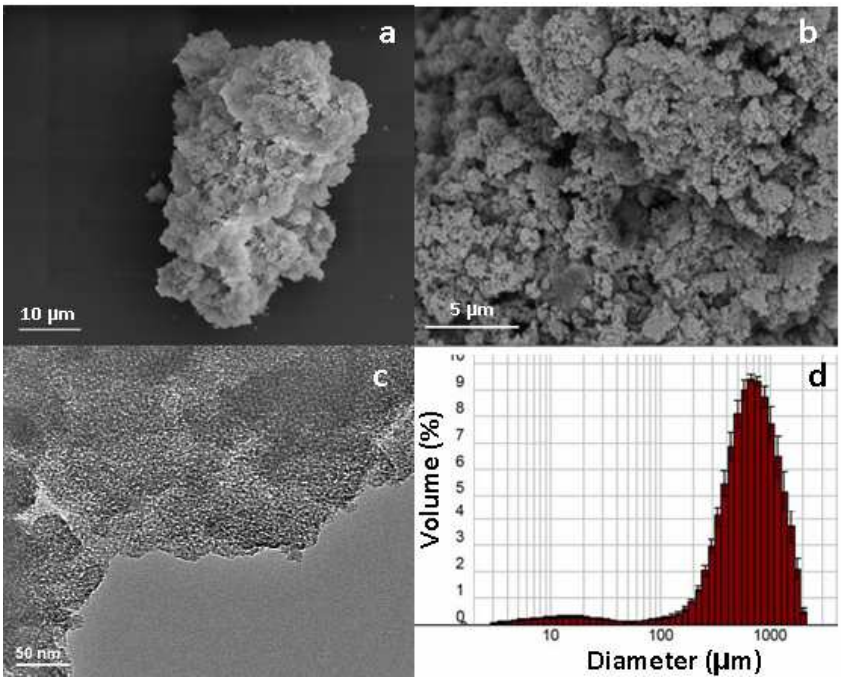

Figure 6.3 SEM (a, b) and TEM (c) images of a casein templated silica particle showing the particle morphology and its internal porous structure, respectively. The histogram (d) shows the particle size distribution obtained from DLS measurements (SD error bars: ±1% volume)

The Lutrol templated silicas had a monomodal particle size distribution (Figure 6.4c) with a mean value of 75±9 µm. These particles had a smoother external surface and a more ordered microporous structure (Figures 6.4a and 6.4b) compared to the casein templated ones.

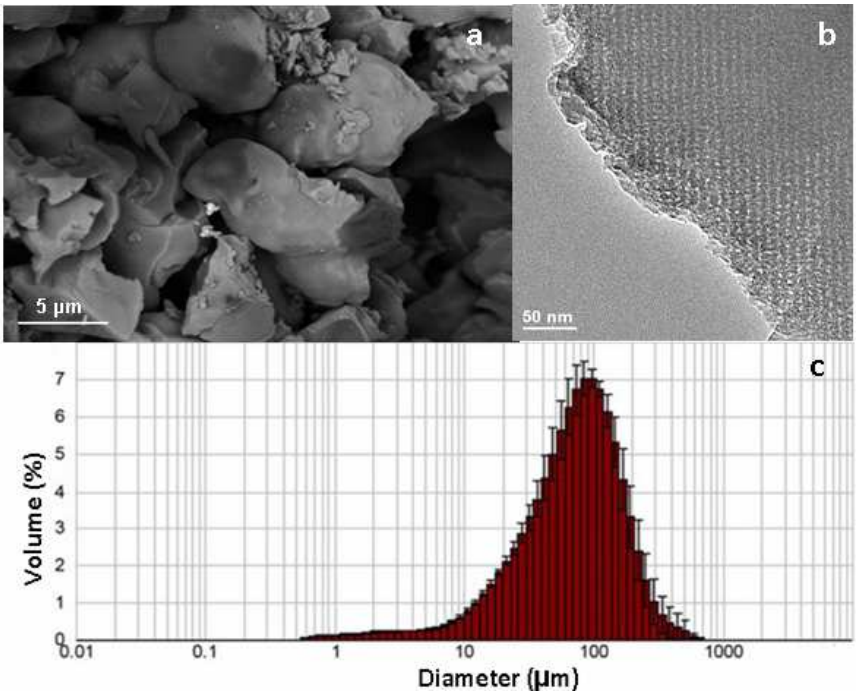

Figure 6.4 SEM (a) and TEM (b) images of a Lutrol templated silica particles showing the particle morphology and its internal porous structure, respectively. The histogram (c) shows the particle size distribution obtained by DLS (SD error bars: ±1% volume)

The chemical composition of both types of silicas was characterized by FTIR and are shown in Figures A4.4 and A4.5, in the Appendix. The results are representative of the formation of amorphous Lutrol and casein templated silica particles. Both types of silicas contain approximately the same amount of silicon oxide, with a conversion efficiency of 96 % of the initial sodium silicate solution used.

6.8.2 Nitrogen sorption and NMR cryoporometry studies

Nitrogen sorption isotherms for casein and Lutrol templated silicas, Figure 6.5, show nearly reversible adsorption/desorption curves. Both materials have a high gas uptake in the micropore region (P/P_0 <0.01), corresponding to ~2/3 of the total pore volume of the particles. The volume uptake increases slightly in the multilayer adsorption region and capillary condensation only occurs between P/P_0 =0.35-0.51. These indicate that both materials are highly microporous and exhibit only a low mesoporosity.

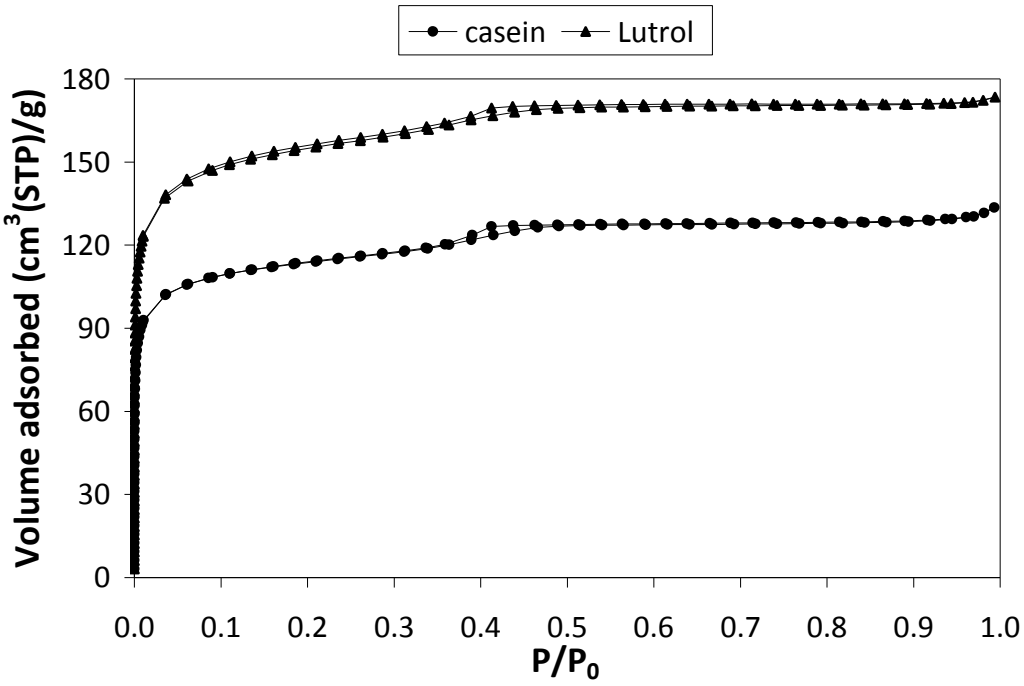

Figure 6.5 Nitrogen adsorption isotherms for casein and Lutrol templated silicas

The micropore size distribution extends over the range of 0.86-2 nm for both materials, but casein templated silicas have a rather more ordered microporous structure than the Lutrol ones, exhibiting a mean size of ~0.94 nm, as shown from Figure 6.6a. Similarly to this, casein templated silicas show a slightly narrower mesopore size distribution, with a mean PSD of 2.93 nm compared to 2.75 nm for the Lutrol, Figure 6.6b.

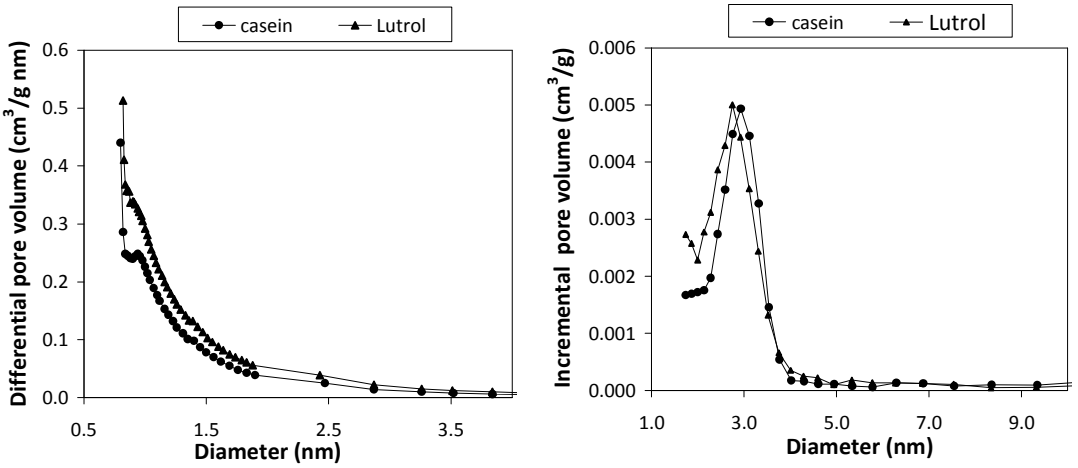

Figure 6.6 a) Micropore and b) mesopore size distribution of casein and Lutrol templated silicas calculated from HK and BJH algorithms, respectively

When casein was used as a templating agent, the silica particles had a lower total pore volume, V_0, micropore volume, Vp, and a lower Langmuir surface area S_L compared to Lutrol templated silicas as shown from Table 6.1.

Template	Micropore volume, V_p (cm^3/g)	Langmuir surface area, S_L (m^2/g)	Mean size of mesopores d (nm)	Total pore volume, V_0 (cm^3/g)	Porosity, ε
Casein	0.13	488.88	2.93	0.21	0.31
Lutrol	0.18	518.33	2.75	0.27	0.37

Table 6.1 Porosity and surface area measurements of casein and Lutrol templated silicas

Figure 6.7 represents the freeze/thaw curves of water imbibed in Lutrol and casein templated silicas. It is obvious that ice within the pores of Lutrol templated silicas melts over a wider temperature range compared to the casein templated ones. This indicates that Lutrol silicas contain a wider pore size distribution than casein templated ones, extending over a diameter size of 0.6-1.2 nm (inset in Figure 6.7). However, the PSD estimated by cryoporometry, for both types of silicas, is narrower compared to the one obtained from nitrogen adsorption (Figure 6.6). This is because cryoporometry NMR is an indirect pore size characterization technique, since, the calculation of absolute pore sizes, requires a calibration of the k_{GT} parameter against pore size measures from another technique. Also, it was shown in Chapter 3 that cryoporometry suffers advanced melting phenomena, which are more severe than the advanced adsorption effects in nitrogen sorption studies, therefore it is likely that the PSD derived by this method to be underestimated.

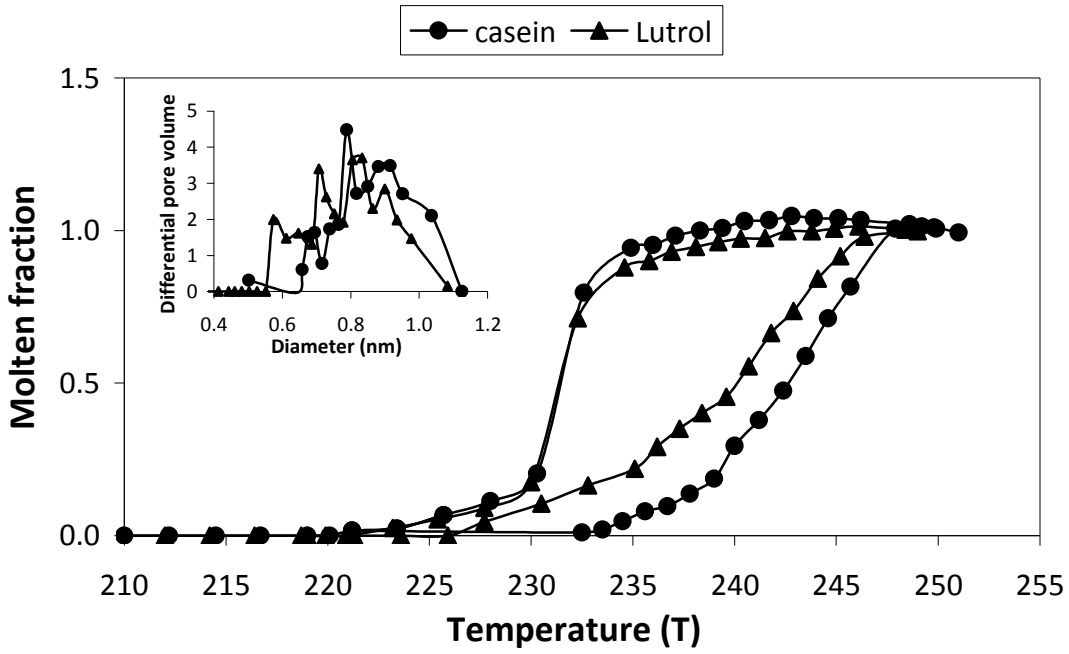

Figure 6.7 Cryoporometry hysteresis loops obtained from freeze-thawing of water imbibed in the casein and Lutrol templated silicas. Molten fraction of 1 corresponds to the total pore volume. The inset shows the pore size distribution, as a change of the molten fraction with the pore diameter, where the diameter is calculated via the Gibbs-Thomson equation from the boundary melting curves of the silicas

6.8.3 PFG NMR

As presented in Table 6.2, the two silicas exhibit different tortuosities and the heptane molecules are able to diffuse at different length-scales at the same time. In particular, casein templated silicas have a smaller (average) tortuosity compared to Lutrol silicas, indicating better pore connectivity. The rms displacement within casein silica particles is longer than the Lutrol ones, suggesting that heptane molecules encounter less restrictions allowing them to diffuse up to ~93.36 μm. As the rms displacement values for both silicas exceed their pore size (0.5-2.94 nm), this would mean that the molecules are free to diffuse along the pore channels at all possible directions. However, heptane molecular motion in casein silicas is restricted to an (average) distance shorter than the silica particle size (650 μm) itself indicating that species present at the centre of the particles will not be able to reach the edges of the particles. On the contrary, the molecules within the Lutrol templated silicas can cross over onto a length-scale

comparable to the silica particle size (~75 μm) and as such diffuse more easily into the bulk. These results show a more heterogeneous porous structure in the casein silicas, where the casein particle could potentially comprise of similar sized clusters (ie of a 93.36 μm diameter) of well connected pores, but the channels connecting these clusters are more complex, prohibiting the free diffusivity of the molecules through the whole particle. On the contrary pores within Lutrol particles have an evenly distributed complexity which is averagely higher than casein.

Heptane	D_{PFG} (x10^9) ±error (m^2/s)	Tortuosity,τ_p ±error	rms displacement, r_{rms} ±error (μm)
Bulk	3.18 ± 0.04	–	–
Casein	1.46 ± 0.19	2.22 ± 0.30	93.36 ± 8.83
Lutrol	0.71 ± 0.15	4.48 ± 0.94	65.36 ± 9.63

Table 6.2 Tortuosities and rms displacement values of heptane within casein and Lutrol templated silicas for Δ=0.1 s and δ=0.0015 s. The error is found as described in Section A2.1, in the Appendix

6.8.4 Small angle X-ray scattering (SAXS)

The SAXS results seen from Figure 6.7, show that both casein and Lutrol templated silicas have a distinct diffraction peak at 0.636 and 0.649 1/nm and a broad peak with a mean at ~1.105 and 1.092 1/nm, respectively.

These peaks are close to having the relationship 1:√3 (particularly for the casein templated silica) suggesting that the structures could be composed of hexagonally close packed micelles. However, it is not excluded the case of having broad diffraction peaks consisting of several merged peaks of a polydisperse cubic-like (although their relationship is not closer to 1:√2). Also, it should be mentioned that it is quite surprising that such a high mesostructure order is observed for casein silicas as compared to the more unordered form depicted in the TEM images (Figure 6.3c).

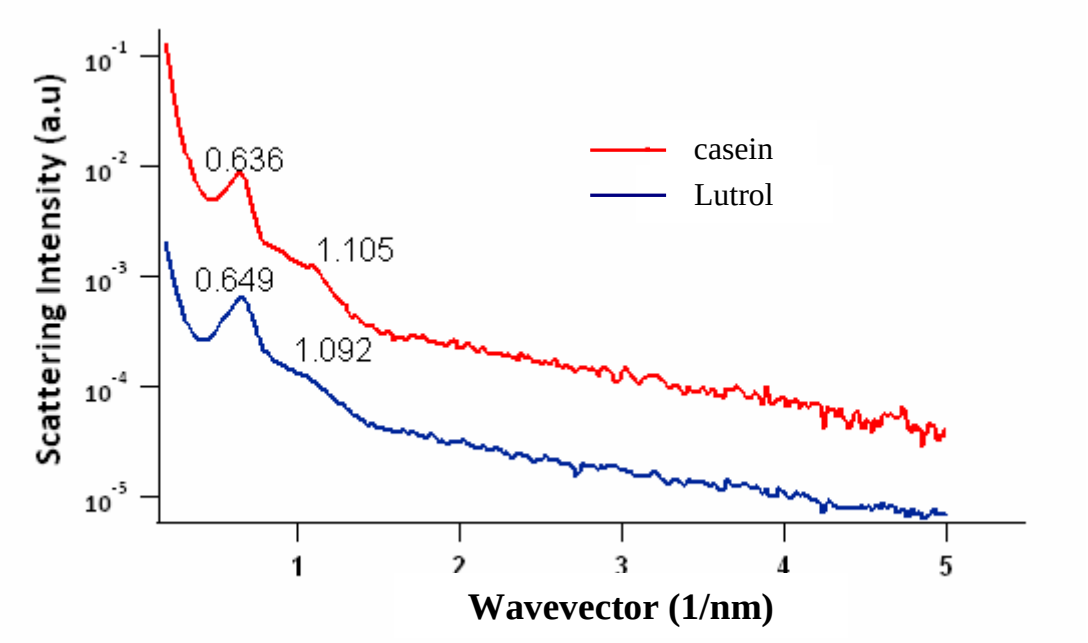

Figure 6.8 Diffraction peaks of the casein and Lutrol templated silica powders. Casein scattering intensity has been shifted on the y-axis by a multiple of 12. The values displayed on the graph, show the mean q value of each diffraction peak

Usually silica particles synthesized from Lutrol template under acidic conditions have a cubic structure, similar to SBA16 (*Im3m*). However, a slight modification of the experimental synthesis conditions, such as the silica source, pH, aging temperature and time or, the polydispersity in the MW of the polymer can inherently lead to a different structural organisation of the porous material. Sodium casein comprises of a mixture of α-, β- and κ- casein proteins, and each of them contains a different amount of hydrophilic and hydrophobic groups. The charge distribution along the chain differs hence in the presence of acidic conditions the ionisable groups will cause different protein conformations, characteristic of each protein. Therefore, the structure of casein templated silicas is expected to be more disordered compared to Lutrol, as the proteins are likely to form micelles with different shapes and sizes.

The interplanar d-spacing of the casein and Lutrol templated silicas is 9.87 nm and 9.68 nm, respectively calculated from the first diffraction peak via Bragg's law for cubic structure (Equation A4.3, Appendix). Taking into account that the size of the mesopores is 2.93 and 2.75 nm (Table 6.1) then, the wall thickness of the silicas is 6.94 and 6.93 nm for casein and Lutrol silicas, respectively. However, if we assume 2D-hexagonal phases,

d-spacing is 11.40 nm and 11.17 nm for casein and Lutrol silicas, respectively, with wall thicknesses, 8.47 nm and 8.42 nm. Similar wall thickness would mean similar mechanical properties for both silicas. TEM images though (Figures 6.3c and 6.4b) reflect a wall thickness of ~2.5 nm for casein and ~3.9 nm for Lutrol silicas. Overall, the real structure of both silicas is ambiguous and their mesostructure can be either 2D-hexaganal or cubic.

6.8.5 CsA loading and *in-vitro* drug release studies

CsA mean loading efficiency in the Lutrol and casein templated silicas was 54±7% and 61±5%, respectively, as measured by HPLC analysis. It would be expected that CsA loading will occur in a multilayer form in an amorphous structure. As ethanol evaporates, some particle regions will be saturated with CsA and deposition may occur through crystallization. Therefore it is possible that CsA exists in different forms, likely to affect the drug release rate. Moreover, CsA may adopt different conformations within the silicas, due to its particular H-bonding pattern and the large size of the molecule as compared to the pore size of the silicas. FTIR spectra may detect those conformations, thus FTIR measurements were performed for the drug loaded Lutrol templated silicas. However, the contributions from the silica in the IR region were higher than the contribution from the CsA, so further analysis was not possible.

The conformation of the purchased CsA (in powder form) was compared to the loaded CsA being recovered and re-crystallized after sonication of Lutrol particles in ethanol. It was found that encapsulation of CsA in these particles did not degrade the peptide structure. The results are presented and further discussed in Section A4.4, Appendix. Drug dissolution studies were performed in simulated intestinal and gastric fluid. The dissolution of free CsA is compared to the encapsulated CsA in Lutrol and casein templated silicas. The results are shown in Figures 6.9 and 6.10. It is shown that drug solubility in the IF is slower and overall lower than in GF for the 3 types of formulations. Furthermore, a burst drug release occurs from the silicas within the first 2 h of dispersion in the GF, but a more gradual one is facilitated in the IF. It is also observed that encapsulation of CsA in the silicas increased its solubility by ~5 times in the IF and ~1.5-2

times in the GF, against the free drug in each respective dispersion medium. In addition to this, CsA loaded in Lutrol silicas had a high release over the first 3 h which becomes more steady at later times. On the contrary, CsA in the casein silicas followed a gradual release over the whole period of time. The total drug released from all the formulations in IF is likely to be increased over 28% at longer experimental times, judging by the trend of the dissolution profiles in Figure 6.9. CsA dissolution profiles in GF, Figure 6.10, show that both free and CsA loaded in Lutrol silicas, exhibit a high burst release within 1 h, which remains constant afterwards. On the contrary, only 35 % of the loaded CsA in the casein silicas is released within 3 h and its amount alters gradually over higher time intervals.

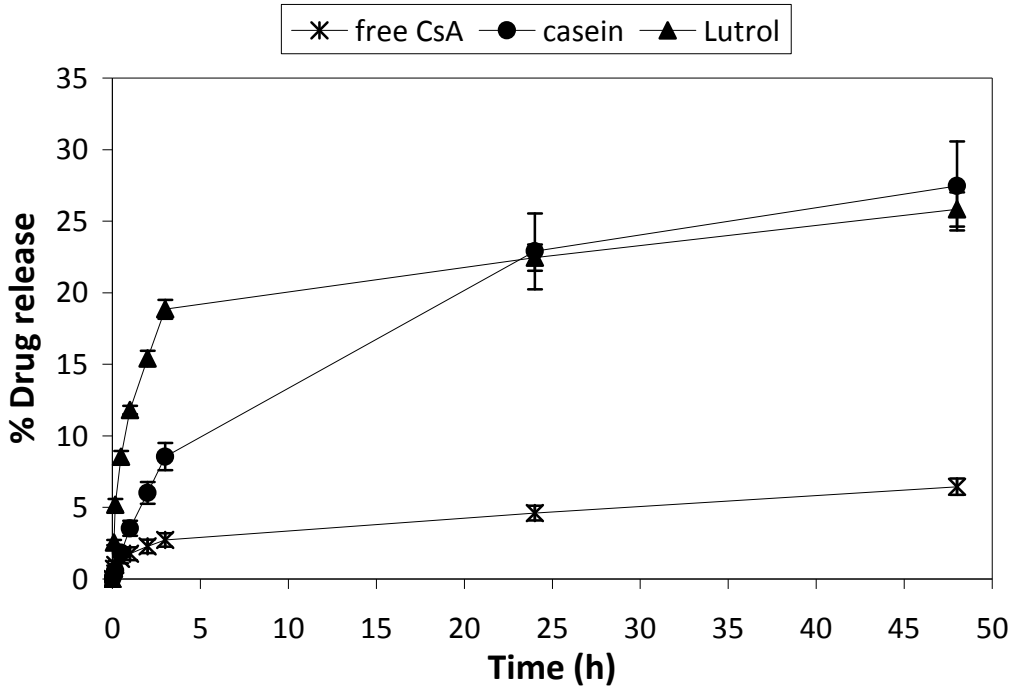

Figure 6.9 Drug release profile of CsA from casein and Lutrol templated silicas in simulated intestinal fluid. Solubility of the encapsulated CsA is compared with that of the free CsA. Error bars show the SD error for release studies performed in triplicate

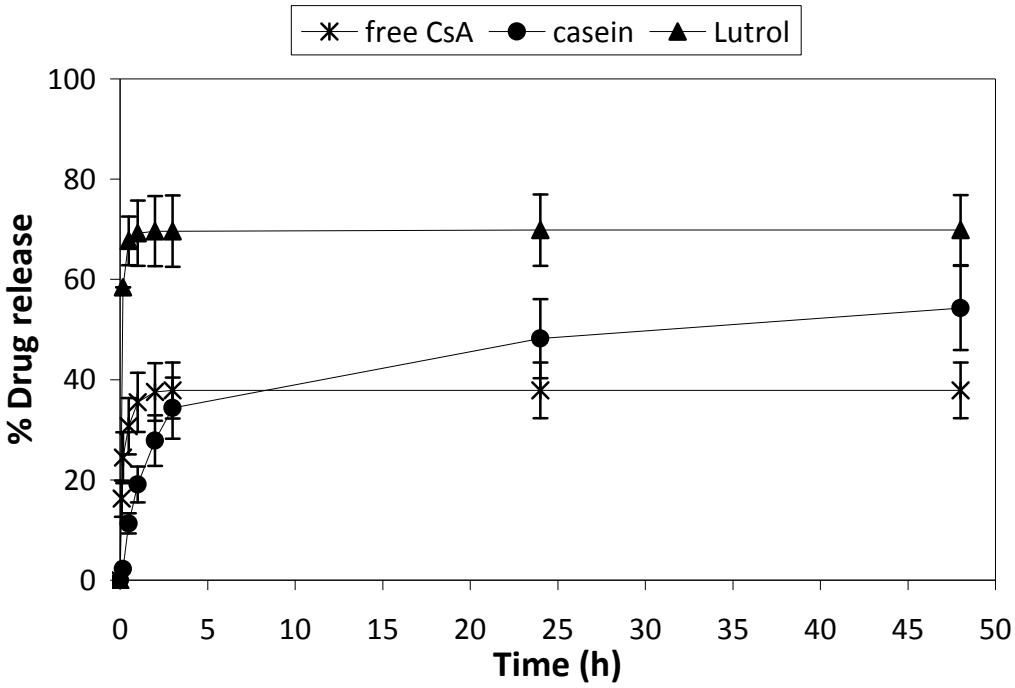

Figure 6.10 Drug release profile of CsA from casein and Lutrol templated silicas in gastric fluid. Solubility of the encapsulated CsA is compared with that of the free CsA. Error bars show the SD error for release studies performed in triplicate

6.8.6 Drug release models fitted into the CsA release profiles

Drug release models predicted by Higuchi (equation 6.2), Model 2 (equation 6.5), LDF (equation 6.6), and Weibull (equation 6.7) are presented in Figures 6.10-6.13. CsA release profiles from Lutrol and casein templated silicas in intestinal and gastric fluids are best described by the LDF and Weibull models. Higuchi and Model 2, derived by assuming a planar system and for drug release up to ~0.4 relative fraction (although sometimes it is accurate for higher fractions as well), respectively, fail to predict the CsA release from the systems studied.

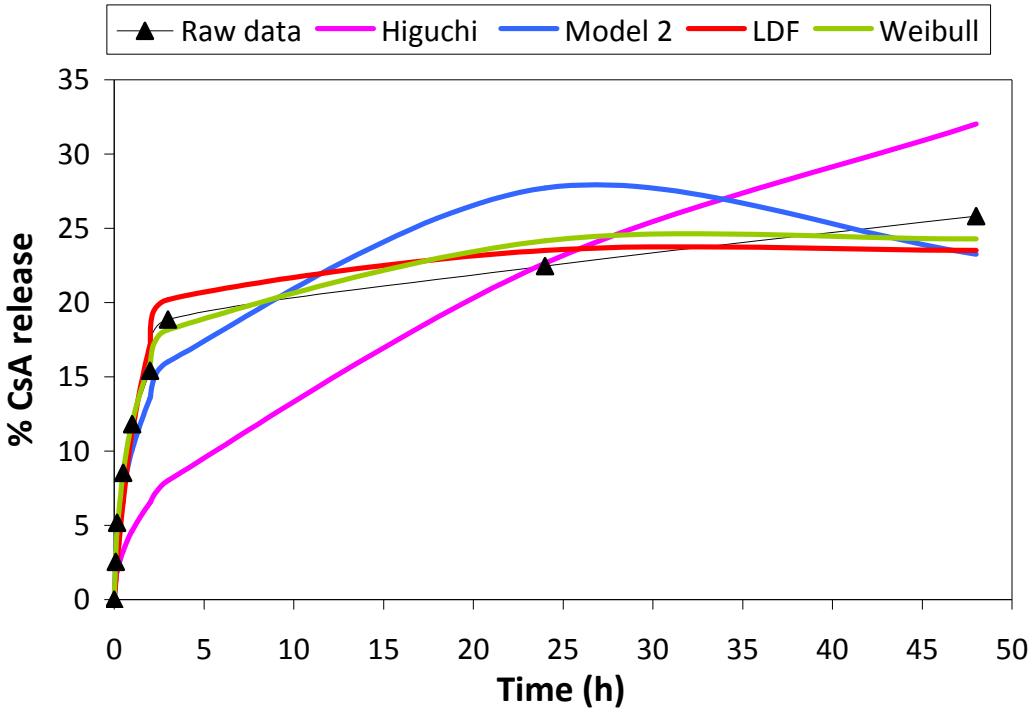

Figure 6.11 Drug release profile models fitted into the raw data of CsA released from Lutrol templated silicas in intestinal fluid using Higuchi (equation 6.2), Model 2 (equation 6.5), LDF (equation 6.6), and Weibull (equation 6.7) models

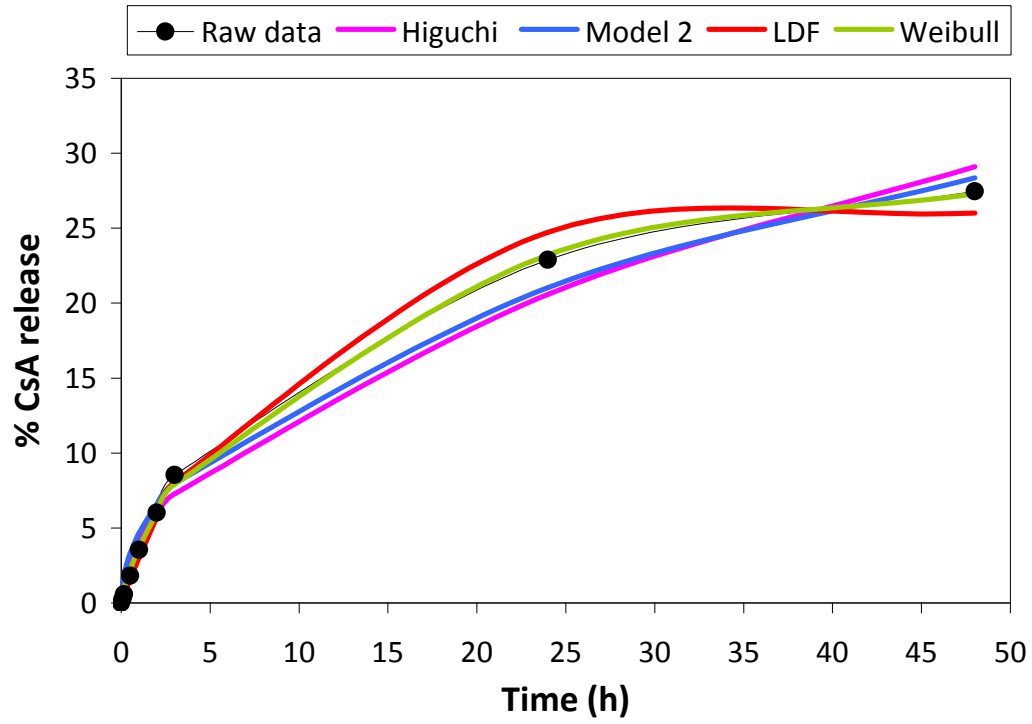

Figure 6.12 Drug release profile models fitted into the raw data of CsA released from casein templated silicas in intestinal fluid, using Higuchi (equation 6.2), Model 2 (equation 6.5), LDF (equation 6.6), and Weibull (equation 6.7) models

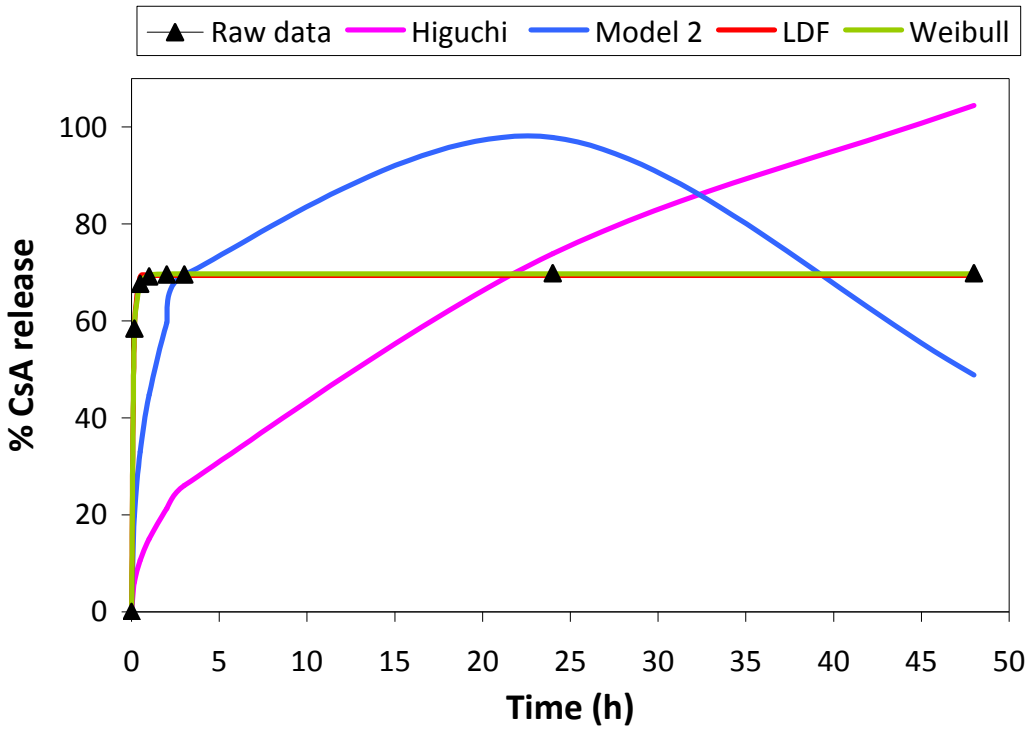

Figure 6.13 Drug release profile models fitted to the raw data of CsA released from Lutrol templated silicas in gastric fluid, using Higuchi (equation 6.2), Model 2 (equation 6.5), LDF (equation 6.6), and Weibull (equation 6.7) models

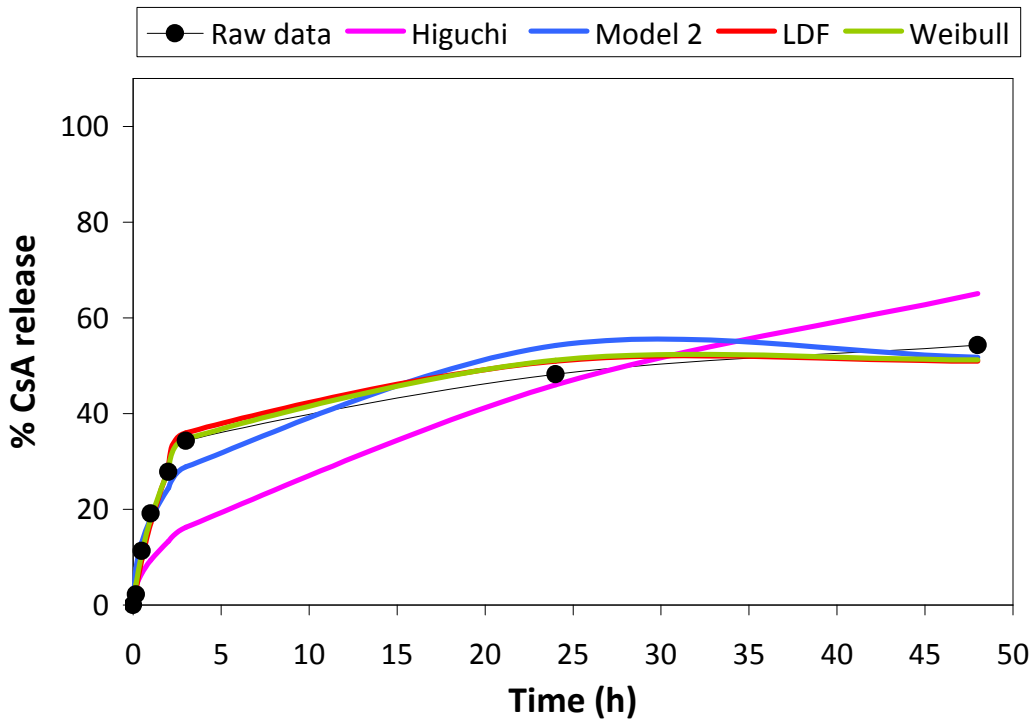

Figure 6.14 Drug release profile models fitted to the raw data of CsA released from casein templated silicas in gastric fluid, using Higuchi (equation 6.2), Model 2 (equation 6.5), LDF (equation 6.6), and Weibull (equation 6.7) models

In Table 6.3 are presented only the time constants predicted from the LDF and Weibull models, as these models were found to best fit into the CsA release profiles observed with respect to the fitting error. It is seen that the *b* constant lies between 0.6-0.65 for Lutrol silicas and 0.77-0.87 for caseins. This indicates that diffusion in Lutrol silicas may follow that in a fractal or disordered space, whereas drug release from caseins is driven by a normal Euclidiean diffusion disturbed by contributory release mechanisms.

	LDF	**Weibull**	
Sample/ Release medium	**Time constant, k_2 (1/min)**	**Time constant, k_3 (1/min)**	**b**
Lutrol/IF	0.011±0.002	0.048±0.014	0.65±0.07
Casein/ IF	0.002±0.0002	0.006±0.001	0.77±0.03
Ratio/IF	5.30	8.39	
Lutrol/GF	0.184±0.006	0.459±0.018	0.60±0.02
Casein/ GF	0.0067±0.0006	0.012±0.006	0.87±0.11
Ratio/GF	27.02	**38.19**	

Table 6.3 Parameters predicted by LDF (k_2) and Weibull (k_3, *b*) models. The number in bold is to show that its value is quasi-similar to the one predicted from Model III, Table 6.4

The time constants, *k*, calculated from Models I-IV are presented in Table 6.4 to account for the particle porosity, hindrance, particle size and tortuosity of the particles. However, Models I-IV do not take into consideration the release medium characteristics, thus only one value for each templated silica is estimated. The ratio between the time constant of Lutrol and casein templated silicas for each release medium, found from LDF and Weibull fitting curves, can be compared to the ratio of the time constants between the silicas, calculated from Models I-IV. From Tables 6.3 and 6.4, it is observed that only CsA release into the gastric fluid, predicted from the empirical Weibull equation (*k*=38.19 1/min) can be described by Model III (*k*=35.26 1/min). This shows that the faster drug release rate from Lutrol silicas compared to the casein ones in GF, is affected by their different pore connectivity, pore size, particle porosity and particle size in a relationship proposed by Mace and Wei (equations 6.10, 6.12 and 6.13). Drug release in intestinal fluid must be influenced by additional parameters, or a different relationship of the aforementioned ones. For instance IF alkalinity increases the solubility of silica particles themselves as opposed to the GF acidity, implying that drug release in IF was

essentially controlled by the silicas dissolution rates rather than their pore characteristics. Moreover, the dissolution rate of the Lutrol silica particles is possibly faster than the casein silica particles, due to the smaller size of the Lutrol particles, although their pore walls are thicker (3.9 nm) than the casein pore walls (2.5 nm) as seen from the TEM images, Figures 6.3 and 6.4.

	Model I	**Model II**	**Model III**	**Model IV**
Sample	***k*** **(1/min)**	***k*** **(1/min)**	***k*** **(1/min)**	***k*** **(1/min)**
Lutrol	58.58	2.34	0.93	0.67
Casein	0.64	0.03	1.97	0.02
Ratio	91.17	79.17	**35.26**	34.66

Table 6.4 Time constants for Lutrol and casein templated silicas, calculated from $k=15D_{intra}/r^2$, where D_{intra} was estimated from equations 6.9 and 6.11 (Model I), equations 6.11, 6.12 and 6.14 (Model II), equations 6.10, 6.12 and 6.13 (Model III), equations 6.10, 6.12 and 6.15 (Model IV). The number in bold is to show that its value is quasi-similar to the one found from the fit of Weibull model into the GF release profiles, Table 6.3

6.9 Discussion

In this work, amphiphilic sodium casein was successfully used as a templating agent for the synthesis of porous silicas particles under acidic conditions with 96 % silicon conversion into particles (Section A4.4, Appendix). The CD measurements (Section A4.3, Appendix) showed that casein peptides obtained a random coil conformation at pH 2 and 2.5 similarly to the results observed by other authors (Chakraborty and Basak, 2007; Portnaya et al., 2008). As the total concentration of the casein used for the synthesis (26 mg/ml) is higher than its CMC (1 mg/ml), casein must have self assembled initially into micelles (~120 nm) composed by α-, β- and κ-caseins submicelles (or nanoclusters), even in the absence of interactions with calcium phosphate (Liu and Guo, 2008) at pH 2-2.5. Gas sorption (Figure 6.6, Table 6.2), cryoporometry (Table 6.2) and TEM (Figures 6.3c and 6.4b) characterization techniques show that casein templated silicas are highly microporous with a low mesopore volume. These findings suggest silica

precursor penetrated within the micelles through the void spaces, and condensed over the submicelles (or nanoclusters) forming the pore walls. This further implies that electrostatic interactions between the silica and α-, β- and κ-caseins dominated over the hydrophobic and H-bonding interactions between the casein submicelles, responsible for the integrity of the larger micelle.

As previously reported, β-caseins obtain a flat disk-like structure, α_{s1}-caseins are arranged into a wormlike or spherical structure, and a_{s2}- and κ- caseins into a spherical or ellipsoidal shaped submicelles, with sizes of ~7-25 nm. The size of these submicelles again extends over the pore size obtained from gas sorption and cryoporometry experiments. This implies that casein micelles consisted of nanoclusters with denser regions of peptide mini-clusters, as proposed by de Kruif rather than submicelles proposed by Hansen *et al*. After calcination the nanoclusters formed the small mesopores (~2.9 nm) and the mini-clusters along with the κ-casein hairy layer, formed the micropores. Although calcium phosphate is dissolved under acidic conditions, hydrophobic interactions between the caseins must have kept unchanged the 3D architectural morphology of these clusters. This templating model can explain the disordered porous structure and the roughness of the external surface of casein templated silica particles.

Lutrol templated silicas have a smaller particle size (75 μm) and a smoother external surface than casein silicas (650 μm), shown by Figures 6.3 and 6.4. The different macroscopic structure is not only affected by the properties of each amphilphilic template but it is also due the variation in the temperature, pH, counterions and agitation speed used for each synthesis. Elevation of synthesis temperature at pH>7, increases silica solubility and inherently silica growth, by dissolution of many small particles and their deposition into larger ones (Brinker, 1990). Kosuge *et al*., observed that increasing the temperature under acidic conditions, the shape of the particles change from aggregated (298 K) to fiber-like (303 K) whereas by increasing the stirring rate silicas shape changes from monodisperse rod-like to fiber-like with a bigger size (Kosuge et al., 2004b). Moreover, it seems that amphiphilic Lutrol decreases the surface tension on the growing particles more than casein, and as such Lutrol is able to stabilize

the particles at a smaller size. Moreover, Teixeira *et al.* (2011) found that (under the same templating conditions) the higher the polarizability of the counterions, the smaller and better-defined particles are formed. Thus [Cl^-] counterions are expected to give smaller silica particles as compared to [CH_3COO^-].

The mesostructure of silicas is mainly influenced by the templating agent. Pluronics such as Lutrol (F127) within acid media usually favour the formation of cubic structures such as SBA-16 (*Im3m*), SBA-11 (*Pm3m*) (Zhao et al., 1998a) as opposed to caseins whose micellar structure is disordered. TEM images (Figures 6.3c and 6.4b) show that Lutrol silicas can have either a cubic or a 2D-hexagonal structure whereas a wormlike structure is seen for the casein ones. Their SAXS patterns though (Figure 6.8), are characteristic of materials with poor long range order, with Lutrol silicas showing a slightly higher disorder than casein ones, judging by their wider diffraction peaks. This is in accordance to the XRD results found by Kosuge *et al*. showing a disordered structure for F127 templated silicas in HNO_3 media. Gas sorption studies showed a wider mesopore and micropore size distribution for Lutrol silicas (assuming cylindrical pores) (Figure 6.6b). The contradicting results in the pores arrangement can be explained by a model where the pores of Lutrol particles have many interconnections or wall regions with lower silica density as is commonly seen in pluronic templated silicas due to the EO groups penetrating into the walls during synthesis, thus mimicking disordered phases (Reichhardt et al., 2011). Moreover, counterions have other effects as well. [Cl^-] anions cause dehydration of the PEO groups of Lutrol by an osmotic effect depleting the concentration of water in the corona on these sites, hence increasing their hydrophobicity (Kabalnov et al., 1995; Teixeira et al., 2011). This facilitates an increase in the aggregation number of the polymer chains forming the micelles, causing the EO groups to collapse into the core or just collapse together, and subsequently increases the pore size in the silica walls and decreases the mesostructure order. Therefore, the mesostructure of the materials under study, was not solely dependent on the amphiphilicity of the templating agent used but on the pH and counterions present in each synthesis as well.

As shown by SAXS, the wall thickness of both materials was similar (6.94 nm), implying that casein silicas can exhibit similar thermal and mechanic properties to Lutrol block

copolymer. The N_2 sorption studies show that micropores occupy ~67 and 63 % of the void space of Lutrol and casein silicas, respectively, and the remaining ones are mesopores (Table 6.1). PFG NMR shows a higher tortuosity for Lutrol silicas (4.46) compared to the casein ones (2.28). This is consistent with Kosuge *et al*. studies who found that block copolymers with PPO groups having a MW>3000 g/mol, lead to formation of highly tortuous particles comprising of both meso- and micropores. Therefore it must be the case that mesopores in the Lutrol silicas are arranged into most probably a cubic phase with a high amount of interconnecting micropores, as discussed earlier, however a 2D-hexagonal structure is suggested by SAXS results, thus further investigation with TEM images obtained at different directions to the micelle lattice are necessary to disambiguate the real structure of these Lutrol-templated silicas. The mesopores are formed from the hydrophobic PPO groups and the micropores from the PEO chains of the polymer, extending through the silica walls. In the casein silicas a model of casein arrangement into clusters was proposed above; the micropores are formed from the mini-clusters and the hairy layer of the κ-caseins, and the mesopores from clusters formed by association of α- and β-caseins. As κ-caseins form only ~8 % of the sodium casein, then 55 % of the micropores must have been formed by the crosslinking of some hydrophilic parts of α- and β-caseins, facing out the clusters. Of course it is not excluded the case where some of the α- and β-casein clusters shrunk during silica condensation, forming some additional micropores. It should be though pointed out that the mean pore size of both materials, found from nitrogen adsorption is higher than that calculated from cryoporometry melting curve, assuming cylindrical pores in both techniques. This is indicative of the error induced in the PSD from inaccurate assumptions on Kelvin and Gibbs-Thomson equations as previously discussed in Chapters 3 and 4, and it is further likely to affect equations 6.13-6.15, applied in the CsA release models.

Encapsulation of highly hydrophobic CsA into the casein and Lutrol templated silicas increased drug solubility by 4-4.5 times in the simulated intestinal fluid, and 1.5-2 times in gastric fluid, as compared to the free drug (Figures 6.9 and 6.10), showing great potential as drug delivery carriers. As CsA is pH insensitive, it must be the presence of SDS surfactant in the GF that increases CsA solubility. In fact, SDS concentration in GF

(8.7 mM) exceeds its CMC in acidic environment (<8.2 mM), therefore it exists in a micellar form and as such promotes CsA solubility in this media by drug incorporation into the micelle core. This is further justified by the fact that solubility of the free drug in GF is ~6 times higher than that in IF. The SDS micelles formed in the presence of salts obtain an elongated disk-like or a tablet-like shape, where the width and the length reach up to 2.4 and 4.6 nm, respectively (Bergstrom and Pedersen, 1999). This mean that some of the micelles can diffuse through the biggest mesopores (4 nm), if the latter are placed on the surface of the particles, and facilitate CsA solubility within the particles as well. Moreover, any non-micellar SDS can enhance drug solubility by adhering their hydrophobic tail group onto the CsA peptide and enhance peptide solubility.

CsA release from casein silicas has a gradual, controlled release as compared to the faster one induced by Lutrol silicas at the early stages of release, in both media. This is either due to the bigger particle size of casein silicas, hence there is a longer distance for CsA to diffuse, or due to the pore structure characteristics. Forsgren *et al.* (2010) found that Fentanyl release was faster from crushed pellets rather than the intact ones of the same batch. The authors attributed this to the larger external surface area of smaller particles exposed to the dissolution media. This is in agreement with CsA release from Lutrol silicas, whose particle size is ~10 times smaller than caseins, hence higher external surface area arising from all the particles.

The Higuchi model, most commonly used to describe drug release kinetics, did not fit to any of the release profiles obtained, and neither did Model 2. This implies that CsA peptides undergo a more complicated diffusion path than that experienced in a planar, or a spherical system for drug released fractions >0.4. A better fit was observed from application of Weibull and LDF equations, especially at the early release times (3 h). In particular, the *b* constant for Lutrol is <0.69 (Table 6.3), implying that CsA release from Lutrol is mediated by a highly disordered/fractal structure (Papadopoulou et al., 2006). In fact, these particles have many interconnections between the mesopores and micropores as seen from the TEM and SAXS patterns, along with the tortuosity value found independently via PFG NMR (Table 6.1). On the contrary, casein silicas consist of less micropores and mesopores and its tortuosity is half that of Lutrol, with *b*>0.75 from

the Weibull model. Hence, diffusivity in the casein silicas appears as a hindered form of diffusion in Euclidian mass. The ratio between the release constants of Lutrol and casein silicas in IF, calculated from Models I-IV (Table 6.4), deviated from those found from both LDF (5.3) and Weibull models (8.4). This implies that the true relashionship(s) between the tortuosity, porosity, particle size and molecular hindrance, which describe the CsA release, are other than those applied in Models I-IV, as it is likely that the different dissolution rate of each silica matrix in alkaline fluids influences the release of CsA too.

Similar behaviour is seen in GF for the LFD model. A better correlation though between these parameters and the release kinetics obtained from Weibull equation is found for CsA release in GF. Here, the difference in the CsA dissolution, enhanced by the two types of silica, is concomitantly controlled by the particle size, the molecular hindrance of the protein and the total pore volume in a relationship described by Model I (Spry and Sawyer, 1975; Mace and Wei, 1991). These models though assume that the shape of the protein molecules within the silicas is spherical and does not change during protein adsorption/release into/from the pores. However, proteins go through structural conformations dependant on the polarity of the solvent and the size of the pore channels. CsA exposes the H-bonded groups on the surface, in the presence of polar ethanol during drug loading, and aqueous media during drug release studies (el Tayar et al., 1993). Also, the peptide bond between the 9^{th} and 10^{th} aminioacids (Figure 6.2) is uncharged in water but has a large dipole moment and CsA can line up in certain secondary structures. This, in conjunction with the repulsive interactions between the hydrophilic silica and hydrophobic CsA, and the competitive adsorption between the drug and water molecules into the silica pore surface, enhances drug diffusivity out of the particles (Mellaerts et al., 2007). Its penetration through narrow pores, eventually causes stretching of the protein, and turns the CsA shape into a worm-like one which diffuses more easily. Monte Carlo simulations show that polymers passing through a series of connected chambers and pores (equivalently pores and necks), line up and diffuse fast during their translocation through small sized chambers, but they wrap up within big sized chambers (Saltzman and Muthukumar, 2009). Consequently the degree of CsA stretching into Lutrol silicas can possibly be higher than that in casein silicas if these pore sizes and connectivity conditions are satisfied.

Furthermore, there is a more rapid CsA release from Lutrol particles than casein particles within 3 h, in both the IF and GF. Apart from the particle size effect and the pores characteristics, this effect is further attributed to a higher concentration of CsA present in the shell and outer part of the Lutrol silicas as compared to that in casein particles. In the presence of micellar SDS in the GF, this effect is favoured as some drug is directly in contact with the micelles surrounding the particles in the dispersion medium, elevating drug solubility. Comparing the total dissolution of CsA in silicas, it is obvious from the graphs that drug solubility continues to increase after 48 h in IF. CsA though released from Lutrol silicas in GF, remains constant after 3 h. This means that a fraction of encapsulated CsA exists in a crystal form in supersaturated pore regions, unable to penetrate through the porous matrix, as compared to that entrapped in the casein silicas, but further investigation via XRD or DCS techniques is required.

6.10 Conclusion

In this study the potential of sodium casein as a templating agent for synthesis of porous silica materials, under acidic conditions was first investigated. It was found that although caseins have a random coil conformation at low pH, at concentrations above their CMC they are able to form clusters of different sizes driven by their amphiphilic nature. Attractive electrostatic and hydrophilic interactions between caseins and silica precursors led to the production of worm-like mesostructures, with high microporosity and surface area. Lutrol templated silicas, synthesized under the same conditions, showed a disordered cubic or 2D-hexagonal mesostructure with higher microporosity and worse overall interconnectivity than casein silicas. The yield of silica particles was high for both templating agents indicating that they can be scaled-up at a low cost.

CsA loading efficiency reached ~60% and 54% for casein and Lutrol silicas, respectively, without being denatured. Drug solubility in simulated intestinal and gastric fluids was improved, with Lutrol silicas achieving more rapid release in both media compared to casein silicas. Drug solubility in gastric fluid was higher for both the free and encapsulated drug as compared to that in intestinal fluid, but to different degrees for each system. It was also found that CsA release from porous silicas is driven by Fickian

diffusion, represented equally well from the LDF and Weibull models. Further investigations on the effect of the particle size and pores characteristics into the release kinetics showed that drug release is mainly controlled from the particle size but confinement effects (pore connectivity, PSD, mesostructural disorder), and silica dissolution and protein conformations in the different pH, should be taken into account.

Chapter 7
Synthesis and characterization of poly(lactic-*co*-glycolide) nanoparticles for convection-enhanced drug delivery into the brain

7.1 Introduction

In Chapter 6 gas sorption and NMR cryoporometry techniques were adopted to study the pore structure characteristics of two different templated silicas, with an aim to interpret their drug release kinetics into the environments present, and therefore their therapeutic activity. However, gas sorption technique requires thermal pretreatment of the sample at high temperatures, to ensure complete removal of any physisorbed species (i.e. water), before the actual experiment is performed. Hence the method is subject to inaccuraces for porous systems which exhibit low melting or glass transition temperatures, such as polymer particles, and therefore the samples are thermally pretreated close to room temperatures. Moreover, imaging techniques, such as TEM, do not provide sufficient information about the porous structure, due to the limited resolution of the technique in the nanoparticle scale. For this, NMR cryoporometry technique is proposed instead for pore size measurements, under the assumption that the polymer structure and morphology remain unchanged at low temperatures.

Poly(lactic-*co*-glycolic acid) (PLGA) is a biodegradable and biocompatible polymer, which can be easily functionalized to provide additional properties to the material. Due to these properties, it can be used for transportation and controlled release of therapeutic agents in the area of interest. However, the presence of biological barriers and the hydrophilicity of the target area do not permit the free passage of all the drugs and their wide distribution, thus more sophisticated drug delivery methods are required. Drug delivery into the brain is of particular interest, as the blood brain barrier (BBB) prevents the diffusion of hydrophilic molecules with a mass bigger than 500 Da, thus intravenous

injections are not efficient for the treatment of Alzheimer's disease or brain cancer. For this, convection-enhanced drug delivery (CED) into the brain was suggested, where the drug loaded vehicles are infused directly and continuously, under pressure using neurosurgically-placed microcatheters in order to enhance their distribution over a large tissue volume. However, successful CED into the brain can only be achieved if the size (radius) of the nanoparticles (NPs) is less than 100 nm, to ensure that the catheter will not block, and the charge of the particles is negative, to prevent strong attachment of the NPs onto the negatively charged cell membrane, at the site of injection.

In this chapter, the reader will be initially introduced to the importance of PLGA NPs as drug delivery systems and the current synthesis methods, with an aim to optimize their size and charge by adopting various synthesis protocols. The most promising synthesis methods are then chosen for further drug encapsulation studies, and the therapeutic activity of the NPs is then examined via *in-vitro* cell studies and *in-vivo* direct CED into the mice brain. The sensitivity of gas sorption and NMR cryoporometry techniques to characterize the porous structure of the NPs, aiding to the understanding of drug loading efficiency and release mechanism is also tested.

7.2 Background theory to poly(lactic-*co*-glycolic acid) polymer and synthesis methods for nanoparticles

Poly(lactic-*co*-glycolic acid) (PLGA) is a random copolymer synthesized by co-polymerization of two different types of monomers, lactic acid and glycolic acid, linked together by ester bonds (Figure 7.1) or lactide and glycolide to obtain PLGA polymer with a high MW. It has been approved for medical use by the FDA organization due to its biodegradability and biocompatibility thus making it of great interest in the biomedical area as drug delivery systems (DDS) (Benoit et al., 2000; Menei et al., 1999; Chen et al., 1997; Rafati et al., 1997; Zhang et al., 2012; Xie et al., 2011). PLGA exhibits a glass transition temperature in the range of 313-333 K and can be either ester end-capped or acid end-capped. Poly (DL-lactic-*co*-glycolide) (50:50) with MW ~50,000 g/mol, such as that used in this Chapter, exhibits a glass transition temperature of 313-220 K

and an approximate degradation time of 2 months. Hydrolysis is the main degradation mechanism but polymer formulations present in intra- or extracellular spaces are also subject to enzymatic degradation (Anderson and Shive, 1997). Hydrolysis is facilitated when polymer molecules exposed to water initiate the formation of carboxylic acid groups. These acids then will catalyse the cleavage of ester bonds (autocatalytic degradation) to form non-toxic monomers (Li et al., 2008) (Figure 7.2) which will be further metabolized to carbon dioxide and water, or excreted from the body via the kidneys (Liu et al., 2003). The time required for degradation is related to the ratio of the two monomers, the pH of the environment and the presence of other agents (ie drugs, stabilizers or enzymes). The higher the content of glycolide monomer, the more acidic the conditions and the greater the presence of acid-ended PLGA polymer, the faster the degradation will be (Miller et al., 1977; Park, 1995; Engineer et al., 2011). Thus by varying the polymer composition, the manipulation of its degradation becomes possible. In principle, matrices disappear either by surface or/and bulk erosion (García-Contreras et al., 1997).

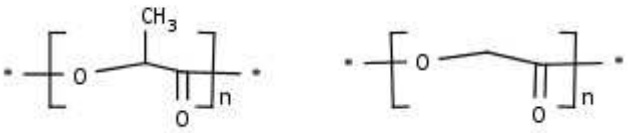

Figure 7.1 Chemical structures of poly(lactic acid) (left) and poly(glycolic acid) (right)

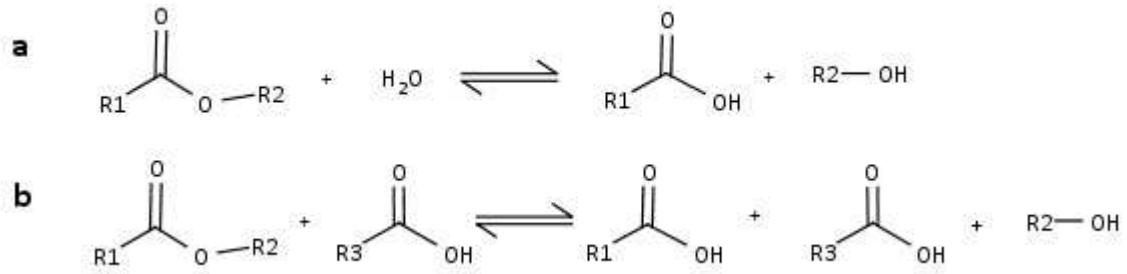

Figure 7.2 a) Hydrolytic and b) autocatalytic degradation of PLGA co-polymer

PLGA nanoparticles (NPs) can be used as DDS systems due to their small size (radius<0.5μm) and big surface to volume ratio (Astete and Sabliov, 2006; Hans and

Lowman, 2002). They are spherical particles ranging in size from a few nanometers to several hundred nanometers according to the preparation technique, solvents, surfactants, presence of active molecule (ie. drug) and the molecular weight of the PLGA polymer. They have tunable surface properties which can modulate the interactions of the particles with blood proteins and mucosa thus controlling their *in-vivo* fate (Vauthier and Bouchemal, 2009).

PLGA NPs can be formulated by several techniques, which can be classified into the bottom-up methods (emulsion, microemulsion polymerisation, interafacial polymerisation, and precipitation polymerisation) which employ a monomer as a starting point and the top-down methods (emulsion evaporation, emulsion diffusion, solvent displacement, salting out) in which the particles are formed from the pre-formed polymer. During the preparation of PLGA nanoparticles it is possible to incorporate active agents such as drugs (Xie et al., 2011), vitamins (Mu and Feng, 2002), proteins and RNA (Wang et al., 2009), which will be released once the environment is changed and the PLGA finally degrades. The drug release rate will be affected by the particle size (Jeong et al., 2002), degradation rate and the environment it is delivered to (García-Contreras et al.; 1997, Menei et al., 1999).

A common technique for NP formulation is the oil in water (o/w) or water in oil in water (w/o/w) emulsification-solvent evaporation method, in which emulsions are created with polymer solutions prepared in volatile solvents (oil phase) such as dichloromethane, chloroform and ethylacetate. An additional water phase containing a surfactant is introduced in the system and thus the water miscible polymer solvent starts diffusing slowly. Once the limiting concentration for the polymer precipitation is reached, phase separation occurs and, while the solvent diffuses through the emulsion phase, finally evaporates. This way each emulsion droplet forms a particle (Song et al., 1997). The method comprises a fast and a slow evaporation period for the complete removal of the solvent (Allemann et al., 1993). During the fast evaporation, 90% of the polymer solvent evaporates and the size of the particles decreases, while during the second slow period, the dispersed particles increase their size again due to coalescence of droplets. A surfactant is used to stabilize the oil-water interface by reducing the interfacial tension

between the two phases, and minimizing the adsorption of polymer into it. A high speed homogenizer, a probe sonicator (Song et al., 1997) or a high pressure homogenizer (Dong and Feng, 2007; Julienne et al., 1992) can be used to further reduce the size of the particles by applying high shear stress during the emulsification stage. The o/w emulsion is usually used for the entrapment of hydrophobic compounds whereas w/o/w is more preferentially used for hydrophilic drug encapsulation. Important parameters to be considered are polymer molecular weight, concentration, co-polymer end-groups, surfactant nature (Mu and Feng, 2002), phase ratio, solvent nature, shear stress and the drug encapsulated (Panyam et al., 2004). Julienne *et al*. (1992) found that an increase of the surfactant concentration and the speed or pressure of the homogenizers, reduces the particle size. The decrease of the oil/water ratio and organic phase in the mixture, also led to a decrease in the particle size.

Another procedure for NP formulation is the emulsification-solvent diffusion method, in which the polymer is dissolved in a partially miscible organic solvent. The organic phase is mixed with the water phase containing a suitable surfactant, under stirring. The formation of particles is obtained by diffusion of the organic solvent and the counter diffusion of water into the emulsion droplets (Niwa et al., 1993). It is suggested that NPs are formed because of a physicochemical instability produced by solvent transport. The mechanism is similar to the one that occurs during the spontaneous emulsification processes. In principle, diffusion of solvent from the globules formed during o/w emulsification carries molecules into the aqueous phase, creating regions of supersaturation from which new globules or polymer aggregates are formed. A stabilizer is crucial to avoid particle coalescence and the formation of agglomerates and it remains at the liquid-liquid interface during the diffusion process. Then NPs will form after complete diffusion of solvent. This method is suitable for hydrophobic active components. The hydrophilic ones have a high migration tendency due to the diffusion of the polar solvent to the aqueous phase therefore, the encapsulation efficiency is low. Parameters that affect the nanoparticle size are PLGA co-polymer ratio (Konan et al., 2003), polymer concentration (Kwon et al., 2001), solvent nature (Song et al., 2006), surfactant and polymer MW (Choi et al., 2002; Kumar et al., 2004b; Kumar et al., 2004a) viscosity (Ahlin et al., 2002), stirring rate, solvent nature and the flow of water added

(Choi et al., 2003). Niwa et al., (1993) found that addition of acetone into the organic phase and a lactic/glycolide ratio of 50:50 decreases the particle size and that encapsulation efficiency (EE) of hydrophilic drugs (5-Flouroracil) is increased with water miscible solvents but decreases with loading content due to a higher leakage of drug into the water phase. The latter is consistent with findings by Govender *et al*. (1999) who used nanoprecipitation method (described earlier) to encapsulate procaine hydrochloride, and showed the importance of decreasing drug water solubility and its ionization, in the EE. For this, the authors increased the pH of the aqueous phase and replaced procaine hydrochloride with procaine dihydrate (base form). Higher ionization of the carboxyl groups of the polymer will also lead to smaller particle size due to higher repulsive forces between these groups. Higher EE of Nafarelin acetate was achieved by (Niwa et al., 1994) who co-mixed PLGA with low and high MW to improve the ionic interactions between the carboxyl groups of the polymer and drug. These results are in contrast to Govender *et al.* who found that addition of PLA or Poly(methyl methacrylate-co-methacrylic acid) did not significantly improved the EE where the drug might have precipitated separately from the PLGA polymer. The presence of fatty acid salts (i.e. lauric acid), increased the EE as lipophilicity was increased (Govender et al., 1999).

A third method for NP formation is the dialysis method. This is a precipitation, surfactant free, technique based on interfacial deposition of the polymer, following displacement of the water miscible polar solvents from a lipophilic solution. It consists of a dialysis tube in which the solvent, the polymer and the active component are placed. The organic solution is dialyzed against water and particle formation is enhanced while the organic phase is exchanged with the aqueous phase. The exact mechanism of nanoparticle formation by a dialysis method is not fully understood at present, but it is thought that it may be based on a mechanism similar to that of nanoprecipitation proposed by (Fessi et al., 1989). This process involves interfacial hydrodynamic phenomena. Diffusion of water into the tube results in a spontaneous emulsification of the oily solution in the form of nanodroplets due to a decrease in interfacial tension and rapid diffusion. Interfacial turbulence or agitation of the interface between the two unequilibrated liquid phases involving flow, diffusion and surface processes (the Marangoni effect) leads to the formation of nanoparticles (Jeong et al., 2001). Turbulence is prompted when the organic

solvent is transferred towards the solution with lower viscosity. To achieve this, steep concentration gradients near the interface and an interfacial tension sensitive to the solvent's concentration, also helps. As the water diffuses in the tube, hydrophobic interactions between the polymer chains increase due to a decrease in the polymer solubility in the organic solvent-water mixture. Also, interfacial tension decreases and the hydrophobic polymer migrates towards the o/w interface leading to the formation of a nanodroplet and thereafter a nanoparticle. Stabilization of the particles will be solely due to the presence of charged groups at the surface of the nanoparticles in the absence of the surfactant (Govender et al., 1999). The size will be affected by the miscibility of the solvent with the water (Jeon et al., 2000), the ratio between hydrophilic/hydrophobic chains (Jeon et al., 2000) and the drug loading efficiency (Kim et al., 1999). Studies on the particle formation from PLA polymer, at different concentrations, in various solvents, and with or without initial water in the dialysis tube were performed by (Liu et al., 2007). These authors found that high concentration of polymer lead to large particle sizes and initial addition of water in the tube lead to smaller but more aggregated particles for over 60%water content. It was also possible to encapsulate hydrophilic Epirubicin hydrochoride drug, which led to a bigger particle size compared to the blank spheres.

Finally, nanoprecipitation is a solvent diffusion or displacement method, adopted for both hydrophilic and hydrophobic drugs. The polymer is dissolved in a water miscible solvent such as acetone, acetonitrile or ethanol and poured drop-wise on an aqueous solution containing a stabilizer (ie polyvinylalcohol, poly-L-lysine, lipid, etc). Slight modification of this method by using PEGylated lipids and fast sonication leads to formation of lipid-polymer hybrid nanoparticles and it will be referred as the simple mixing synthesis method. The solvent diffuses into the water and is eventually removed by pressure reduction. Similar to the above methods, the parameters to be considered for particle size and encapsulation efficiencies are the polymer/surfactant ratios and the type of surfactant and solvent.

7.3 Drug delivery to the central nervous system and recent studies

Effective drug delivery to the central nervous system (CNS) is achieved when the drug has access to the brain, is stable, its dose is controllable and also it is localized to a specific area. Nowadays, drug delivery to the CNS has become a challenging research area due to the difficulty that the drug encounters in penetrating the blood-brain barrier (BBB) and the spinal cord. The impact of the BBB, shown in Figure 7.3 (left), in the drug therapy of CNS has been reviewed by Pardridge (Pardridge, 2003; Pardridge and Boado, 2012; Pardridge, 2007). The brain extracellular fluid is separated from the blood by two cellular barriers, the brain capillary endothelial cells that form the BBB, and the blood-cerebrospinal fluid barrier (BCSFB), which is composed of endothelial cells and choroid epithelial cells. In both cases junctions between the epithelial or endothelial cells restrict the passive diffusivity of drugs from the blood to the extracellular fluid. Only drugs with molecular mass less than 500 Da and high lipophilicity (Kamphorst et al., 2002) can pass through the BBB via passive diffusion but unfortunately, many types of brain diseases such as Alzheimer's, brain and spinal cord injury, brain cancer, HIV infection of the brain, various ataxia-producing disorders, amytrophic lateral sclerosis (ALS) etc might be cured only by large molecule drugs. The BCSFB barrier, Figure 7.3 (right), is slightly more permeable than the BBB but given the large number of capillaries and their position close to neuronal cells, studies are concentrated on either increasing the transport of the drug through the BBB or circumventing it.

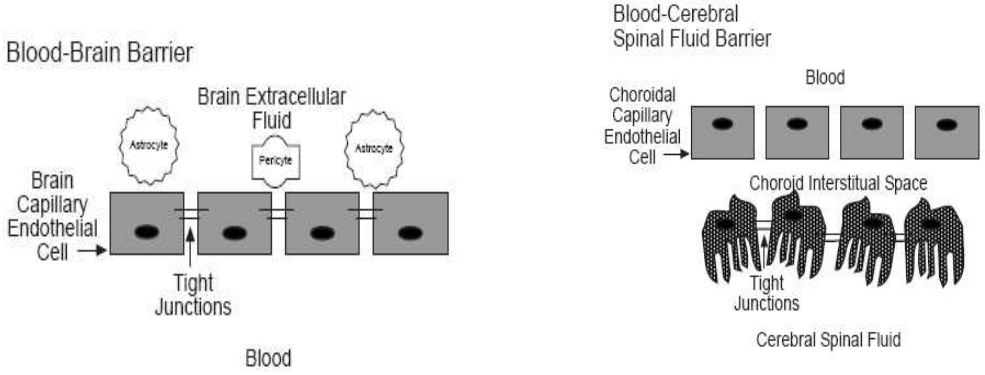

Figure 7.3 Blood – Brain Barrier and Blood-Cerebral Spinal Fluid Barrier (re-drawn from Zhang and Miller, 2005)

Drug delivery to the CNS is conventionally achieved 1) via systemic administration (intravenous injection for targeted action), 2) directly by introduction into cerebrospinal fluid pathways, cerebral arterial circulation or brain substances and 3) by manipulating the BBB junctions. High doses of drugs are often required which can cause significant side effects and toxicity. Recently, more novel administration techniques have been developed such as direct injection or intracranial implantation of drug loaded formulations (conjugates, liposomes, nanoparticles, microparticles, gels) (Fernandez-Fernandez et al., 2011). Also, drug delivery devices such as pumps or catheters for specific targeting into the brain parenchyma to bypass the BBB are in use. However, drug diffusivity from the injection or implantation site to the target area, is limited by the tissue affinity.

Bobo *et al.* (1994) introduced convection-enhanced delivery (CED) to the brain. The principle feature of this method is the direct, continuous infusion of agents under pressure through neurosurgically-placed microcatheters as a means to enhance their distribution over a large tissue volume. Bobo *et al.* found that 24 h post infusion, sucrose and transferrin (359 Da and 80 kDa) were well distributed and delivery of higher concentrations of drug than could conventionally be achieved was accomplished. CED also facilitates highly accurate anatomical targeting and has therefore been widely adopted in pre-clinical and clinical trials for treatment of tumours (Sampson et al., 2008; White et al., 2012) and Parkinson's disease (Gill et al., 2003; Lam et al., 2011; Kells et al., 2010). In this method, the main parameters to be controlled to achieve predictable and clinically relevant volumes of drug distribution are the surface charge, the size and the tissue affinity (MacKay et al., 2005). The brain tissue is lipophilic and exhibits negative charge hence CED is currently limited to anionic, hydrophobic drugs which are effectively distributed over large brain tissue volumes. However, some infusates are prone to rapid clearance, resulting in a limited therapeutic efficacy.

To overcome these obstacles, nanotechnology was then applied to directly deliver drug loaded nanocarriers, such as liposomes or polymer nanoparticles, into the brain through CED (Yang, 2010; Patel et al., 2012). MacKay *et al.* (2005) studied the effect of the size and charge of liposomes into their distribution in the brain. The authors used CED to

deliver radiolabelled and fluorescent liposomes, and found that positively charged liposomes remained at the site of infusion, in contrast to neutral and negatively charged liposomes that perfused outwards easily. They also found that liposomes' systemic circulation half life could be increased by PEGylation but liposomes of radius ~100 nm undergo retention at the site of infusion. However, PEGylated liposomes can lead to activation related pseudoallergy, which can potentially be life-threatening. Grahn and co-workers used CED of non-PEGylated liposomal formulations to deliver the anticancer drug topotecan and paramagnetic gadodiamide to directly visualize their distribution in the brain using Magnetic Resonance Imaging (MRI) (Grahn et al., 2009; Luz et al., 2009). These authors found excellent co-convection of these two agents, an increased median overall survival of the rats compared to the free topotecan delivery and lack of drug toxicity at the clinical doses studied.

PLGA co-polymer drug encapsulation has not yet been optimised for convection-enhanced drug delivery to the brain on a nanometric scale. PLGA NPs could potentially be effective drug carriers for CED due to the ease of manipulation of their surface charge, size and morphology. Intracranial injection of imatinib mesylate loaded PLGA microspheres was performed by Benny *et al.* (2009). The authors used PLGA polymer with different PL/PG ratios and found that drug release can range from weeks to months according to the polymer ratio used. This was justified by means of the degradation rate each polymer type exhibits. Cirpanli *et al.* synthesized camptothecin loaded PLGA nanoparticles, with a radius of 90 nm, for brain tumour treatment via nanoprecipitation method (Cirpanli et al., 2011) and studied the survival time of rats treated with each of the formulations post CED. They found that PLGA nanoparticles had only 6 %w/w EE and survival time did not increase significantly compared to the untreated rats. Sawyer *et al.* also synthesized camptothecin loaded PLGA nanoparticles, with a radius of less than 50 nm, via a single emulsion method and found that EE was significantly increased to 26%w/w (Sawyer et al., 2011). The survival time of the rats increased 6-50% compared to the drug-free spheres. However, neither of the groups analysed volumes of drug distribution in the brain. The inconsistency in the results between the two groups can be attributed to the significant difference in the drug

loading efficiencies, particle size, particle charge and/or the area of distribution within the brain.

In this Chapter the following hypothesis will be tested. Firstly, encapsulation of lipophilic and hydrophilic agents in PLGA NPs can facilitate effective CED in the brain by reducing the tissue affinity. Secondly, PLGA nanoparticles can promote cellular uptake of the encapsulated agent and thirdly, these nanocarriers can prevent drug clearance from the brain. However, NP infusion via microcatheters is restricted to a NP radius that has to be less than 100 nm to prevent blockage of the microcatheters. As mentioned in Section 7.2, particle size and drug encapsulation efficiency vary according to the synthesis method, polymer, solvents, drug hydrophilicity and stabilizer. For concomitant optimization of NP size and drug EE for *in-vivo* CED in the brain, o/w, emulsion-solvent diffusion, dialysis, nanoprecipitation and simple mixing synthesis methods were adopted, as reported in the literature. The effect of ester and acid-ended PLGA polymer and PLGA-PEG in the presence of various organic solvents and non-ionic, positively charged and lipid stabilizers are also tested. Nile Red (NR) was chosen as a highly lipophilic fluorescent model drug and Paclitaxel as clinically used drugs for cancer treatment. Trifluoromethylumbelliferone, fluorescein isothiocyanate dextran and Rhodamine B were used as hydrophilic fluorescent model drugs whereas 5-Fluororacil and Neprilysin are therapeutic agents for brain tumor and Alzheimer's disease treatment. A detailed description of each formulation will be given at the method Section, 7.5, and the NPs will be characterized for size, charge, morphology and EE. Their influence on the *in-vitro* drug release profiles, *in-vitro* cell uptake and *in-vivo* CED will be then discussed.

All the formulations and the *in-vitro* particle characterisation experiments were carried out and analyzed by me, whereas all the cell studies and the *in-vivo* experiments in the rats brain were carried out and analyzed by Dr. Neil Barua.

7.4 Materials

Poly(DL-lactic-*co*-glycolic acid) (PLGA) polymer with lactic/glycolide molar ratio of 50:50 having either ester end groups (RG504, MW:52,600 g/mol) or acid end groups (RG504H, MW:59,100 g/mol) were a gift from Boehringher Ingelheim. [N-(carbonyl-methoxypolyethyleneglycol-2000)-1,2-distearoyl-sn-glycero-3 phosphoethanolamine, Sodium Salt] (mPEG 2000–DSPE, Sodium Salt) lipid was a gift from Lipoid. Polyethylene glycol (11,300) monomethyl ether amino terminated (NH_2-PEG-CH_3) was purchased from Lancaster Synthesis. Dichloromethane (DCM), acetonitrile (MeCN), dimethylformamide (DMF), filter membranes (pore size 0.45-0.8 µm) and centrifuge filter tube (0.7 ml, MCOFF:12,000) were purchased from Fisher. Dimethyl sulfoxide (DMSO) was purchased from Alfa Aesar and polyvinyl-alcohol (PVA) from MP Biomedicals. Dialysis tubes (MWCO:12,000 g/mol), Nile Red (NR), 5-Fluorouracil (5-FU), 1-ethyl-3-(3-dimethylaminopropyl) carbodiimide (EDC), N,N-diisopropylethylamine (DIEA), Poly-L-Lysine hydrobromide (PLL) (MW: 30,000-70,000 g/mol) and Phosphate buffered saline tablets, pH 7.4 (PBS) were purchased from Sigma Aldrich. Rhodamine B and N-hydroxysuccinimide (NHS) were purchased from Acros Organics and 4-(trifluoromethyl)-umbelliferone (TFMU) was purchased from Bio Chemicals. Ultra pure water (resistivity 18 mΩ) was generated from a Milli-Q water purification unit.

Paclitaxel (LC Laboratories), Neprilysin (110 kDa, R&D Systems), artificial spinal fluid (AcSF, refer to Section A5.5, Appendix, for AcSF composition) and fluorescein isothiocyanate dextran (FITC-Dextran, 70 kDa and 150 kDa, Sigma Aldrich) were provided by Dr. Neil Barua. The cell line was an SNB19 Human glioblastoma and was donated by Professor Geoff Pilkington, Department of Neuro-oncology, University of Southampton, to Dr. Neil Barua who then conducted all the *in-vitro* cell studies. The molecular structure of the drugs and stabilisers used for the synthesis of NPs are presented in Figures 7.4 and 7.5. Additional instruments used for NPs synthesis: bath ultrasonicator (Elmer Transonic, T310/H, 35 kHz) probe sonicator (Sonics & Materials, VC 600, 20±3 kHz), rotaevaporator (R-125, BUCHI, Switzerland), high speed homogenizer (Ultra Turrax IKA T18 basic), freeze drier (Mini Lyotrap, LTE Scientific), cell disrupter (one shot cell disruption system-version No V4-53-5/97), ultracentrifugator (Beckman L8-7014 Ultracentrifuge).

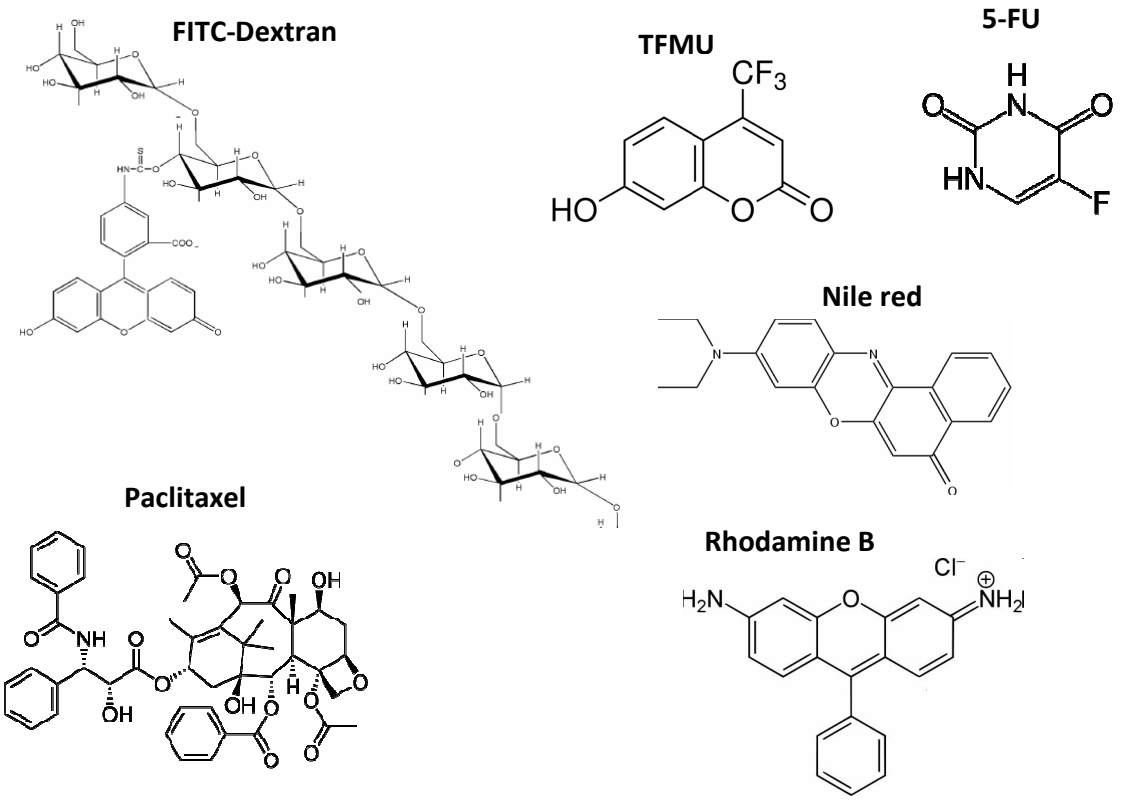

Figure 7.4 Molecular structure of the drugs encapsulated in the PLGA NPs

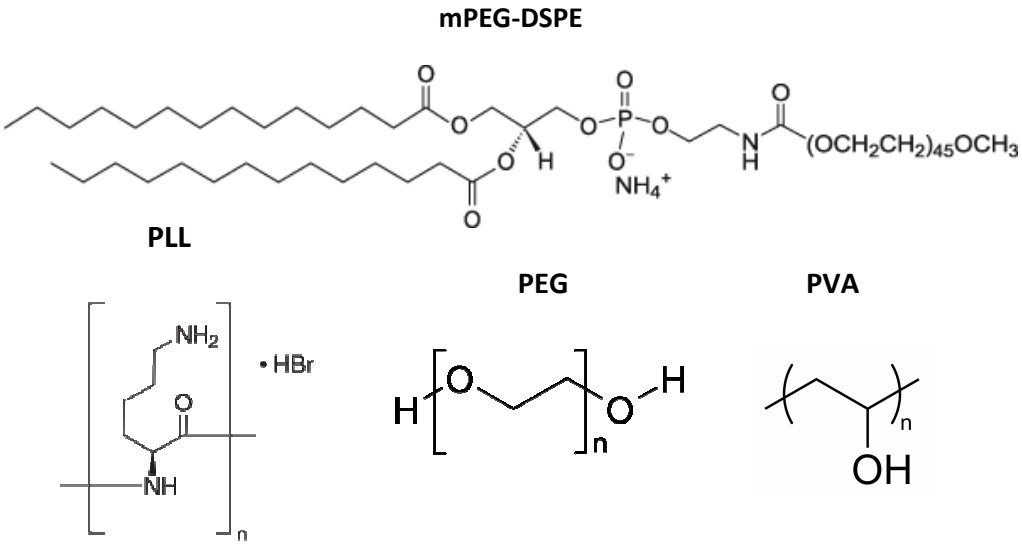

Figure 7.5 Molecular structure of stabilizers used for NPs synthesis

7.5 Experimental procedures

PLGA NP formulations are summarized in Tables 7.1, 7.2 and 7.3 and a detailed description of the synthesizing procedure for each of them will be provided. Incubation of *in-vitro* glioma cell with drug loaded NPs and *in-vivo* CED of NP into the brain parenchyma is also described.

Synthesis method	Polymer	Stabilizer	Solvent	Loaded agent
O/W emulsion-solvent evaporation (probe sonicator)	RG504 RG504H	PVA	DCM Acetone	-
O/W emulsion-solvent evaporation (cell disrupter)	RG504 RG504H	PVA	DCM	-
Emulsion-solvent diffusion	RG504	PVA	DCM Acetone MeOH	-
Dialysis	RG504 RG504H	-	DMSO MeCN DMF	-
	RG504 RG504H	-	DMSO MeCN DMF	NR TFMU
	RG504	PVA	DMSO	-
	RG504	PVA	DMSO	Paclitaxel NEP
	RG504	-	DMSO	FITC-Dextran
Simple mixing	RG504 RG504H	-	DMF DMSO	5-FU
	RG504 RG504H	mPEG-DPSE	MeCN	-
	RG504 RG504H	mPEG-DPSE	MeCN	TFMU
	RG504	mPEG-DPSE	MeCN	NR Rhd

Table 7.1 Summary of PLGA NP formulations, using acid (RG504H) and ester-ended (RG504) polymer

Synthesis method	Polymer	Solvent	Initial water content in the dialysis bag (% v/v)
Dialysis	RG504	DMSO, MeCN, DMF	0
Dialysis	RG504	DMSO, MeCN, DMF	20
Dialysis	RG504	DMSO, MeCN, DMF	80

Table 7.2 Summary of experimental conditions used to investigate the effect of initial water content on PLGA NP size and morphology, using dialysis method

Synthesis method	Conjugated copolymer	Solvent	Loaded agent
Dialysis	PLGA-PEG[a]	DMSO, DMF	TFMU
Nanoprecipitation	PLGA-PEG[a]	DMF	TFMU

Table 7.3 PLGA-PEG NP formulations. [a] PLGA-PEG was synthesized according to (Cheng et al., 2007). Stepwise description is provided in Section A5.1, Appendix.

7.5.1 O/W emulsion-solvent evaporation: Use of probe sonicator

The experimental procedure followed for nanoparticle synthesis was that proposed by Song *et al.* (1996). The effect of the polymer end-group upon the application of shear stress, was tested. Briefly, PLGA polymer (RG504 or RG504H) was dissolved in an organic mixture of DCM and acetone (8:2 v/v) at a final concentration of 25 mg/ml. Then, 10 ml PVA solution (2.5% w/v) were mixed with the organic solution under stirring and sonicated for 10 min with a probe sonicator at 13.1 W/cm^2 power intensity. The o/w emulsion formed was stirred for 20 h and left under reduced pressure for 1 h to ensure complete evaporation of the solvents. The particles were collected by ultra-centrifugation at 46,000 rpm, washed 3 times with ultra pure water and freeze dried.

7.5.2 O/W emulsion-solvent evaporation: Use of cell disrupter

High pressure homogenization was employed in the current procedure to prepare PLGA nanoparticles as described by (Dong and Feng, 2007). High pressure was provided by a

cell disrupter which converts each volume of emulsion exposed to consistent forces (turbulence and cavitation) into fine particles having a narrow polydispersity. Briefly, PLGA polymer (RG504 or RG504H) was dissolved in DCM (22 mg/ml). Then, 25 ml PVA solution (1% w/v) were added into the mixture and a primary o/w emulsion was formed. 5 ml of emulsion were pressurised by the cell disrupter at 155 MPa three times to form a secondary emulsion and left still for 12 h until the DCM evaporated. The particles were collected by centrifugation at 11,000 rpm.

7.5.3 Emulsion-solvent diffusion

PLGA nanoparticles were synthesized according to the method previously described by Niwa *et al.* (1993). In detail, PLGA (RG504) polymer was dissolved in DCM:Acetone:MeOH (1:50:10 v/v) mixture to form the oil phase (3.93 mg/ml). The resultant organic solution was emulsified into nanodroplets by addition of 25 ml of aqueous PVA solution (2.0% w/v) under mechanical stirring at 17,500 rpm using a high speed homogenizer. The organic solvents were removed by continuously stirring the mixture for 12 h, and then under reduced pressure using a rotary evaporator for 6 h and a vacuum line for 13 h. The big particles were filtered out from the solution using membrane filters, 0.45 and 0.8 µm, and the small ones were freeze dried.

7.5.4 Dialysis method

A combination of the synthesis methods proposed by Jeon *et al.* (2000) and *Liu et al.* (2007) was adopted to investigate the influence of solvent nature, polymer end group and initial water concentration within the dialysis tubes on the mean size of the drug-free particles formed, and their morphology. Briefly, PLGA polymer (RG504 and RG504H) was dissolved in an organic solvent (DMSO, DMF or MeCN) under stirring for 20 min and then amounts of water were added to the mixture, to give a final concentration of 0%, 20%, 80% v/v. The concentration of the polymer in the solvent/water mixture was kept constant at 2 mg/ml. The dialysis tubes were immersed

into 500 ml ultra pure water and left to dialyse at room temperature for 2 days as shown from Figure 7.6.

Figure 7.6 RG504/DMSO mixture within the dialysis tubes, dialysed against water. Left bottle: mixture at the beginning of dialysis (t=0 min). Right bottle: mixture after ~2 days of dialysis showing the emulsion formed

Hydrophobic and hydrophilic agents used as model or clinically used drugs were then encapsulated into the polymer for 0 % initial water content. For Nile red encapsulation, PLGA polymer (RG504 or RG504H) was first dissolved in DMSO, MeCN or DMF to a final concentration of 2 mg/ml. Nile red from 1 mM stock solution was added to the mixture to obtain PLGA:NR=1:2500 w/w, and left under stirring for 30 min. 12.5 ml of the mixture was transferred into a dialysis tube and immersed in 500 ml pure water. The TFMU and 5-FU loaded PLGA and PLGA-PEG nanoparticles were synthesized in same way except that polymer:drug ratio was 10:1 w/w. The same procedure was followed for encapsulation, with PLGA:Paclitaxel=10:1 w/w. The PVA/DMSO solution was also added into the PLGA/DMSO mixture to a final PVA concentration of 0.05 % and 0.1 %w/v, to avoid Paclitaxel denature and subsequent polymer precipitation. For Neprilysin loading, 100-200 µl of stock NEP solution (1 mg/ml in PBS) were added drop-wise into the PLGA/DMSO solution to obtain ratios of PLGA:NEP=125:1, 151.5:1 and 250:1 w/w and the mixtures were stirred for 3 h. PVA/DMSO solution was also added to a final concentration of 0.1 %w/v, to avoid protein denaturation and polymer precipitation. The mixtures were continuously stirred for another 2 h.

All samples were then left to dialyse (under water stirring) at room temperature. The water was changed initially after 2 h and then every 1 h until the organic solvent was completely removed. This was further tested by ^{1}H NMR (300 MHz) on dialysing water samples. The emulsions formed were collected by ultracentrifugation at 46,000 rpm for 25 min, washed 3 times to remove any remaining traces of solvent, drug or PVA within the dialysis bags and then they were freeze dried. A fine powder of PLGA nanoparticles was formed and stored at 277 K.

7.5.5 Simple mixing

Hybrid polymer-lipid nanoparticles from RG504 and RG504H polymer and mPEG-DSPE lipid were synthesized via simple mixing as described by (Fang et al., 2010). The mPEG-DSPE:PLGA ratio was 3:10 w/w and water:MeCN was 10:1 v/v to obtain the smallest particle size possible. PLGA serves as a hydrophobic core for encapsulation of hydrophobic molecules while mPEG-DSPE provides electrostatic and steric stabilization, a longer circulation half life for *in-vivo* studies and offers functional end-groups for possible attachment of hydrophilic molecules or peptides, antibodies, etc onto the NP.

Blank nanospheres were synthesized as follows: 6 ml of mPEG-DSPE solution (1 mg/ml aqueous solution) were added drop-wise under stirring into 8 ml PLGA/MeCN solution (2.5 mg/ml) and stirred for 20 min. To adjust the aqueous:MeCN solution to 10:1 v/v, 74 ml more water were then added. The final mixture was bath sonicated for 5 min and then probe sonicated for 1 min (power intensity 14.25 W/cm^2). MeCN was removed under reduced pressure using a rotary evaporator at 225 rpm, for 40 min. The NR and Rhd loaded spheres were synthesized following the same procedure except that NR/MeCN solution (1 mM) was added into the PLGA/MeCN mixture, or Rhd/water solution (1 mM) was added into the lipid aqueous solution, before polymer and lipid were mixed. For NR and Rhd model drug encapsulation, the PLGA:drug ratio was 1:2500 and 1:8333 w/w, respectively. All NPs were collected by centrifugation at 45,000 rpm for 25 min and washed 3 times to remove any unencapsulated agent and free polymer or lipid. The samples were freeze dried and stored at 277 K.

7.5.6 Nanoprecipitation

Empty and TFMU loaded PLGA nanoparticles were synthesized via nanoprecipitation method in the presence of PVA and PLL stabilizers as proposed by Yallapu *et al.* (2010). The following ratios between the ingredients and phases were selected to obtain the smallest particle size possible, as found by Yallapu *at al*.: PLGA:Acetone:TFMU:PLL=10:1.1:1:1 w/v/w/w, acetone/aqueous solution=0.47:1 v/v. Briefly, for drug-free NP formulation, 30 mg PLGA polymer (RG504 or RG504H) were dissolved in 3.3 ml acetone and the mixture was added drop-wise into 7 ml of aqueous solution containing 1% w/v PVA and 3 mg PLL, under stirring. The system was left overnight under continuous stirring for acetone evaporation. TFMU loaded NPs were synthesized in the same way, except that 3 mg TFMU were first dissolved in acetone and then added into the PLGA solution.

The TFMU loaded PLGA-PEG NPs were synthesized as proposed by Cheng *et al*. (2007); 20 mg of PLGA-PEG conjugate were dissolved in 3 ml DMF following 1 ml of TFMU/DMF (2 mg/ml) solution. The system was stirred for 45 min and then added drop wise into 40 ml ultrapure water under continues stirring. It was then left overnight under stirring and DMF was further removed under reduced pressure using a rotary evaporator for 1 h. All PLGA formulations were firstly centrifuged at 6000 rpm for 10 min, to remove the big NPs formed. The small NPs were collected by centrifugation at 45,000 rpm for 20 min and washed 3 times. The PLGA-PEG NPs were directly centrifuged/washed at 45,000 rpm. The mass of the nanoparticles retained was ~30% of the initial PLGA polymer used. The collected samples were freeze dried and stored at 277 K for further use.

7.5.7 *In-vitro* analysis of glioma cell uptake of nanoparticles

These studies were performed and analysed by Dr. Neil Barua. SNB-19 cell cultures were used for the study of cellular uptake of PLGA nanospheres by tumour cells. SNB-19 is an established glioblastoma (GBM, grade IV) cell line derived from a 47-year old male. Cell cultures were grown in modified Eagle's medium containing antibiotics (penicillin and streptomycin) and L-glutamine (InVitrogen, Carlsbad, CA, USA). Cells of passages 15 to 18

were grown to confluence then 10,000 cells per well were incubated with 50 µl of 0.5 mg/ml RG504/NR nanospheres for 2, 24 and 48 h on cover slips at 310 K in a 5 % CO_2 incubator. The same procedure was followed for RG504/Paclitaxel, PLGA-PEG/TFMU and Rhd, NR loaded RG504/mPEG-DSPE NPs for 24 h incubation time. At the pre-determined incubation times, cells were washed with PBS, fixed with 2 % paraformaldehyde and washed twice with PBS. Fluorescence microscopy was performed with a Leica DM5500 microscope, (Leica Microsystems, Wetzler, Germany) and digital camera (CX9000 Microbrightfield, VT, USA).

7.5.8 *In-vivo* CED in the brain parenchyma

All the *in-vivo* studies were performed in accordance with the University of Bristol animal care policies and with the authority of appropriate Home Office licences, by Dr. Neil Barua. Adult male Wistar rats (B&K, UK, 225 to 300 g) were anaesthetised with intraperitoneal (i.p.) ketamine and medetomidine, and then placed in a stereotactic frame (Stoelting, Illinois, USA). All CED procedures were performed using a custom-made catheter with an outer diameter of 0.22 mm and inner diameter of 0.15 mm. The cannula was attached to a 1 ml syringe (Hamilton, Switzerland) and placed at stereotactic co-ordinates derived from the Paxinos and Watson stereotactic rat brain atlas (0.75 mm anterior and 3 mm lateral to bregma, depth 4.5 mm) in order to target the striatum.

Nile red and RG504/NR NPs were suspended in phosphate buffered solution (PBS) in 1 mg/ml, 0.5 mg/ml and 0.1 mg/ml concentration. RG504/NR solutions were sonicated for 1 h in a Grant Ultrasonic Water Bath prior to delivery (Grant Instruments, Cambridge, UK). A total volume of 10 µl of NR or PLGA/NR was delivered into the striatum. All CED procedures were performed at 2.5 µl/min infusion rate. On completion of CED the cannula remained in situ for 10 min in order to minimise reflux, then it was withdrawn at a rate of 1 mm/min. The wound was closed with 4/0 Vicryl, a dose of intramuscular buprenorphine was administered (30 µg/kg) and the anaesthetic reversed with 0.1 mg/kg i.p. of atipamezole hydrochloride (Pfizer, Kent, UK). Rats were terminated by anaesthetic

overdose at either 1 h or 24 h after infusion and brains were removed and placed fresh in 10% w/v formalin for 24 h, then cryoprotected in 30 %w/v sucrose.

The RG504/FITC-Dextran NPs were infused unilaterally into rat brain at a concentration of 1 mg/ml. Rats were terminated at 3 h after withdrawal of the cannula (n=3). The brains were explanted following transcardial perfusion fixation. Fluorescence microscopy was subsequently performed on 35 µm brain tissue coronal sections using a Leica DM5500 microscope and Microbrightfield digital camera to study NR and FITC-Dextran distribution.

The volume of distribution was calculated for NR or PLGA/NR only, using NIH Image J software by tracing contours around the outer margins of fluorescence on serial sections. The RG504/NEP loaded NPs were infused unilaterally into rat brain at a concentration of 1mg/ml. The rats were euthanized at 0, 1, 2, 3, 4, 5 & 6 h (n=3 per time point). NEP ELISA was performed on 200 mg dissected samples of fresh frozen brain tissue from the infused hemisphere, and compared to the contralateral non-infused control hemisphere. NEP concentration in the infused hemisphere was then compared to the control one.

7.6 Nanoparticle characterization methods

7.6.1 Electron microscopy

Scanning electron microscopy (SEM) imaging was used to investigate the structure of the PLGA particles (RG504, RG504H) synthesized via o/w emulsion-solvent evaporation. The freeze dried samples were placed on an alumina plate and sputter-coated with gold to complete the electric circuit required for electron transfer. SEM experiments were conducted on a JEOL JSM6480LV system operating at 15 kV (University of Bath, UK). Transmission electron miscroscopy (TEM) imaging was used to investigate the structure of drug-free PLGA particles (RG504) synthesized via the dialysis method, for 0-80 %v/v initial water content in the dialysis tubes. The freeze dried samples were suspended in pure water and sonicated for 20 min. A drop of particles' suspension was placed onto a carbon/plastic grid and stained with phosphotungstic acid (0.01% w/v) (PTA) for 2 min.

TEM experiments were conducted at room temperature on a JEOL 1200EXII instrument, operating at maximum voltage of 120kV (University of Bath, UK).

Scanning transmission electron microscopy (STEM) was used to obtain information about the surface and morphological structure of RG504 nanoparticles synthesized via dialysis into 100 % DMSO or in a DMSO/PVA mixture, and for RG504/mPEG-DPSE nanoparticles synthesized via simple mixing. For this, samples were taken from nanoparticle emulsion (prior to freeze drying) as high particle dispersion is required. A drop of particle suspension was placed on a carbon grid pre-coated with gold particles. Tomographic STEM technique (tomo-TEM) in particular was used to visualize a single RG504 nanoparticle and investigate the presence of pores within the NP core and surface. This was achieved by obtaining xy-plane image slices from the top of the sphere to the bottom of the carbon film and by tilting it at different angles. The images obtained were reconstructed to produce a movie of the xy-plane slices and a 3D volume texture rotating movie. The program used for the image alignment was IMOD, for the 3D reconstruction (using the SIRT algorithm) was Inspect3D and for the visualization, Amira. The thickness of the particles is calculated from the projected shape of the gold particles. RG504/mPEG-DPSE nanoparticles were also visualized to investigate the morphology of the NP and the location of mPEG-DSPE lipid in the hybrid NP. For this, a single sphere was tilted until 70^{o} angle, however, no 3D or xy-plane reconstructed movie was produced for this. The intensity profile from one edge of the particle to the other, reflecting the projected mass-thickness of the particle, was produced to study its core/shell density. All experiments were conducted on a FEI Titan 80-300 (aberration corrected) STEM at Karlsruhe Institute of Technology (KIT), Germany. Dr. Di Wang prepared the sample grids and performed the STEM experiments in my presence but reconstructed the images for the tomo-TEM in my absence. The imaging results were also interpreted by Dr. Wang and Dr. Christian Kuebel.

7.6.2 Dynamic and electrophoretic light scattering

The mean hydrodynamic particle size (intensity average) was measured by dynamic light scattering (DLS) using a Malvern 4700, nano-s, autosizer. The charge measurements were performed with a Zetaplus zeta potential analyser (Brookhaven Instruments). The size and charge were measured before and after freeze drying when stated. The freeze dried particles were re-suspended in pure water (~0.1% w/v) and sonicated for 30 min prior to the size and charge measurements. The refractive index was 1.59 and both the size and charge measurements were run in triplicate.

7.6.3 Fluorescent and spectrometry techniques

Drug encapsulation efficiencies and their release in different media were measured fluorometrically or spectrophotometrically depending on the sensitivity of each technique. A detailed description for each sample preparation prior to each measurement will now be given.

The encapsulation efficiency of FITC-Dextran loaded nanoparticles was measured fluorimetrically by an extraction method described previously by Pistel *et al.* (2001). Briefly, 7.4-10 mg of 70 kDa and 150 kDa loaded NPs were dissolved in 0.5 ml DCM. This was followed by the addition of 4 ml of water and stirring for 24 h at room temperature. The mixture was then left in a static condition for 2 h. The two immiscible solvents were thus separated and the concentration of the water soluble FITC-Dextran in the aqueous phase was measured fluorimetrically (excitation: 495 nm, emission: 505 nm, Fluorosens, Gilden pλotonics). The calibration curves for FITC-Dextran in ultrapure water are presented in Figures A5.4, Appendecis.

NR, TFMU, 5-FU and Rhd encapsulation efficiencies in the nanoparticles were measured spectrophotometrically using a UV-vis spectrometer (Agilent 8453). For this, 2.7-4.3 mg of NR loaded NPs were dissolved in 1.5 ml DMSO, 1.3-4.7 mg of TFMU loaded NPs were dissolved in DMF, or 1.8-3.4 mg 5-FU loaded NPs were dissolved in DMF, and their absorbance was measured at 553 nm, 336 nm and 266 nm wavelengths, respectively.

3.9 mg Rhd loaded NPs were firstly dissolved in DMSO, which was then removed under reduced pressure. The solid mixture (polymer and Rdh) was re-suspended in 2 ml water and Rhd absorbance was then measured at 554 nm wavelength.

NR release from RG504/NR NPs (synthesized in DMSO and MeCN) in AcSF was tested over 37 days, to investigate whether AcSF can facilitate the mass transport of NR through the polymer matrix. The results will be used to interpret partially the *in-vivo* findings performed in the rat brain. For this, 8-12.3 mg of RG504/NR nanoparticles were suspended over 0.7 ml AcSF and placed within a centrifuge filter tube (MCOFF:12,000), at 38°C. The AcSF induced a slight particle aggregation during the course of the release studies, implying that the nanoparticles can be charge stabilized and the presence of salts in the AcSF solution causes their aggregation. At certain periods of time, the samples were centrifuged at 11,000 rpm for 15 min and all the AcSF solution was collected and replaced with a new aliquot of AcSF solution. The former was then freeze dried and 2 ml DMSO was added to dissolve any possibly released NR. Its concentration was measured at 553 nm absorbance wavelength. At the end of the release studies the amount of unreleased NR was compared to the encapsulated one by re-freeze drying the NPs and dissolving them in DMSO.

TFMU release studies were performed by NP suspension in PBS for 180 h, to mimic the extracellular environment of the *in-vitro* glioma cells incubated with TFMU loaded NPs. For this, 8.4-10.6 mg of TFMU loaded NPs (summarized in Table 7.11) were suspended over 0.7 ml PBS (pH 7.4) and placed within a centrifuge filter tube (MWCOFF: 12,000). The samples were centrifuged at 11,000 rpm for 15 min and all the PBS solution was collected and replaced with a new one. The former was then freeze dried and re-suspended in 2 ml DMF. TMFU concentration was measured at 336 nm absorbance wavelength. The solvent background was removed by performing a 'blank' experiment of the suspension liquid itself prior to each UV-vis measurement.

The encapsulation efficiency of Paclitaxel within RG504 nanoparticles was measured by liquid chromatography coupled with ultraviolet and mass spectrometric detectors (LC-UV-MS). The dry NPs were first dissolved in 0.6 ml MeCN and then 0.4 ml water were

added. A micrOTOF electrospray time-of-flight (ESI-TOF) mass spectrometer (Bruker Daltonik GmbH, Bremen, Germany) was used coupled to an Agilent 1200 LC system (Agilent Technologies, Waldbronn, Germany) with C18 column (50x2 mm, 20^{o}C) as an autosampler. 10 µl of 5 mM sodium formate were injected before the sample. This acted as a calibrant over the mass range 50-1500 m/z. The observed mass and isotope pattern perfectly matched the corresponding theoretical values as calculated from the expected elemental formula. Paclitaxel concentration was measured at 227 nm absorbance wavelength with 30 µl injected sample volume and 0.4 ml/min flow rate.

The theoretical drug loading (TDL), actual drug loading (ADL) and %EE are defined as follows:

TDL = mass of total drug / mass of (total drug + polymer)

ADL = mass of encapsulated drug / mass of (encapsulated drug + polymer)

%EE= ADL/TDL x 100

7.6.4 Gas sorption studies

Nitrogen and krypton sorption studies were performed using a Micrometric Accelerated Surface Area and Porosimetry (ASAP) 2010 apparatus at 77 K. The porous structure of RG504 nanoparticles synthesized via dialysis method in DMSO, was investigated. Before each analysis, 0.219 g of (the same) dry sample was degassed for 48 h at 298 K to remove any physisorbed species from the surface of the nanoparticles. This temperature was chosen to prevent thermal transition of the sample (T_g=319-323^{o}C, manufacturer's product specification). Firstly, the BET surface area was measured from N_2 sorption, S_{BET} (N_2). A krypton sorption experiment was then performed due to the low surface area of the material. The molecular cross-sectional area, σ, for nitrogen and krypton were 0.162 nm^2 and 0.210 nm^2, respectively, assuming closed-packed liquid monolayer adsorbed on the surface. The pressure range for the $S_{BET}(N_2)$ calculation was P/P_0=0.037-0.314 and for S_{BET}(Kr), P/P_0=0.221-0.301.

7.6.5 NMR cryoporometry

NMR cryoporometry was used to measure the pore size distribution (PSD) of the RG504 nanoparticles, synthesized in DMSO via dialysis, and investigate any possible structural change of the particles after 1-4 days of immersion in pure water. The experiments were conducted on a 400 MHz Bruker Avance (9.4 T) and ^{1}H NMR was used as previously described in Chapter 3.

The sample preparation and cryoporometry experiment was performed as follows: ~7 mg of PLGA NPs were placed in a plastic pipette tip and 70 µl of ultrapure water were added. This ensures that the NMR tube will not break below 0^{o}C due to water expansion on freezing. Both the top and the bottom of the tip were sealed with Parafilm to avoid water leakage. The tip was left at room temperature for 1-4 days, before it was placed in a 5 mm NMR tube between two susceptibility plugs. A nonmagnetic thermocouple (provided by Bruker) was used to measure the real temperature within the sample. The tube was then placed into the NMR spectrometer and the sample was subjected to supercooling, pore melting and finally bulk melting. The system was left to reach thermal equilibrium for 12 min at each temperature point and spectra were recorded with 4 scans. Both values were chosen based on the NMR cryoporometry experiments on C10 mesoporous silica samples and it was assumed that this time is sufficient for thermal equilibrium within the PLGA system. Increase of equilibration time or number of scans would increase the experimental time which is limited by the capacity of the liquid nitrogen container used for cooling the sample. The same PLGA sample was used for all the series of freeze-thaw experiments. It is possible that repetitive freezing cause particle aggregation, however, this could not be tested due to the resolution limits of the experimental set-up. If particles aggregate, the external surface area is reduced relative to the dispersed samples, thereby the rate of their breakdown changes.

7.7 Results. Drug free nanoparticles

7.7.1 Morphology of drug-free particles

Particles formulated via o/w emulsion (using a probe sonicator), dialysis and simple mixing methods led to formation of particles with different morphological characteristics and sizes. However, the use of a cell disrupter, as an alternative way to induce high shear stress instead of using high speed homogenization was not efficient. The volatile solvent, DCM, reacted with the rubber O-rings within the cup and contaminated the sample. In addition, the emulsion-solvent diffusion method employed, led to large particles. Indeed, during filtration, particles synthesized from ester-ended group polymer (RG504), were unable to pass through the 0.45 µm pore size membranes, leading to the conclusion that most of the particles obtained had a diameter higher than 0.45 µm or they are highly aggregated. Despite the fact that particles formed by acid-ended polymer (RG504H) could pass through the same size membranes the yield was extremely low. Thus, this synthesis procedure was found inefficient to generate particles less than 100 nm.

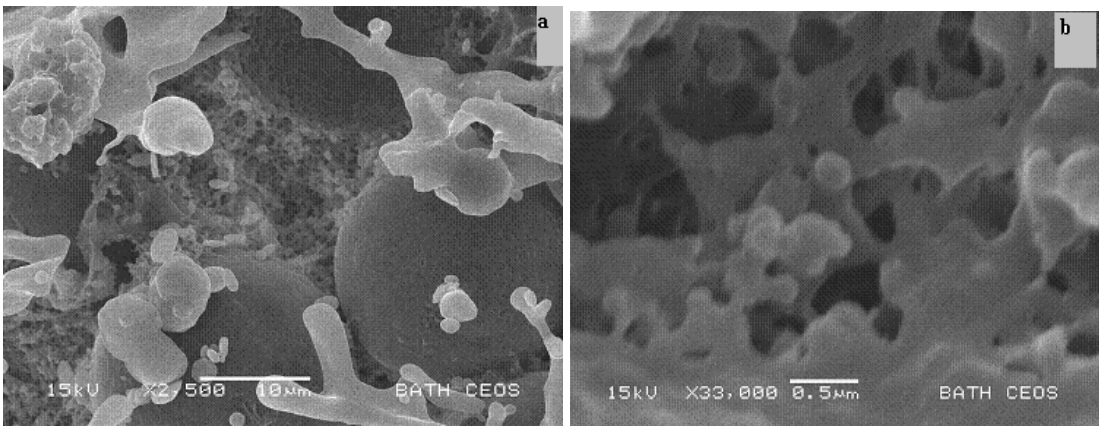

Figure 7.7 SEM images of PLGA spheres synthesized via o/w emulsion-solvent evaporation (probe sonicator) method from a) acid-ended (RG504H) and b) ester-ended (RG504) PLGA polymer

Figure 7.7 shows SEM images of the particles formed by acid and ester-ended PLGA polymer, via o/w emulsion method. It is seen that the particles synthesized with acid-ended PLGA polymer (Figure 7.7a) have variable sizes, with a radius between 50 nm to 20 µm. In contrast, ester ended PLGA polymer formed particles with a smaller size

(radius=50-100 nm) but they were highly aggregated or they were possibly incompletely formed as seen from Figure 7.7b.

TEM images of ester-ended PLGA nanoparticles (Figure 7.8) synthesized via the dialysis method show the effect of solvent and initial water content in the dialysis bag on the particle size and structure. Polymer solubility and interaction with each of the organic solvents along with solvent miscibility and interaction with dialysing water, influenced the thermodynamic and kinetic energy of the system, thus resulting in different sized NPs. The presence of initial water content within the dialysis bags favoured formation of smaller particles (Figures 7.8 b, d, e, h and k) whose polydispersity changed according to fraction of water and solvent used. The size of particles for 0% water content increased in order DMSO<MeCN<DMF. For 20-80% initial water content in the bags the systems were aggregated when they were synthesized in DMSO or DMF but they were better formed, stable NPs when MeCN was used.

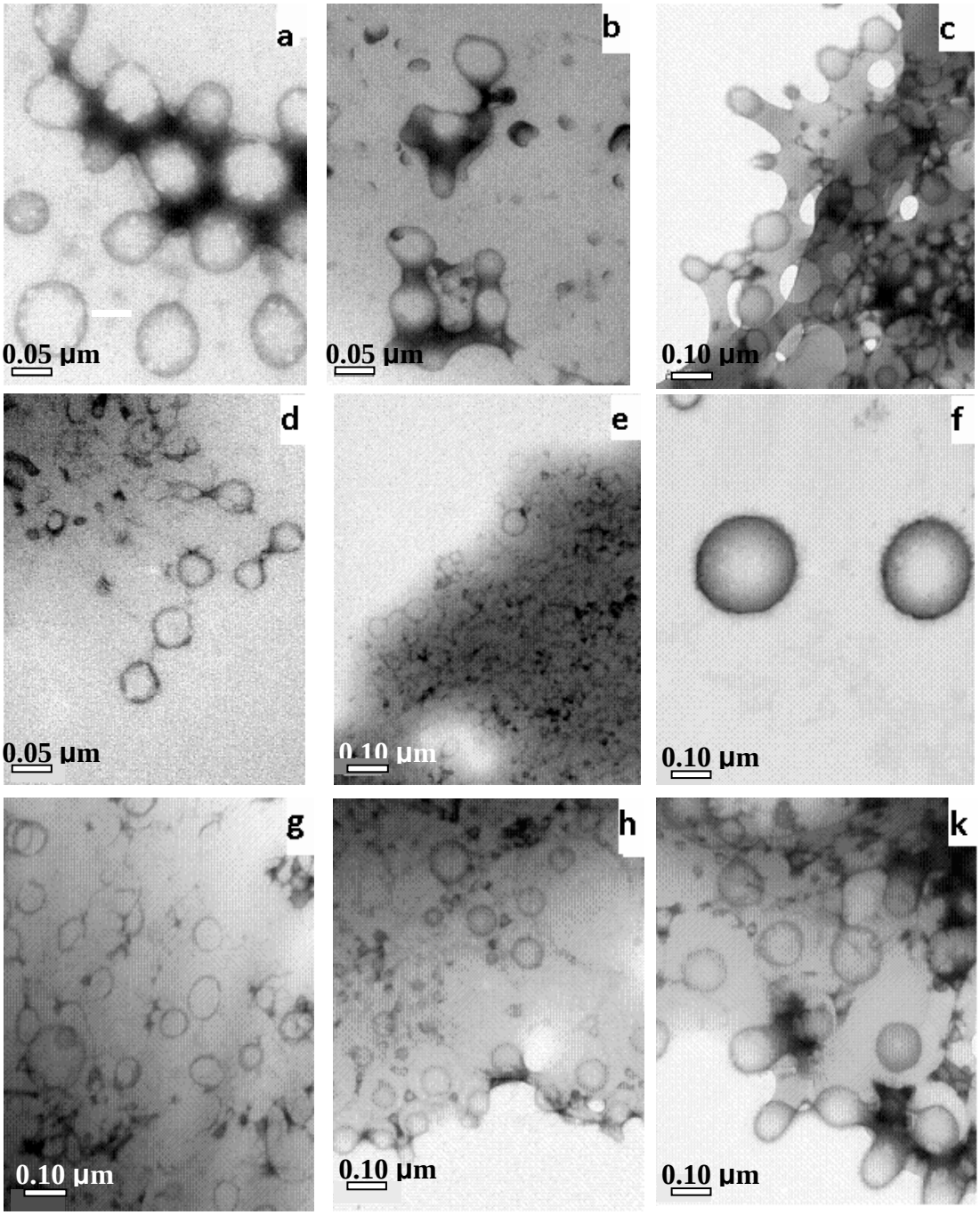

Figure 7.8 TEM images of PLGA nanoparticles prepared from a) 100% DMSO and 0% H_2O, b) 20% DMSO and 80% H_2O, c) 100% DMF and 0% H_2O, d) 80% DMF and 20% H_2O, e) 20% DMF and 80% H_2O, f) and g) 100% MeCN and 0 % H_2O, h) 80% MeCN and 20 % H_2O, k) 20% MeCN and 80 % H_2O v/v, and dialyzed against H_2O

The surface roughness and the inner structure of the NPs synthesized from ester-ended PLGA polymer in 100% DMSO were studied via tomo-TEM due to the high resolution imaging that this technique offers. Two xy-plane slices of a single NP are presented in Figure 7.10 showing that densely packed nanoparticles are formed and that PLGA

polymer is homogeneously distributed within the core of the sphere. Figure 7.9 and Figure 7.10 show that the NPs exhibit a rough surface or, they have regions with different polymer density; however, there is no concrete evidence of internal or surface porosity up to the resolution limitations of the instrument. The staining agents, such as uranil acetate (1% w/v) (not shown here), did not increase further the imaging contrast (in discussion with Dr. Di Wang, KIT, Germany).

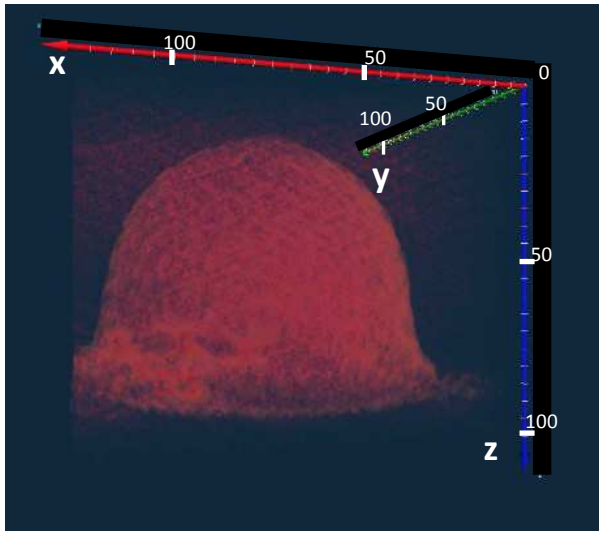

Figure 7.9 Snapshot image from a re-constructed 3D volume texture rotating movie of a single PLGA NP synthesized via dialysis, from ester-ended PLGA polymer in DMSO, using tomo-TEM.

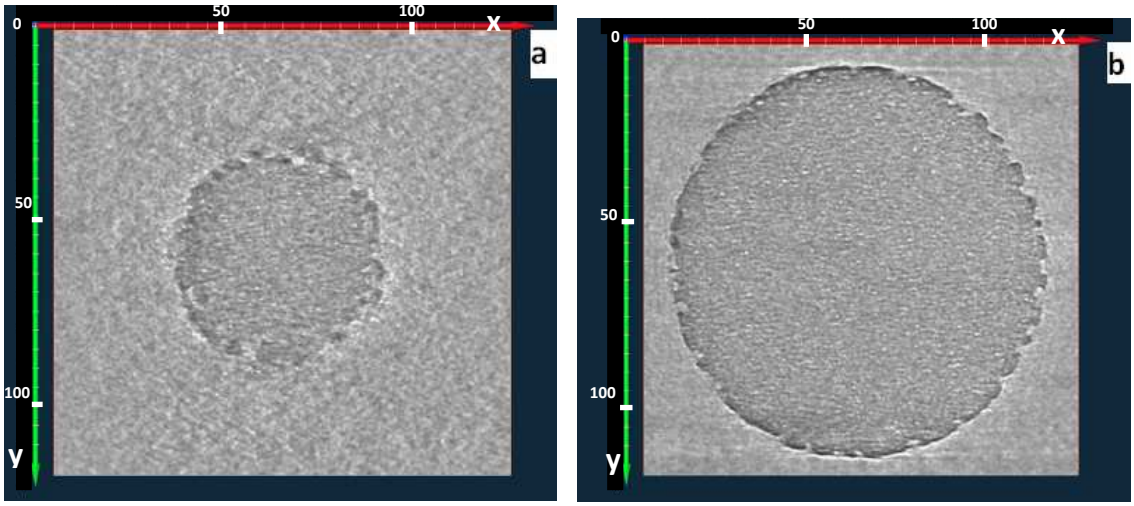

Figure 7.10 Snapshot images taken from a re-constructed movie of a single PLGA NP synthesized via dialysis, from ester-ended PLGA polymer in DMSO, using tomo-TEM. Each image represents a slice (inner structure) of the NP at two different positions, perpendicular to the carbon grid

Introduction of PVA solution within the dialysis bag, using the same synthesis method and ester terminated polymer as all the particles above, also led to formation of spherical NPs (Figure 7.11) of a radius ~100 nm as it will be further proved by DLS results.

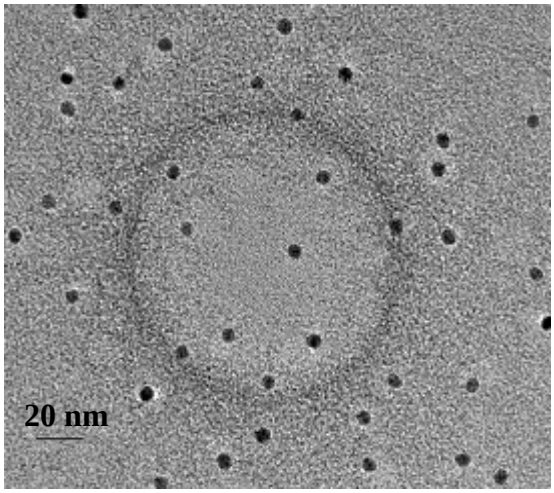

Figure 7.11 STEM image of a single RG504 nanoparticle synthesized via dialysis in 0.05 %w/v PVA/DMSO mixture. The black dots are gold nanoparticles coating the carbon grid

Simple mixing of RG504 polymer with mPEG-DSPE lipid also resulted in formation of spherical nanaparticles, which are shown by the STEM images (Figures 7.12a and b) to have a radius of ~100 nm. The intensity profile from one edge of the particle to the other (Figure 7.12c) reflects the projected mass-thickness of the particle which is proportional to the particle density. The intensity remains ~1400 throughout the particle showing that densely packed polymer spheres are formed. The lipid is expected to form a shell around the dense polymer core with the hydrophilic head group (PEG) (attached onto the phosphate group of the lipid) facing the aqueous phase and the hydrophobic acyl tails of the lipid attached onto the PLGA polymer (Fang et al., 2010). However, a significant difference in the intensity profile throughout the particle slice is not seen, possibly due to the similar densities of PLGA and mPEG-DSPE chains. A slight only increase is seen towards the edges of the particle, which might be attributed to a thin layer of PEG formed around the pellet, of 10-20 nm thickness assuming that an extended PEG group of MW=2000 mol/g is ~20 nm long

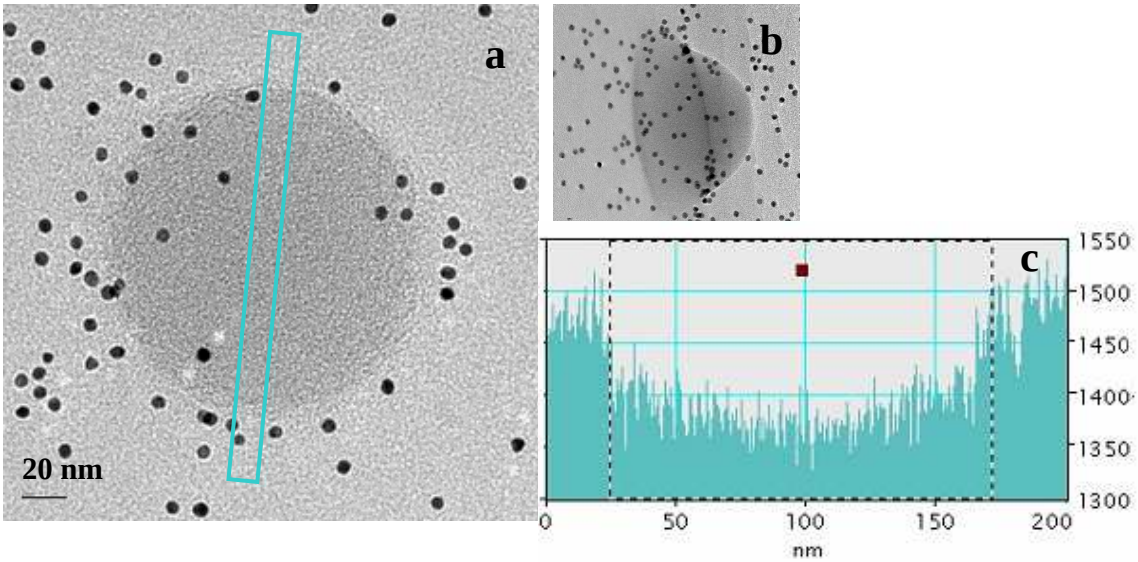

Figure 7.12 STEM image at a) 0° and b) 70° tilted angle of a single RG504/mPEG-DPSE nanoparticle synthesized by simple mixing and c) intensity profile measured at the region shown by the blue rectangle on the sphere

7.7.2 Size and charge of drug-free nanoparticles

Nanoparticles synthesized via the dialysis method had a small size and a narrow size distribution as shown from the TEM images which is necessary for CED. Moreover, these particles are stabilized without the presence of stabilizers, which may be toxic for drug delivery into the brain, if any residues are left. Hence, the size and the charge of the NPs formed via dialysis method are studied in this section in more detail. It was found that these NPs exhibited different size and surface charge depending on the polymer end-groups, solvent and the initial concentration of water within the dialysis tubes, as seen in Figure 7.8 and Table 7.4. For some formulations, the NP size was measured before (E) and after freeze drying (FD) to investigate the effect of FD in particle agglomeration and the results are given in the Appendix, Table A5.1. For 0% v/v initial water content in the dialysis tubes, NPs synthesized from acid end-groups (RG504H) had a smaller mean size than the ester ended ones (RG504), as shown in Table 7.4. The former NP size increased in order DMSO>MeCN>DMF whereas the latter increased in the inverse order. Size also decreased as the initial concentration of water within the dialysis mixture increased from 0-80% v/v as shown from Figure 7.8.

				Solubility parameter difference, ($MPa^{1/2}$)		Interaction parameter	
Polymer	**Solvent**	**Mean particle size, *r*±SD (nm)**	**Zeta potential, ζ±SD (mV)**	**$\Delta\delta_{ps}$**	**$\Delta\delta_{sw}$**	**χ_{ps}**	**χ_{sw}**
RG504	DMSO	112.8±2.3	-46.2±1.4	8.64	32.23	0.59	13.20
RG504	MeCN	107.5±3.4	-43.2±0.6	12.30	36.26	0.36	11.98
RG504	DMF	116.0±0.8	-5.8±0.8	5.81	31.14	0.38	16.71
RG504H	DMSO	96.7±2.8	-42.9±1.0	8.65	32.23	0.58	13.20
RG504H	MeCN	88.6±10.3	-19.7±0.5	12.31	36.26	0.36	11.98
RG504H	DMF	85.7±1	-17.2±0.4	5.82	31.14	0.38	16.71

Table 7.4 Comparative analysis of NP size and charge synthesized from ester and acid ended PLGA polymer via dialysis, at 0% v/v initial water content. Effect of solubility and interaction parameters between polymer-solvent and solvent-water on the particle size and charge

To study the influence of the polymer-solvent-water interactions on the NP size, the solubility parameter difference $\Delta\delta$ by Hansen's approach, and the modified Flory-Huggins interaction parameter, χ, between polymer-solvent and solvent-water ($\Delta\delta_{ps}$, $\Delta\delta_{sw}$, χ_{ps}, χ_{sw}) were calculated and displayed in Table 7.4 (Hansen, 2007; Brandrup et al., 2005). Following the rule of thumb, the lower the values of these parameters, the better the affinity and miscibility between the solvent-water and solvent-polymer systems providing ease of solvent diffusion, which thus should result in smaller particles. However, the results show that there is no clear relationship between the size of the particles and the interaction and solubility parameters. Only for RG504 nanoparticles, χ_{sw} appear to maintain a correlation with particle size, leading to its decrease in solvent order MeCN<DMSO<DMF. Furthermore, comparing RG504 to RG504H, there is insignificant difference between their $\Delta\delta$ and χ values.

Synthesis method	Nanoparticle formulation	Solvent	Mean particle size, *r*±SD (nm)	Zeta potential, ζ±SD (mV)
Dialysis	RG504 (0.05 %PVA)	DMSO	~60-90[a]	
	RG504 (0.1 %PVA)	DMSO	~65-80[a]	
Simple mixing	RG504/mPEG-DSPE	MeCN	115.8±0.8	-26.5±0.5
	RG504H/mPEG-DSPE	MeCN	120.9±6.1	-25.2±0.9
Nanopreci-pitation	RG504 (PVA, PLL)	Acetone	124.9±1.1	-11.9±0.8
	RG504H (PVA, PLL)	Acetone	134.1±1.9	-4.1±0.3

Table 7.5 NP size and charge synthesized by simple mixing (MeCN) and nanoprecipitation (Acetone) in the presence of lipid or PVA/PLL mixture, respectively. [a]: size of NPs as visualized via TEM

The size of PLGA nanoparticles decreased when initial water content within the dialysis tube was increased, however, less compact (Figures 7.8d and g) or less uniform (Figures 7.8d, e and h) particles were formed with respect to size and shape depending on the solvent. The zeta potential of the NPs increased in solvent order, DMF<MeCN<DMSO for both types of polymers. This proves that the molecular arrangement of the polymeric chains differs according to the solvent nature. Introduction of PVA surfactant within the dialysis bag resulted in formation of smaller particles which decreased in size as PVA concentration increased to 0.1%. This means that PVA prevented aggregation of smaller particles initially formed, by decreasing the surface tension between the solvent and water, or by steric stabilization from adsorbed PVA polymer chains. The presence of lipid and PVA and poly-L-lysine (PLL) composites as a mean to stabilise and provide hydrophilic functional groups on the surface of the NPs also resulted in negatively charged nanoparticles (Table 7.5). Hydrophilic poly-L-lysine decreased the surface charge of NPs and also led to slightly bigger size particles.

7.7.3 Nitrogen and krypton sorption studies for pore characterization of nanoparticles

Gas sorption studies for determination of pore size distribution and specific surface area (S_{BET}) of polymer microparticles and nanoparticles were reported in the past (Sant et al.,

2005; Sant et al., 2007; Buske et al., 2012). These authors studied the drug release behaviour from different formulations of PEGylated PLA and PLGA particles and correlated it to the differences obtained in the surface area of the particles and their size. It is thus expected that controlled drug release can be achieved by manipulating the void space characteristics of the particles.

The S_{BET} and the BET constant measurements for nitrogen and krypton adsorption are presented in Table 7.6. The results are compared to the total external surface area of all the NPs in the sample, calculated geometrically, assuming that they are monodisperse and spherical, with an average radius of ~100 nm, as found by DLS and TEM, and polymer density 1.414 g/cm^3. As shown from Table 7.6, S_{BET} (N_2) is within the experimental error of the surface area estimated geometrically. This means that all the N_2 molecules were adsorbed on the external surface of the NPs. Comparing the $S_{BET}(N_2)$ with the S_{BET}(Kr), it is seen that the latter is underestimated. This suggests that the packing of the molecules in the liquid monolayer is looser than the one assumed for close-packed liquid monolayer, with σ(0.21nm^2) (Karnaukhov, 1985). This is because the interaction of the krypton molecules with the PLGA polymer might be different to that found for silicon oxide surfaces. As discussed in Chapter 1 the cross-sectional area is affected by the nature of the adsorbant. The $S_{BET}(N_2)$ and S_{BET}(Kr) become equal by correcting the cross-sectional area of krypton with σ(0.345nm^2). The low BET constant for both gases suggests a low energy of adsorption on the polymer, thus weak interactions between adsorbate and adsorbent. The adsorption isotherms for nitrogen and krypton are presented in the Appendix, Figures A5.2 and A5.3.

Adsorbate	***C***	***S_{BET}* ± error (m^2/g)**	**Total geometrical surface area of all NPs in the sample (m^2/g)**
N_2, σ(0.165 nm^2)	20.54	20.57±0.20	21.22
Kr, σ(0.21 nm^2)	4.06	12.44±0.40	
Kr, σ(0.345 nm^2)		20.44±0.65	

Table 7.6 BET constant and surface area values estimated from gas adsorption and geometrically

7.7.4 NMR cryoporometry studies for pore characterization of nanoparticles

NMR cryoporometry technique was used to investigate the presence of pores within the PLGA NPs via freeze-melting the water imbibed within the sample. Its advantage relies on the fact that the sample does not require high temperature pre-treatment. The random distribution of polymer chains within the particle can lead to the creation of void spaces - pores - that will be filled with water once immersed in aqueous solution. Any changes in the structural organization of those chains, thus pores, over time of immersion in water will be detected as a change in the melting temperature and fraction of molten phase since they are relative to the pore size and pore volume, respectively via Gibbs-Thomson equation 2.19.

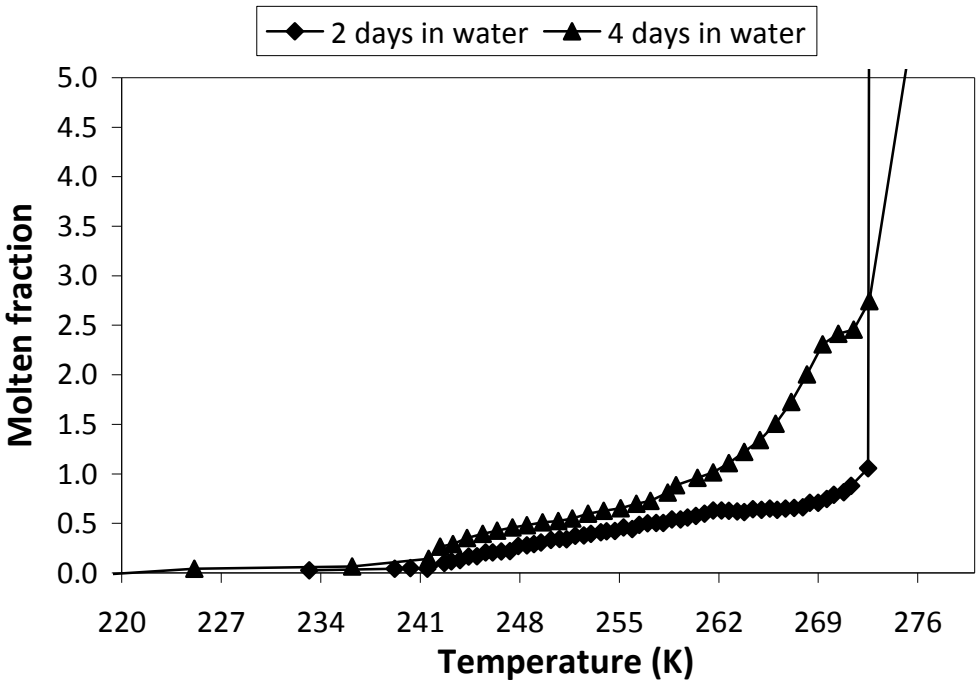

Figure 7.13 NMR cryoporometry melting curves of water in the PLGA NPs after 2 and 4 days of immersion in water. The molten fraction is normalized to the total volume of water melting at 272.8 K after 2 days of immersion in water

For both periods of immersion time in water, melting starts at 241 K. It is seen that after 2 days in water, melting occurs at the temperature range of 241-262 K, and then flattens, whereas after 4 days, water melts continuously at the temperature range of 241-273 K. It

is also observed that the volume of molten water at 273 K which would correspond to the total water within the voids, increased after 4 days in water. Above 255 K this increase is gradual and continues until the bulk melting (273 K).

7.8 Discussion. Drug free nanoparticles

7.8.1 Effect of synthesis method on particle size and morphology

The purpose of utilizing different techniques for NPs synthesis was to investigate which of these synthesis methods provides the optimal particles for drug delivery into the brain via CED. Specifically the aim was the synthesis of negatively charged particles with a radius of less than 100 nm. For this, blank spheres were synthesized following o/w emulsion-solvent evaporation (probe sonicator and cell disrupter), emulsion-solvent diffusion, dialysis, simple mixing and nanoprecipitation techniques. Each formulation was prepared by adopting the optimum combination and concentrations of polymers, stabilisers and solvents as previously reported in the literature that would lead to the desired particle size. Further to this, the effect of different polymer end groups on particle morphology was also tested.

It was found that particles formed via the o/w emulsion-solvent evaporation method, using an ultrasound probe sonicator as a high energy source for solvent-nonsolvent homogenization, were either not well formed (ester-ended polymer) or polydisperse (acid-ended polymer) (Figure 7.5). The use of PVA stabilizer, did not prevent particle collisions and coalescence, nor reduced the interfacial tension between the diffusing liquids. Also, addition of water soluble acetone in the primary mixture inadequately increased DCM water miscibility to promote its diffusion through the aqueous phase. Therefore, polymer precipitation and thereafter, phase separation of water-solvent mixture led to aggregated systems. The results are consistent with Song *et al.* (2006) and Kwon *et al.* (2001) who found that aggregated particles are formed when water immiscible (such as DCM) or completely miscible solvents are used during particle formation. Particle size might have decreased if the sonication time was higher, as proposed by Feczkó *et al.* (2011). Acid-ended PLGA polymer (RG504H) precipitation led

to more polydisperse systems compared to ester-ended PLGA polymer (RG504). The slightly more hydrophilic RG504H is better dispersed into the aqueous phase, resulting in slower precipitation than RG504. It must also be noted that the local pressure within a liquid changes over time and place when ultrasonic waves propagate through the liquid (Riesz et al., 1985). A cavitation bubble present in the liquid will expand and contract in response to these pressure changes generating free radicals (ie $^{\cdot}H$, $^{\cdot}OH$, $^{\cdot}Cl$) produced from water, DCM, MeOH and acetone involved in NP synthesis. Moreover, radicals might be produced from the polymers depending on the bond dissociation energy and, reactions can occur within a collapsing bubble involving all free radicals. Therefore, it would be expected that carboxyl groups of RG504H polymer would provide an $^{\cdot}H$ easier than ester-ended RG504 polymer, thus offering free sites for interaction with the other radicals. Alternatively, it could be that an acid ended polymer due to higher amphiphilicity than the ester ended polymer, is located around the edges of the bubbles rather than in the hydrophobic droplets-being at the interface it is more susceptible to be attacked by radicals in the aqueous phase. These random polymer-solvent-radicals interactions will influence their thermodynamic and kinetic state, hence leading to more polydisperse particle sizes, compared to the more stable ester-ended PLGA polymer.

The o/w emulsion-solvent evaporation method, using a cell disrupter to induce shear stress, as an alternative to the high pressure homogenizer proposed by Dong and Feng (2007) was not efficient as seen in the experimental Section 7.5.2. Even though the pressure applied was the same for both types of equipment, the cell disrupter contains rubber parts that react with DCM, thus restricting NP formation into a particular type of device or requires the choice of other solvents, non-reactive with rubber.

Samples synthesized via emulsion-solvent diffusion technique also led to formation of large particles (>225 nm). These results are inconsistent with literature (Niwa et al., 1993; Kwon et al., 2001) implying that this method is not highly repeatable. Parameters that could have increased the particle size were the long time required for complete solvent evaporation (~40 h) compared to Niwa *et al.* (~4 h) or the lower molecular weight of PLGA employed here.

Simple mixing of PLGA polymer (RG504) with mPEG-DSPE lipid also led to spherical nanoparticles (Figure 7.10) with a radius ~115 nm whereas acid-ended polymer (RG504H) led to slightly bigger NPs (Table 7.5). This could be attributed to competitive interaction forces between the carboxylic end groups of the PLGA and the lipid during particle formation that resulted in less adsorption of lipid on the shell, hence slightly less stabilized NPs. However, Fang *et al.* (2010) obtained particle sizes of less than 80 nm for the same polymer/lipid/solvent ratios. Nevertheless, hybrid PLGA NPs synthesized via this method can be used as potential hydrophobic and hydrophilic drug carriers due to their hydrophobic core and hydrophilic shell.

Nanoprecipitation of PLGA polymer in the presence of PVA and PLL stabilizers generated bigger NPs than simple mixing. PLL chains are attached on the surface of the particles with the hydrophilic amine groups facing the aqueous phase. Again acid-ended polymer led to bigger particles and this is explained by means of additional electrostatic interactions between negatively charged carboxyl groups of the polymer and the positively charged amine groups of the PLL. Less negative charge on the particles, by neutralising some of them by the PLL, prevent their fusing.

Nanoparticles synthesized via dialysis method were spherical and had a mean radius of ~100 nm. RG504 polymer formed smaller NPs in the most polar solvents (MeCN, DMSO) and bigger for the less polar DMF. The results are consistent with those found by Jeong *et al.* (2001) and Nah *et al.* (2000). The inverse behaviour occurs for the RG504H NPs. Mora-Huertas *et al.* (2011) gave a critical review of the approaches proposed to explain emulsification following solvent displacement. The authors concluded that the size of the particles is controlled simultaneously by the interfacial tension differences between the solvent/nonsolvent and the energetically more favourable (spontaneous) nucleation of the polymer molecules forming small particles. Solubility and/or interaction of the polymer with the solvent and nonsolvent do not govern the particle size. These findings are consistent with those presented in Table 7.4. Moreover, the size of the PLGA nanoparticles decreased when the initial water content within the dialysis tube was increased. This is consistent with Liu *et al.* (2007), who studied the effect of initial water content on PLA particle formation in DMF. The authors attributed this to the different

conformations of the polymer chains in various water/solvent mixtures and the slow speed of dialysis at high water contents. However, these authors found that for 80% v/v initial water content, polydispersity decreased and particles formed were more uniform than 0% water content. As seen from Figure 6.6e, the particles formed from 80 % v/v water content in DMF, were not uniform and possibly there were polymer chains that did not result in particle formation at all. This could be due to the different polymer (hence hydrophilicity) used in our studies. PLGA polymer contains glycolide chains which will favour hydrophilic interactions with water compared to the highly hydrophobic PLA. Liu *et al.* proposed the following stepwise mechanism for nanoparticle formation: 1) aggregation of the polymer, 2) formation of particles and their disruption while water diffuses into the dialysis tubes and 3) solidification of the particles; PLGA chains turn from dispersed to compressed solid state. During the first step, aggregates start to form at the inner surface of the dialysis membranes once the water diffuses within the tube. During the second step, a supersaturated layer is created, while the water displaces the solvent and primary particles are formed (Errico et al., 2009). Collisions due to Brownian motions result in the aggregation of the primary particles and the formation of secondary particles having a bigger size (Molina-Bolivar and Ortega-Vinuesa, 1999; Privman et al., 1999). As the water further penetrates into the membrane, stabilization of particles is obtained (step 3). Two factors are responsible for that effect, surface charge and hydration.

It is thus possible that solvent miscibility with water will initially play the key role on the speed of water diffusivity within the tubes, affecting the aggregates' size; migration of water into DMSO and MeCN will be faster compared to DMF. Thereafter, concurrent hydrophobic and repulsive forces, between polymer chains and polymer-water, respectively, will control the primary particle size. The exact lactic/glycolide ratio would strongly impact on their size. Finally, distribution and amount of charged groups on the particle surface will facilitate interparticle repulsive or attractive electrostatic interactions, resulting in smaller and more defined NPs or bigger and more aggregated NPs. For 0% initial water content, the dialysis speed is fast due to the big difference in osmotic pressure and large droplets were formed. When initial water content is higher than 20%, smaller nanoparticles are formed but they are less uniform for DMSO and

MeCN as seen from Figures 7.8b,e and h. In this case, both aggregation and formation of the particles seem to happen simultaneously. The initial addition of water into the solvent provides a lower energy path for hydrophobic interactions between the polymer chains and their polar heads are exposed onto the surface of the particles. As DMF is the less water miscible solvent, hydrophobic interactions will be delayed and it will require further water penetrating into the tubes for complete particle formation. This could be the reason that particles at 80% initial water content, shown in Figure 7.8e, were less uniform compared to the "abruptly" formed DMSO and MeCN ones for the same water content. In general samples prepared in the presence of initial water had some amorphous structures formed (Figure 7.8e and k). These can be polymer chains that did not result in particle formation due to non-efficient decrease of interfacial tension in certain areas of the tube. Another explanation would be that these were pieces of particles which were destroyed during sonication prior to TEM imaging.

Even though the advantage of dialysis method is the ability to form monodisperse nanoparticles without a stabilizer, the presence of Paclitaxel and Neprilysin drugs led to polymer agglomeration. This can be caused if Paclitaxel and Neprilysin break down during water penetration into the dialysis tubes, thus creating charged groups which interact with the charged polymer via electrostatic forces, and cause polymer agglomerates/precipitates before particle formation. The addition of PVA possibly stabilized the particles by coating them. Zhang and Feng (2006) synthesized Paclitaxel loaded NPs via dialysis but no reference to drug denaturation was given. Drug free nanoparticles prepared in the presence of PVA stabilizer, were spherical (Figure 7.11) with less than 90 nm radius (Table 7.5). They are smaller than surfactant free NPs (Table 7.4) implying that PVA decreased polymer-solvent interactions and increased diffusivity of the organic solvent into the aqueous phase. Indeed, PVA acted as a stabilizer similarly to w/o emulsion-diffusion or evaporation synthesis techniques where an emulsifier/stabilizer is required to prevent particle aggregation. An increase in the PVA concentration up to 0.1% led to even smaller particles which is consistent with other studies (Feng and Huang, 2001; Feczkó et al., 2011).

Summarizing, it was found that dialysis method leads to formation of small particles, as compared to the other methods, therefore it seems a promising method for CED studies. For this reason, it will be studied in more detail in the following sections for encapsulation of hydrophobic and hydrophilic drugs. However, as the presence of drugs can influence the size of the particles, but at the same time the synthesis method has a great effect on the drug encapsulation efficiency, the other formulation techniques will be also adopted but in less extent.

7.8.2 Charge of nanoparticles

The NPs used for CED studies must have a high negative charge to ensure particle stability and allow high volumes of distribution in the brain. As the charge of the cell membrane is negative, formulation of positively charged particles would result in the distribution of particles only at the site of injection. Moreover, if the particles are not stable, for example they have a low charge, they will agglomerate/precipitate easily.

All formulations synthesized via simple mixing, nanoprecipitation and dialysis resulted in negatively charged NPs. During particle formation the more hydrophilic (negatively charged) carboxyl groups of the polymer are predominantly facing the water-polymer interface during water migration into the polymer-solvent mixture. This explains why in the dialysis method, the highest hydrophilic solvent, DMSO (dielectric constant: 46.7, 298 K (anone)) resulted in higher negatively charged NPs compared to DMF (dielectric constant: 32.7, 298 K (anone)). Surprisingly, the acid-ended polymer resulted mainly in lower charge compared to the ester-ended polymer (Table 7.4). This suggests that there are additional to the electrostatic solvent behaviour factors accounting for the surface charge of the NPs. For example it could be the lactic/glycolide monomer ratio present in each polymer, affecting the number of the hydrophobic/hydrophilic groups respectively. Even though, both polymers have a 50:50 monomers ratio (company specification) the real value might differ, depending on the batch co-polymerization efficacy. Nanoparticles synthesized via simple mixing exhibit less negative charge compared to dialysis when PLGA polymer is dissolved in MeCN (Table 7.5). This is because the carboxyl groups of the

PLGA polymer are shielded by the mPEG-DSPE lipid. RG504 and RG504H nanoparticles have similar charge (within the error range) suggesting that similar amount of lipid was required to stabilize and coat the different polymers. Nanoprecipitation, led to much lower negative charge and this is due to the positively charged PLL, coating the PLGA core. Less PLL was required to stabilize the ester-ended NPs compared to the acid-ended ones (Yallapu et al., 2010).

To sum up, NPs formed via the aforementioned methods were all negatively charged, however, the charge decreased in the presence of stabilizers, especially when positively charged ones were used.

7.8.3 Pore characterization of nanoparticles synthesized via dialysis method

Regarding, the morphological and pore characterization of the NPs synthesized from ester-ended PLGA polymer dissolved in DMSO via dialysis, nitrogen and krypton sorption studies provide evidence that all the gas molecules were adsorbed on the external surface of the NPs. There are three possible reasons for this 1) there exist no pores within the NPs, 2) there are weak interactions between the gas molecule and the polymer chains, preventing multilayer adsorption, or 3) NPs consist of a porous core but a nonporous shell, hence gas molecules will only be adsorbed on the NP outer surface or within the interparticle voids created from particle agglomeration after freeze-drying. Tomo-TEM experiments of the same formulation prove that NPs are spherical and have a rough external surface. However, there exists no evidence of pores in the core, down to the resolution limits (4 nm) of this imaging technique. The porous structure of PLGA particles is created when internal water droplets evaporate after drying leaving behind void spaces. If NP solidification during synthesis is rapid or/and the polymer walls collapse after drying, it is possible that these pores will not be accessible to water when re-dispersed in aqueous phase due to the high hydrophobic nature of the polymer (Yang et al., 2000). Moreover, Messaritaki *et al*. (2005) found that freeze drying decreases the number of core pores, restricting water penetration. Other authors conducted nitrogen and krypton sorption studies to characterize the porous structure of PLGA nanoparticles

synthesized via emulsion solvent evaporation or double emulsion techniques (Wu et al., 2012; Wang et al., 2010; Sant et al., 2008; Buske et al., 2012; Sant et al., 2005). These authors though, ignored the possibility of gas condensation within the interparticle space despite the fact that their observed specific pore volumes were small or the pore size distribution was contradicting the DLS particle size measurements and the imaging results.

NMR cryoporometry melting curves (Figure 7.14) show an increase in the total volume of water melting before the bulk, after 4 days of immersion in water. This could be interpreted as an increase in the amount of water diffusing within the polymer matrix. However, the signal-to-noise-ratio of the NMR spectra for the low temperature range (241-258 K) was low (~9). At higher temperatures and after 4 days, water melts close to the bulk melting. Applying the Gibbs-Thompson equation to both melting curves using k_{GT} =26 nmK (Perkins et al., 2010), the size of the ice crystals melting at 241-262 K and 241-272.9 K would correspond to void spaces of 0.9-2.36 nm and 0.9-260 nm respectively. However, pores over 4 nm were not observed in the tomo-TEM imaging technique.

Therefore, it is not certain whether water melting at low temperatures can be attributed to the presence of small pores and necks ~0.9 nm not visible in the TEM or tomo-TEM imaging. At higher temperatures, there will possibly be interparticle water melting instead of water within big pores. Particles after freeze drying become aggregated (Figure 7.8a) thus forming void spaces of diameter at least of 1/6 of the particle size (200/6=33 nm); these will freeze and melt (at 272.22 K) similarly to big pores. The increase in volume fraction of molten water is explained as redistribution of NPs within the aqueous suspension, due to interaction of surface polymer groups with water. Alternatively, it can be due to structural change of NPs themselves after repeated freeze-thaw cycles (Allen et al., 1998). It must be noted that these results were not reproducible for other samples synthesized via the same method where only insignificant NMR signal (with respect to S/N ratio) was observed below 273 K. Petrov *et al.* (2006) also used NMR cryporometry to investigate pore size distribution of PLGA microparticles in aqueous environment after 1-4 days. These authors though, used different samples to

study the hydration levels of the polymer matrix for each period of time neglecting the intra-batch variability effect and NP aggregation levels. Moreover, optimization of the NMR receiver gain (RG) parameter, will differ according to the total amount of water present in the NMR tube, leading to false interpretation of molten fractions (thus pore volumes) at each temperature, if precise calibration of signal intensity had not been done.

Summing up, a combination of pore characterization techniques such as TEM and tomo-TEM imaging, nitrogen and krypton sorption and NMR cryoporometry, were used to investigate the morphological and intraparticle structural organization of PLGA NPs synthesized via dialysis method. The external surface of the NPs was rough, but there was no concrete evidence of pores present within these NPs up to the resolution limits of each technique adopted.

7.9 Results. Drug loaded nanoparticles

7.9.1 Size and surface charge of nanoparticles

In Section 7.7 it was shown that dialysis, simple mixing and nanoprecipitation methods gave promising results for creating NPs of the desired shape, size and charge for convection-enhanced drug delivery into the brain. Therefore these methods were further used to synthesize drug loaded NPs with an aim to optimize their size, charge and encapsulation efficiency for CED studies. Hydrophobic (NR) and hydrophilic (TFMU, Rhd, FITC-Dextran) model drugs, and clinically used hydrophobic (Paclitaxel) and hydrophilic (5-FU, NEP) drugs were loaded into the NPs.

The ester-ended NR loaded nanoparticles synthesized via the dialysis method, increase in size and negative charge in the order DMSO<MeCN<DMF (Table 7.7). NR loaded NPs formulated in DMSO and MeCN decrease in size and charge compared to the drug-free NPs (Table 7.4), whereas NPs formed in DMF increase in size and charge. Although the zeta potential is not a direct measure of the surface charge density it self, it changes when the surface charge changes. Any added species, such as NR, change the surface

chemistry and thus will cause some change on the zeta potential. The acid-ended NR loaded particles increase in size in order MeCN<DMSO<DMF but their charge increases in the inverse order. This shows that the charge is controlled primarily by the solvent-polymer-NR interactions during particle formation and the subsequent arrangement of carboxylic groups within the NP core. Also, both the size and the charge of RG504H NPs increased after NR encapsulation. When Paclitaxel was present in the NP synthesis, the size also increased proving that Paclitaxel allows the particles to fuse more readily, instead of stabilizing small particles. Increasing the PVA concentration, the size decreased, indicating that PVA stabilized the interface between the particles and droplets better, preventing their fusion and as such formation of larger particles. Nile Red encapsulation on the RG504/mPEG-DSPE NPs increased their size and charge too (Tables 7.7 and 7.8).

Synthesis method	**Nanoparticle formulation**	**Solvent**	**Loaded agent**	**Mean particle size, *r*±SD (nm)**	**Zeta potential, ζ±SD(mV)**
Dialysis	RG504	DMSO	NR	98.15±2.1	-30.4±0.7
	RG504	MeCN	NR	109.9±4.9	-34.7±1.0
	RG504	DMF	NR	147.1±0.8	-40.1±2.7
	RG504H	DMSO	NR	99.66±2.4	-40.2±1.2
	RG504H	MeCN	NR	93. 90±4.1	-47.4±2.1
	RG504H	DMF	NR	115.0±0.7	-35.3±0.7
	RG504 (0.05 % PVA)	DMSO	Paclitaxel	133.7±0.02	
	RG504 (0.1 % PVA)	DMSO	Paclitaxel	129.9±1.8	
Simple mixing	RG504 /mPEG-DSPE	MeCN	NR	137.9±1.0	-64.9±1.2

Table 7.7 Mean (hydrodynamic) radius and zeta potential of NPs loaded with hydrophobic agents

Synthesis method	Nanoparticle formulation	Solvent	Loaded agent	Mean particle size, *r*±SD(nm)	Zeta potential, ζ ±SD(mV)
Dialysis	RG504	DMSO	TFMU	179.9±4.1	
	RG504	MeCN	TFMU	167.1±7.4	
	RG504	DMF	TFMU	104.5±1.7	
	RG504H	DMSO	TFMU	135.7±19.5	-28.4±0.8
	RG504H	MeCN	TFMU	247.5±9.5	-57.6±0.7
	RG504H	DMF	TFMU	167.2±3.8	
	PLGA-PEG	DMSO	TFMU	159.6±3.3	-48.9±1.4
	PLGA-PEG	DMF	TFMU	152.7±5.9	-36.5±0.7
	RG504	DMSO	FITC-Dextran (70 kDa)	108.2±15.0	
	RG504	DMSO	FITC-Dextran (150kDa)	104.1±3.4	
	RG504	DMSO	5-FU	105.5±17.8	
	RG504	DMF	5-FU	118.8±3.4	
	RG504H	DMSO	5-FU	108±5.2	
	RG504H	DMF	5-FU	102.1±3.5	
	RG504	DMSO	NEP (125:1)[a]	145.5±1.3	
	RG504	DMSO	NEP (151.5:1)[a]	157.7±3.9	
	RG504	DMSO	NEP (251:1)[a]	119.9±1.8	

Table 7.8 Mean size and zeta potential of NPs loaded with hydrophilic agents as synthesized via dialysis method. [a]: refers to PLGA:NEP ratio

Encapsulation of hydrophilic drugs into PLGA nanoparticles, as synthesized via dialysis, generally increased the particle size (TFMU, NEP) or they influenced it slightly (5-FU, FITC-Dextran) as shown in Table 7.8. Again, the particle size is highly dependant on the solvent, the polymer end group and the MW of the drug. There is no specific trend of the solvent behaviour when comparing ester and acid ended polymers, although it obvious that the size of PLGA particles is smaller for small MW molecules such as 5-FU (MW: 130 g/mol) compared to high MW proteins such as NEP (110 kDa). TFMU loaded nanoparticles formed from conjugated PLGA-PEG polymer had similar sizes in DMF and

DMSO, showing the insignificant effect of solvent nature on the NP size. All types of formulations led to negatively charged NPs and its value was following the trend of particle size.

Encapsulation of hydrophilic molecules via simple mixing increased the size of NPs as seen form Table 7.9. TFMU decreased only slightly the negative charge of the NPs which is expected if the molecules are adsorbed on the surface of the NPs. Rhodamine B loaded NPs despite their smaller size (~129.3 nm) compared to the TFMU loaded ones (~157-198 nm), exhibit higher negative charge (~-50.3 mV). Rhodamine B is a positively charged molecule and it would be expected to be adsorbed on the lipid shell by hydrophilic interactions with the PEG groups, thus reducing the total surface charge, compared to the drug free nanoparticles (~-26 mV). Also, if the electrostatic interactions were stronger and Rhd was attached onto the carboxyl groups of the PLGA or the methoxy and phosphate part or of the lipid, their negative charges would be cancelled out.

Synthesis method	**Nanoparticle formulation**	**Solvent**	**Loaded agent**	**Mean particle size, r (nm) ± SD**	**Zeta potential, ζ (mV) ± SD**
Simple mixing	RG504 /mPEG-DSPE	MeCN	TFMU	157.5±5.2	-23.45±0.5
	RG504H /mPEG-DSPE	MeCN	TFMU	198.1±7.8	-23.94±0.6
	RG504 /mPEG-DSPE	MeCN	Rhd	129.3±3.8	-50.29±1.1
Nanopreci-pitation	RG504 (PVA, PLL)	Acetone	TFMU	86.39±2.2	-6.16±0.3
	RG504H (PVA, PLL)	Acetone	TFMU	106.3±8.8	**+1.96±0.5**
	PLGA-PEG[a]	DMF	TFMU	82-268	**+35±0.9**

Table 7.9 Mean size and charge of NPs loaded with hydrophilic agents as synthesized via simple mixing and nanoprecipitation methods. Bold font is used to emphasize (the only) positively charged NPs formulated. [a]: there was no PVA or PLL used for this formulation

The use of PVA and PLL stabilizers during nanoprecipitation decreased the surface charge with the RG504H and PLGA-PEG polymer particles exhibiting positive charge. PLL is a positively charged amino acid polymer whereas PVA is non-ionic polymer. An increase towards positively charged surface means that there is a thick PLL shell covering the RG504H core. Moreover, there was more PLL polymer required to stabilize the acid-ended PLGA compared to the ester-ended one (RG504). Such a high positive charge value of PLGA-PEG NPs was unexpected as the PEG groups would neutralize the particles. It could be possible that the sample was contaminated with positively charged ions (ie, from water), but the measurement was not repeated to confirm this result due to time limitations.

7.9.2 Encapsulation efficiencies

Total theoretical drug loading and encapsulation efficiencies for hydrophobic and hydrophilic agents are summarized in Table 7.10 and Table 7.11 respectively. Loading efficiencies varied according to the formulation method adopted, solvent, polymer end-group and hydrophilicity and size of drug molecule.

Synthesis method	Nanoparticle formulation	Solvent	Loaded agent	TDL	% EE
Dialysis	RG504	DMSO	NR	0.0004	11.09
	RG504	MeCN	NR	0.0004	50.35
	RG504H	DMSO	NR	0.0004	25.95
	RG504H	MeCN	NR	0.0004	63.39
	RG504 (0.05% PVA)	DMSO	Paclitaxel	0.09	IE[a]
	RG504 (0.1% PVA)	DMSO	Paclitaxel	0.09	IE[a]
Simple mixing	RG504/mPEG-DSPE	MeCN	NR	0.0004	26.87

Table 7.10 Theoretical drug loading (TDL) and encapsulation efficiency (EE) of hydrophobic drugs for different nanoparticle formulations. IE[a]: insufficient encapsulation as determined from LC-UV-MS and *in-vitro* cell citotoxycity studies

Synthesis method	Nanoparticle formulation	Solvent	Loaded agent	TDL	% EE
Dialysis	RG504	DMSO	TFMU	0.09	0.34
	RG504	MeCN	TFMU	0.09	3
	RG504	DMF	TFMU	0.09	0.66
	RG504H	DMSO	TFMU	0.09	0.50
	RG504H	MeCN	TFMU	0.09	3.23
	RG504H	DMF	TFMU	0.09	0.94
	PLGA-PEG	DMSO	TFMU	0.09	0.77
	PLGA-PEG	DMF	TFMU	0.09	0.92
	RG504	DMSO	5-FU	0.1	0.0004
	RG504	DMF	5-FU	0.1	0.02
	RG504H	DMSO	5-FU	0.1	0.0057
	RG504H	DMF	5-FU	0.1	0
	RG504	DMSO	FITC-Dextran (70 kDa)	0.09	5.94
	RG504	DMSO	FITC-Dextran (150 kDa)	0.09	2.67
	RG504	DMSO	NEP (125:1)[b]	0.008	IE [a]
	RG504	DMSO	NEP (151.5:1)[b]	0.007	IE [a]
	RG504	DMSO	NEP (251:1)[b]	0.004	IE [a]
Simple mixing	RG504/mPEG-DSPE	MeCN	TFMU	0.07	4.70
	RG504H/mPEG-DSPE	MeCN	TFMU	0.07	3.82
	RG504/mPEG-DSPE	MeCN	Rhd	0.0001	1.25
Nanopreci-pitation	PLGA-PEG	DMF	TFMU	0.09	2.17
	RG504 (PVA, PLL)	Acetone	TFMU	0.08	6.75
	RG504H (PVA, PLL)	Acetone	TFMU	0.08	5.93

Table 7.11 Theoretical drug loading and encapsulation efficiency of hydrophilic drugs for different NP formulations. IE[a]: insufficient encapsulation as determined from the *in-vivo* brain tissue studies (ELISA assay).

Nile red loading efficiency was higher when nanoparticles were formed in MeCN and acid-ended PLGA polymer. On the contrary, hydrophobic Paclitaxel was not efficiently

encapsulated in the NPs regardless the concentration of PVA used, indicating that the presence of the stabilizer only participated on the emulsification process to prevent polymer aggregation rather than improve Paclitaxel adherence onto the polymer. Paclitaxel molecules must have either broken down, or diffused out of the dialysis bag (due to its small MW) before the particles were formed.

TFMU loaded spheres increased their EE in the synthesis method order: dialysis < simple mixing < nanoprecipitation, as shown from Table 7.11, implying that use of emulsifiers such as PVA, PLL and lipids are necessary to improve drug EE. For the dialysis method, samples prepared from acid-ended PLGA polymer in MeCN resulted in the highest EE, similarly to the Nile red. Conjugation of PEG groups onto the PLGA polymer increased only slightly the EE to 0.77-0.92%, compared to the pure PLGA polymer, 0.34-0.94% as synthesized via dialysis, but led to 2.17% for nanoparticles prepared via nanoprecipitation, without the presence of stabilizers. On the contrary, hydrophilic 5-FU loading efficiency was low (0-0.02%). Overall, small MW hydrophilic drug molecules diffused rapidly out of the dialysis tube (MWCO: 12,000) before particle formation. Introduction of lipid as molecular moieties offering hydrophilic sites onto the PLGA polymer shell, increased the TFMU encapsulation efficiency, but this was not the case for Rhodamine whose EE was poor (0.37%).

In order to comprehend whether it is the fast migration of small drug molecules before particle stabilization or the affinity of the drug molecule towards the polymer the key parameter to control EE, in dialysis method, FITC-dextran (MW: 70-150 kDa) and NEP (MW: 110 kDa) were used as loading agents. Table 7.11 shows that both dextran and protein had poor EE, implying that both molecules had low affinity towards the hydrophobic PLGA polymer.

7.9.3 *In-vitro* TFMU and NR release studies

TFMU release studies in PBS (pH 7.4, 311 K) were conducted for four different nanoparticle formulations to investigate the effect of emulsifiers and hydrophilic groups onto the TFMU release. Table 7.11 shows both EE and the total drug released increased

as the NP size decreased and that PLGA-PEG had the lowest amount of TFMU released within 187 h.

Synthesis method	Nanoparticle Formulation /solvent	Size, *r*±SD(nm)	%EE	% Total drug released[a]	% Drug unreleased[b]	%Drug loss[c]
Dialysis	RG504 / MeCN	237.2±7.7	3	36	58	6
Simple mixing	RG504 /mPEG-DSPE / MeCN	157.5±5.1	4.70	34	52	14
Nanopreci-pitation	PLGA-PEG / DMF	82-268	2.17	11	87	2
	RG504 (PVA, PLL) /Acetone	86.4±2.2	6.75	44	17	39

Table 7.12 Fractions(%) of encapsulated, released and unreleased TFMU from NPs synthesized from ester-ended PLGA polymer and conjugated PLGA-PEG polymer. [a]: Total drug released(%) = 100x(mass of cum. drug released)/(mass of encapsulated drug), [b]: Measured via UV-vis by dissolving the NPs in DMF at the end of the release studies, [c]: Drug loss(%) = 100-(total drug released + drug unreleased)

All the formulations gave a burst release (Figure 7.14) within the first 4 h and then a retarded controlled release. This means that a high concentration of TFMU was located onto the surface of the NPs. However, only 11% of the encapsulated drug was released from the PLGA-PEG NPs suggesting high hydrophilic interactions of TFMU with the PEG groups of the polymer or that TFMU is mainly distributed within the PLGA core. Alternatively, its burst release could be initiated from the small particles and delayed by the big ones, as the NPs have a wide particle size range (82-268 nm).

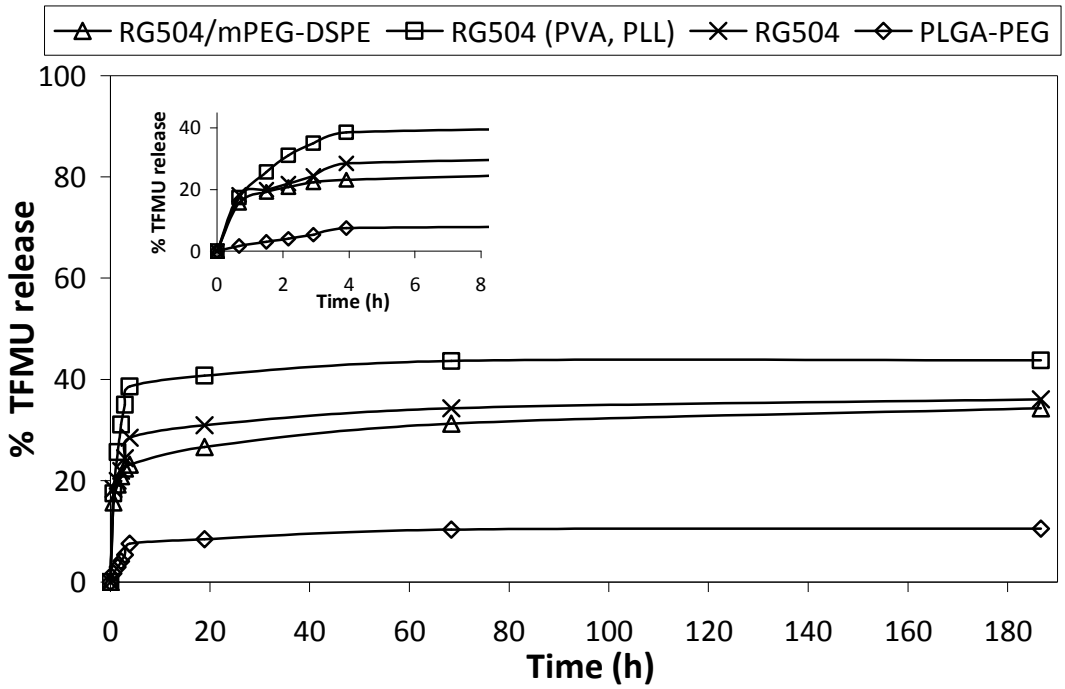

Figure 7.14 Cumulative TFMU release profile from different NP formulations in PBS (pH 7.4, 38^{o}C) over time. The inset graph shows a burst release of TFMU within the first 4 h

On the contrary, hydrophobic NR was not released from RG504 (DMSO and MeCN) NPs suspended in AcSF, at 311 K over 1.2 months. UV-vis measurements performed on the collected AcSF aliquots at different periods of time, showed no absorbance in the UV-vis. Total concentration of NR within the nanoparticles remained the same before and after the release studies as further measured by UV-vis. This shows that hydrophobic NR-polymer interactions prevented NR diffusivity throughout the polymer matrix and that no polymer degradation, that would facilitate NR release, occurred during this period of time. Blanco *et al.* (2006) found that drug-free PLGA microspheres (lactic:glycolic=50:50, MW~39,000 g/mol), had a fast degradation rate the first 1.4 months of incubation and a slower degradation thereafter. Complete degradation was reached within 2 months of incubation, although, the particle degradation time are subject to vary according to the size of the particles and the MW of the polymer used.

7.10 Discussion. Drug loaded nanoparticles

This section will discus the experimental results obtained from the drug encapsulation and the *in-vitro* release studies. The synthesis methods will be compared in order to

evaluate which of them is the most efficient to optimize the encapsulation efficiency, the size and the charge of the NPs for CED studies. Moreover, an interpretation of the effect of the encapsulated hydrophilic and hydrophobic drugs drugs, or their presence during the synthesis, in the morphological characteristics of the particles as compared to the drug-free particles will be provided in this section.

7.10.1 Size and charge of nanoparticles

Drug loaded NPs can be successfully formulated having the desired size and charge required for CED into the brain. However, the size and charge of the drug loaded NPs are influenced by a combination of factors namely synthesis method, solvent, polymer end group, the hydrophilicity of the loaded/present agent, its molecular weight and the drug encapsulation efficiency, rather than by each of them separately.

Encapsulation or the presence of hydrophobic molecules (NR, Paclitaxel) into NPs synthesized via dialysis and simple mixing, overall led to an increase of the particle size. This is attributed to the different interactions between the polymer and drug and their solubility in water or organic solvent as previously reported by others (Panyam et al., 2004; Govender et al., 1999). The zeta potential of NPs also increased showing that any intraparticle interactions between the polymer chains and NR, changed the surface chemistry of the particles after NR encapsulation. The zeta potential of the PLGA/mPEG-DPSE NPs increased after NR encapsulation, providing more stability to the particles. It is therefore seen that encapsulation or the presence of hydrophobic drugs during NP synthesis overall increases the size and the charge of the particles, enhancing their stability in aqueous suspensions.

Encapsulation or presence of hydrophilic drug molecules during NP synthesis via dialysis increased (TFMU, NEP) or had little effect (5-FU, FITC-Dextran) on the particle size. It must be the size of the drug molecule itself and its concentration that increased the overall size of the particles- the hydrophobic PLGA polymer chains are more spread as they will be opposing the hydrophilic drug molecules, hence the NP will tend to ‘swell’.

Especially in the case of FITC-Dextran, the MW is higher (70 kDa, 150 kDa) than that of the PLGA polymer it self, thus the molecular size of the drug will contribute onto the total particle size. The EE of NEP and 5-FU was insignificant, as seen from Table 7.11, but their presence during synthesis influenced the equilibrium and solvent-drug-polymer interactions and consequently the mean size of the NPs. The TFMU and Rhodamine loaded NPs formed via simple mixing were bigger than those formed via nanoprecipitation possibly due to less stabilization of the former by the lipid as compared to the PVA and PLL in the latter system.

Positively charged TFMU loaded NPs (+1.96 mV) were formed via nanoprecipitation implying that positively charged PLL is highly adsorbed onto the NP surface and in combination with PVA are shielding the carboxyl polymer groups. This type of NPs can easily adhere onto the negatively charged membrane-bound oligosaccharides of the cells and get taken up through endocytosis at the site of injection, rather than distribute at high volumes of brain tissue.

Conjugation of PEG groups onto PLGA polymer also increased the particle size via dialysis (152-159 nm) and led to a wide size distribution after nanoprecipitation (82-268 nm). Avgoustakis *et al.* (2003) reported a decrease in the size and charge of drug-free PLGA NPs after PEGylation but an increase in NP flocculation as the PEG:PLGA ratio increased. It is thus possible that PEG groups in conjunction with the TFMU presence result in more aggregated structures.

7.10.2 Drug encapsulation efficiencies and release profiles

Drug loading efficiencies varied according to the synthesis method, drug hydrophilicity and structure, polymer end-group, solvent and stabilizers (Tables 7.9 and 7.10). NR and Paclitaxel as highly hydrophobic molecules were expected to strongly attach onto the PLGA polymer. However, there was no detectable Paclitaxel encapsulated into the spheres compared to NR which had ~11-63% EE, depending on the formulation (Table 7.9). It must be that Paclitaxel was more miscible with the solvent compared to the

polymer (Panyam et al., 2004) and hence it diffused out of dialysis bag before particle formation. This is in contrast to the results found by Zhang and Feng (2006) who measured 60% EE for Paclitaxel loaded in NPs synthesized via the same method but in the absence of PVA in the dialysis bag. PVA was chosen to prevent polymer precipitation prior to NP formation. Higher NR loading efficiency for slightly less hydrophilic acid-ended PLGA polymer is perhaps due to a higher microporous area compared to the ester-ended polymer, rather than stronger NR-polymer interactions. Also, during dialysis, it is likely that NR is more soluble in DMSO compared to MeCN thus it is diffusing out of the dialysis bag faster compared to NR dissolved in MeCN. The presence of lipid during nanoprecipitiation also led to fast stabilization of the NPs reducing NR precipitation into the aqueous phase. NR did not release from ester-ended PLGA NPs synthesized in DMSO or MeCN, within 1.2 months of release studies into AcSF medium, which could be due to 1) stronger NR-polymer hydrophobic interactions compared to its mass transport into the aqueous phase, 2) highly tortuous microporous matrix that restricts NR diffusivity out of the particle, and 3) no polymer degradation under those experimental conditions.

Hydrophilic molecules had, overall, low encapsulation efficiency via dialysis, 0.33-3.2 % for TFMU, 2.7-5.9% FITC-Dextran and less than 0.02% for 5-FU. This shows that molecules with similar molecular structure (Figure 7.4) such as the fluorinated drugs have different affinity towards the polymer and solvent. Ester-ended PLGA polymer is slightly less hydrophobic, hence, TFMU loading is lower compared to the acid-ended polymer. Dextran molecules do not diffuse out the dialysis membrane (MW higher than MCOFF of the membrane) and subsequently the probability of colliding with the polymer is high. This explains their high EE compared to the small molecules. Low loading efficiencies of FITC-Dextran (~0.24 %w/w) in microspheres was reported by Kim and Park (2004) following w/o/w emulsion but, 55-100% EE was reported by Mao *et al.* (2007) depending on the polymer end-group, PVA and PLGA concentration, the MW of the drug and the theoretical drug loading. Mao *et al*. also found that dextran loaded microparticles had a high internal and low external porosity for ester-ended polymer, but the inverse porosity for acid-ended polymer, which could be manipulated by varying the particle drying process. 5-FU loaded nanoparticles were also prepared by other authors (Boisdroncelle et al., 1995) who found that EE of 5-FU is predominantly controlled by the solvent ratios

and the size of the microparticles–the faster the polymer deposition, the higher the EE. For NEP loaded nanoparticles, NEP ELISA assay performed in brain tissue, post infusion in the brain, showed that there was no detectable increase in the NEP concentration in the infused hemisphere compared to the contralateral non-infused control hemisphere. This indicates there was low or no encapsulation of NEP into the nanoparticles, or there was no NEP release enhanced by particle degradation under this experimental conditions (experiments were performed and analysed by Neil Barua). PVA was introduced in the dialysis tube prevented polymer precipitation, but it is possible that NEP degraded in the presence of DMSO. Degradation of proteins in high concentrations of DMSO has been previously reported by (Arakawa et al., 2007) or, by other degradation mechanisms previously reviewed by van de Weert *et al.* (2000) (i.e. interactions with DMSO, storage, NP drying). Alternatively, NEP may have remained at the solvent/water interface, attached onto the PVA rather than being adsorbed onto the PLGA polymer, if more preferential interactions with PVA were facilitated.

It is apparent that smaller sized TFMU loaded NP had higher EE, which is true when intraparticle surface area is big (Table 7.11). The micropore size is dependent on the size of water droplets during NP synthesis. Their connectivity though, is controlled by the pathway undertaken by the vapour phase formed from ice crystals following sublimation (Mao et al., 2007), which is further affected by the presence of any groups attached onto the NPs. Burst drug release is attributed to the presence of drug molecules on the particle surface whereas the sustained release is controlled by their inner morphology and the presence of additional functional groups onto the particle, that would increase or decrease particle hydration. Thus, it is both the core and the shell morphology, and the size of the NPs that controls the TFMU release. Figure 7.12 shows that all NPs initially had a fast release within 4 h but a similarly sustained release afterwards. The latter is true when the diffusion time constant ($15D_{eff}/r^2$), and thus the ratio of the drug effective diffusivity to the particle size, is similar for all types of formulations as described by the Linear Driving Force model, shown by equation 6.6. Inherently this would mean that the small NPs (RG504(PVA, PLL)) have highly tortuous interconnected micropore channels that provide pronounced restrictions to TFMU diffusivity compared to the bigger NPs (PLGA-PEG). The TFMU concentration on the NP surface decreased in order

PLGA-PEG<RG504/lipid<RG504<RG504(PVA,PLL) whereas their pore sizes are expected to decrease in the inverse order to explain the release profiles obtained. Alternatively to this, TFMU release is also controlled by the PEG, PVA and PLL groups. Slow release from PLGA-PEG NPs can be attributed to possible arrangement of hydrophilic PEG groups along the pore surface, where water droplets were present. Thus a higher concentration of hydrophilic TFMU attached onto those groups will have a retarded release. For PLGA/mPEG-DSPE nanoparticles the lipid shell must be acting as a fence to prevent PLGA core hydration and subsequently TFMU diffusivity out of the spheres via polymer degradation (Chan et al., 2009), hence delaying its release. Hydrophilic PVA and PLL polymer, attached onto the NP surface, as synthesized by nanoprecipitiation, have additionally increased NP hydration and as such more drug released. The dialysis method resulted in low EE of TMFU which most probably was attached onto the surface of the NP judging by the high concentration released at early stages. A third possible interpretation can be given taking into account partial crystallization of TFMU within the NPs, depending on the formulation method, which will decrease its diffusivity towards the aqueous phase (Gref et al., 1994). Messaritaki *et al.* (2005) reported 29-36% EE of TFMU in microspheres synthesized by w/o/w double emulsion method. The authors found that 50% of the loaded drug was released over 2.5 h. It is thus possible that by varying the synthesis method and stabilizing agents, hydrophilic drug concentration and release can be controlled.

In summary, it was found that dialysis method seems promising for encapsulation of hydrophobic molecules whereas nanoprecipitation method is more efficient for encapsulation of hydrophilic drugs. The encapsulation efficiency of hydrophilic molecules via dialysis, can be increased by conjugating PEG groups in the PLGA polymer, although the size of the nanoparticles is beyond the required one for CED into the brain. In general, encapsulation or the presence of hydrophobic drugs during the NP synthesis led to negatively charged particles, and in principle it increased as compared to the drug-free NPs. On the contrary, encapsulation of hydrophilic drugs or introduction of stabilizers, which posses a positive charge, decreased the negative charge of the particles which would make them more unstable. Moreover, hydrophobic NR was not released within the time course of the experiment, in contrast to the hydrophilic TFMU which released

rapidly from all types of formulations. This suggests that more prolonged drug release can be achieved for hydrophobic drugs as compared hydrophilic drugs. As the NR and TFMU molecules fluoresce, apart from good hydrophobic and hydrophilic model drugs, they can be used as tracing agents to detect the location of the NPs in the brain or to test the NP uptake from the cells. Therefore, these two agents will be further used in the later sections for *in-vivo* studies

7.11 Results. *In-vitro* and *in-vivo* studies

The previous sections showed that NR loaded NPs synthesised via dialysis had the desired size, charge and encapsulation efficiency for CED studies. Therefore these particles will be further used for CED studies. The slightly bigger NPs, synthesised via simple mixing or after PEG conjugation will be only used for *in-vitro* cell studies to test their uptake from glioma cells. It will be shown that NR loaded particles are efficiently distributed in the brain, at high tissue volumes in contrast to free NR it self, which is only distributed at the site of injection. These results seem promising for further CED studies.

7.11.1 *In-vitro* analysis of glioma cell uptake of drug loaded nanoparticles and cytotoxicity studies

Brightfield and fluorescence images of glioma cells, 24 and 48 h post incubation with drug loaded nanoparticles, were merged to show the degree of intracellular uptake of NP. Figure 7.15 shows that glioma cell uptake of NR loaded RG504 nanoparticles was detected as early as 2 h post incubation. Cell uptake of nanoparticles continued to increase over 48 h as cells are rapidly dividing.

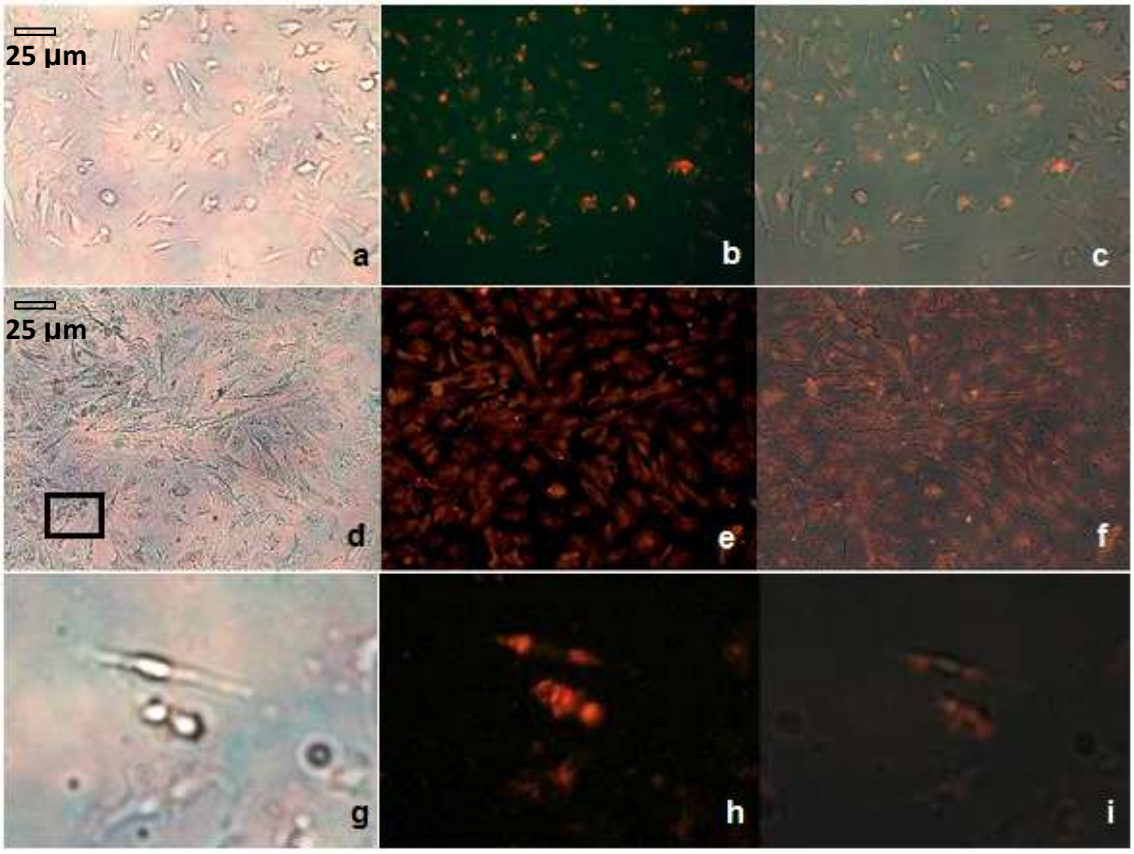

Figure 7.15 Brightfield, fluorescence and merged images of glioma cells incubated with RG504/NR nanoparticles (synthesized via dialysis in DMSO) at 2 h (a, b, c) and 48 h (d, e, f). Magnified image of boxed area in d: Brightfield, fluorescence and merged images (g, h, i)

PLGA-PEG TFMU loaded NPs synthesized via nanoprecipitation, and Rhodamine, NR loaded hybrid RG504/mPEG-DSPE nanoparticles synthesized via simple mixing show different degrees of fluorescence and intracellular uptake 24 h post incubation as seen from Figure 7.16. This is firstly, due to the different encapsulation efficiency of each drug (2.17, 1.25 and 26.87%, respectively) and secondly, due to their charge (+35, -50.29, -64.87 mV) and shell type.

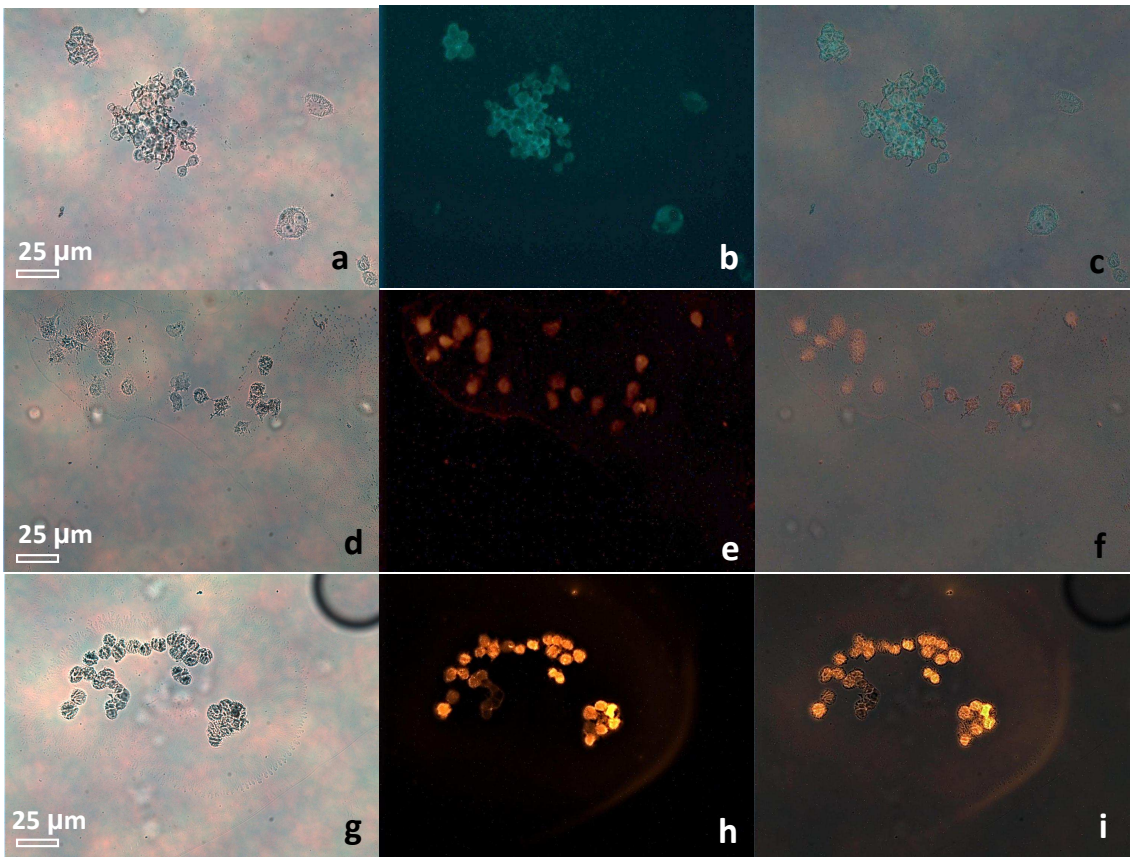

Figure 7.16 Brightfield, fluorescence and merged images of glioma cells incubated with TFMU loaded PLGA-PEG nanoparticles (synthesized via nanoprecipitation) (a, b, c), Rhodamine loaded RG504/mPEG-DSPE (synthesized via simple mixing) (d, e, f) and Nile red loaded RG504/mPEG-DSPE (synthesized via simple mixing) (g, h, i), at 24 h post incubation

Paclitaxel loaded nanoparticles were incubated with a glioma cell line and a methylthiazol tetrazolium (MTT) citotoxicity assay was performed. No increase in cytotoxicity compared to control (PBS) was detected at 24, 48 or 72 h post incubation indicating low (or no) drug encapsulation efficiency. Moreover, MAS spectroscopy measurements showed that there was no Paclitaxel encapsulated in the NPs, down to the resolution limits of this technique.

7.11.2 *In-vivo* CED studies of drug loaded nanoparticles

Convenction-enhanced delivery studies into the rat brain were conducted for unencapsulated NR and NR loaded nanoparticles, as well as for NEP and FITC-Dextran loaded nanoparticles. A summary of the infusions is shown in Table 7.13.

Infusate	Solvent	Concentration (mg/ml)	Volume (µl)	Rate (µl/min)	Target	Number of infusions
NR	MeOH	1	10	2.5	Striatum	2
	MeOH	0.5	10	2.5	Striatum	2
	MeOH	0.1	10	2.5	Striatum	2
RG504/NR	DMSO	1	10	2.5	Striatum	6
	DMSO	0.5	10	2.5	Striatum	6
RG504/FITC-Dextran (70 kDa)	DMSO	1	10	2.5	Striatum	3
RG504/FITC-Dextran (150 kDa)	DMSO	1	10	2.5	Striatum	3
RG504/NEP	DMSO	1	10	2.5	Striatum	3[a]

Table 7.13 Summary of CED infusions into the rat brain. [a]: Number of rats euthanized at 0,1,2,3,4,5 and 6 h post infusion

CED of unencapsulated NR resulted in minimal distribution with the majority of NR restricted to within 500 µm of the cannula track (Figure 7.17). CED of RG504/NR NPs resulted in widespread distribution throughout the striatum and also into the adjacent cortex. Fluorescence microscopy of rat brain sections from animals sacrificed at 1 h (Figure 7.18) and 24 h (Figure 7.19) post infusion confirmed the continuous presence of RG504/NR NPs. There was no evidence of haemorrhage or tissue trauma related to delivery of PLGA NPs in any animal.

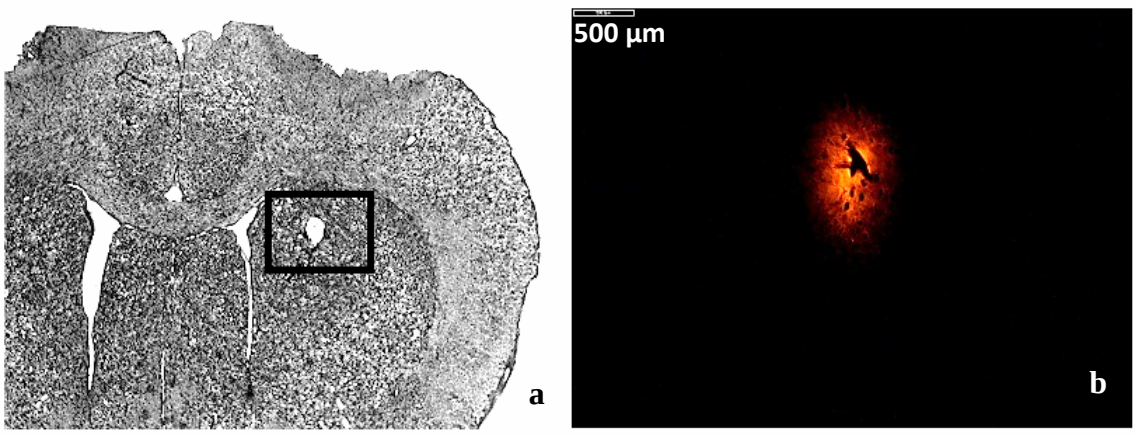

Figure 7.17 CED of 1 mg/ml unencapsulated Nile red into the striatum of rat brain. The images show a) the site of injection and b) the Nile red distribution around it

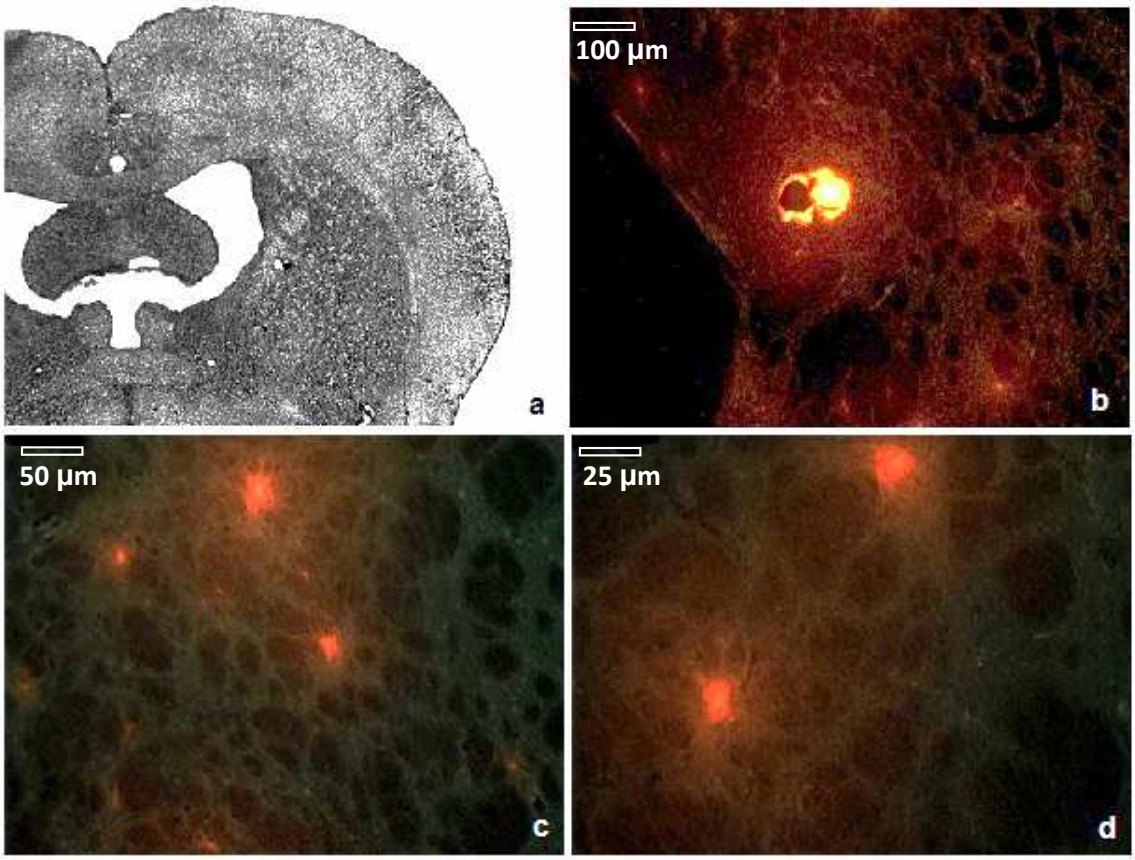

Figure 7.18 CED of 0.5 mg/ml Nile red loaded RG504 NPs (synthesized via dialysis in DMSO). Brightfield (a) and fluorescence images at different maginifications (b,c,d) 1 h post infusion

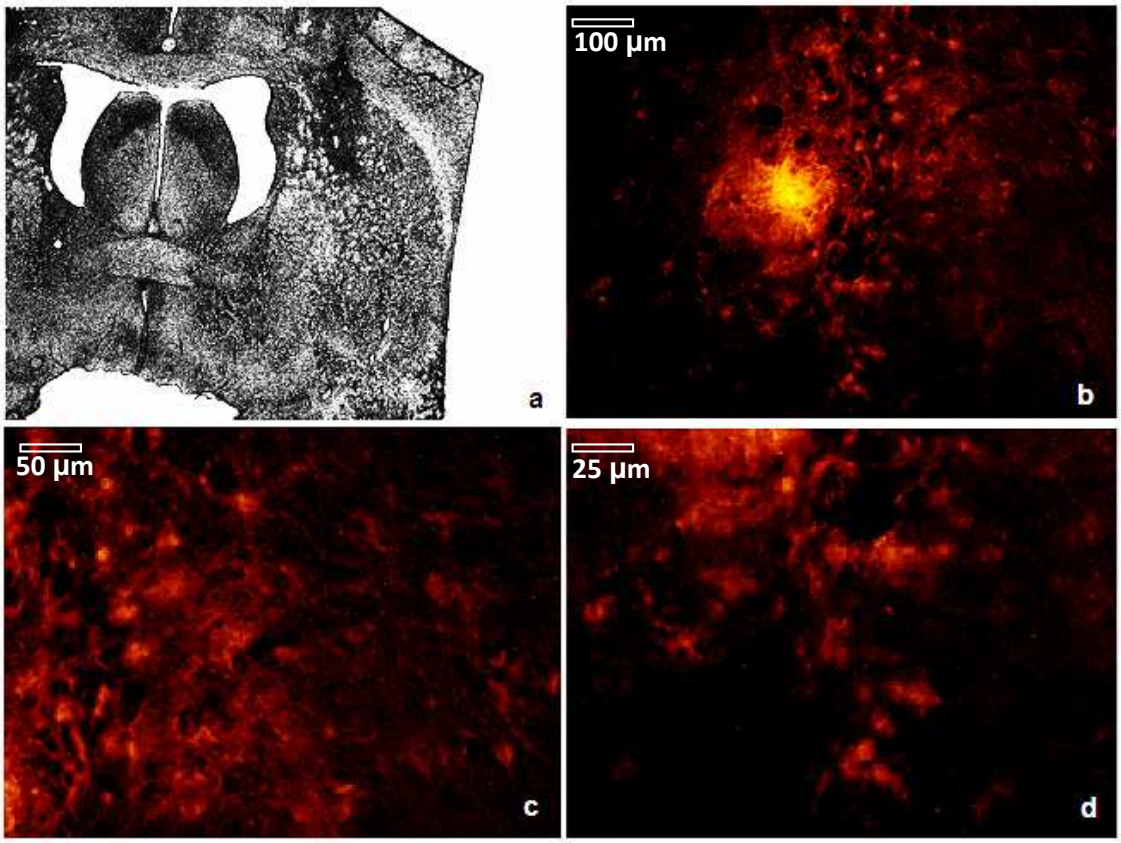

Figure 7.19 CED of 0.5 mg/ml Nile red loaded RG504 NPs (synthesized via dialysis in DMSO) Brightfield (a) and fluorescence images at different maginifications (b,c, d) 24 h post infusion

The mean volume of distribution following CED of 0.5 mg/ml unencapsulated NR was 4.14 mm^3, and 0.91 mm^3 for 1 mg/ml NR. The volume of distribution following CED of 0.5 mg/ml PLGA/NR was 51.02 mm^3, and 42.58 mm^3 for 1 mg/ml PLGA/NR. There was therefore a statistically significant increase of distribution for CED of 0.5 mg/ml RG504/NR compared with unencapsulated NR (p=0.01, Student's t-test). The volumes of distribution (Vd) and the ratio of Vd to the volume of infusion (Vi) are shown in Figures 7.20 and 7.21.

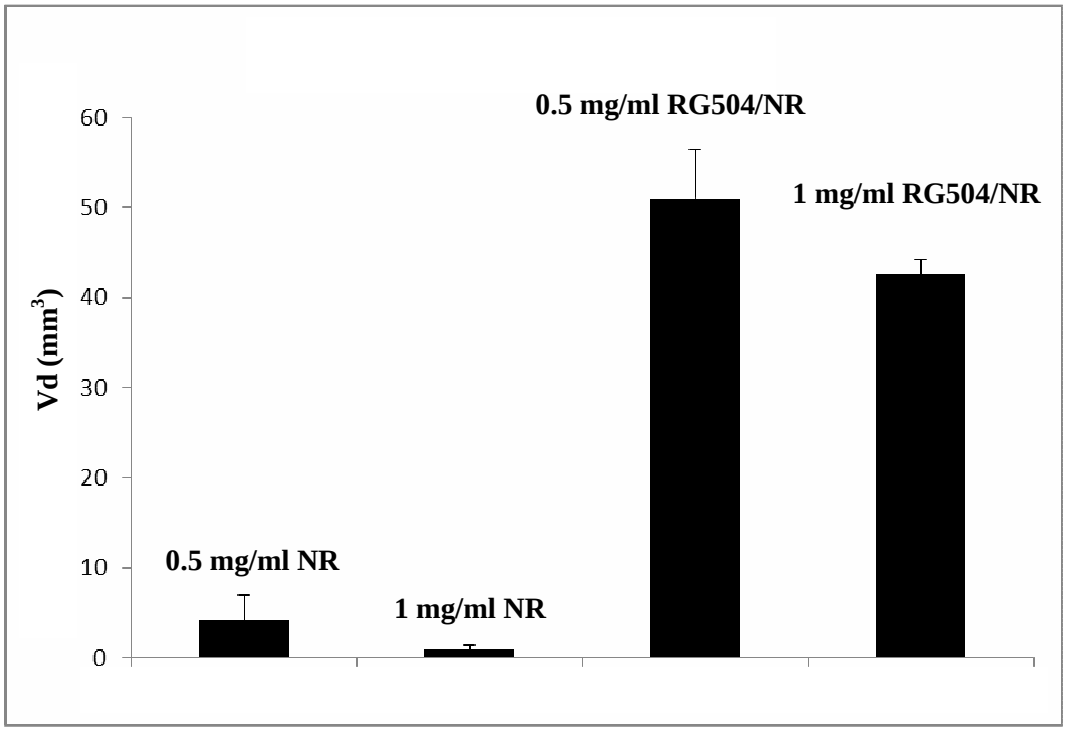

Figure 7.20 Volumes of distribution (Vd) following CED of NR and RG504/NR NPs (synthesized via dialysis in DMSO)

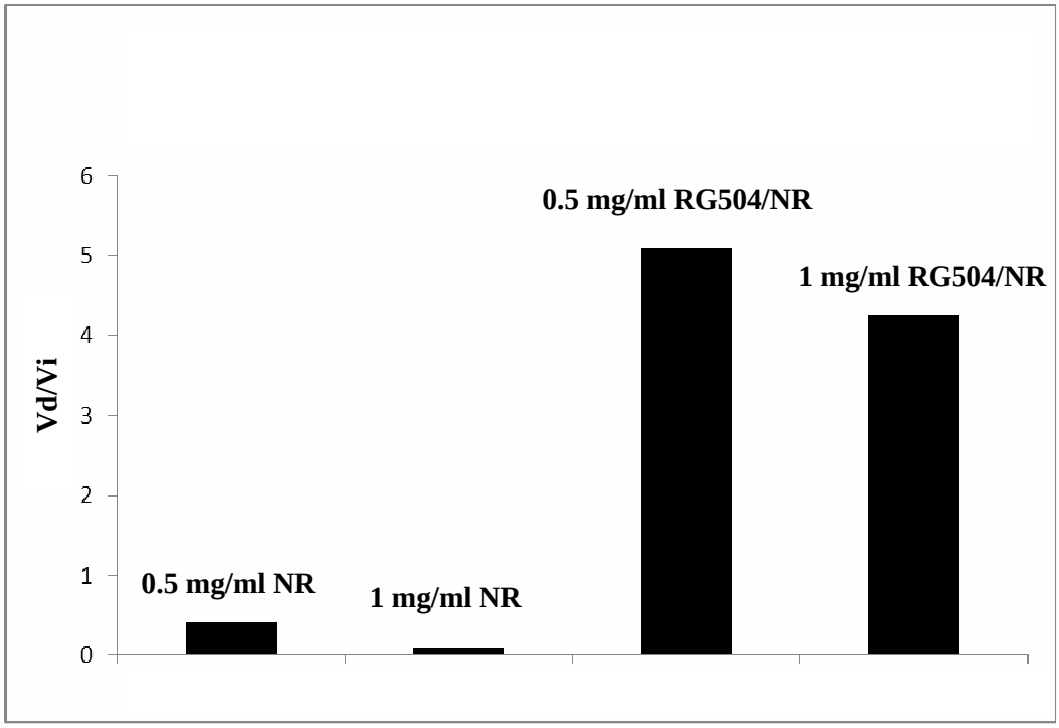

Figure 7.21 Ratio of volume of distribution /volume of infusion (Vd/Vi) following CED of NR and RG504/NR NPs (synthesized via dialysis in DMSO)

For FITC-Dextran loaded nanoparticles there was no detectable increase in the fluorescence in the infused brain hemisphere compared to the control brain hemisphere indicating that the encapsulation of FITC-Dextran was lower than the threshold detectable by standard fluorescence microscopy of brain tissue sections.

NEP ELISA assay (as discussed in Section 7.10.2) showed that there was no detectable increase in NEP concentration in the injected part of the brain revealing that EE of NEP in PLGA NPs was insignificant.

7.12 Discussion. *In-vitro* and *in-vivo* studies

Successful convection-enhanced drug delivery into the brain was achieved by using biodegradable, negatively charged PLGA nanoparticles of radius ~100 nm. Encapsulation of NR into the NPs as a model hydrophobic drug, increased its volume of distribution in the brain tissue by 5 times compared to the injected free NR. The effect of NP size in the CED was studied by MacKey *et al.* (2005) and Allard *et al.* (2009). The authors reported that CED of polystyrene NPs (10-100 nm) led to Vd=1-9 mm^3 due to the restricted mobility of NPs in the small extracellular space in normal rat brain (35-64 nm). However, ~100 nm sized PLGA/NR NPs led to Vd=40-50 mm^3 showing an improved CED via PLGA spheres (Figure 7.18). Non-specific binding onto negatively charged structures in the brain parenchyma was also prevented due to their repulsive electrostatic interactions with the negatively charged NP (~-30 mV). Drug remained in the striatum for at least 24 h post infusion (Figure 7.19) and the *in-vitro* studies on glioma cells, showed a high intracellular uptake of NR. However, the *in-vitro* release studies of NR from PLGA NP in AcSF showed that there was no drug released within 1.2 months via diffusivity through the polymer matrix, or by polymer degradation. This indicates that PLGA does not degrade in AcSF by polymer interactions with the ions present in the release medium (Na^+, K^+, Ca^{2+}, Mg^{2+}, Cl^-, SO_4^{2-}, PO_4^{3-}, HCO_3^-, refer to Appendix, Section A5.5 for ions concentration) and inherently there is no free NR present in the extracellular space. Moreover, efflux through the leaky endothelial cells and their drainage from the brain via systemic circulation is prevented by the large size of the NP. Therefore, NR loaded PLGA nanoparticles must have been taken up by the cells indicating they can potentially be

used as effective drug delivery systems of highly hydrophobic therapeutics. Even though the exact mechanism of NP uptake is not exactly known, other authors (Wang et al., 2011, Fonseca et al., 2002) have previously reported uptake of both hydrophobic (Paclitaxel) and hydrophilic (Doxorubicin) drug loaded PLGA NP by tumor cells. It is though believed that NPs are engulfed by either endocytosis or receptor mediated phagocytosis. Intracellular PLGA nanoparticels are then subject to hydrolysis or enzymatic degradation due to the presence of lytic enzymes and the drug itself, that create an acidic intracellular environment (Anderson and Shive, 1997; Xu et al., 2009). The shorter polymer chains will eventually efflux from the cells and drain out of the brain whereas the drug itself will cause cell death.

Paclitaxel loaded nanoparticles did not increase *in-vitro* cell cytotoxycity because of the insufficient drug encapsulation efficiency as further shown by MAS spectroscopy. However, by modifying the experimental conditions (ie synthesis method, stabilizer, solvent) it would be possible to increase Paclitaxel EE and successfully deliver drug loaded PLGA NPs via CED, over high brain tissue volumes. NEP was not expressed in the brain tissue as found by ELISA assay and NEP encapsulation in PLGA NPs has not been reported before in the literature. Further studies are required to examine the protein stability under the experimental conditions chosen and its affinity towards the PLGA polymer. FITC-Dextran loaded NPs had encapsulation efficiency of 2.67 and 5.94 % (Table 7.10) measured by fluorescent spectroscopy. However, following *in-vivo* CED in the brain and at 24 h post infusion, the NPs exhibited low fluorescence intensity. This is either because FITC-Dextran molecules were released in the extracellular space before the NPs were taken up by the cells or, NP fluorescence was below the threshold of the imaging technique adopted. The former case is likely to occur only if all the dextran molecules were adsorbed on the surface of the PLGA NP, in direct contact with spinal fluid, as drug encapsulation within the NP core would require polymer degradation, which is not observed within 24 h of *in-vivo* studies. Hence it is possible that (most of) the FITC-Dextran is located in the NP shell, and due to its low encapsulation efficiency, it fluoresces little.

The *in-vitro* glioma cell uptake of TFMU loaded PLGA-PEG NPs and Rhd loaded PLGA/mPEG-DSPE NPs (Figure 7.14) shows that surface modification of particles with hydrophilic groups does not prevent their influx within the cells. Moreover, NP uptake was not restricted by their positive and negative charge, respectively showing that NP uptake is not surface charge mediated (at least) in the presence of PEG or lipid groups. However, for *in-vivo* CED in the brain negatively charged NPs are required to facilitate NP distribution into big tissue volumes, unless extension of drug systemic circulation is more crucial. In the later case, PEGylated NPs can be used to reduce the interactions with proteins or tissue affinity (Allard et al., 2009). NR loaded PLGA/mPEG-DSPE NPs were also taken up by the cells, indicating that these hybrid NPs can efficiently be used for drug delivery of both poorly (NR) and water soluble agents (Rdh), for advanced systemic circulation time. Vij *et al.* (2010) also used NR stained PLGA/mPEG-DSPE NPs for intranasal drug delivery into the lungs, and they observed more efficient NP uptake by the cells compared to PLGA/DSPE NPs.

Summing up, successful convection-enhanced drug delivery into the brain, over a wide tissue volume, was achieved using negatively charged Nile red loaded PLGA NPs. The *In-vitro* cell studies showed intracellular uptake of PLGA, PLGA-PEG and PLGA/mPEG-DPSE NPs, loaded with both hydrophilic and hydrophobic agents. Further experimental studies will be needed to reduce the size of these NPs for potential CED into the brain, where fluorescent staining agents are required to investigate the drug location.

7.13 Conclusions

This chapter explored different synthesis routes and conditions that would lead to NP formation with the desired properties, for CED into the brain. The NPs produced, were loaded with fluorescent hydrophilic (TFMU, Rhd) and hydrophobic (NR) agents to trace the location of the NPs in the brain and their uptake by the cells. The encapsulation of these agents also suggested the possibility that real drugs, other than those tried, can be encapsulated via the same mechanism if the synthesis method was the same. Moreover,

the NPs with the features required were also characterized via gas sorption, NMR cryoporometry and tomo-TEM imaging techniques, to further investigate whether the polymer matrix contained any void spaces.

It was found that the dialysis method led to formation of NPs with the size and charge required for CED studies, and this synthesis method is mostly recommended for encapsulation of highly hydrophobic drugs and drugs with a high molecular weight, to prevent drug diffusivity out of the dialysis tube. In this method, the size, the charge and drug encapsulation efficiency of both NR and TFMU could be modified by varying the solvent and polymer end groups. NPs formed from acid ended PLGA had a higher encapsulation of both NR and TFMU compared to the ester ended PLGA, whereas the presence of hydrophilic drugs or stabilizers, in general decreased the negative charge of the NPs. Furthermore, nanoprecipitation seems a better synthesis method for the encapsulation of hydrophilic drug molecules, compared to dialysis and simple mixing, as seen by the higher TFMU loading achieved via this technique. *In-vitro* glioma cell studies also showed that all types of NPs, loaded with model drugs, were taken up by the cells, irrespective of their size and surface charge. However, undetectable amounts of real drugs (as Paclitaxel, NEP and 5-FU), were observed via spectroscopy and *in-vitro*/*vivo* studies for the NPs synthesized via dialysis, possibly due to the rapid diffusion of the small drug molecules through the dialysis bag, or drug degradation/denaturation by the solvents used. Direct infusions of NR loaded NP into the mice brain via CED facilitated NP distribution at high tissue volumes which remained in the brain for at least 24 h post infusion, in contrast to the free drug which was concentrated at the site of injection. This shows that direct infusion of negatively charged NPs, with a radius of less than 100 nm, is a promising drug delivery technique for the treatment of brain diseases although further investigations are needed to improve the loading efficiency of the real drugs (Paclitaxel, NEP and 5-FU).

Chapter 8
Reducing the time of PFG diffusion NMR experiments

8.1 Introduction

The PFG NMR experiments in this thesis, and elsewhere in the literature, often take a substantial amount of time. For example, a set of PFG measurements (performed at four different diffusion times), requires ~80-150 min depending on whether it was bulk or imbibed liquid, and the type of molecule. As discussed in Section 2.5 this is because the (recycle) delay time, *d1*, required for ~99 % of the phase to be recovered from the x-y plane onto the z-axis between two successive scans, is 4.6xT_1. Therefore, a value of 5xT_1 is often chosen for PFG studies to obtain higher accuracy on the measurements. In this chapter it will be shown that by using a bipolar pulse longitudinal eddy current delay (BPP-LED) sequence to perform a PFG NMR experiment the recycle delay time can be significantly reduced, speeding up the experimental time.

8.2 Literature review

If a value less than 5xT_1 is used between the scans of an NMR experiment, the magnetisation only has time to partially recover back to its equilibrium position along the z-axis before the next scan. After each successive scan, the magnetisation will therefore recover to a slightly lower level, until after several scans it will reach a steady state, always returning to this value. Therefore, NMR experiments are often conducted using dummy scans at the start of each run – this is where the pulses are applied as normal and the magnetisation left to relax, but no data is acquired. In this way, the magnetisation reaches a steady state before any data are collected. Earlier work by Strait-Gardner *et al.* (2008) has shown that when using a simple PGSE experiment for diffusion studies, the magnetisation does indeed reach steady-state equilibrium. These authors used 16 dummy scans although they showed, theoretically, that one should have been sufficient.

They also pointed out that as long as a steady state is achieved between scans, the diffusion coefficient observed should be independent of the recycle time used. Moreover, they added a crusher gradient to the PGSE sequence to eliminate the rogue, unwanted magnetisation, remaining in the x-y plane before each scan. They were then able to reduce the recycle delay time to slightly less than 5xT_1, with no significant change on the observed diffusion coefficient for the solvents studied (Stait-Gardner et al., 2008). However, when the recycle delay was reduced to less than 3xT_1, deviations to the diffusion values were observed. These variations could be somewhat eliminated by omitting the data acquired at the low gradient strength values from the monoexponential data fitting (equation 8.2), or by fitting all the data into a biexponential model, however, they were not completely understood. In addition, such data fitting is not suitable for routine use. In later study Sørland *et al.* (2011) put a spoiler recovery sequence, comprising of two 90^{o} r.f. pulses and a pair of bipolar gradients, in front of a PGSE pulse sequence and a PFG-STE pulse sequence to remove any magnetization remaining on the z-axis. The authors used these sequences to measure the diffusion coefficient of pure water at various delay times. They found that the diffusion coefficients of water remained nearly constant and the logarithm of the attenuation was linear for both pulse sequences regardless of the delay time between the scans. Moreover, other modified versions of the PFG-STE sequence, such as the bipolar alternating pulse gradient stimulated echo (APGSTE) pulse sequence, have been adopted to measure diffusion coefficients of imbibed liquids in porous media (Mitchell et al., 2008a). The bipolar gradients are important in the case of porous media where internal magnetic gradients can be produced in the presence of high magnetic fields (>1 T), due to the inhomogeneous distribution of the liquid phase.

More sophisticated pulse sequences, though, such as the BPP-LED sequence, which is currently in widespread use, have been developed where the crusher gradients are already built in the pulse sequence to remove residual magnetization on the x-y plane, hence, no further modification is required. Moreover, data acquisition is routinely performed after the use of dummy scans, where the magnetization vectors have already reached an equilibrium steady-state along the z-axis before the acquisition scans are performed. A background theory to the BPP-LED sequence was already provided in

Chapter 2, Section 2.4, and the schematic diagram of the pulse sequence applied is presented again in Figure 8.1 for ease of access.

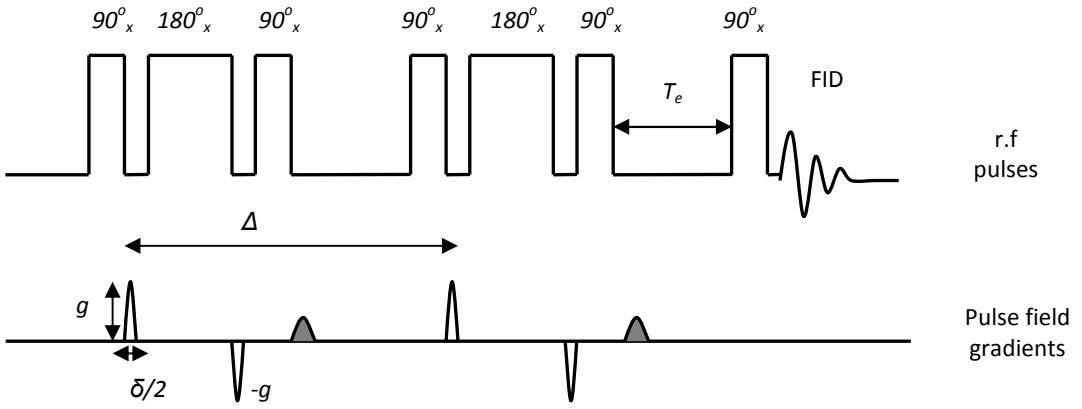

Figure 8.1 BPP-LED pulse sequence. The empty and grey filled lines placed on the pulse field gradients row, represent the applied magnetic gradients and the small field (crusher) gradients, respectively

Achieving complete magentization recovery was of high importance particularly for the partially saturated or partially molten systems in Chapters 3 and 4, where the signal-to-noise ratio needed to be maximized. However, for many systems, where the signal-to-noise level is reasonably high, full recovery of the magnetisation is not needed, and lower recycle times could be employed to speed up data acquisition. The aim of this chapter is to study whether accurate diffusion experiments can be performed at lower than 5xT_1 delay times, using a BPP-LED pulse sequence, in order to eliminate the time of the PFG experiments. The repetition time, $t_r=t_{aq}+d1$, is taken as the total (recycle) delay time, though, which is made up of the time during data acquisition, t_{aq}, and the time between the acquisition ending and the next scan starting, *d1*. Diffusion experiments are performed for bulk liquids and for liquids imbibed into a fully saturated mesoporous S1 material, where the signal-to-noise ratio is lower compared to the bulk liquids. The efficiency of the BPP-LED sequence to measure the correct diffusivity values at repetition times below the conventionally used ones has not been studied in the literature, therefore it was of interest to investigate the case. It will be shown that the repetition time for all the samples studied can be reduced with confidence below 3xT_1, which is

useful to speed up the time of the NMR cryodiffusometry experiments, for adequate signal-to-noise ratios.

8.3 Experimental procedure and methodology

The cyclohexane and cyclooctane bulk liquids used for these experiments were purchased from Acros Organics (≥99%) and Alfa Aesar (≥99%), respectively. All the experiments were performed at 298 K on a 500 MHz Bruker Avance II+ spectrometer which has a static field strength of 11.75 T.

The bulk liquids (cyclohexane or cyclooctane or water) were initially placed in a glass capillary tube sealed at the top with a Bunsen burner to prevent liquid evaporation during the course of the experiments. This tube was then placed within an NMR tube for the T_1 and PFG NMR measurements.

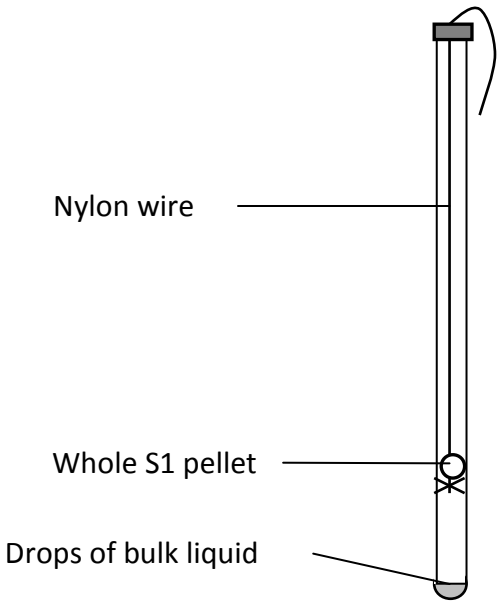

Figure 8.2 Experimental set-up for the T_1 and PFG NMR measurements performed on the saturated whole S1 pellet

A single whole pellet of a mesoporous S1 material was chosen as an adsorbant of cyclohexane, cyclooctane and water and the experimental set up was as follows. The

pellet was degassed under vacuum, at 393 K. Then the pellet was fully saturated with liquid and placed within an NMR tube containing a few drops of the same bulk liquid at the bottom of the NMR tube. A nylon wire was used to keep the pellet in place by preventing its direct contact with the solution at the bottom of the tube, and thereby eliminating the bulk layer fraction developed around the pellet. This fraction would otherwise contribute to the overall T_1 relaxation and diffusivity values. The NMR tube was then tightly sealed at the top with Parafilm and the system was left to equilibrate for 20 min, as shown in Figure 8.2. These conditions ensured that the pellet remained fully saturated throughout the course of the experiments without any vapour exchange with the atmosphere.

Initially, the T_1 relaxation time was measured using an inversion recovery pulse sequence employing a sequence of 15 delay times varying between 0.1 and 15 s. The decay in the signal intensities was plotted against the delay times. The estimation of T_1 relaxation time was then found by the following relationship:

$$I(\tau) = I_0\left[1 - P\exp\left(-\frac{\tau}{T_1}\right)\right] \tag{8.1}$$

where I is the signal intensity measured after a delay time, τ. The signal intensity at time zero is I_0 and P is a constant which takes a value of 2 for a perfect 180^o pulse. It must be noted that T_1 relaxation measurement for water suffered radiation dumping effects at high concentrations. This is because the water signal induces currents in the NMR coil, generating magnetic fields that will cause the magnetization spins to recover at different rates. Such an effect is observed as a broadened NMR spectrum peak, where the outer parts of the peak have recovered at a different speed to central ones, resulting in the estimation of much lower T_1 relaxation values (i.e. 0.3 s as compared to the real value of 3.64 s). This problem was resolved by using a modified version of the inversion recovery pulse sequence where a gradient pulse of 10 ms duration and 50% power is introduced between the 180^o and 90^o pulses to destroy any magnetization present on the x-y plane. Figure 8.3 shows a schematic diagram of the modified pulse sequence used.

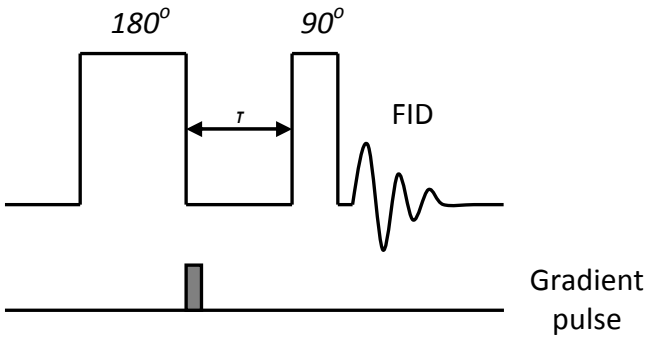

Figure 8.3 Modified inversion recovery pulse sequence. A gradient pulse is introduced after the 180^o pulse to destroy any transverse magnetization created

The PFG experiments were performed at an acquisition time of 5.45 s and different repetition times, so that t_r/T_1 varies from ~0.1 to 5. The lower values of this range were obtained by reducing the acquisition time down to 0.5 s, ensuring though that the FID signal was completely recorded. Ten data points were taken at increasing gradient strengths between 1.7 and 33.1 G/cm, and each point was obtained with 16 scans. Also, 16 dummy scans were performed at the start of each acquisition. The diffusion length, δ, was kept constant at 0.002 s for all the experiments whereas the diffusion time, Δ, varied between the samples at the range of 0.05-0.15 s for optimization of the signal decay function, which is important to obtain a good absolute diffusion coefficient, D_{PFG}. The reduction in the signal intensity with increasing gradient strength squared, g^2, was monoexponential and it was thus fitted into the following equation (introduced to the reader in Chapter 2):

$$I = I_0 \exp\left(- D_{PFG} \gamma^2 \delta^2 g^2 \left(\Delta - \frac{\delta}{3} - \frac{\tau_0}{2} \right) \right) \qquad (8.2)$$

The absolute diffusion coefficient measured at each repetition time is then divided by that obtained at $5xT_1$, D_{5T1}, and this value will be referred to as relative diffusion time, D_{PFG}/D_{5T1}.

The raw data was fitted into Origin program and the fitting error was estimated as described in the Appendix, Section A2.1.

8.4 Results and discussion

The T_1 relaxation values of the bulk and imbibed liquids in the S1 pellet are included in Table 8.1. The plots of the absolute diffusion coefficients are presented in Figure 8.4. Moreover, the relative diffusion coefficients are presented in Figure 8.5 to make clearer the change in the diffusion coefficients with the repetition times.

Sample	T_1 **(s)**
water	3.64±0.002
cyclohexane	5.32±0.002
cyclooctane	2.96±0.014
S1-water	0.35±0.009
S1-cyclohexane	2.95±0.006
S1-cyclooctane	2.14±0.014

Table 8.1 T_1 relaxation values of the bulk liquids and when imbibed in the S1 pellet, measured at 298 K

It is seen that the diffusion coefficient of the bulk hydrocarbons remains constant for repetition times (at least) down to 1.2xT_1. Water diffusivity also, remains constant within the error range until ~2.5xT_1, but then a small hump occurs at ~0.5xT_1, where the diffusion value increases to 2.35×10^{-9} m^2/s, as compared to that at 5xT_1 which is 2.21×10^{-9} m^2/s. Strait-Gardner *et al.* (2008) measured the diffusion coefficient of semiheavy water (HDO) in deuterated water and observed a similar hump at ~0.5xT_1, however, the diffusion coefficient increased up to ~10×10^{-9} m^2/s as compared to that at 5xT_1 which was 1.9×10^{-9} m^2/s. Although the authors managed to diminish this discrepancy in the diffusion value by including crasher gradients in the PGSE pulse sequence, the measured diffusion coefficient at the top of the hump was still high (~2.8×10^{-9} m^2/s).

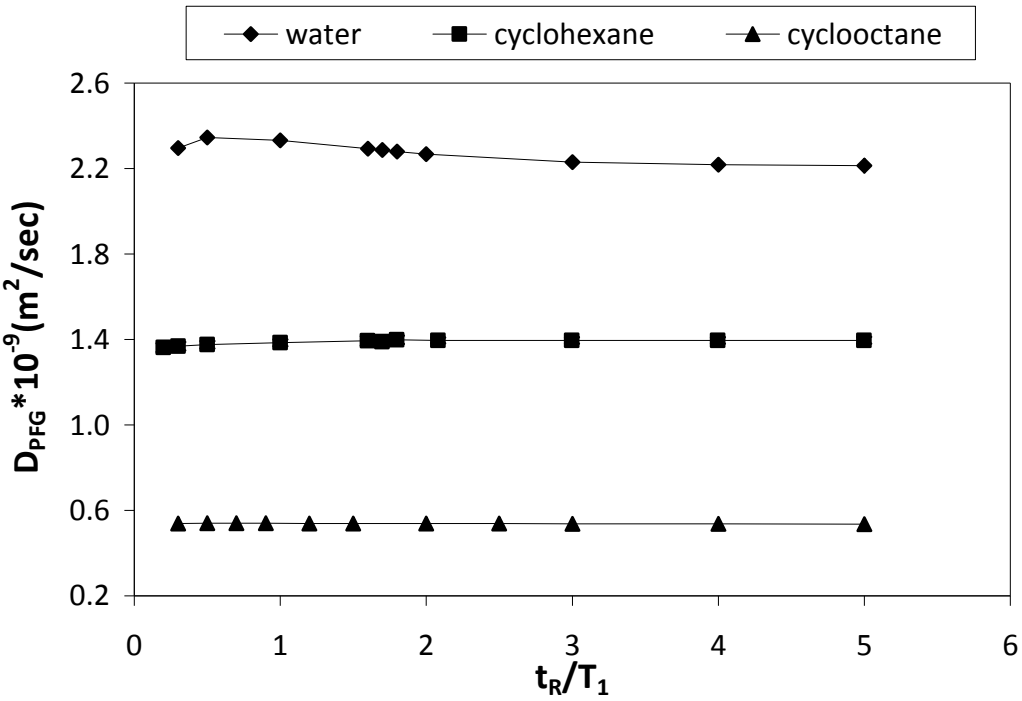

Figure 8.4 Absolute diffusion coefficients of the bulk liquids, measured at 298 K. The error bars included in the figure are smaller than the symbols. The lines are shown to guide the eye

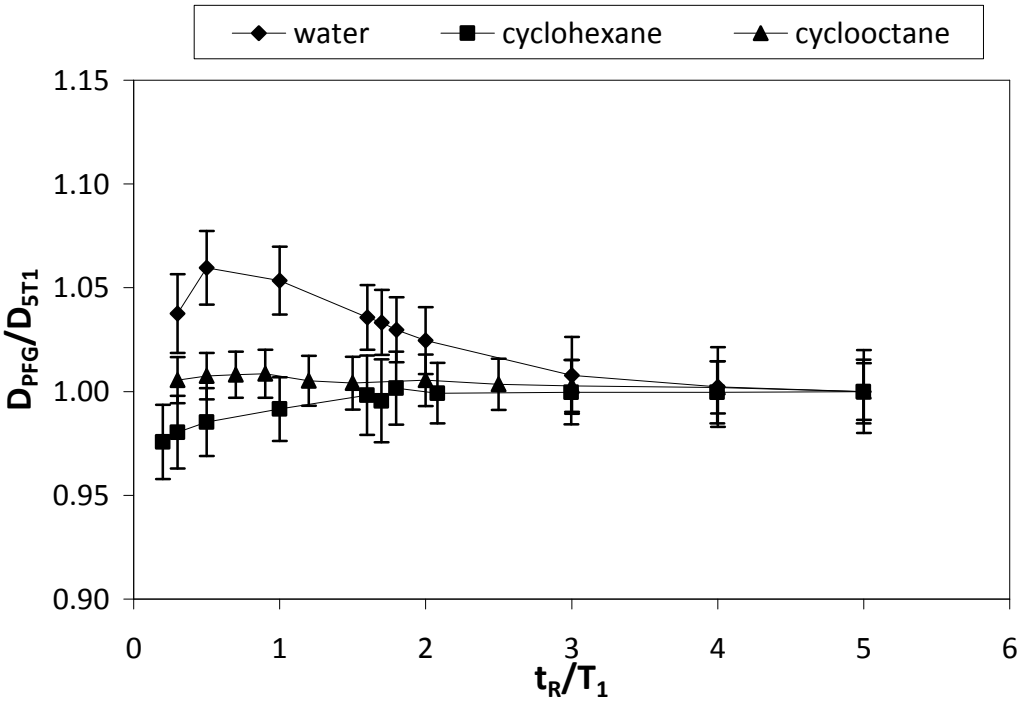

Figure 8.5 Relative diffusion coefficients of the bulk liquids found by dividing the absolute diffusion coefficients by the diffusion coefficients value measured for t_r/T_1=5, for each respective bulk liquid. The error bars are included. The lines shown are to guide the eye

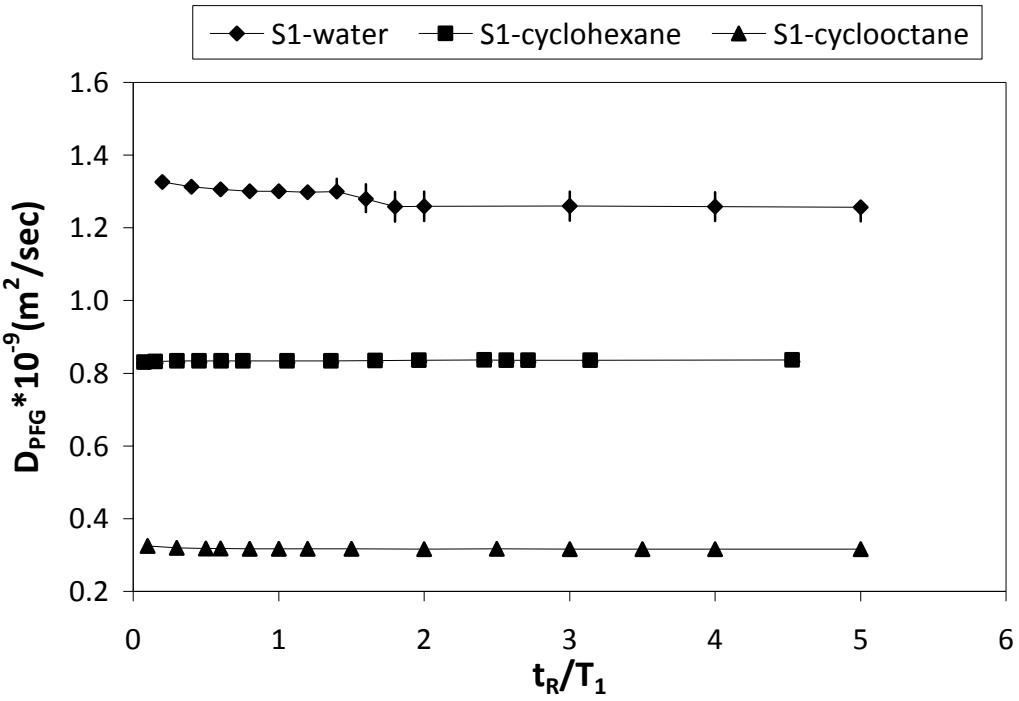

Figure 8.6 Absolute diffusion coefficients of the imbibed liquids within a S1 pellet, measured at 298 K. The error bars are included in the figure. The lines shown are to guide the eye

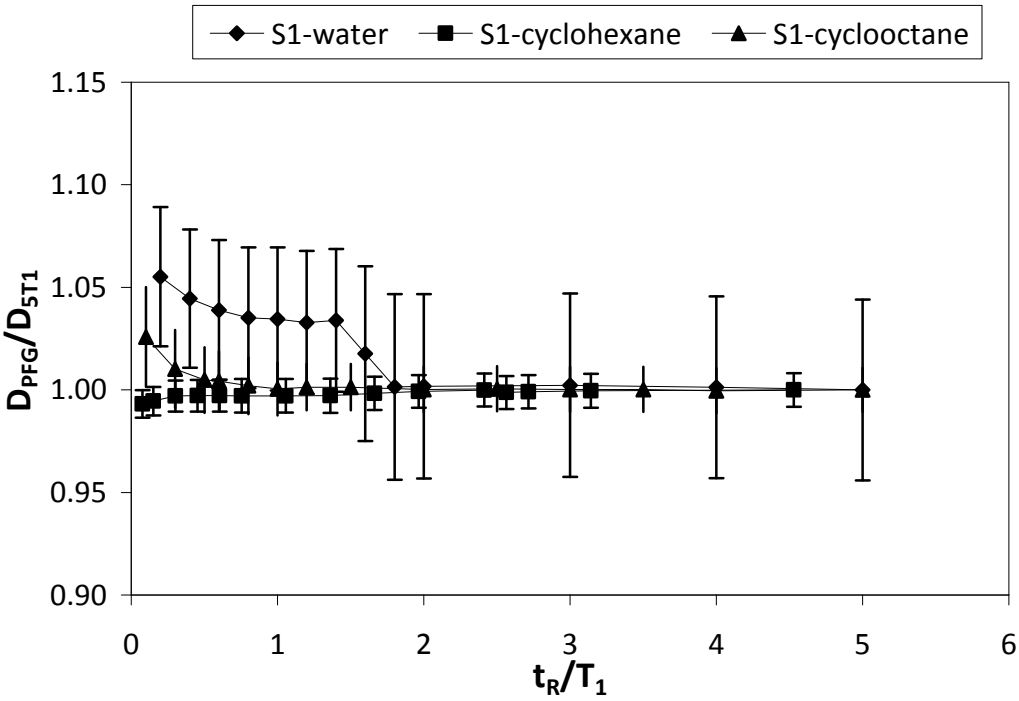

Figure 8.7 Relative diffusion coefficients of the imbibed liquids in the S1 pellet found by dividing the absolute diffusion coefficients with the diffusion coefficients value measured for t_r/T_1=5, for each respective imbibed liquid. The error bars are included in the figure. The lines shown are to guide the eye

The diffusion coefficient of water, cyclohexane and cyclooctane imbibed in S1 mesoporous silica pellet are shown in Figures 8.6 and 8.7. It is seen that D_{PFG} remained constant for the hydrocarbons as repetition time decreased down to 0.54xT_1, whereas for the imbibed water, it was constant until 1.8xT_1 and increased only slightly (~5%) for lower repetition times.

The results observed for both the bulk and imbibed liquids suggest that when a BPP-LED pulse sequence is used, diffusion coefficients remain constant down to repetition times much lower than those predicted by the theory. In fact, for the bulk and imbibed hydrocarbons studied, the repetition time can be reduced to ~ 1xT_1 with no significant change in the observed diffusion coefficient. For water, reducing the repetition time below 2-3xT_1 results in small but significant deviations of the observed diffusion coefficient from the correct one. This means that the experimental time required for a PFG can be significantly decreased with confidence. This is especially important for the PFG measurements performed on hydrocarbons, such as cyclohexane, which has a high T_1 relaxation time therefore the repetition time has to be increased to allow complete recovery of the magnetization vector into the z-axis, before the next gradient is applied. For example, when cyclohexane was imbibed into an S1 pellet, the experimental time required for a PFG experiment using a repetition time of 5xT_1 (δ=0.002 s, Δ=0.05 s) was ~20 min, but by reducing the repetition time down to 0.54xT_1, the experiment was performed within 4 min. The results have also shown that the BPP-LED pulse sequence is less prone to diffusion errors at short repetition rates than the simple PGSE sequence.

8.5 Conclusions

In this chapter, it was tested the efficiency of the BPP-LED sequence to perform accurate diffusion coefficient measurement at fast repetition times has been tested. It was found that the repetition time in the bulk liquids studied can be reduced even below 2.5xT_1, without inducing any major errors (<5%) in the calculation of the diffusion coefficient. Moreover, it was found that diffusivity within a S1 porous pellet, remains constant even when the repetition time decreases down to 1.8xT_1. In the case of hydrocarbons, which

have a high T_1 relaxation time, the diffusion coefficient did not vary until 0.54xT_1. Therefore, the time required for diffusion experiments can confidently be reduced by significantly shortening the repetition time. This has the potential to speed up time-demanding experiments such as the cryodiffusometry experiments described in this thesis, along with a whole range of diffusion NMR experiments which have become very common in industry and academia.

Chapter 9
Conclusions and proposed future work

9.1 Conclusions

In this work, the sensitivity and accuracy of gas sorption and NMR techniques for characterization of a void space were tested. The independent domain theory as applied to adsorption and cryoporometry melting, was studied by concomitantly using the cryodiffusometry and NMR relaxation techniques along the capillary condensation and evaporation branches of the isotherm. Further information on the sorption mechanism was obtained by adoption of an integrated N_2-H_2O-N_2 experiment. The void space descriptors (surface area, pore size, pore volume) were also used further to investigate the structure-transport relationships in drug delivery systems, in order to interpret the drug release rates observed in simulated gastrointestinal fluids. Moreover, the efficiency of both techniques to characterize the void space of biodegradable polymer nanoparticles, synthesized to improve drug delivery into the brain, was investigated. The following subsections will provide the main finding of this work in more details.

9.1.1 Probing cooperative effects in water vapour sorption and NMR cryoporometry

The adsorption isotherm and melting curve from a gas sorption and NMR cryoporometry experiment, respectively, were used for derivation of pore size distributions emplying the assumption of thermodynamic independent pores. Gas desorption and pore freezing are prone to pore blocking effects that can lead to inaccurate calculation of pore sizes, and thus are not generally recommened for pore size estimations by IUPAC. Assuming that both adsorption and melting occur via a cylindrical type meniscus the BJH and Gibbs-Thomson equations are fouynd to be applied in the literature to convert the adsorption and melting curves into pore sizes. However, advanced adsorption and melting are known to occur (Esparza et al., 2004; Hitchcock et al., 2011), where the pore

fill and melt via hemispherical menisci initiated from the neighbouring pores. In this work it is suggested that gas sorption, NMR cryodiffusometry and relaxation techniques can concomitantly be used to study the onset and the progress of these advanced phenomena, at different pressures on the water sorption hysteresis curve. The study of the partially saturated samples allowed the stepwise identification of the critical pore sizes that greatly impact the advanced melting process in a fully saturated sample, and therefore produce uncertainty. The cryoporometry melting curves along with the PFG and T_2 relaxation measurements at the end of the boundary melting curve showed that the onset of advanced melting, in a whole pellet S1 sample, is associated with an increased interconnectivity of the adsorbed ganglia and the filling of big pores. T_2 relaxation studies also showed that some big pores have already filled at lower pressures via advanced condensation and some small pore filled at higher pressures. Freezing scanning loops and curves initiated from a certain molten fraction on the boundary melting curve, and T_2 measurements along the loops further showed that advanced melting becomes more severe as saturation increases and that the new pores filled change the melting mechanism of the previously filled pores. By fragmenting the sample the necks and bodies were separated, and the pores melted over a wider temperature range compared to the whole pellet sample, as shown by the cryoporometry melting curves, suggesting that (at least) part of advanced melting was curtailed. This was further supported by the shape of the scanning loops observed and the PFG and T2 results. Moreover, it was shown that freezing is governed by a percolation-controlled penetration of the freezing front via heterogeneous nucleation, for both the whole and fragmented samples, with additional supercooling effects in the absence of nucleation sites. Particle fragmentation, though, can lead to similar mechanisms of cryoporometry freezing and vapour desorption, once the pore blocking effects are removed. These findings overall suggest that by breaking into steps the sorption process, it was possible to detect the extent of the cooperative effects in both vapour sorption and NMR cryoporometry and show that gas sorption is a more sensitive technique to probe the real pore size distribution in disordered mesoporous systems.

9.1.2 Probing the cyclohexane sorption hysteresis

The pore filling and emptying mechanism varies for different strengths of adsorbate-adsorbent interaction and the spatial arrangement of the adsorbate is also affected by the history of the pore filling/emptying processes. The hysteric and cooperative effects in gas sorption, influenced by the intermolecular interactions, were probed in this work via NMR cryoporometry and T_2 relaxometry. Cryoporometry melting curves showed that the configuration of the liquid condensate varied with the amount adsorbed at corresponding positions on the adsorption and desorption branches of the hysteresis loop, suggesting that assumptions about single pore filling and emptying mechanism can be invalid. Subsequently, this means that the derived pore size distribution, based on these assumptions, is subject to major errors. Moreover, the reversible scanning loops proved that freezing and melting in some pores occurred via a retreating hemispherical meniscus, suggesting that some pores melted via advanced melting mechanism. The non monotonic relationship between condensation and pore size, as shown from the nearly constant T_2 values measured at the end of the boundary melting curves when the pressure is raised, is evident of some advanced condensation taking place at low pressures, whereas higher T_2 values measured for the systems saturated via desorption, showed that pore blocking effects have prevented the emptying of some big pores. The presence of advanced adsorption and pore blocking effects were further proved via the sorption scanning curves. These findings show that both cryoporometry and cyclohexane sorption are influenced by cooperative effects. Hence, care must be taken when converting an adsorption or melting curve into a pore size distribution as equilibrium adsorption via cylindrical menisci (or spinodal condensation), or independent melting, respectively, may not be the only mechanisms taking place.

9.1.3 Testing independent (single) pore theory and the cause of hysteresis via an integrated N_2-H_2O-N_2 experiment

The aim of this work was to compare the mechanism of water sorption to that of nitrogen, and to test the validity of the Cohan and DFT approaches to explain the real

cause of hysteresis, as such the real pore size distribution derived from the sorption curves, by applying either these approaches. The Kelvin-Cohan equations are based on macroscopic approaches assuming that the gas and liquid phases are in equilibrium, thereby the cause of hysteresis is due to the different geometry shapes of the menisci developed during adsorption and desorption. The relative pressures in desorption and adsorption are related by a power of 2. However, these equations were suggested not to be applicable for pores greater than 10 nm. The DFT model assumes spinodal adsorption and equilibrium desorption processes in open cylinders, arising from the differences in the gas-liquid-solid interactions, but this method has been calibrated from standard materials, of known surface chemistry and it has been validated only for ordered materials (MCM-41 and SBA-15) thought to fill and empty like independent pores. The DFT method (Neimark and Ravikovitch) predicts that for pore sizes between 10-20 nm the relative pressures in desorption and adsorption are related by a power of 1.8. However, Hitchcock (2011) performed an integrated N_2-Hg-N_2 experiment in a S1 sample and found that pores occupied by mercury filled and emptied with nitrogen like independent pores, but the relative pressures were instead related by a power of 1.5, proving that the DFT method is not always valid or the interactions parameters are rather more sample specific than thought. From the integrated N_2-H_2O-N_2 experiment it was shown that the pores which were not filled with water, behaved like independent pores and the relative pressures in the adsorption and desorption processes were related by a power of 1.8. However, FHH fractal analysis showed that the pore surface where N_2 adsorbed, was wetted by water molecules, thereby additional intermolecular interactions were developed between the nitrogen, ice and silica. Moreover, when the pellets were fragmented, and the pore blocking effects in desorption were curtailed, the relationship between the nitrogen desorption and adsorption relative pressures, taking place in a non-partially saturated sample, became a power of 1.65. These findings show that the DFT model can predict the hysteresis width in the S1 sample, only when the surface chemistry of the silica is modified, suggesting that the DFT model needs further calibration before it is applied for the calculation of PSD in disordered porous material. Moreover, it was shown that water adsorption took place in some big pores, which nitrogen would fill at higher pressures, suggesting that the water and nitrogen filling mechanisms are not the same, with water adsorption exhibiting more severe advanced

phenomena within the relative pressure range studied. Furthermore, water pre-adsorption in the pores promoted independent pore filling with nitrogen into the remaining pores, which previously (at least some of them) would be influenced by cooperative effects in adsorption and desorption. In summary, these findings proved experimentally that water and nitrogen sorption mechanism are different, and that Kelvin and DFT models are not valid for disordered materials with a PSD between 15-20 nm such as that used in this work.

9.1.4 Structure-transport studies for interpretation of CsA release profiles

The aim of this work was firstly the pore characterization of two types of silicas, one templated with Lutrol (F127) and one templated with casein. These materials were used for encapsulation of CsA protein, in order to improve its dissolution in the gastrointestinal fluids. The *in-vitro* release studies in simulated fluids, showed that CsA release rate from the Lutrol and casein templated silicas differed between silicas and the release medium. Therefore, the second aim of the work was to investigate the influence of the structure-transport relationships of these porous media on the CsA release profiles obtained, taking also into account the size of the particles, and the local environment. The gas sorption and NMR cryoporometry studies showed that both silicas were mesoporous, with a high micropore volume and the PFG NMR measurements showed that the pore connectivity in Lutrol silicas was higher. The SAXS results showed a possibly cubic structure for Lutrol silicas and a wormlike structure for the casein silicas. Taking into account the porosity, pore size, tortuosity and particle size, different diffusion models were applied into the release profiles. It was found that CsA release was governed by Fickian diffusion, where the major factor controlling the release was the particle size of the silicas. Moreover, it was found that the pH of the environment affected the silicas dissolution itself, thereby contributing into the release rate of the CsA. Also, the presence of surfactant micelles in the gastric fluid, to mimic the role of the bile salts in the gastric area, might have enhanced further solubility of the CsA by either penetrating into the silicas through the pores, or by prolonging the chains into the entrance of the pores, thus transporting the protein outside the pores. To sum up, the studies suggested that the pore characteristics alone, only slightly influenced the CsA

release rates of CsA. The process was mainly controlled by the particle size and the release medium.

9.1.5 Optimization of PLGA nanoparticles for convection-enhanced drug delivery into the brain

PLGA NPs are biocompatible and biodegradable polymer systems which can potentially be used as drug delivery systems when controlled and sustained release is required. Therefore, their applicability as carriers of therapeutic and fluorescent agents via convection-enhanced delivery into the brain was tested in this work. To prevent the catheter blockage and ensure high volumes of distribution in the brain, the radius of the NPs had to be less than 100 nm and the charge had to be negative. For their optimization different synthesis methods and experimental conditions were initially tested for the formation of drug-free NP and the most promising conditions were used for encapsulation of hydrophobic (NR) and hydrophilic fluorescent (TFMU, Rdh) model drug molecules. This was done to investigate their location via imaging techniques, after their *in-vivo* infusion into the mice brain and their *in-vitro* uptake by the glioma cells. It was found that the dialysis method led to formation of NPs with the morphological characteristics required and with high NR loading efficiency. The *in-vivo* and *in-vitro* studies showed that a large distribution volume of NPs, and as such model drug in the brain, was achieved as opposed to the free NR which was attached into the brain tissue around the injection site only. The NR loaded NPs remained in the brain at least 24 h post infusion and the cell studies showed that they were taken up by the glioma cell, without causing cell death. These finding suggest that these formulations can be used as potential drug carriers via CED. However, the method needs further improvement to increase the loading efficiency of real hydrophobic drugs, such as Paclitaxel. Moreover, the encapsulation of hydrophilic molecules was found to be low, due to weak interactions with the hydrophobic PLGA polymer chains and rapid diffusivity of the molecules with small molecular weight through the dialysis bags. For example 5-FU loading was very low as measured by the UV-vis spectrometry technique. Conjugation of hydrophilic PEG groups into the PLGA polymer, increased the encapsulation of the hydrophilic TFMU via the dialysis method although the size of the particles was big. *In-vitro* cytotoxicity studies

in the cells also showed that hydrophilic NEP was not efficiently loaded in the NPs or at least in concentrations with therapeutic activity. The other methods, such as nanoprecipitation and the simple mixing were more efficient for encapsulation of TFMU molecules although their size or charge was not the desirable one. The *in-vitro* release studies of TFMU from the NPs in PBS, showed that all the NPs exhibited a burst release at the early times, however, the release from the bigger NPs extended over longer periods of time, indicating that TFMU release from the NPs is possibly driven by the size of the particles, rather than the evolution of the internal polymer matrix. On the contrary, NR was not released from the NPs in the AcSA medium, within 1.2 months probably due to the high hydrophobic interactions with the polymer, and the absence of polymer degradation in the period of time studied. The gas sorption and TEM imaging techniques were not sensitive to detect any possible porosity in the NPs synthesised via dialysis. NMR cryoporometry was further adopted to probe the structure of the polymer matrix and its evolution in pure water with time, which is thought to contribute into the drug release rate. From the melting curves obtained it was not certain whether the change in the structure was caused by the freeze/thaw cycles which may affect the NP structure, or due to interparticle rather than intraparticle water. Summarizing, the studies showed that dialysis method can potentially be used for formation of NPs for convection-enhanced drug delivery, although the method requires further improvement to increase the loading efficiency of real drugs. Moreover, the pore characterization techniques were not sensitive enough to provide information about the internal structure of the NP.

9.1.6 Reducing the experimental time of a PFG NMR experiment

The PFG NMR experiments in this thesis took a substantial amount of time because the (recycle) delay time required for ~99 % of the magnetization to be recovered from the x-y plane onto the z-axis between two successive scans, is at least 4.6xT_1. This was done to obtain accurate PFG values. In this part of work, the PFG values of bulk and imbibed (into a porous S1 pellet) water, cyclohexane and cyclooctane, were measured at at repetition times between 0.1xT_1 and 5xT_1. It was shown that the PFG values of the bulk liquids were

constant down to 2.4xT_1 and 1.8xT_1 for the water and hydrocarbons, respectively. For the fast relaxing imbibed fluids the repetition time could be reduced even lower, down to ~0.54xT_1. These findings suggest that the time of the PFG experiments can be reduced with confidence by ~80% if the BBP-LED sequence is used.

9.2 Proposed future work

This section will discuss some possible experiments to be carried out in the future based on the findings in this thesis.

9.2.1 Comparing the influence of the meniscus geometry and surface chemistry for nitrogen condensation via an integrated N_2-H_2O-N_2 experiment

Integrated experiments involving two successive adsorbates can be used to isolate pores with certain characteristics and study them separately. When a S1 pellet sample is partially saturated with water via adsorption, a part of the adsorbed phase resides in the completely filled pores, whereas another fraction remains on the pore walls as puddles or films with non-uniform thickness. The former type of pore water is expected to create dead ends in the neighbouring pores, where nitrogen will condense at lower relative pressures than those in the absence of these dead ends. The latter type of pore water will (further) change the microscopic interactions developed at the silica-ice-nitrogen interfaces and as such change the wetting angle in both adsorption and desorption mechanisms. To study these effects separately, it is proposed that an integrated experiment is run for the S1 material when the sample is partially saturated with water up to a few monolayers where there are no completely saturated pores. If the nitrogen adsorption curve post-water saturation occurs over a narrower pressure range than that pre-water saturation, then it must mean that the surface wetting properties are more severly changing the adsorption mechanism, compared to those generated by advanced adsorption from the created dead end pores.

9.2.2 Studying the effect of pore connectivity into water and nitrogen sorption via an integrated N_2-H_2O-N_2 experiment

From cryoporometry NMR experiments it was found that less advanced melting and advanced condensation occurred when the pellet sample was fragmented. This was because the S1 pellet has macroscopic heterogeneities in the spatial distribution of the pore size, leading to advanced melting effects which were curtailed after the sample fragmentation. It would be thus of interest to investigate the water sorption mechanism in the fragmented S1 sample via equilibrium adsorption and compare it to that of nitrogen. Then, an integrated N_2-H_2O-N_2 sorption experiment can be performed when the sample is partially saturated with water, following the experimental procedure described in Chapter 5.

Measurements	Adsorbate occupying the pores	V_0 (cm^3/g)	S_{BET} (m^2/g)	V_m (cm^3(STP)/g)
Pre water	Nitrogen	0.89 (0.89)	198.43 (199.2)	46.12 (46.3)
Post water	Nitrogen	0.60 (0.29)	71.46 (25.2)	16.51 (5.9)
	Water	0.3 (0.51)		

Table 9.1 Pore volume and surface area of the fragmented S1 pellet sample, pre and post partial saturation with water at water relative pressure of 0.91. The values in brackets correspond to the whole pellet sample, presented in Table 5.1

Table 9.1 shows some preliminary findings for this type of experiment. It is seen that the pore volume of the fragmented sample which is occupied with water is less than that occupied in the whole pellet sample, implying that advanced adsorption for water is reduced. However, nitrogen adsorption post partial saturation with water occurred over a very narrow relative pressure range as seen from Figure 9.1. This is expected to occur when water condensation creates dead ends into the empty neighbouring pores, enhancing advanced adsorption of nitrogen into these empty pores. These dead ends formed at both sides of the water filled pores, can initiate advanced adsorption for nitrogen into both the adjoining empty pores, and therefore they will fill at lower pressure via the hemispherical menisci.

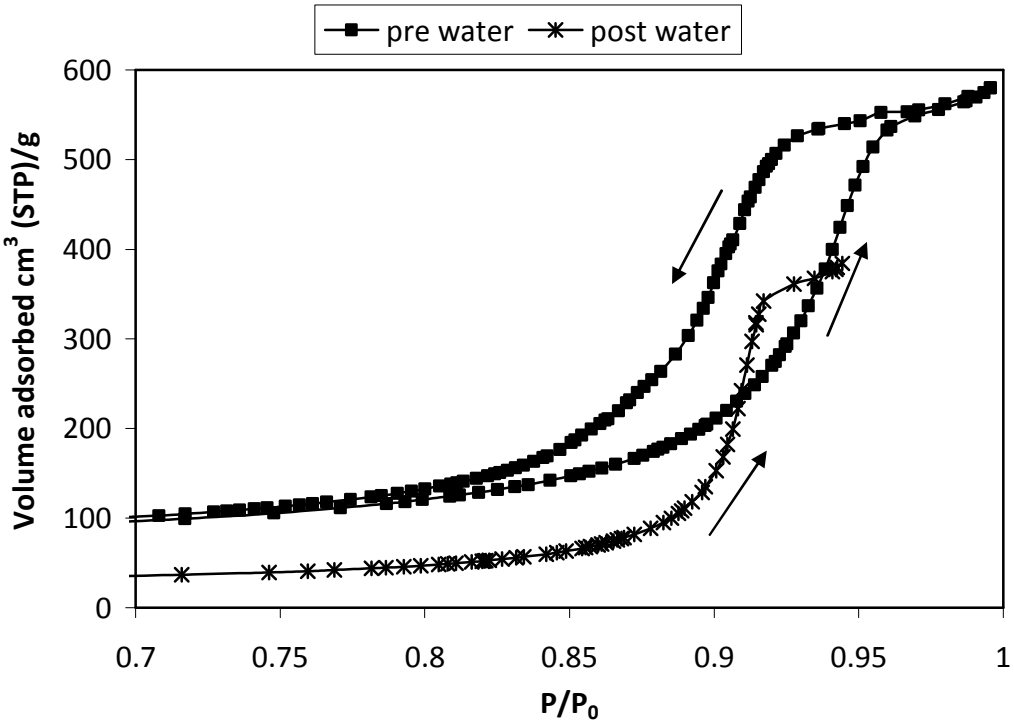

Figure 9.1 Nitrogen adsorption and desorption isotherms of the fragmented S1 sample pre-water saturation, along with the adsorption isotherm post-water saturation. The arrows show the direction in the change of the pressure

9.2.3 Probing the location of CsA in the pores of Lutrol and casein templated silicas

From the CsA encapsulation and release studies, it was not clear in which pores CsA was encapsulated. Therefore the accomplishment of an integrated N_2-CsA-N_2 and a CO_2-CsA-CO_2 sorption experiments in both casein and Lutrol templated silicas are proposed. In detail, a N_2 sorption experiment (77.3 K) in the drug free silicas could be run to probe the total pore volume, the pore size distribution and the specific surface area of the porous silicas. Afterwards, the samples can be loaded with CsA as previously described in the experimental section. Another nitrogen sorption experiment following CsA loading, could then be run on the same sample. The difference observed on the pore volume, PSD and surface area pre- and post-CsA loading will be attributed to the space occupied by CsA and as such would provide information about the location of CsA in the pores. Also, an additional fractal analysis may show the way CsA resides on the surface of the pores. If the pore surface roughness is retained or smoothened, then it will mean that the protein adsorbed on a 'layer-by-layer' form. However, if the roughness increased

this would mean that protein-protein attractive interactions dominated the protein-silica ones. Moreover, as the silica particles showed a high microporous volume, CO_2 adsorption (273 K) pre and post CsA loading can be run. CO_2 is also a useful adsorbate due to its ability to get adsorbed on the amine sites. Therefore CO_2 is expected to adsorb on the amine groups of the CsA and as such produce a better understanding of any CsA located in the micropores.

9.2.4 Synthesis of PLGA NPs for magnetic resonance imaging (MRI)

PLGA NPs synthesised in this thesis were loaded with fluorescent agents (NR, TFMU) in order to trace their location in the mice brain post CED. The volume of NP distribution in the brain was then estimated as follows. The brain tissue, where the NPs were infused via a catheter, was sliced into layers of equal thickness and each layer was then placed into a fluorescence microscope to detect the tissue surface covered by NPs. The surface and the depth of the tissue that NPs diffused through were then converted via a software to a volume of distribution. However, this method is time consuming and it may underestimate the value of the volume of distribution. Therefore it is proposed the use of T_1 or T_2-weighted MRI technique, to probe the location of the PLGA NPs in the brain, without the need of tissue slicing. For this the NPs have to be loaded with a contrast agent which decreases either the T_1 or T_2 relaxation time of the water on the site of the brain where they are delivered into. For example gadolinium-based contrast agents (Gd) contain a paramagnetic centre which binds into the water molecules and reduces mainly the T_1 relaxation at the site where it is delivered. Gd^{3+} ion is toxic as a free ion, therefore chelated compounds such as gadolinium diethylenetriamine pentaacetic acid (Gd-DTPA) are used, which can be delivered as bulk solutions or alternatively they are encapsulated into polymer particles for more controlled release (Chen et al., 2005). Usually Gd is either loaded in the particles via w/o/w synthesis method or it is conjugated in the polymer chains in advance, before particle formation. As dialysis method led to formation of NPs with the size and charge required for successful CED into the brain, the same method is thus suggested for the synthesis of PLGA NPs for MRI studies. The contrast in the MRI procedures is generated by the morphological changes in the tissue, and not by specific

intermolecular interactions between Gd and the damaged tissue. As via CED the NPs are delivered directly into the damaged tissue, the Gd-loaded NPs will provide further information of which part of this tissue is covered by NPs and potentially the exact location of the drugs.

Appendices

Appendix A1 Examples of log-attenuation plots from a T_2 and a PFG NMR experiment

Figure A1.1 shows an example of a log-attenuation plot for the data from a T_2 relaxometry experiment, from the partially saturated at relative pressure 0.84. Figure A1.2 shows an example of a log-attenuation plot of a PFG-NMR experiment. Both graphs show monoexponential decay, implying that there is no exchange between the liquid and vapour phase of water within the pores, at very low saturation levels.

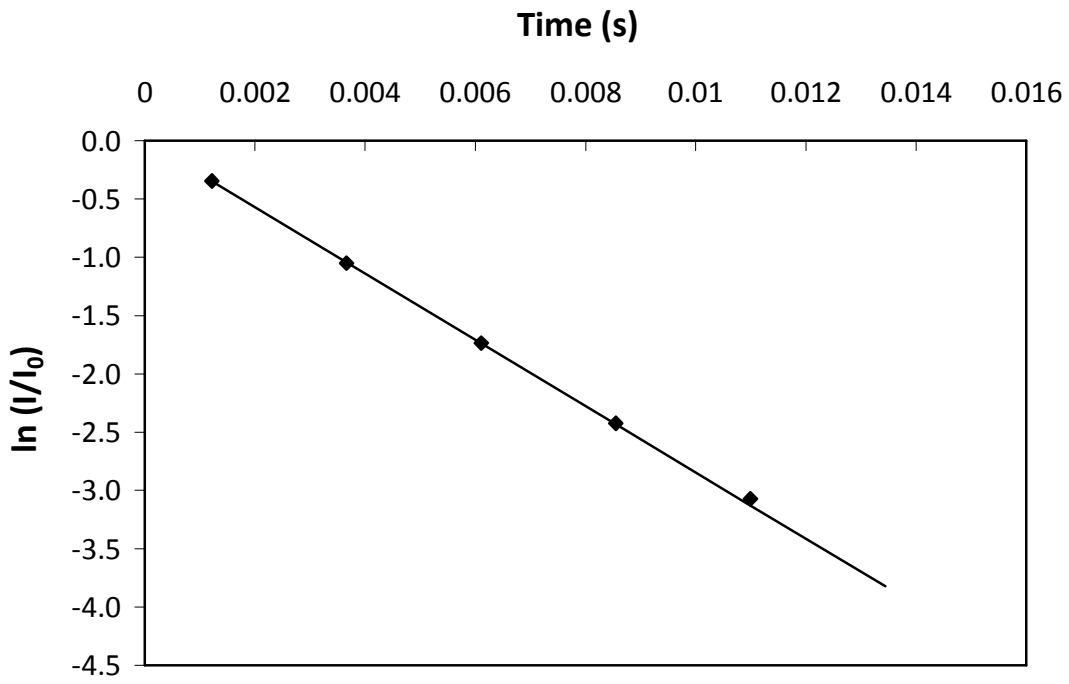

Figure A1.1 Log-attenuation plot of data from a T_2 relaxation experiment conducted on the 100% molten fraction of the single S1 pellet, at 273 K. The sample was saturated at P/P_0=0.84, 294 K. The solid line shows the fit to equation 3.1

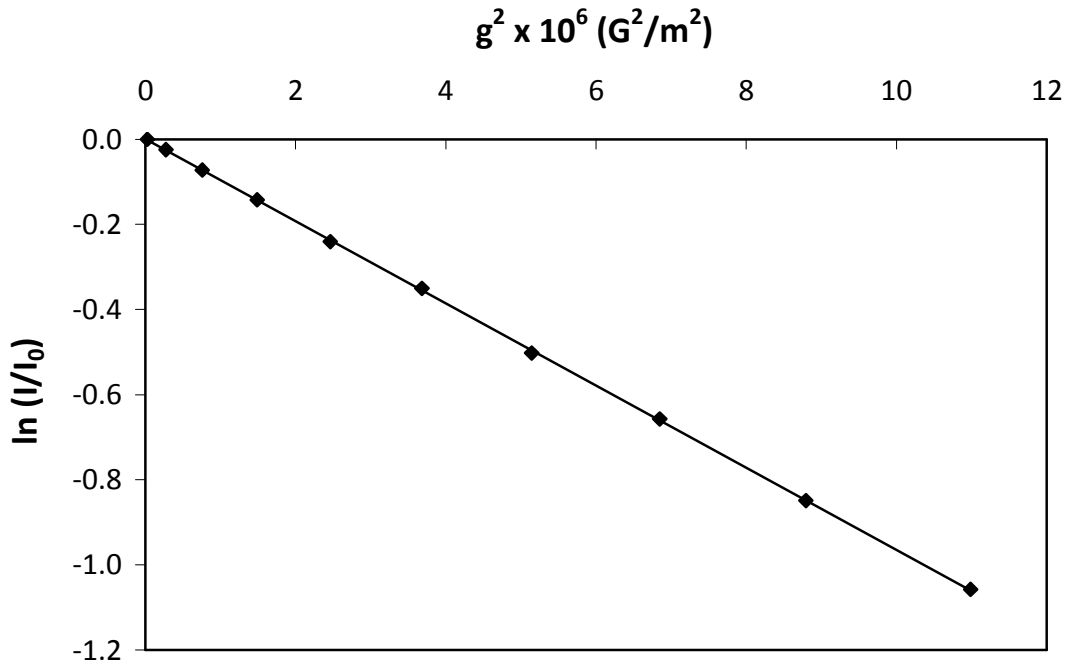

Figure A1.2. Log-attenuation plot of data from a PFG experiment (Δ=0.15 s and δ=0.002 s) performed for pellet 1. The sample was partially saturated at P/P_0=0.84 and the diffusion value was measured 273 K when the sample was completely molten. The raw data (diamonds) are fitted to equation 2.10

Appendix A2 Calculation of errors

A2.1 Levenberg-Marquardt error analysis

The error in the T_2 relaxation values and the diffusion coefficients from the data fitting into one or two component model are determined from non-linear curve fitting function using Origin program. The standard error for each of the fitting parameters is calculated within the fitting process via the Levenberg-Marquardt algorithm. The aim of the method is to minimise the reduced Chi-squared, X^2, as follows:

$$X^2 = \frac{1}{DoF}\sum_{i=1}^{n} w_{ij}[Y_i - E_i]^2 \qquad \text{(A2.1)}$$

where w_{ij} is the weight of the experimental points (taken as unity) , Y_i are the raw data collected, E_i are the values predicted by the model and *DoF* represents the degrees of freedom, calculated by:

$$DoF = n_{eff} - n_{prm} \qquad \text{(A2.2)}$$

where n_{eff} is the total number of the experimental data points and n_{prm} is the number of the parameters fitted into the model.

The error in the calculation of the free diffusion coefficient of bulk water at low temperatures was estimated by Perkins (2009) to be 3% of the calculated value, whereas the diffusion coefficient of the diffusion coefficient of water in the pores was estimated by the Levenberg-Marquardt algorithm from Origin. Both these errors were combined for the estimation of the total error in the tortuosity, $e(\tau_p)$, via the following equation:

$$e(\tau_p) = \tau_p \left[\left(\frac{e(D_{PFG})}{D_{PFG}} \right)^2 + \left(\frac{e(D_b)}{D_b} \right)^2 \right]^{0.5} \quad \text{(A2.3)}$$

where $e(D_{PFG})$ is the error of the diffusion coefficient of water in the pores, and $e(D_b)$ is the error of the free diffusion coefficient in the bulk water.

A2.2 Standard deviation error (SD)

This method was used to discriminate the true change in the incremental volume of nitrogen from that attributed to noise, in Chapter 5. Also, it was used to estimate the error in the average concentration of CsA released, measured via HPLC, the average particle size of the silicas and PLGA NPs measured via DLS, and the average zeta potential measurements.

The SD method is indicative of how spread out the numbers are, by using as a measure the squared differences of the values from the mean value. For this, the following algorithm is applied:

$$\sigma^2 = \frac{\sum_{i=1}^{N} x_i^2 - \frac{\left(\sum_{i=1}^{N} x_i\right)^2}{N}}{N} \quad \text{(A2.4)}$$

where σ is the SD error for a population N of values x.

A2.3 Cumulative error in a gas sorption experiment

Gas sorpion studies performed with ASAP 2020, have an error in the volume adsorbed of ±0.30 cm^3/g, at each pressure point. This is because at each pressure point, successive doses of gas are introduced into the sample, until the system reaches its equilibrium and the change in the adsorbed volume between two doses is lower than 0.30 cm^3/g. The cumulative error, ΔE, in the total volume adsorbed is a summary of the errors at each pressure point and it is calculated as follows:

$$\Delta E=(\Delta A^2+\Delta B^2+\ldots)^{1/2} \quad \text{(A2.5)}$$

where ΔA, ΔB, etc are the errors at each pressure point.

Appendix A3 Conversion of the relative pressure of water into relative pressure of nitrogen

Capillary condensation in the pores is predicted by Kelvin equation, expressed as follows:

$$\ln\left(\frac{P}{P_0}\right)=-\frac{\gamma V_M}{RTr_p} \quad \text{(A3.1)}$$

For saturation with water at 294 K, γ=72.8 N/m, T=294 K and V_M=18 cm^3/mol. For saturation with nitrogen at 77.3 K, γ=8.85 N/m, T=77.3 K and V_M=34.6 cm^3/mol. By substituting these values into equation A3.1 for both nitrogen and water, and by dividing the relations obtained, the relative pressure of water can be converted into nitrogen relative pressure as follows:

$$\left(\frac{P}{P_0}\right)_{N_2}=\exp\left[0.889\ln\left(\frac{P}{P_0}\right)_{H_2O}\right] \quad \text{(A3.2)}$$

Appendix A4 Background theories

A4.1 Small angle X-ray scattering (SAXS)

Small angle X-ray scattering technique is applied for characterization of small structures on the regime of 10-100 nm. X-ray radiation, having a typical wavelength range of ~1 Å, is

used to interact with the matter and scatter towards all directions. There exist two types of scattering; the Compton (or incoherent scattering) and Rayleigh (or coherent scattering). The former is produced when photons interact with the electrons of the matter but are bounced away, leading to a loss of energy and therefore does not carry any structural information about the material. The latter is produced by photons colliding onto the electrons, initiating their oscillation at the same frequency as the radiation beam and emitting radiation containing all the structural information of the material. These re-emitted waves, interfere with one another constructively or destructively producing a diffraction pattern. Bragg diffraction is produced for constructive interference and can be represented in a simple model presented in Figure A4.1

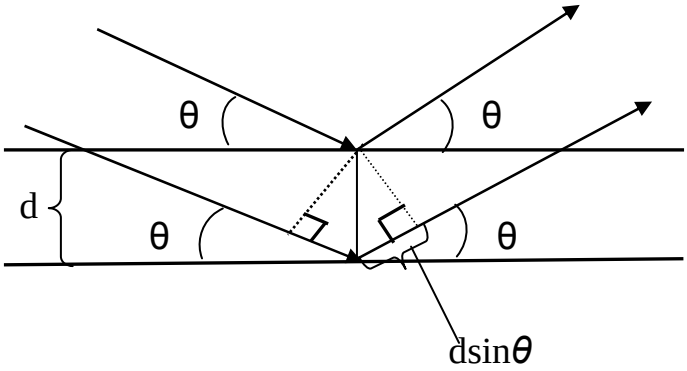

Figure A4.1 Representation of Bragg's diffraction of two X-ray beams, from two parallel plans of a crystal lattice

Here the X-ray beams (with identical wavelength) approach a crystalline solid, exhibiting high lattice periodicities and consisting of parallel plans separated with a spacing d. They will then both scatter, with the lower beam having a path length of *2dsinϑ*. When this length is equal to an integer multiple (*n*) of the wavelength radiation (*λ*), constructive interference occurs and it is described by Bragg's law:

$$n\lambda = 2d\sin\theta \tag{A4.1}$$

Where, ϑ is the angle (<2° for small angle scattering) between the beam and the scattering planes as depicted in Figure A4.1. An alternative expression of equation A4.1 is equation A4.2 which correlates the diffraction angle to the wavevector, *q*:

$$q = 4\frac{\pi \sin\theta}{\lambda} \quad \text{(A4.2)}$$

where

$$q=2\pi/d \quad \text{(A4.3)}$$

The scattering pattern observed is dependant on the electron density of the species and as such contains information about individual molecules (ie polymer chains, lipid molecules) or bigger aggregated moieties (ie polymer micelles, liposomes). The scattered intensity *I(q)* of the particles present in a solvent is shown by the following relationship:

$$I(q) = NV^2(\Delta\rho)^2 P(q)S(q) + background \quad \text{(A4.4)}$$

where *N* and *V* is the number and the volume of the particles, *Δρ* is the difference in the scattering length density between the particle and the solvent, *P(q)* is the scattering of a single particle, *S(q)* is the structure factor due to interparticle interactions (=1 for dilute systems) and the *background* is the scattering arising from the solvent itself.

As scattering occurs at the boundaries between phases with differences in electron density, in a porous inorganic system diffraction occurs between the planes containing the pores and on the surface of the pores. Therefore it is possible to study the lattice structure and pore surface roughness on the low and high *q* range, respectively. The pores can be arranged in an amorphous, worm-like, lamellar, hexagonal or cubic structure defined by the Miller indices (*h*, *k*, *l*) at each diffraction peak. The d-spacing, in a porous system is calculated from the 1st order diffraction peak via equation A4.3 and it is characteristic of the space between the centres of the pores. For a cubic system the unit cell value, *a*, is equal to the d-spacing of the 1st order peak but for a 2D-hexagonal phase the distance between the pore centres is the d-spacing x 2/√3.

A4.2 High Performance Liquid Chromatography (HPLC) analysis

The CsA concentration present in the collected aqueous solutions was determined using a Surveyor PlusTM HPLC system from Thermo Electron Corporation. This analysis was performed using a Hypersil Gold 5 µm x 4.6 mm x 150 mm size exclusion column, from Thermo Scientific, on the HPLC device. The column used has a pore size of 175 Å, suitable

for measuring peptides up to 2 KDa. For each run, a mobile phase consisting of a EtOH/H_2O mixture was used, at a flow rate of 3.5 ml/min. Each run duration was 16 min with the mobile phase being ethanol/water 60:40 v/v for the first 4 min, and then gradually linearly increasing the concentration of EtOH to 100% until the 12th minute of the run. In the remaining 4 min, the volume fraction of EtOH was decreased gradually back to the initial ratio of 60:40 v/v, and was maintained as such until the end of the run. A calibration curve for CsA solubility in EtOH as measured by HPLC was produced using as standard concentrations 5, 10, 25, 50, 75 and 100 µg/mL of CsA in EtOH. The curve obtained is presented in Figure A4.2.

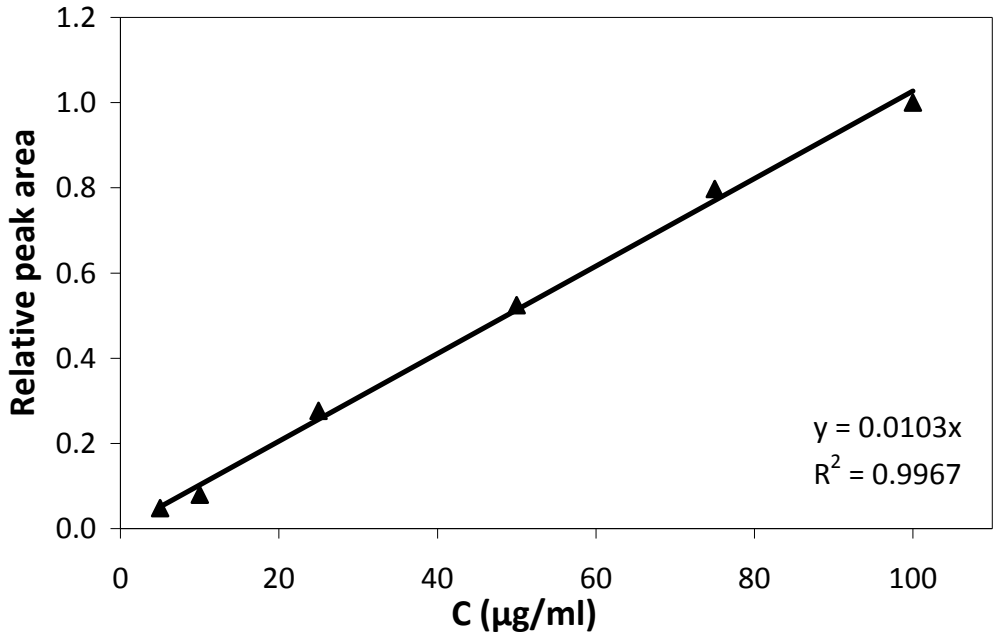

Figure A4.2 CsA standard calibration curve obtained by HPLC

A4.3 Circular Dichroism (CD)

As casein conformation is expected to influences its templating activity, circular dichroism (CD) was used to determine the peptide backbone structure (Whitmore and Wallace, 2008) under the templating experimental conditions. Although casein was initially dissolved in acetic acid solution at pH 2, addition of silica precursor will increase the pH to 2.5. Therefore CD spectra are recorded at both pH values. The results are compared to the casein structure at neutral condition. For this CD spectra were obtained in the far UV range (180-250 nm). The scans were recorded using a ChirascanTM circular

dichroism spectrometer from Applied Photophysics. The casein solution was placed in a quartz cell of 0.5 mm path length to be scanned with a step size of 1 nm bandwidth, 3 s time per point and 3 repeats. The solutions were prepared at a concentration of 0.5 mg/ml of sodium casein. For each pH, the background scans of acetic acid were removed from the sample scans. The recorded results are presented in Figure A4.3.

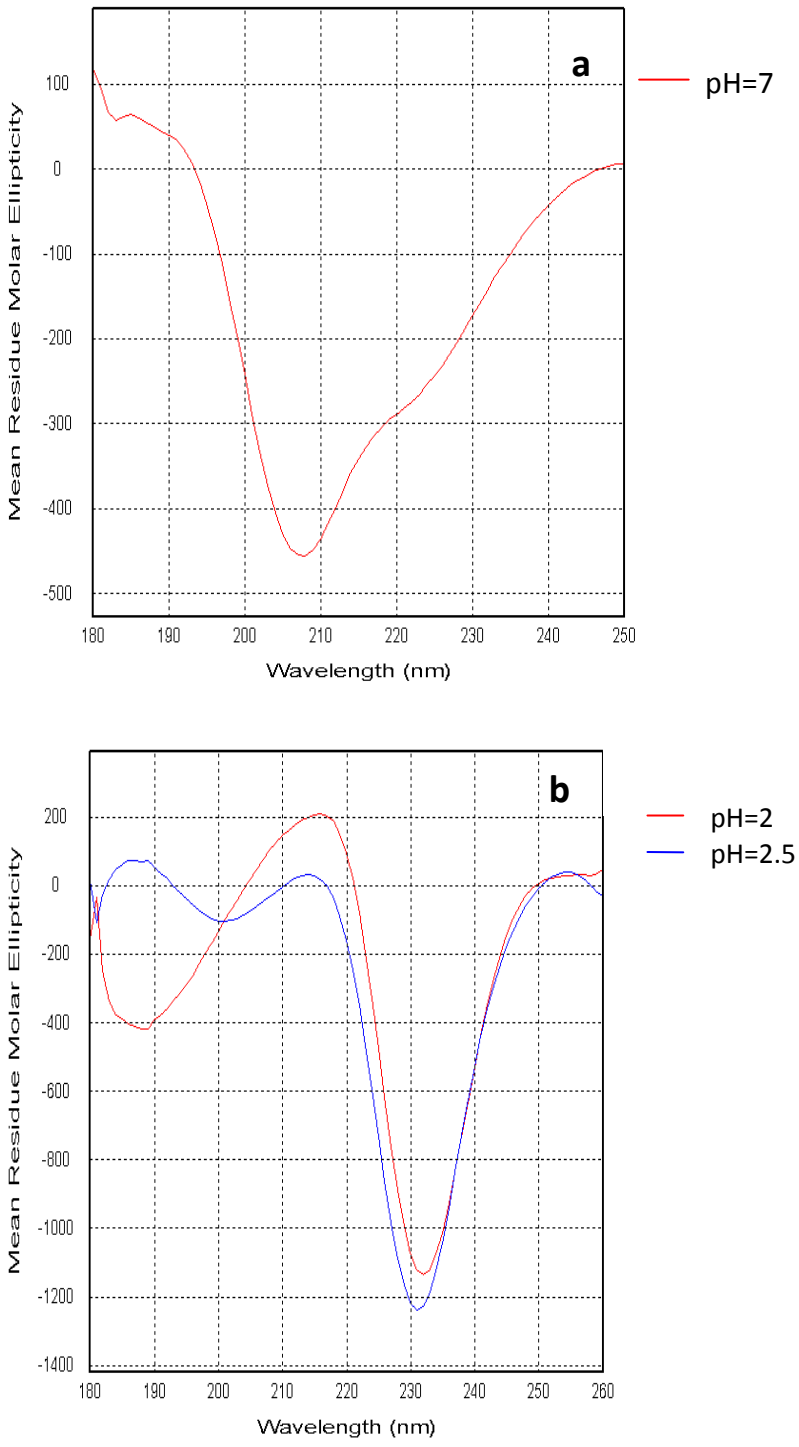

Figure A4.3 Far-UV CD spectra of sodium casein in media with a) pH 7 and b) pH 2 and pH 2.5. The ellipticities are expressed in (deg cm^2 d/mol)

In Figure A3a it is seen that CD spectra of casein at pH 7, exhibits a large negative ellipticity at ~208 nm, a positive ellipticity at ~190 nm and a small negative ellipticity at ~222 nm, which are indicative of an α-helix structure. However, the transition seen at ~222 nm is not very clear, suggesting that there is a large degree of disorder in the structure, arising from the different structures of α- (mainly helix), β- and κ-caseins (mainly random coils). From Figure A3b it is seen that casein structural elements at pH 2 are completely replaced by random coils. This is shown by the weak minima of the spectrum at ~230 nm with no ellipticities at ~190-208 nm which would be characteristic of α-helix or β-sheet/turn. At pH 2.5, only slight conformational changes are observed with casein, suggesting that addition of sodium silicate does not affect the overall structure of sodium casein-the conformation remains a random coil. Similar variations in protein conformation from helix to random coils, with decreasing pH from 2.5 to 1.5, were found by Chakraborty and Basak who studied each type of casein separately (Chakraborty and Basak, 2007).

A4.4. Fourier transform infrared spectroscopy (FTIR)

Initially, the final amount of dry silica obtained for each template used was measured gravimetrically. This amount varied slightly between batches but it could be assumed as approximately 2.5 g of dried silica. The sodium silicate solution used has ~17% of SiO_2, meaning that there is 2.6 g of SiO_2 in the 15.3 g used to prepare the batches. This corresponds to 96% efficiency of the method.

Infrared spectroscopy was then adopted to confirm amorphous silica formation for both templated particles. For this FTIR experiments were performed on drug-free silica particles after calcination. Also, FTIR spectrum was recorded to study the CsA conformation when deposited on the silicas. This can be either amorphous or, crystalline or, a mixture of both, and conformations may appear as changes in the FTIR spectra due to a particular H-bonding pattern. For this reason, we attempted to acquire FTIR spectra for CsA *in situ* (loaded in the silicas). However, the contributions from silica in the IR region were far greater than the contributions from CsA, and further analysis was not

possible (data not shown). FTIR spectra, though, were recorded to characterize bulk cyclosporin before (as purchased) and after re-crystallization in absolute ethanol. This was done to detect any alteration into the drug structure during the loading process into the silica particles. For this CsA loaded silica particles were initially sonicated in ethanol to collect all the encapsulated drug and then, the suspension was left until all the ethanol was evaporated and the dry re-crystallized CsA was obtained. The measurements were performed a Thermo-ScientificNicolet iS10 FT-IR Spectrometer, in the range of 400-4000 1/cm. The Smart iTR accessory allows the reading of samples without the need of mixing a potassium bromide pellet with the sample. For each sample the mean of 16 consecutive readings was calculated.

The recorded IR spectra for the dry silicas are shown in Figure A4.4. Spectra from both silicas display a peak around 1100 1/cm which can be representative of the formation of siloxane bonds in the Si-O-Si condensed silica network and a peak around 800 1/cm indicating Si-OH stretching, indicative of an amorphous silicon network.

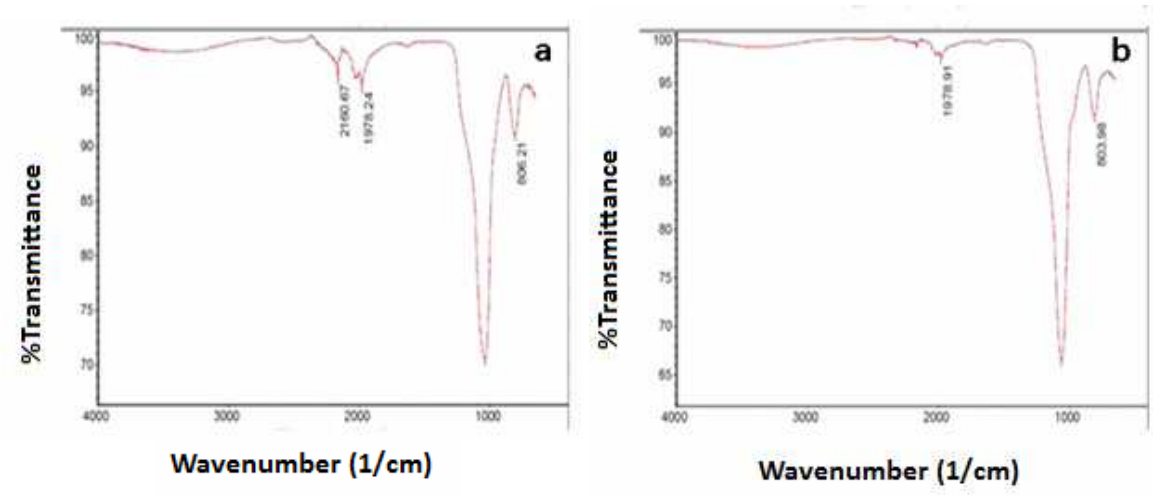

Figure A4.4 FTIR spectra of a) Lutrol (F127) and b) sodium casein templated silicas

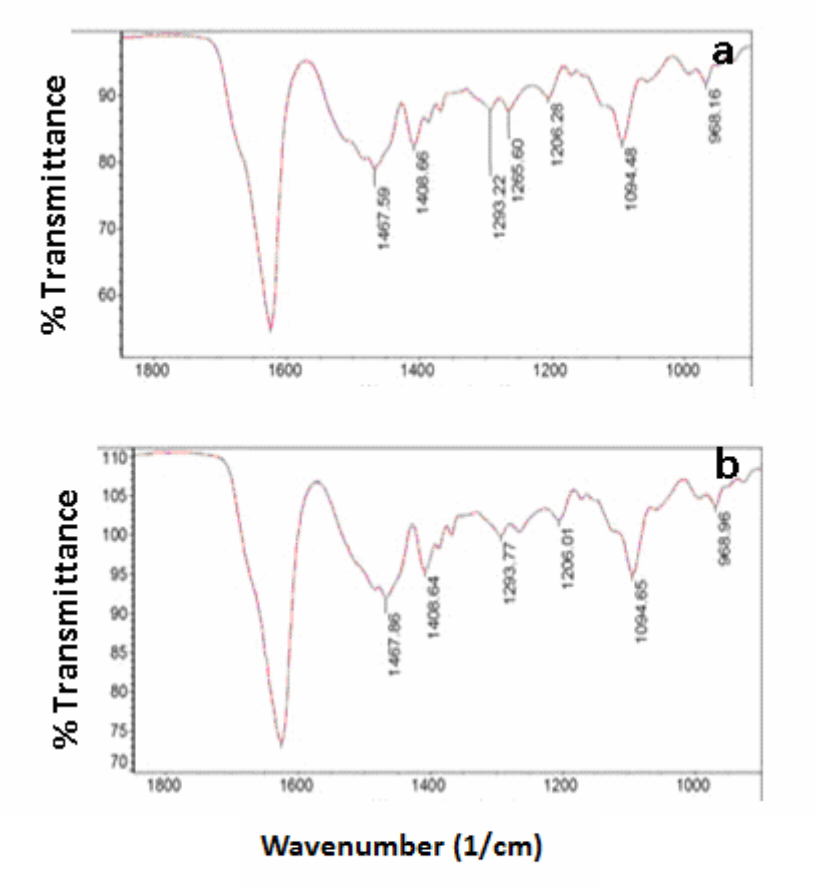

Figure A4.5 FTIR spectra of a) purchased and b) re-crystallized CsA recovered from absolute ethanol dissolution

The data for the purchased and re-crystallized CsA are shown in Figure A4.5. Here the characteristic bands for the amide-I and ester groups are examined. The amide-I bands ranging between 1600-1700 1/cm are particularly important in protein IR spectroscopy due to the fact that they are native to all proteins and influenced by secondary structure, without being strongly influenced by side chains (Ganim et al., 2008). In this study the FTIR spectrum for bulk CsA re-crystallized from ethanol, displays an intensity for all peaks similar to the spectrum of the purchased bulk CsA. The position and shape of the peaks, particularly that for the β sheet structure absorption band near 1625 1/cm remains unaltered. Therefore, the dissolution of CsA in ethanol for loading into the mesoporous silicas did not degrade the peptide structure.

Appendix 5 Experimental results

A5.1 Synthesis of PLGA- PEG copolymer

Carboxylate-functionalized PLGA-PEG co-polymer was synthesized by conjugation of acid ended PLGA into NH_2-PEG-CH_3 as proposed by Cheng et al., (2007). Specifically, 5 gr (0.105 mmol) PLGA-COOH (Purac, MW:47,581 g/mol, PD: 1.65, GPC, THF and lactic:glycolid acid=1:0.84, ^{1}H-NMR, 300 MHz, CD_3CN) was dissolved in 27ml dehydrated DCM and converted into PLGA-NHS in the presence of 47.43 mg (0.412 mmol) NHS and 70.73 mg (0.45 mmol) EDC. PLGA-NHS was then precipitated in 5ml dehydrated ethyl ether and washed at with ice-cold 50/50 mixture of MeOH/ethyl ether. The precipitate was dried under vacuum for 3hrs. Thereafter, 1 gr (0.021 mmol) of PLGA-NHS were left to dissolve overnight in 8ml dehydrated $CHCl_3$. To this, 0.298 mg (26.3 μmol) NH_2-PEG-CH_3 (MW:11,300 g/mol) was added in the presence of 10.097 mg (0.078 mmol) DIEA and stirred for 12 hrs. The CH_3-ended PLGA-PEG copolymer was precipitated and washed with ice-cold MeOH to remove any unreacted PEG and then dried under vacuum. There was 50.1% wt. product yield and the resulting copolymer was stored at -20 ^{o}C for nanoparticle formulations. PLGA-PEG polymer was characterized with regard to its composition by ^{1}H-NMR and its Mn and MW distribution, PD=MW/Mn, by gel permeation chromatography (GPC).

^{1}H NMR (CD_3CN, 300 MHz) (Figure A5.1): δ 1.5 [d, $(OCH(C\underline{\mathbf{H}}_3)C(O)OCH_2(CO))_x$–$(CH_2CH_2O)_y$], 3.6 [s, $(OCH(CH_3)C(O)OCH_2(CO))_x$–$(C\underline{\mathbf{H}}_2C\underline{\mathbf{H}}_2O)_y$], 4.8 [m, $(OCH(CH_3)C(O)OC\underline{\mathbf{H}}_2(CO))_x$– $(CH_2CH_2O)_y$], 5.2 [m, $(OC\underline{\mathbf{H}}(CH_3)C(O)OCH_2(CO))_x$– $(CH_2CH_2O)_y$]. The C**H**, C$\mathbf{H}_2$ and C$\mathbf{H}_2$C$\mathbf{H}_2$ groups are representative of the lactic, glycolic, and PEG monomers, respectively. It was found that in the PLGA-PEG conjugated polymer, the lactic:glycolic:PEG monomer ratio is 1:0.84:0.05 (i.e. for every 100 groups of lactic there exist 84 groups of glycolic and 5 groups of PEG). This was calculated by taking the ratio between the integrated spectrum intensity at 5.2, 4.8 and 3.6 ppm, for lactic acid, glycolic acid and PEG, respectively. The MW of PLGA-PEG was 27,171 g/mol and PD=1.72, which is smaller than the starting PLGA polymer used for conjugation, or the sum of the starting PLGA (47,581 g/mol) and PEG (11,300 g/mol) polymers, and the literature report itself (Cheng et al., 2007). This shows that the PLGA or/and PEG polymer chains broke in one of the synthesis steps, and this is due to an interplay of the polymerization

conditions adopted (i.e. reactions time, polymer purity) (Beletsi et al., 1999). The synthesis of PLGA-PEG polymer was only done once, and the same polymer was used for all the NP formulations in this thesis.

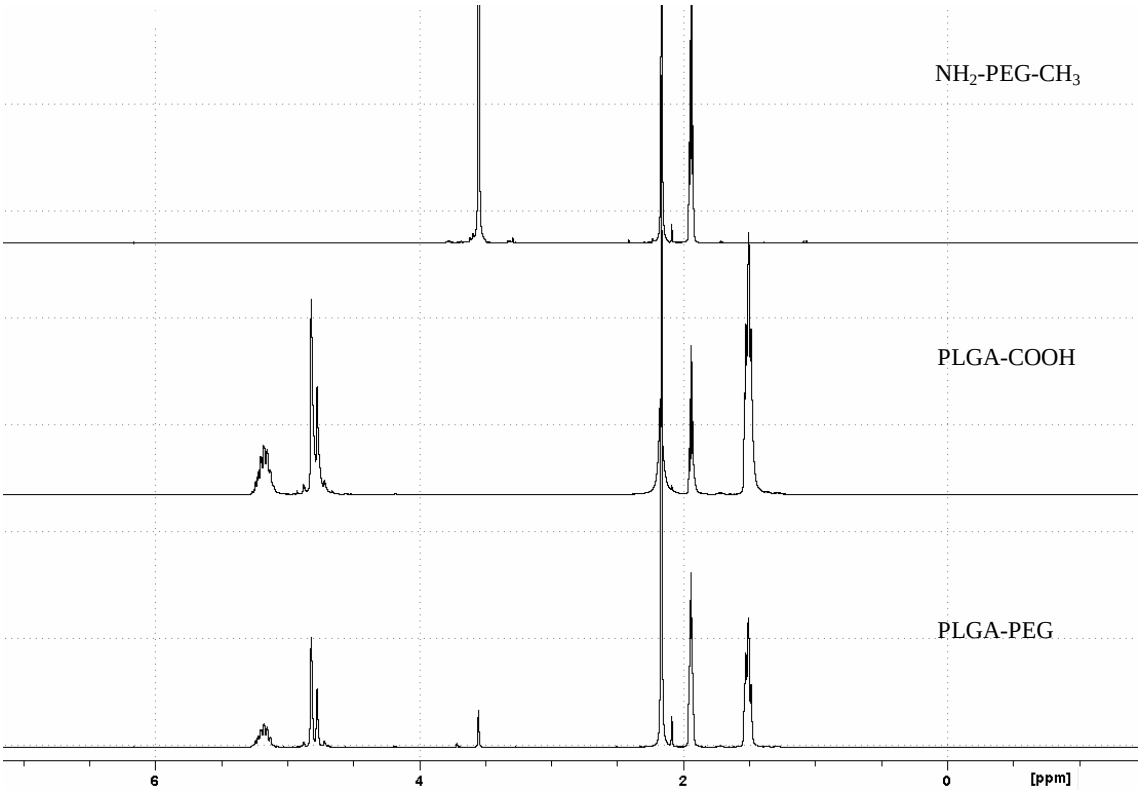

Figure A5.1 ^{1}H NMR (300MHz) spectra for NH_2-PEG-CH_3 and PLGA-COOH polymers and conjugated PLGA-PEG copolymer

A5.2 Gas sorption studies for PLGA NPs

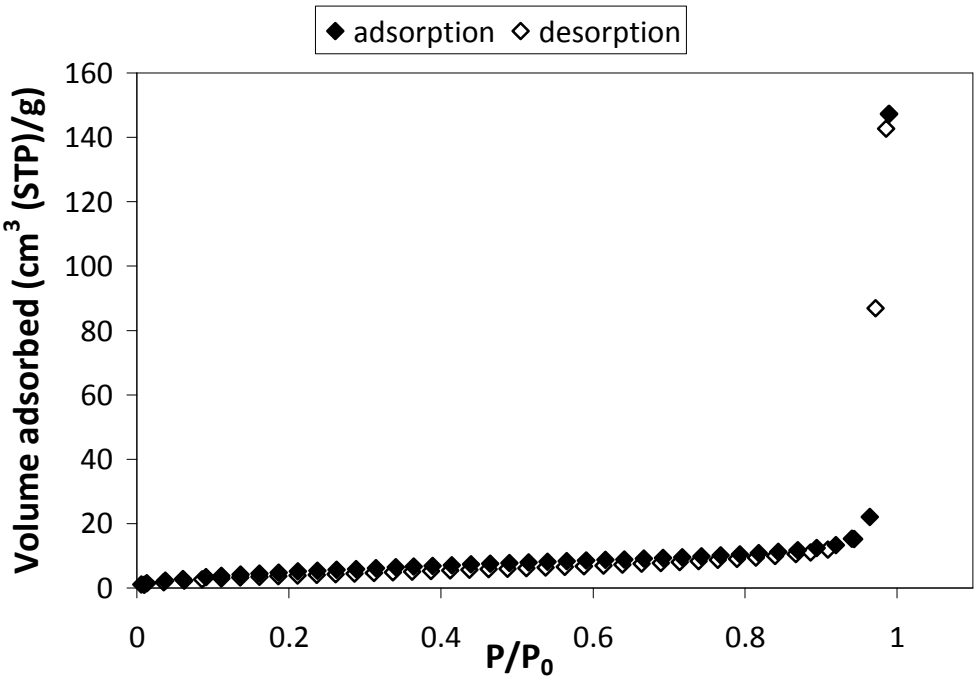

Figure A5.2 Nitrogen sorption isotherm (77.3 K) of PLGA NPs synthesized via dialysis method in DMSO. The high nitrogen uptake above P/P_0=0.96 corresponds to the interparticle nitrogen condensation

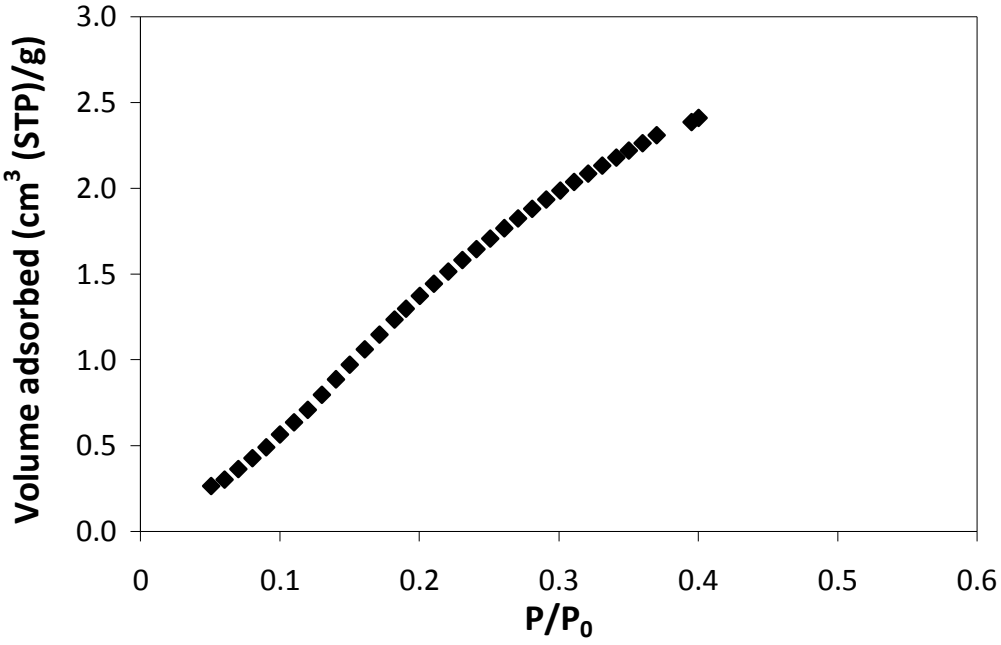

Figure A5.3 Krypton adsorption isotherm (77.3 K) for PLGA NPs synthesized via dialysis method in DMSO

A5.3 Calibration curves from UV-vis and fluorescent spectroscopy studies

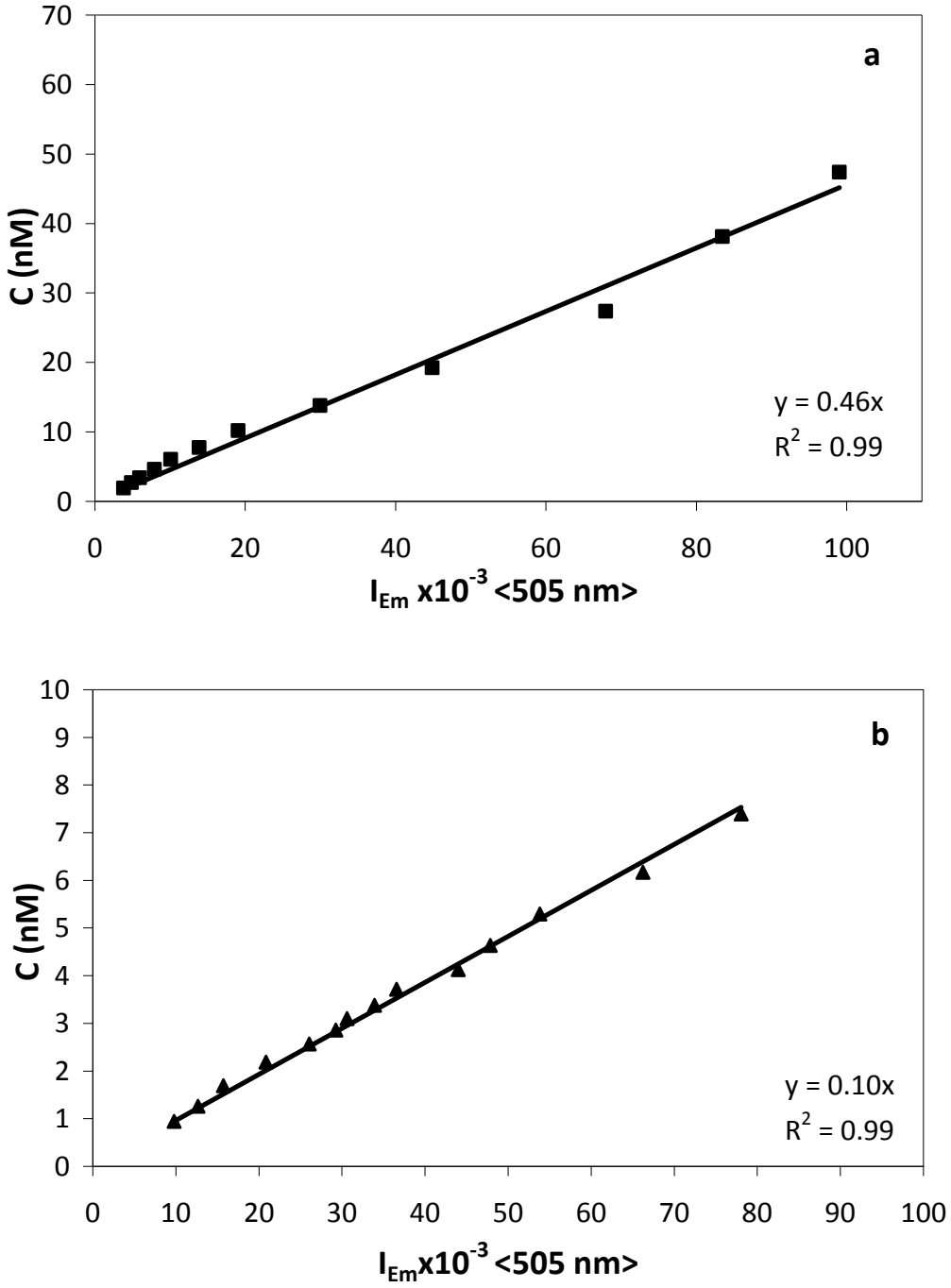

Figure A5.4 Calibration curves for a) 70 kDa and b) 150 kDa FITC-Dextran in ultrapure water measured fluorimetrically (wavelength excitation: 495nm, emission: 505nm)

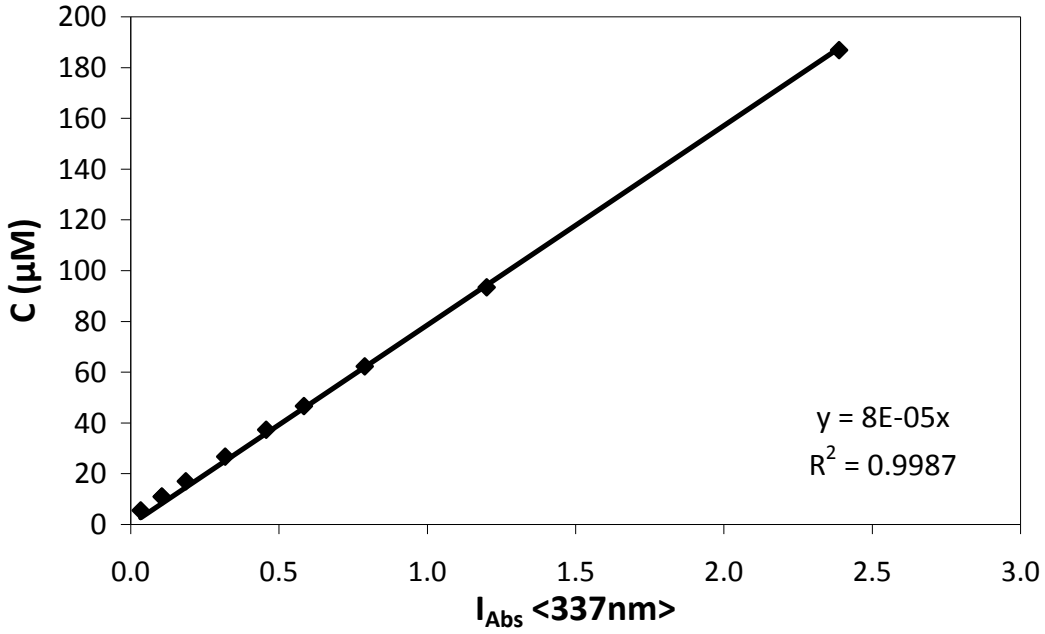

Figure A5.5 Calibration curve of TFMU dissolved in DMF measured via UV-vis spectroscopy at 337 nm absorbance wavelength

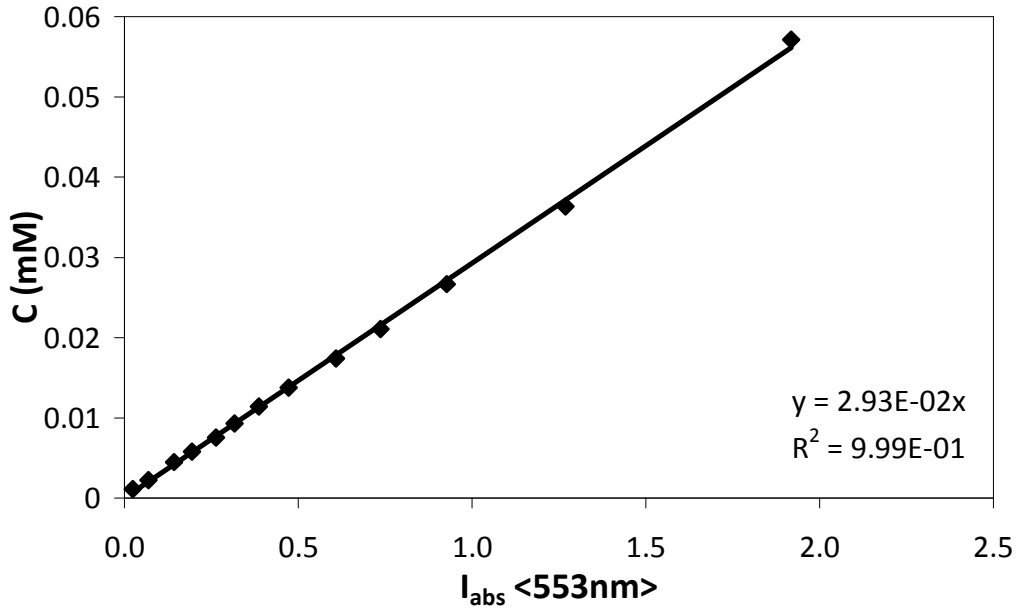

Figure A5.6 Calibration curve of Nile Red dissolved in DMSO measured via UV-vis spectroscopy at 553 nm absorbance wavelength

A5.4 Size of PLGA NP after freeze-drying measured by DLS

Polymer/solvent	Loaded agent	Mean particle size, *r*±SD(nm)
RG504/DMSO	-	114.8±0.8
RG504/DMSO	NR	108.3±1.5
RG504/DMF	-	133±20.1
RG504/DMF	NR	141.2±17.8
RG504H/DMSO	NR	164.60±4.1
RG504H/DMF	-	120.48±5.7
RG504H/DMF	NR	129.8± 2.5
RG504 (0.05% PVA) /DMSO	Paclitaxel	140±0.02
RG504 (0.1% PVA) /DMSO	Paclitaxel	151.9±9.2
RG504/DMSO	TFMU	179.9±4.1
RG504/MeCN	TFMU	167.1±7.4
RG504/DMF	TFMU	132.4±2.8
RG504H/DMF	TFMU	167.2±3.8
RG504/DMSO	FITC-Dextran (70 kDa)	108.0±0.3
RG504/DMSO	FITC-Dextran (150 kDa)	95.71±0.4

Table A5.1 Size of nanoparticles synthesized via dialysis, with and without loaded agent, after freeze drying

A5.5 Composition of AcSF

The AcSF was composed of the following salts: sodium (148 mM), potassium (4.02 mM), magnesium (1.22 mM), calcium (1.36 mM), chloride (133.8 mM), phosphate (0.58 mM), sulfate (1.22 mM), and bicarbonate (22 mM)

Bibliography

AHLIN, P., KRISTL, J., KRISTL, A. & VRECER, F. 2002. Investigation of polymeric nanoparticles as carriers of enalaprilat for oral administration. *International Journal of Pharmaceutics,* 239**,** 113-120.

AKSNES, D. W., FORLAND, K. & KIMTYS, L. 2001a. Pore size distribution in mesoporous materials as studied by H-1 NMR. *Physical Chemistry Chemical Physics,* 3**,** 3203-3207.

AKSNES, D. W., FORLAND, K. & KIMTYS, L. 2004. H-1 and H-2 NMR studies of cyclohexane nanocrystals in controlled pore glasses. *Journal of Molecular Structure,* 708**,** 23-31.

AKSNES, D. W., FORLAND, K., KIMTYS, L. & STOCKER, M. 2001b. Pore-size determination of mesoporous materials by H-1 NMR spectroscopy. *Applied Magnetic Resonance,* 20**,** 507-517.

AKSNES, D. W., FORLAND, K. & STOCKER, M. 2005. H-1 NMR relaxation and diffusion studies of cyclohexane and cyclopentane confined in MCM-41. *Microporous and Mesoporous Materials,* 77**,** 79-87.

AKSNES, D. W. & GJERDÅKER, L. 1999. NMR line width, relaxation and diffusion studies of cyclohexane confined in porous silica. *Journal of Molecular Structure,* 475**,** 27-34.

ALLARD, E., PASSIRANI, C. & BENOIT, J.-P. 2009. Convection-enhanced delivery of nanocarriers for the treatment of brain tumors. *Biomaterials,* 30**,** 2302-2318.

ALLEMANN, E., GURNY, R. & DOELKER, E. 1993. Drug-Loaded Nanoparticles - Preparation Methods and Drug Targeting Issues. *European Journal of Pharmaceutics and Biopharmaceutics,* 39**,** 173-191.

ALLEN, S. G., STEPHENSON, P. C. L. & STRANGE, J. H. 1997. Morphology of porous media studied by nuclear magnetic resonance. *Journal of Chemical Physics,* 106**,** 7802-7809.

ALLEN, S. G., STEPHENSON, P. C. L. & STRANGE, J. H. 1998. Internal surfaces of porous media studied by nuclear magnetic resonance cryoporometry. *Journal of Chemical Physics,* 108**,** 8195-8198.

ANDERSON, J. M. & SHIVE, M. S. 1997. Biodegradation and biocompatibility of PLA and PLGA microspheres. *Advanced Drug Delivery Reviews,* 28**,** 5-24.

ANONE. *Dielectric constant* [Online]. Available: http://macro.lsu.edu/HowTo/solvents/Dielectric%20Constant%20.htm [Accessed 25 May 2012].

ARAKAWA, T., KITA, Y. & TIMASHEFF, S. N. 2007. Protein precipitation and denaturation by dimethyl sulfoxide. *Biophysical Chemistry,* 131**,** 62-70.

ASTETE, C. E. & SABLIOV, C. M. 2006. Synthesis and characterization of PLGA nanoparticles. *Journal of Biomaterials Science, Polymer Edition,* 17**,** 247-289.

ATKINS, P. & DE PAULA, J. D. 2010. Atkins' physical chemistry.].

AVGOUSTAKIS, K., BELETSI, A., PANAGI, Z., KLEPETSANIS, P., LIVANIOU, E., EVANGELATOS, G. & ITHAKISSIOS, D. S. 2003. Effect of copolymer composition on the physicochemical characteristics, in vitro stability, and biodistribution of PLGA-mPEG nanoparticles. *International Journal of Pharmaceutics,* 259**,** 115-127.

BAGSHAW, S. A., PROUZET, E. & PINNAVAIA, T. J. 1995. Templating of Mesoporous Molecular-Sieves by Nonionic Polyethylene Oxide Surfactants. *Science,* 269**,** 1242-1244.

BALL, P. C. & EVANS, R. 1989. Temperature-Dependence of Gas-Adsorption on a Mesoporous Solid - Capillary Criticality and Hysteresis. *Langmuir,* 5**,** 714-723.

BARRETT, E. P., JOYNER, J. G. & HALENDA, P. P. 1951. The Determination of Pore Volume and Area Distributions in Porous Substances. I. Computations from Nitrogen Isotherms. *J.Am.Chem.Soc,* 73.

BECK, J. S., VARTULI, J. C., ROTH, W. J., LEONOWICZ, M. E., KRESGE, C. T., SCHMITT, K. D., CHU, C. T. W., OLSON, D. H., SHEPPARD, E. W., MCCULLEN, S. B., HIGGINS, J. B. & SCHLENKER, J. L.

1992. A New Family of Mesoporous Molecular-Sieves Prepared with Liquid-Crystal Templates. *Journal of the American Chemical Society,* 114**,** 10834-10843.

BECK, R. E. & SCHULTZ, J. S. 1970. Hindered Diffusion in Microporous Membranes with Known Pore Geometry. *Science,* 170**,** 1302-1305.

BELETSI, A., LEONTIADIS, L., KLEPETSANIS, P., ITHAKISSIOS, D. S. & AVGOUSTAKIS, K. 1999. Effect of preparative variables on the properties of poly(dl-lactide-co-glycolide)–methoxypoly(ethyleneglycol) copolymers related to their application in controlled drug delivery. *International Journal of Pharmaceutics,* 182**,** 187-197.

BENNY, O., MENON, L. G., ARIEL, G., GOREN, E., KIM, S.-K., STEWMAN, C., BLACK, P. M., CARROLL, R. S. & MACHLUF, M. 2009. Local Delivery of Poly Lactic-co-glycolic Acid Microspheres Containing Imatinib Mesylate Inhibits Intracranial Xenograft Glioma Growth. *Clinical Cancer Research,* 15**,** 1222-1231.

BENOIT, J. P., FAISANT, N., VENIER-JULIENNE, M. C. & MENEI, P. 2000. Development of microspheres for neurological disorders: From basics to clinical applications. *Journal of Controlled Release,* 65**,** 285-296.

BERGSTROM, M. & PEDERSEN, J. S. 1999. Structure of pure SDS and DTAB micelles in brine determined by small-angle neutron scattering (SANS). *Physical Chemistry Chemical Physics,* 1**,** 4437-4446.

BLANCO, M. D., SASTRE, R. L., TEIJON, C., OLMO, R. & TEIJON, J. M. 2006. Degradation behaviour of microspheres prepared by spray-drying poly(D,L-lactide) and poly(D,L-lactide-co-glycolide) polymers. *International Journal of Pharmaceutics,* 326**,** 139-147.

BLOCH, F., HANSEN, W. W. & PACKARD, M. 1946. Nuclear Induction. *Physical Review,* 69**,** 127-127.

BOBO, R. H., LASKE, D. W., AKBASAK, A., MORRISON, P. F., DEDRICK, R. L. & OLDFIELD, E. H. 1994. Convection-enhanced delivery of macromolecules in the brain. *Proceedings of the National Academy of Sciences of the United States of America,* 91**,** 2076-2080.

BOGDAN, A., KULMALA, M. & AVRAMENKO, N. 1998. Reduction of enthalpy of fusion and anomalies during phase transitions in finely divided water. *Physical Review Letters,* 81**,** 1042-1045.

BOISDRONCELLE, M., MENEI, P. & BENOIT, J. P. 1995. PREPARATION AND CHARACTERIZATION OF 5-FLUOROURACIL-LOADED MICROPARTICLES AS BIODEGRADABLE ANTICANCER DRUG CARRIERS. *Journal of Pharmacy and Pharmacology,* 47**,** 108-114.

BOOTH, H. F. & STRANGE, J. H. 1998. Organic nanocrystals: an NMR study of cyclohexane in porous silica. *Molecular Physics,* 93**,** 263-269.

BORM, P. J. A., TRAN, L. & DONALDSON, K. 2011. The carcinogenic action of crystalline silica: A review of the evidence supporting secondary inflammation-driven genotoxicity as a principal mechanism. *Critical Reviews in Toxicology,* 41**,** 756-770.

BRANDRUP, J., IMMERGUT, E. H., GRULKE, E. A., ABE, A. & BLOCH, D. R. 2005. Polymer Handbook (4th ed.). 4th ed.: John Wiley & Sons.

BRINKER, C. J., SCHERRER, G. W 1990. *Sol-gel science: The Physics of Chemistry of Sol-Gel processing,* San Diego, Academic Press, inc.

BROEKHOF.JC & DE BOER, J. H. 1968a. Studies on Pore Systems in Catalysts .11. Pore Distribution Calculations from Adsorption Branch of a Nitrogen Adsorption Isotherm in Case of Ink-Bottle Type Pores. *Journal of Catalysis,* 10**,** 153-&.

BROEKHOF.JC & DEBOER, J. H. 1968b. Studies on Pore Systems in Catalysts .12. Pore Distributions from Desorption Branch of a Nitrogen Sorption Isotherm in Case of Cylindrical Pores .A. An Analysis of Capillary Evaporation Process. *Journal of Catalysis,* 10**,** 368-&.

BROWNSTEIN, K. R. & TARR, C. E. 1977. Spin-Lattice Relaxation in a System Governed by Diffusion. *Journal of Magnetic Resonance,* 26**,** 17-24.

BRUNAUER, S., EMMETT, P. H, TELLER, E 1938. *Journal of the American Chemical Society,* 60**,** 309-319.

BRUSCHI, L., MISTURA, G., LIU, L., LEE, W., GOSELE, U. & COASNE, B. 2010. Capillary Condensation and Evaporation in Alumina Nanopores with Controlled Modulations. *Langmuir,* 26**,** 11894-11898.

BUSKE, J., KÖNIG, C., BASSARAB, S., LAMPRECHT, A., MÜHLAU, S. & WAGNER, K. G. 2012. Influence of PEG in PEG–PLGA microspheres on particle properties and protein release. *European Journal of Pharmaceutics and Biopharmaceutics,* 81**,** 57-63.

CASANOVA, F., CHIANG, C. E., LI, C. P. & SCHULLER, I. K. 2007. Direct observation of cooperative effects in capillary condensation: The hysteretic origin. *Applied Physics Letters,* 91.

CHAKRABORTY, A. & BASAK, S. 2007. pH-induced structural transitions of caseins. *Journal of Photochemistry and Photobiology B-Biology,* 87**,** 191-199.

CHAN, H. B. S., BUDD, P. M. & NAYLOR, T. D. 2001. Control of mesostructured silica particle morphology. *Journal of Materials Chemistry,* 11**,** 951-957.

CHAN, J. M., ZHANG, L. F., YUET, K. P., LIAO, G., RHEE, J. W., LANGER, R. & FAROKHZAD, O. C. 2009. PLGA-lecithin-PEG core-shell nanoparticles for controlled drug delivery. *Biomaterials,* 30**,** 1627-1634.

CHEN, W., HE, J., OLSON, J. J. & LU, D. R. 1997. Carboplatin-Loaded PLGA Microspheres for Intracerebral Implantation: In Vivo Characterization. *Drug Delivery,* 4**,** 301-311.

CHENG, J., TEPLY, B. A., SHERIFI, I., SUNG, J., LUTHER, G., GU, F. X., LEVY-NISSENBAUM, E., RADOVIC-MORENO, A. F., LANGER, R. & FAROKHZAD, O. C. 2007. Formulation of functionalized PLGA-PEG nanoparticles for in vivo targeted drug delivery. *Biomaterials,* 28**,** 869-876.

CHOI, S.-W., KWON, H.-Y., KIM, W.-S. & KIM, J.-H. 2002. Thermodynamic parameters on poly(d,l-lactide-co-glycolide) particle size in emulsification–diffusion process. *Colloids and Surfaces A: Physicochemical and Engineering Aspects,* 201**,** 283-289.

CHOI, S. W., KIM, W. S. & KIM, J. H. 2003. Surface modification of functional nanoparticles for controlled drug delivery. *Journal of Dispersion Science and Technology,* 24**,** 475-487.

CHUNG, T. W., HUANG, Y. Y. & LIU, Y. Z. 2001. Effects of the rate of solvent evaporation on the characteristics of drug loaded PLLA and PDLLA microspheres. *International Journal of Pharmaceutics,* 212**,** 161-169.

CIRPANLI, Y., ALLARD, E., PASSIRANI, C., BILENSOY, E., LEMAIRE, L., CALIS, S. & BENOIT, J. P. 2011. Antitumoral activity of camptothecin-loaded nanoparticles in 9L rat glioma model. *International Journal of Pharmaceutics,* 403**,** 201-206.

CLARIDGE, T. D. W. 2009. *High-resolution NMR technique in organic chemistry*, Elsevier.

COASNE, B., GALARNEAU, A., DI RENZO, F. & PELLENQ, R. J. M. 2007. Effect of morphological defects on gas adsorption in nanoporous silicas. *Journal of Physical Chemistry C,* 111**,** 15759-15770.

COASNE, B., GUBBINS, K. E. & PELLENQ, R. J. M. 2005. Domain theory for capillary condensation hysteresis. *Physical Review B,* 72.

COASNE, B., HUNG, F. R., PELLENQ, R. J. M., SIPERSTEIN, F. R. & GUBBINS, K. E. 2006. Adsorption of sample gases in MCM-41 materials: The role of surface roughness. *Langmuir,* 22**,** 194-202.

COHAN, L. H. 1938. Sorption Hysteresis and the Vapor Pressure of Concave Surfaces. *Journal of the American Chemical Society,* 60**,** 433-435.

CRANK, J. 1975. *The Mathematics of Diffusion,* Oxford, Clarendon Press.

CZOGALLA, A. 2009. Oral cyclosporine A - the current picture of its liposomal and other delivery systems. *Cellular & Molecular Biology Letters,* 14**,** 139-152.

D'AGOSTINO, C., MITCHELL, J., GLADDEN, L. F. & MANTLE, M. D. 2012. Hydrogen Bonding Network Disruption in Mesoporous Catalyst Supports Probed by PFG-NMR Diffusometry and NMR Relaxometry. *The Journal of Physical Chemistry C,* 116**,** 8975-8982.

DALGLEISH, D. G., SPAGNUOLO, P. A. & GOFF, H. D. 2004. A possible structure of the casein micelle based on high-resolution field-emission scanning electron microscopy. *International Dairy Journal,* 14**,** 1025-1031.

DE BOER, J. H. 1958. The shapes of capillaries in the structure and properties of porous solids. *In:* EVERETT, D. H. A. F. S. S. (ed.). London: Butterworths Scientific Publications.

DE KRUIF, C. G. & GRINBERG, V. Y. 2002. Micellisation of beta-casein. *Colloids and Surfaces a-Physicochemical and Engineering Aspects,* 210**,** 183-190.

DE KRUIF, C. G., HUPPERTZ, T., URBAN, V. S. & PETUKHOV, A. V. 2012. Casein micelles and their internal structure. *Advances in Colloid and Interface Science,* 171–172**,** 36-52.

DETCHEVERRY, F., KIERLIK, E., ROSINBERG, M. L. & TARJUS, G. 2004. Mechanisms for Gas Adsorption and Desorption in Silica Aerogels: The Effect of Temperature. *Langmuir,* 20**,** 8006-8014.

DOADRIO, A. L., SOUSA, E. M. B., DOADRIO, J. C., PÉREZ PARIENTE, J., IZQUIERDO-BARBA, I. & VALLET-REGí, M. 2004. Mesoporous SBA-15 HPLC evaluation for controlled gentamicin drug delivery. *Journal of Controlled Release,* 97**,** 125-132.

DOETSCH, I. H., RUTHVEN, D. M. & LOUGHLIN, K. F. 1974. Sorption and Diffusion of n-Heptane in 5A Zeolite. *Canadian Journal of Chemistry,* 52**,** 2717.

DONG, Y. & FENG, S.-S. 2007. Poly(d,l-lactide-co-glycolide) (PLGA) nanoparticles prepared by high pressure homogenization for paclitaxel chemotherapy. *International Journal of Pharmaceutics,* 342**,** 208-214.

DOPPENSCHMIDT, A. & BUTT, H. J. 2000. Measuring the thickness of the liquid-like layer on ice surfaces with atomic force microscopy. *Langmuir,* 16**,** 6709-6714.

DORE, J., WEBBER, B., STRANGE, J., FARMAN, H., DESCAMPS, M. & CARPENTIER, L. 2004. Phase transformations for cyclohexane in mesoporous silicas. *Physica A: Statistical Mechanics and its Applications,* 333**,** 10-16.

DOSSEH, G., XIA, Y. D. & ALBA-SIMIONESCO, C. 2003. Cyclohexane and benzene confined in MCM-41 and SBA-15: Confinement effects on freezing and melting. *Journal of Physical Chemistry B,* 107**,** 6445-6453.

DUFRESNE, A., BÉGIN, R., DION, C., JAGIRDAR, J., ROM, W. N., LOOSEREEWANICH, P., MUIR, D. C. F., RITCHIE, A. C. & PERRAULT, G. 1998. Angular and fibrous particles in lung in relation to silica-induced diseases. *International Archives of Occupational and Environmental Health,* 71**,** 263-269.

EL TAYAR, N., MARK, A. E., VALLAT, P., BRUNNE, R. M., TESTA, B. & VAN GUNSTEREN, W. F. 1993. Solvent-dependent conformation and hydrogen-bonding capacity of cyclosporin A: evidence from partition coefficients and molecular dynamics simulations. *Journal of Medicinal Chemistry,* 36**,** 3757-3764.

ENGINEER, C., PARIKH, J. & RAVAL, A. 2011. Effect of copolymer ratio on hydrolytic degradation of poly(lactide-co-glycolide) from drug eluting coronary stents. *Chemical Engineering Research & Design,* 89**,** 328-334.

ERRICO, C., BARTOLI, C., CHIELLINI, F. & CHIELLINI, E. 2009. Poly(hydroxyalkanoates)-Based Polymeric Nanoparticles for Drug Delivery. *Journal of Biomedicine and Biotechnology***,** -.

ERTAN, A., KODUMURI, P., TALU, O. & TEWARI, S. 2009. Effect of synthesis time and treatment on porosity of mesoporous silica materials. *Adsorption-Journal of the International Adsorption Society,* 15**,** 81-86.

ESPARZA, J. M., OJEDA, M. L., CAMPERO, A., DOMINGUEZ, A., KORNHAUSER, I., ROJAS, F., VIDALES, A. M., LOPEZ, R. H. & ZGRABLICH, G. 2004. N2 sorption scanning behavior of SBA-15 porous substrates. *Colloids and Surfaces a-Physicochemical and Engineering Aspects,* 241**,** 35-45.

EVERETT, D. H. 1954. A General Approach to Hysteresis .3. A Formal Treatment of the Independent Domain Model of Hysteresis. *Transactions of the Faraday Society,* 50**,** 1077-1096.

EVERETT, D. H. 1955. A General Approach to Hysteresis .4. An Alternative Formulation of the Domain Model. *Transactions of the Faraday Society,* 51**,** 1551-1557.

EVERETT, D. H. & WHITTON, W. I. 1952. A General Approach to Hysteresis. *Transactions of the Faraday Society,* 48**,** 749-&.

FANG, R. H., ARYAL, S., HU, C. M. J. & ZHANG, L. F. 2010. Quick Synthesis of Lipid-Polymer Hybrid Nanoparticles with Low Polydispersity Using a Single-Step Sonication Method. *Langmuir,* 26**,** 16958-16962.

FARRHER, G., ARDELEAN, I. & KIMMICH, R. 2007. The heterogeneous distribution of the liquid phase in partially filled porous glasses and its effect on self-diffusion. *Magnetic Resonance Imaging,* 25**,** 453-456.

FECZKÓ, T., TÓTH, J., DÓSA, G. & GYENIS, J. 2011. Influence of process conditions on the mean size of PLGA nanoparticles. *Chemical Engineering and Processing: Process Intensification,* 50**,** 846-853.

FENG, S. S. & HUANG, G. F. 2001. Effects of emulsifiers on the controlled release of paclitaxel (Taxol (R)) from nanospheres of biodegradable polymers. *Journal of Controlled Release,* 71**,** 53-69.

FERNANDEZ-FERNANDEZ, A., MANCHANDA, R. & MCGORON, A. J. 2011. Theranostic Applications of Nanomaterials in Cancer: Drug Delivery, Image-Guided Therapy, and Multifunctional Platforms. *Applied Biochemistry and Biotechnology,* 165**,** 1628-1651.

FESSI, H., PUISIEUX, F., DEVISSAGUET, J. P., AMMOURY, N. & BENITA, S. 1989. Nanocapsule Formation by Interfacial Polymer Deposition Following Solvent Displacement. *International Journal of Pharmaceutics,* 55**,** R1-R4.

FINDENEGG, G. H., GROSS, S. & MICHALSKI, T. 1994. Pore Condensation in Controlled-Pore Glass - an Experimental Test of the Saam-Cole Theory. *Characterization of Porous Solids Iii,* 87**,** 71-80.

FINNIE, K. S., WALLER, D. J., PERRET, F. L., KRAUSE-HEUER, A. M., LIN, H. Q., HANNA, J. V. & BARBE, C. J. 2009. Biodegradability of sol-gel silica microparticles for drug delivery. *Journal of Sol-Gel Science and Technology,* 49**,** 12-18.

FIROUZI, A., KUMAR, D., BULL, L. M., BESIER, T., SIEGER, P., HUO, Q., WALKER, S. A., ZASADZINSKI, J. A., GLINKA, C., NICOL, J., MARGOLESE, D., STUCKY, G. D. & CHMELKA, B. F. 1995. Cooperative Organization of Inorganic-Surfactant and Biomimetic Assemblies. *Science,* 267**,** 1138-1143.

FONSECA, C., SIMOES, S. & GASPAR, R. 2002. Paclitaxel-loaded PLGA nanoparticles: preparation, physicochemical characterization and in vitro anti-tumoral activity. *Journal of Controlled Release,* 83**,** 273-286.

FORSGREN, J., JÄMSTORP, E., BREDENBERG, S., ENGQVIST, H. & STRØMME, M. 2010. A ceramic drug delivery vehicle for oral administration of highly potent opioids. *Journal of Pharmaceutical Sciences,* 99**,** 219-226.

FRASCH, J., LEBEAU, B., SOULARD, M., PATARIN, J. & ZANA, R. 2000. Study of interactions between silicate species and surfactant micelles in the synthesis of organized mesoporous materials. *In:* ABDELHAMID, S. & MIETEK, J. (eds.) *Studies in Surface Science and Catalysis.* Elsevier.

FUKUSHIMA, E. & ROEDER, S. B. W. 1981. *Experimental Pulse NMR: A Nuts and Bolts Approach,* Reading, Mass, Perseus Book

GALARNEAU, A., CAMBON, H., DI RENZO, F. & FAJULA, F. 2001. True Microporosity and Surface Area of Mesoporous SBA-15 Silicas as a Function of Synthesis Temperature. *Langmuir,* 17**,** 8328-8335.

GANIM, Z., CHUNG, H. S., SMITH, A. W., DEFLORES, L. P., JONES, K. C. & TOKMAKOFF, A. 2008. Amide I two-dimensional infrared Spectroscopy of proteins. *Accounts of Chemical Research,* 41**,** 432-441.

GARCÍA-CONTRERAS, L., ABU-IZZA, K. & LU, D. R. 1997. Biodegradable Cisplatin Microspheres for Direct Brain Injection: Preparation and Characterization. *Pharmaceutical Development and Technology,* 2**,** 53-65.

GIACOBBE, F., AYLMORE, L. A. G. & STEELE, W. A. 1972. Thermodynamic properties of argon adsorbed on porous glass plus preadsorbed water. *Journal of Colloid and Interface Science,* 38**,** 277-284.

GILL, S. S., PATEL, N. K., HOTTON, G. R., O'SULLIVAN, K., MCCARTER, R., BUNNAGE, M., BROOKS, D. J., SVENDSEN, C. N. & HEYWOOD, P. 2003. Direct brain infusion of glial cell line-derived neurotrophic factor in Parkinson disease. *Nature Medicine,* 9**,** 589-595.

GIZATULLIN, B. I. & PIMENOV, G. G. 2009. Effect of a porous medium on the phase transitions and mobility of cyclohexane molecules. *Colloid Journal,* 71**,** 308-312.

GJERDAKER, L., SORLAND, G. H. & AKSNES, D. W. 1999. Application of the short diffusion time model to diffusion measurements by NMR in microporous crystallites. *Microporous and Mesoporous Materials,* 32**,** 305-310.

GLUECKAUF, E. 1955. Theory of chromatography. Part 10. Formulae for diffusion into spheres and their application to chromatography. *Transactions of the Faraday Society* 51(0): 1540-1551.

GLUECKAUF, E and J. I. COATES, 1947. Theory of chromatography. 4. The influence of incomplete quilibrium on the front boundary of chromatograms and on the effectiveness of separation." Journal of the Chemical Society(OCT): 1315-1321.

GOVENDER, T., STOLNIK, S., GARNETT, M. C., ILLUM, L. & DAVIS, S. S. 1999. PLGA nanoparticles prepared by nanoprecipitation: drug loading and release studies of a water soluble drug. *Journal of Controlled Release,* 57**,** 171-185.

GRAHN, A. Y., BANKIEWICZ, K. S., DUGICH-DJORDJEVIC, M., BRINGAS, J. R., HADACZEK, P., JOHNSON, G. A., EASTMAN, S. & LUZ, M. 2009. Non-PEGylated liposomes for convection-enhanced delivery of topotecan and gadodiamide in malignant glioma: initial experience. *Journal of Neuro-Oncology,* 95**,** 185-197.

GREF, R., MINAMITAKE, Y., PERACCHIA, M. T., TRUBETSKOY, V., TORCHILIN, V. & LANGER, R. 1994. Biodegradable Long-Circulating Polymeric Nanospheres. *Science,* 263**,** 1600-1603.

GREGG, S. J. & SING, K. S. W. 1982. *Adsorption, Surface Area and Porosity* New York and London, Academic Press.

GROSMAN, A. & ORTEGA, C. 2005. Nature of capillary condensation and evaporation processes in ordered porous materials. *Langmuir,* 21**,** 10515-10521.

GROSMAN, A. & ORTEGA, C. 2008a. Capillary condensation in porous materials. Hysteresis and interaction mechanism without pore blocking/percolation process. *Langmuir,* 24**,** 3977-3986.

GROSMAN, A. & ORTEGA, C. 2008b. Influence of elastic deformation of porous materials in adsorption-desorption process: A thermodynamic approach. *Physical Review B,* 78.

GRÜNBERG, B., EMMLER, T., GEDAT, E., SHENDEROVICH, I., FINDENEGG, G. H., LIMBACH, H.-H. & BUNTKOWSKY, G. 2004. Hydrogen Bonding of Water Confined in Mesoporous Silica MCM-41 and SBA-15 Studied by 1H Solid-State NMR. *Chemistry – A European Journal,* 10**,** 5689-5696.

GUNTHER, H. 1995. *NMR SPECTROSCOPY: Basic Principles, Concepts, and Applications in Chemistry,* Chichester, John Wiley & Sons Ltd.

HANS, M. L. & LOWMAN, A. M. 2002. Biodegradable nanoparticles for drug delivery and targeting. *Current Opinion in Solid State and Materials Science,* 6**,** 319-327.

HANSEN, C. 2007. *Hansen solubility parameters : a user's handbook (2nd ed.),* Florida, CRC Press.

HANSEN, E. W., GRAN, H. C. & SELLEVOLD, E. J. 1997. Heat of fusion and surface tension of solids confined in porous materials derived from a combined use of NMR and calorimetry. *Journal of Physical Chemistry B,* 101**,** 7027-7032.

HANSEN, E. W., STÖCKER, M. & SCHMIDT, R. 1996a. Low-Temperature Phase Transition of Water Confined in Mesopores Probed by NMR. Influence on Pore Size Distribution. *The Journal of Physical Chemistry,* 100**,** 2195-2200.

HANSEN, S., BAUER, R., LOMHOLT, S. B., QUIST, K. B., PEDERSEN, J. S. & MORTENSEN, K. 1996b. Structure of casein micelles studied by small-angle neutron scattering. *European Biophysics Journal with Biophysics Letters,* 24**,** 143-147.

HARKINS, W. D. & JURA, G. 1945. An Absolute Method for the Determination of the Area of a Fine Crystalline Powder. *Journal of Chemical Physics,* 13**,** 449-450.

HIGUCHI, T. 1963. Mechanism of sustained-action medication. Theoretical analysis of rate of release of solid drugs dispersed in solid matrices *Journal of Pharmaceutical Sciences,* 52**,** 1145-&.

HITCHCOCK, I. 2011. *Pore structure characterisation: The challenge to understand heterogeneous catalysts and fuel cells.* Doctor of Philosophy (PhD), University of Bath.

HITCHCOCK, I., CHUDEK, J. A., HOLT, E. M., LOWE, J. P. & RIGBY, S. P. 2010. NMR Studies of Cooperative Effects in Adsorption. *Langmuir,* 26**,** 18061-18070.

HITCHCOCK, I., HOLT, E. M., LOWE, J. P. & RIGBY, S. P. 2011. Studies of freezing-melting hysteresis in cryoporometry scanning loop experiments using NMR diffusometry and relaxometry. *Chemical Engineering Science,* 66**,** 582-592.

HOLLEWAND, M. P. & GLADDEN, L. F. 1995a. Transport Heterogeneity in Porous Pellets . Part 1-Pgse Nmr-Studies. *Chemical Engineering Science,* 50**,** 309-326.

HOLLEWAND, M. P. & GLADDEN, L. F. 1995b. Transport heterogeneity in porous pellets. Part 2-NMR imaging studies under transient and steady-state conditions. *Chemical Engineering Science,* 50**,** 327-344.

HOLT, C., TIMMINS, P. A., ERRINGTON, N. & LEAVER, J. 1998. A core-shell model of calcium phosphate nanoclusters stabilized by beta-casein phosphopeptides, derived from sedimentation equilibrium and small-angle X-ray and neutron-scattering measurements. *European Journal of Biochemistry,* 252**,** 73-78.

HOLZ, M., HEIL, S. R. & SACCO, A. 2000. Temperature-dependent self-diffusion coefficients of water and six selected molecular liquids for calibration in accurate H-1 NMR PFG measurements. *Physical Chemistry Chemical Physics,* 2**,** 4740-4742.

HORCAJADA, P., RAMILA, A., PEREZ-PARIENTE, J. & VALLET-REGI, M. 2004. Influence of pore size of MCM-41 matrices on drug delivery rate. *Microporous and Mesoporous Materials,* 68**,** 105-109.

HORNE, D. S. 1998. Casein interactions: Casting light on the black boxes, the structure in dairy products. *International Dairy Journal,* 8**,** 171-177.

HSU, C.-H., LIN, H.-P., TANG, C.-Y. & LIN, C.-Y. 2006. Synthesis of mesoporous silicas with different pore sizes using PEO polymers via hydrothermal treatment: A direct template for mesoporous carbon. *Materials Chemistry and Physics,* 100**,** 112-116.

HUA, D. W. & SMITH, D. M. 1992. Pore-Size and Surface Texture Modification of Silica Via Trialkylsilylation. *Langmuir,* 8**,** 2753-2757.

ISMAIL, I. M. K. & PFEIFER, P. 1994. Fractal Analysis and Surface-Roughness of Nonporous Carbon-Fibers and Carbon-Blacks. *Langmuir,* 10**,** 1532-1538.

ISMAILOS, G., REPPAS, C., DRESSMAN, J. B. & MACHERAS, P. 1991. Unusual Solubility Behavior of Cyclosporine-a in Aqueous-Media. *Journal of Pharmacy and Pharmacology,* 43**,** 287-289.

ISRAELACHVILI, J. N., MITCHELL, D. J. & NINHAM, B. W. 1976. Theory of self-assembly of hydrocarbon amphiphiles into micelles and bilayers. *Journal of the Chemical Society, Faraday Transactions 2: Molecular and Chemical Physics,* 72**,** 1525-1568.

JACKSON, C. L. & MCKENNA, G. B. 1990. The melting behaviour of organic materials confined in porous solids. *Journal of Chemical Physics,* 93**,** 9002-9011.

JEON, H.-J., JEONG, Y.-I., JANG, M.-K., PARK, Y.-H. & NAH, J.-W. 2000. Effect of solvent on the preparation of surfactant-free poly(-lactide-co-glycolide) nanoparticles and norfloxacin release characteristics. *International Journal of Pharmaceutics,* 207**,** 99-108.

JEONG, Y. I., CHO, C. S., KIM, S. H., KO, K. S., KIM, S. I., SHIM, Y. H. & NAH, J. W. 2001. Preparation of poly(DL-lactide-co-glycolide) nanoparticles without surfactant. *Journal of Applied Polymer Science,* 80**,** 2228-2236.

JEONG, Y. I., SHIM, Y. H., SONG, K. C., PARK, Y. G., RYU, H. W. & NAH, J. W. 2002. Testosterone-encapsulated surfactant-free nanoparticles of poly(DL-lactide-co-glycolide): Preparation and release behavior. *Bulletin of the Korean Chemical Society,* 23**,** 1579-1584.

JULIENNE, M. C., ALONSO, M. J., AMOZA, J. L. G. & BENOIT, J. P. 1992. Preparation of Poly(D,L-Lactide Glycolide) Nanoparticles of Controlled Particle-Size Distribution - Application of Experimental-Designs. *Drug Development and Industrial Pharmacy,* 18**,** 1063-1077.

KABALNOV, A., OLSSON, U. & WENNERSTROM, H. 1995. Salt Effects on Nonionic Microemulsions Are Driven by Adsorption/Depletion at the Surfactant Monolayer. *Journal of Physical Chemistry,* 99**,** 6220-6230.

KAMPHORST, W., DE BOER, A. G. & GAILLARD, P. J. 2002. Brain Drug Targeting: The Future of Brain Drug Development. *Journal of Clinical Pathology,* 55**,** 158-158.

KARGER, J. & RUTHVEN, D. M. 1992. Diffusion in zeolites and other microporous solids. 1st ed. New York: Wiley.

KARNAUKHOV, A. P. 1985. Improvement of methods for surface area determinations. *Journal of Colloid and Interface Science,* 103**,** 311-320.

KEELER, J. 2005. *Understanding NMR spectroscopy*, John Wiley & Sons Ltd.

KELLS, A. P., EBERLING, J., SU, X. M., PIVIROTTO, P., BRINGAS, J., HADACZEK, P., NARROW, W. C., BOWERS, W. J., FEDEROFF, H. J., FORSAYETH, J. & BANKIEWICZ, K. S. 2010. Regeneration of the MPTP-Lesioned Dopaminergic System after Convection-Enhanced Delivery of AAV2-GDNF. *Journal of Neuroscience,* 30**,** 9567-9577.

KERSSEBAUM 2002. Dosy and diffusion manual users guide for xwinnmr 3.1/3.5 version 1.0.

KHOKHLOV, A., VALIULLIN, R., STEPOVICH, M. & KÄRGER, J. 2008. Characterization of pore size distribution in porous silicon by NMR cryoporosimetry and adsorption methods. *Colloid Journal,* 70**,** 507-514.

KIERLIK, E., MONSON, P. A., ROSINBERG, M. L. & TARJUS, G. 2002. Adsorption hysteresis and capillary condensation in disordered porous solids: a density functional study. *Journal of Physics-Condensed Matter,* 14**,** 9295-9315.

KIM, S. Y., SHIN, I. G. & LEE, Y. M. 1999. Amphiphilic diblock copolymeric nanospheres composed of methoxy poly(ethylene glycol) and glycolide: properties, cytotoxicity and drug release behaviour. *Biomaterials,* 20**,** 1033-1042.

KIM, T. H. & PARK, T. G. 2004. Critical effect of freezing/freeze-drying on sustained release of FITC-dextran encapsulated within PLGA microspheres. *International Journal of Pharmaceutics,* 271**,** 207-214.

KONAN, Y. N., CERNY, R., FAVET, J., BERTON, M., GURNY, R. & ALLÉMANN, E. 2003. Preparation and characterization of sterile sub-200 nm meso-tetra(4-hydroxylphenyl)porphyrin-loaded nanoparticles for photodynamic therapy. *European Journal of Pharmaceutics and Biopharmaceutics,* 55**,** 115-124.

KONDRASHOVA, D., REICHENBACH, C. & VALIULLIN, R. 2010. Probing Pore Connectivity in Random Porous Materials by Scanning Freezing and Melting Experiments. *Langmuir,* 26**,** 6380-6385.

KOSMIDIS, K., ARGYRAKIS, P. & MACHERAS, P. 2003. A reappraisal of drug release laws using Monte Carlo simulations: The prevalence of the Weibull function. *Pharmaceutical Research,* 20**,** 988-995.

KOSUGE, K., KIKUKAWA, N. & TAKEMORI, M. 2004a. One-step preparation of porous silica spheres from sodium silicate using triblock copolymer templating. *Chemistry of Materials,* 16**,** 4181-4186.

KOSUGE, K., SATO, T., KIKUKAWA, N. & TAKEMORI, M. 2004b. Morphological control of rod- and fiberlike SBA-15 type mesoporous silica using water-soluble sodium silicate. *Chemistry of Materials,* 16**,** 899-905.

KRUK, M., JARONIEC, M., KO, C. H. & RYOO, R. 2000a. Characterization of the porous structure of SBA-15. *Chemistry of Materials,* 12**,** 1961-1968.

KRUK, M., JARONIEC, M. & SAYARI, A. 1997. Application of large pore MCM-41 molecular sieves to improve pore size analysis using nitrogen adsorption measurements. *Langmuir,* 13**,** 6267-6273.

KRUK, M., JARONIEC, M. & SAYARI, A. 2000b. Nitrogen adsorption study of MCM-41 molecular sieves synthesized using hydrothermal restructuring. *Adsorption-Journal of the International Adsorption Society,* 6**,** 47-51.

KUMAR, M., MOHAPATRA, S. S., KONG, X., JENA, P. K., BAKOWSKY, U. & LEHR, C. M. 2004a. Cationic poly(lactide-co-glycolide) nanoparticles as efficient in vivo gene transfection agents. *Journal of Nanoscience and Nanotechnology,* 4**,** 990-994.

KUMAR, M. N. V. R., BAKOWSKY, U. & LEHR, C. M. 2004b. Preparation and characterization of cationic PLGA nanospheres as DNA carriers. *Biomaterials,* 25**,** 1771-1777.

KWON, H. Y., LEE, J. Y., CHOI, S. W., JANG, Y. S. & KIM, J. H. 2001. Preparation of PLGA nanoparticles containing estrogen by emulsification-diffusion method. *Colloids and Surfaces a-Physicochemical and Engineering Aspects,* 182**,** 123-130.

LAM, M. F., THOMAS, M. G. & LIND, C. R. P. 2011. Neurosurgical convection-enhanced delivery of treatments for Parkinson's disease. *Journal of Clinical Neuroscience,* 18**,** 1163-1167.

LI, J., JIANG, G. Q. & DING, F. X. 2008. The effect of pH on the polymer degradation and drug release from PLGA-mPEG microparticles. *Journal of Applied Polymer Science,* 109**,** 475-482.

LIBBY, B. & MONSON, P. A. 2004. Adsorption/desorption hysteresis in inkbottle pores: A density functional theory and Monte Carlo simulation study. *Langmuir,* 20**,** 4289-4294.

LIU, M., ZHOU, Z. M., WANG, X. F., XU, J., YANG, K., CUI, Q., CHEN, X., CAO, M. Y., WENG, J. & ZHANG, Q. Q. 2007. Formation of poly(L,D-lactide) spheres with controlled size by direct dialysis. *Polymer,* 48**,** 5767-5779.

LIU, X. X., WANG, Q., HUANG, X. F., YANG, S. H., LI, C. X., NIU, X. J., SHI, Q. F., SUN, G. & LU, K. Q. 2010. Liquid-Solid Transition of Confined Water in Silica-Based Mesopores. *Journal of Physical Chemistry B,* 114**,** 4145-4150.

LIU, Y., GUO, L. K., HUANG, L. & DENG, X. M. 2003. Preparation and properties of a biodegradable polymer as a novel drug delivery system. *Journal of Applied Polymer Science,* 90**,** 3150-3156.

LIU, Y. & GUO, R. 2008. pH-dependent structures and properties of casein micelles. *Biophysical Chemistry,* 136**,** 67-73.

LODHA, A., LODHA, M., PATEL, A., CHAUDHURI, J., DALAL, J., EDWARDS, M. & DOUROUMIS, D. 2012. Synthesis of mesoporous silica nanoparticles and drug loading of poorly water soluble drug cyclosporin A. *Journal of pharmacy and bioallied sciences,* 4**,** 92-94.

LOWELL, S., SHIELDS, J. E., THOMAS, M. A. & THOMMES, M. 2004. *Characterization of Porous Solids and Powders: Surface Area, Pore Size and Density,* The Netherlands, Kluwer Academic Publishers.

LUZ, M., GRAHN, A. Y., DUGICH-DJORDJEVIC, M., BRINGAS, J. R., HADACZEK, P., JOHNSON, G. A., EASTMAN, S. & BANKIEWICZ, K. S. 2009. Convection-Enhanced Delivery of Non-Pegylated Liposomes of Topotecan and Gadodiamide in Malignant Glioma. *British Journal of Clinical Pharmacology,* 68**,** 15-15.

MACE, O. & WEI, J. 1991. Diffusion in random particle models for hydrodemetalation catalysts. *Industrial & Engineering Chemistry Research,* 30**,** 909-918.

MACKAY, J. A., DEEN, D. F. & SZOKA, F. C. 2005. Distribution in brain of liposomes after convection enhanced delivery; modulation by particle charge, particle diameter, and presence of steric coating. *Brain Research,* 1035**,** 139-153.

MANZANO, M., AINA, V., AREÁN, C. O., BALAS, F., CAUDA, V., COLILLA, M., DELGADO, M. R. & VALLET-REGÍ, M. 2008. Studies on MCM-41 mesoporous silica for drug delivery: Effect of particle morphology and amine functionalization. *Chemical Engineering Journal,* 137**,** 30-37.

MAO, S., XU, J., CAI, C., GERMERSHAUS, O., SCHAPER, A. & KISSEL, T. 2007. Effect of WOW process parameters on morphology and burst release of FITC-dextran loaded PLGA microspheres. *International Journal of Pharmaceutics,* 334**,** 137-148.

MATTSON, S. M. 1994. Glass-Fiber Dissolution in Simulated Lung Fluid and Measures Needed to Improve Consistency and Correspondence to in-Vivo Dissolution. *Environmental Health Perspectives,* 102**,** 87-90.

MELLAERTS, R., AERTS, C. A., VAN HUMBEECK, J., AUGUSTIJNS, P., VAN DEN MOOTER, G. & MARTENS, J. A. 2007. Enhanced release of itraconazole from ordered mesoporous SBA-15 silica materials. *Chemical Communications***,** 1375-1377.

MELLAERTS, R., MOLS, R., JAMMAER, J. A. G., AERTS, C. A., ANNAERT, P., VAN HUMBEECK, J., VAN DEN MOOTER, G., AUGUSTIJNS, P. & MARTENS, J. A. 2008. Increasing the oral bioavailability of the poorly water soluble drug itraconazole with ordered mesoporous silica. *European Journal of Pharmaceutics and Biopharmaceutics,* 69**,** 223-230.

MENEI, P., VENIER, M.-C., GAMELIN, E., SAINT-ANDRÉ, J.-P., HAYEK, G., JADAUD, E., FOURNIER, D., MERCIER, P., GUY, G. & BENOIT, J.-P. 1999. Local and sustained delivery of 5-fluorouracil from biodegradable microspheres for the radiosensitization of glioblastoma. *Cancer,* 86**,** 325-330.

MESSARITAKI, A., BLACK, S. J., VAN DER WALLE, C. F. & RIGBY, S. P. 2005. NMR and confocal microscopy studies of the mechanisms of burst drug release from PLGA microspheres. *Journal of Controlled Release,* 108**,** 271-281.

MILLER, R. A., BRADY, J. M. & CUTRIGHT, D. E. 1977. Degradation Rates of Oral Resorbable Implants (Polylactates and Polyglycolates) - Rate Modification with Changes in Pla-Pga Copolymer Ratios. *Journal of Biomedical Materials Research,* 11**,** 711-719.

MISRA, A., GANESH, S., SHAHIWALA, A. & SHAH, S. P. 2003. Drug delivery to the central nervous system: a review. *Journal of Pharmacy and Pharmaceutical Sciences,* 6**,** 252-273.

MITCHELL, J., VON DER SCHULENBURG, D. A. G., HOLLAND, D. J., FORDHAM, E. J., JOHNS, M. L. & GLADDEN, L. F. 2008a. Determining NMR flow propagator moments in porous rocks without the influence of relaxation. *Journal of Magnetic Resonance,* 193**,** 218-225.

MITCHELL, J., WEBBER, J. B. W. & STRANGE, J. H. 2008b. Nuclear magnetic resonance cryoporometry. *Physics Reports,* 461**,** 1-36.

MITRA, P. P., SEN, P. N. & SCHWARTZ, L. M. 1993. Short-time behavior of the diffusion coefficient as a geometrical probe of porous media. *Physical Review B,* 47**,** 8565.

MOITZI, C., PORTNAYA, I., GLATTER, O., RAMON, O. & DANINO, D. 2008. Effect of Temperature on Self-Assembly of Bovine β-Casein above and below Isoelectric pH. Structural Analysis by Cryogenic-Transmission Electron Microscopy and Small-Angle X-ray Scattering. *Langmuir,* 24**,** 3020-3029.

MOLINA-BOLIVAR, J. A. & ORTEGA-VINUESA, J. L. 1999. How proteins stabilize colloidal particles by means of hydration forces. *Langmuir,* 15**,** 2644-2653.

MORA-HUERTAS, C. E., FESSI, H. & ELAISSARI, A. 2011. Influence of process and formulation parameters on the formation of submicron particles by solvent displacement and emulsification–diffusion methods: Critical comparison. *Advances in Colloid and Interface Science,* 163**,** 90-122.

MORISHIGE, K. 2009. Hysteresis Critical Point of Nitrogen in Porous Glass: Occurrence of Sample Spanning Transition in Capillary Condensation. *Langmuir,* 25**,** 6221-6226.

MORISHIGE, K. & IWASAKI, H. 2003. X-ray study of freezing and melting of water confined within SBA-15. *Langmuir,* 19**,** 2808-2811.

MORISHIGE, K. & KANZAKI, Y. 2009. Porous Structure of Ordered Silica with Cagelike Pores Examined by Successive Adsorption of Water and Nitrogen. *Journal of Physical Chemistry C,* 113**,** 14927-14934.

MORISHIGE, K., YASUNAGA, H., DENOYEL, R. & WERNERT, V. 2007. Pore-blocking-controlled freezing of water in cagelike pores of KIT-5. *Journal of Physical Chemistry C,* 111**,** 9488-9495.

MORISHIGE, K. & YOSHIDA, K. 2010. Neck Size of Ordered Cage-Type Mesoporous Silica FDU-12 and Origin of Gradual Desorption. *Journal of Physical Chemistry C,* 114**,** 7095-7101.

MU, L. & FENG, S. S. 2002. Vitamin E TPGS used as emulsifier in the solvent evaporation/extraction technique for fabrication of polymeric nanospheres for controlled release of paclitaxel (Taxol (R)). *Journal of Controlled Release,* 80**,** 129-144.

NAH, J.-W., JEONG, Y.-D. & KOH, J.-J. 2000. Drug release from nanoparticles of Poly(DL-lactide-co-glycolide). *Korean Journal of Chemical Engineering,* 17**,** 230-236.

NAUMOV, S., VALIULLIN, R., MONSON, P. A. & KARGER, J. 2008. Probing memory effects in confined fluids via diffusion measurements. *Langmuir,* 24**,** 6429-6432.

NEIMARK, A. V., HANSON, M. & UNGER, K. K. 1993. Fractal Analysis of the Distribution of High-Viscosity Fluids in Porous Supports. *Journal of Physical Chemistry,* 97**,** 6011-6015.

NEIMARK, A. V. & RAVIKOVITCH, P. I. 2000. Density functional theory of adsorption hysteresis and nanopore characterization. *Characterization of Porous Solids V,* 128**,** 51-60.

NEIMARK, A. V. & RAVIKOVITCH, P. I. 2001. Capillary condensation in MMS and pore structure characterization. *Microporous and Mesoporous Materials,* 44**,** 697-707.

NEIMARK, A. V., RAVIKOVITCH, P. I., GRUN, M., SCHUTH, F. & UNGER, K. K. 1998. Pore size analysis of MCM-41 type adsorbents by means of nitrogen and argon adsorption. *Journal of Colloid and Interface Science,* 207**,** 159-169.

NEIMARK, A. V., RAVIKOVITCH, P. I. & VISHNYAKOV, A. 2000. Adsorption hysteresis in nanopores. *Physical Review E,* 62**,** R1493-R1496.

NIWA, T., TAKEUCHI, H., HINO, T., KUNOU, N. & KAWASHIMA, Y. 1993. Preparations of biodegradable nanospheres of water-soluble and insoluble drugs with D,L-lactide/glycolide copolymer by a novel spontaneous emulsification solvent diffusion method, and the drug release behavior. *Journal of Controlled Release,* 25**,** 89-98.

NIWA, T., TAKEUCHI, H., HINO, T., KUNOU, N. & KAWASHIMA, Y. 1994. In-vitro drug release behaviour of D,L-lactide/glycolide copolymer (PLGA) nanospheres with Nafarelin acetate prepared by a novel spontanious emulsification solvent diffusion method. *Journal of Pharmaceutical Sciences,* 83**,** 727-732.

OSSOWSKI, S., JACKSON, A., OBIOLS-RABASA, M., HOLT, C., LENTON, S., PORCAR, L., PAULSSON, M. & NYLANDER, T. 2012. Aggregation Behavior of Bovine κ- and β-Casein Studied with Small Angle Neutron Scattering, Light Scattering, and Cryogenic Transmission Electron Microscopy. *Langmuir*.

OVERLOOP, K. & VANGERVEN, L. 1993. Exchange and Cross-Relaxation in Adsorbed Water. *Journal of Magnetic Resonance, Series A,* 101**,** 147-156.

PANYAM, J., WILLIAMS, D., DASH, A., LESLIE-PELECKY, D. & LABHASETWAR, V. 2004. Solid-state solubility influences encapsulation and release of hydrophobic drugs from PLGA/PLA nanoparticles. *Journal of Pharmaceutical Sciences,* 93**,** 1804-1814.

PAPADOPOULOU, V., KOSMIDIS, K., VLACHOU, M. & MACHERAS, P. 2006. On the use of the Weibull function for the discernment of drug release mechanisms. *International Journal of Pharmaceutics,* 309**,** 44-50.

PARDRIDGE, W. M. 2003. Blood-brain barrier genomics and the use of endogenous transporters to cause drug penetration into the brain. *Current Opinion in Drug Discovery & Development,* 6**,** 683-691.

PARDRIDGE, W. M. 2007. Blood-brain barrier delivery. *Drug Discovery Today,* 12**,** 54-61.

PARDRIDGE, W. M. & BOADO, R. J. 2012. Reengineering Biopharmaceuticals for Targeted Delivery across the Blood-Brain Barrier. *Methods in Enzymology: Protein Engineering for Therapeutics, Vol 203, Pt B,* 503**,** 269-292.

PARK, T. G. 1995. Degradation of Poly(Lactic-Co-Glycolic Acid) Microspheres - Effect of Copolymer Composition. *Biomaterials,* 16**,** 1123-1130.

PATEL, T., ZHOU, J., PIEPMEIER, J. M. & SALTZMAN, W. M. 2012. Polymeric nanoparticles for drug delivery to the central nervous system. *Advanced drug delivery reviews,* 64**,** 701-5.

PELLENQ, R. J. M. & LEVITZ, P. E. 2001. Adsorption/condensation of xenon in a disordered silica glass having a mixed (micro a mixed and meso) porosity. *Molecular Simulation,* 27**,** 353-370.

PERKINS, E. L. 2009. *Nuclear magentic resonance studies of drug release devices.* PhD, Bath University.

PERKINS, E. L., LOWE, J. P., EDLER, K. J. & RIGBY, S. P. 2010. Studies of structure-transport relationships in biodegradable polymer microspheres for drug delivery using NMR cryodiffusometry. *Chemical Engineering Science,* 65**,** 611-625.

PERKINS, E. L., LOWE, J. P., EDLER, K. J., TANKO, N. & RIGBY, S. P. 2008. Determination of the percolation properties and pore connectivity for mesoporous solids using NMR cryodiffusometry. *Chemical Engineering Science,* 63**,** 1929-1940.

PERRY, R. H. & GREEN, D. W. 1997. *Perry's chemical engineers' handbook,* New York, USA, McGraw-Hill.

PETROV, O. & FURÓ, I. 2011. A study of freezing–melting hysteresis of water in different porous materials. Part I: Porous silica glasses. *Microporous and Mesoporous Materials,* 138**,** 221-227.

PETROV, O., FURÓ, I., SCHULEIT, M., DOMANIG, R., PLUNKETT, M. & DAICIC, J. 2006. Pore size distributions of biodegradable polymer microparticles in aqueous environments measured by NMR cryoporometry. *International Journal of Pharmaceutics,* 309**,** 157-162.

PETROV, O. V. & FURO, I. 2009. NMR cryoporometry: Principles, applications and potential. *Progress in Nuclear Magnetic Resonance Spectroscopy,* 54**,** 97-122.

PFEIFER, P., JOHNSTON, G. P., DESHPANDE, R., SMITH, D. M. & HURD, A. J. 1991. Structure analysis of porous solids from the preadsorbed films *Langmuir,* 7**,** 2833-2843.

PISTEL, K. F., BREITENBACH, A., ZANGE-VOLLAND, R. & KISSEL, T. 2001. Brush-like branched biodegradable polyesters, part III - Protein release from microspheres of poly(vinyl alcohol)-graft-poly(D,L-lactic-co-glycolic acid). *Journal of Controlled Release,* 73**,** 7-20.

PORTNAYA, I., BEN-SHOSHAN, E., COGAN, U., KHALFIN, R., FASS, D., RAMON, O. & DANINO, D. 2008. Self-Assembly of Bovine β-Casein below the Isoelectric pH. *Journal of Agricultural and Food Chemistry,* 56**,** 2192-2198.

POST, A. E., ARNOLD, B., WEISS, J. & HINRICHS, J. 2012a. Effect of temperature and pH on the solubility of caseins: Environmental influences on the dissociation of alpha(S)- and beta-casein. *Journal of Dairy Science,* 95**,** 1603-1616.

POST, A. E., WEISS, J. & HINRICHS, J. 2012b. Effect of temperature and pH on the solubility of caseins: I. Structural characteristics of micellar casein and caseinate. *Milchwissenschaft-Milk Science International,* 67**,** 119-123.

PRIVMAN, V., GOIA, D. V., PARK, J. & MATIJEVIC, E. 1999. Mechanism of formation of monodispersed colloids by aggregation of nanosize precursors. *Journal of Colloid and Interface Science,* 213**,** 36-45.

PROUZET, E., BOISSIERE, C., KIM, S. S. & PINNAVAIA, T. J. 2009. Roughness of mesoporous silica surfaces deduced from adsorption measurements. *Microporous and Mesoporous Materials,* 119**,** 9-17.

PRUPPACHER, H. R. 1995. A New Look at Homogeneous Ice Nucleation in Supercooled Water Drops. *Journal of the Atmospheric Sciences,* 52**,** 1924-1933.

PUIBASSET, J. 2009. Monte-Carlo Multiscale Simulation Study of Argon Adsorption/Desorption Hysteresis in Mesoporous Heterogeneous Tubular Pores like MCM-41 or Oxidized Porous Silicon. *Langmuir,* 25**,** 903-911.

PURCELL, E. M. 1946. Spontaneous Emission Probabilities at Radio Frequencies. *Physical Review,* 69**,** 681-681.

QU, F., ZHU, G., HUANG, S., LI, S., SUN, J., ZHANG, D. & QIU, S. 2006. Controlled release of Captopril by regulating the pore size and morphology of ordered mesoporous silica. *Microporous and Mesoporous Materials,* 92**,** 1-9.

RAFATI, H., COOMBES, A. G. A., ADLER, J., HOLLAND, J. & DAVIS, S. S. 1997. Protein-loaded poly(dl-lactide-co-glycolide) microparticles for oral administration: formulation, structural and release characteristics. *Journal of Controlled Release,* 43**,** 89-102.

RAN, Y., ZHAO, L., XU, Q. & YALKOWSKY, S. 2001. Solubilization of cyclosporin A. *Aaps Pharmscitech,* 2**,** 23-26.

RAVIKOVITCH, P. I., HALLER, G. L. & NEIMARK, A. V. 1998. Density functional theory model for calculating pore size distributions: pore structure of nanoporous catalysts. *Advances in Colloid and Interface Science,* 76**,** 203-226.

RAVIKOVITCH, P. I. & NEIMARK, A. V. 2001. Characterization of micro- and mesoporosity in SBA-15 materials from adsorption data by the NLDFT method. *Journal of Physical Chemistry B,* 105**,** 6817-6823.

RAVIKOVITCH, P. I. & NEIMARK, A. V. 2002a. Experimental confirmation of different mechanisms of evaporation from ink-bottle type pores: Equilibrium, pore blocking, and cavitation. *Langmuir,* 18**,** 9830-9837.

RAVIKOVITCH, P. I. & NEIMARK, A. V. 2002b. Experimental Confirmation of Different Mechanisms of Evaporation from Ink-Bottle Type Pores: Equilibrium, Pore Blocking, and Cavitation. *Langmuir,* 18**,** 9830-9837.

RAVIKOVITCH, P. I., ODOMHNAILL, S. C., NEIMARK, A. V., SCHUTH, F. & UNGER, K. K. 1995. Capillary hysteresis in nanopores: Theoretical and experimental studies of nitrogen adsorption on MCM-41. *Langmuir,* 11**,** 4765-4772.

REICHHARDT, N., KJELLMAN, T., SAKEYE, M., PAULSEN, F., SMATT, J. H., LINDEN, M. & ALFREDSSON, V. 2011. Removal of Intrawall Pores in SBA-15 by Selective Modification. *Chemistry of Materials,* 23**,** 3400-3403.

RICE, F. L., PARK, R., STAYNER, L., SMITH, R., GILBERT, S. & CHECKOWAY, H. 2001. Crystalline Silica Exposure and Lung Cancer Mortality in Diatomaceous Earth Industry Workers: A Quantitative Risk Assessment. *Occupational and Environmental Medicine,* 58**,** 38-45.

RIESZ, P., BERDAHL, D. & CHRISTMAN, C. L. 1985. Free-radical generation by ultrasound in aqueous and nonaqueous solutions. *Environmental Health Perspectives,* 64**,** 233-252.

RIGBY, S. P. & CHIGADA, P. I. 2009. Interpretation of integrated gas sorption and mercury porosimetry studies of adsorption in disordered networks using mean-field DFT. *Adsorption-Journal of the International Adsorption Society,* 15**,** 31-41.

RIGBY, S. P., CHIGADA, P. I., PERKINS, E. L., WATT-SMITH, M. J., LOWE, J. P. & EDLER, K. J. 2008. Fundamental studies of gas sorption within mesopores situated amidst an inter-connected, irregular network. *Adsorption-Journal of the International Adsorption Society,* 14**,** 289-307.

RIGBY, S. P. & FLETCHER, R. S. 2004. Experimental evidence for pore blocking as the mechanism for nitrogen sorption hysteresis in a mesoporous material. *Journal of Physical Chemistry B,* 108**,** 4690-4695.

RIGBY, S. P. & GLADDEN, L. F. 1996. NMR and fractal modelling studies of transport in porous media. *Chemical Engineering Science,* 51**,** 2263-2272.

RIIKONEN, J., MAKILA, E., SALONEN, J. & LEHTO, V. P. 2009. Determination of the Physical State of Drug Molecules in Mesoporous Silicon with Different Surface Chemistries. *Langmuir,* 25**,** 6137-6142.

ROJAS, F., KORNHAUSER, I., FELIPE, C., ESPARZA, J. M., CORDERO, S., DOMINGUEZ, A. & RICCARDO, J. L. 2002. Capillary condensation in heterogeneous mesoporous networks consisting of variable connectivity and pore-size correlation. *Physical Chemistry Chemical Physics,* 4**,** 2346-2355.

ROSENBERG, R. 2005. Why is ice slippery? *Physics Today,* 58**,** 50-55.

ROUQUEROL, F., ROUQUEROL, J, SING, K 1999. *Adsorption by powders and porous solids*, Academic Press.

SAITO, A. & FOLEY, H. C. 1995. Argon Porosimetry of Selected Molecular-Sieves - Experiments and Examination of the Adapted Horvath-Kawazoe Model. *Microporous Materials,* 3**,** 531-542.

SALTZMAN, E. J. & MUTHUKUMAR, M. 2009. Conformation and dynamics of model polymer in connected chamber-pore system. *The Journal of Chemical Physics,* 131**,** 214903.

SAMPSON, J. H., AKABANI, G., ARCHER, G. E., BERGER, M. S., COLEMAN, R. E., FRIEDMAN, A. H., FRIEDMAN, H. S., GREER, K., HERNDON, J. E., KUNWAR, S., MCLENDON, R. E., PAOLINO, A., PETRY, N. A., PROVENZALE, J. M., REARDON, D. A., WONG, T. Z., ZALUTSKY, M. R., PASTAN, I. & BIGNER, D. D. 2008. Intracerebral infusion of an EGFR-targeted toxin in recurrent malignant brain tumors. *Neuro-Oncology,* 10**,** 320-329.

SANT, S., NADEAU, W. & HILDGEN, P. 2005. Effect of porosity on the release kinetics of propafenone-loaded PEG-g-PLA nanoparticles. *Journal of Controlled Release,* 107**,** 203-214.

SANT, S., THOMMES, M. & HILDGEN, P. 2007. Microporous structure and drug selease kinetics of polymeric nanoparticles. *Langmuir,* 24**,** 280-287.

SANT, S., THOMMES, M. & HILDGEN, P. 2008. Microporous structure and drug release kinetics of polymeric nanoparticles. *Langmuir,* 24**,** 280-287.

SAWYER, A., SAUCIER-SAWYER, J., BOOTH, C., LIU, J., PATEL, T., PIEPMEIER, J. & SALTZMAN, W. 2011. Convection-enhanced delivery of camptothecin-loaded polymer nanoparticles for treatment of intracranial tumors. *Drug Delivery and Translational Research,* 1**,** 34-42.

SCHMIDT, D. G. 1970. The association of αs1-casein B at pH 6.6. *Biochimica et Biophysica Acta (BBA) - Protein Structure,* 207**,** 130-138.

SCHMIDT, R., HANSEN, E. W., STOCKER, M., AKPORIAYE, D. & ELLESTAD, O. H. 1995. Pore-Size Determination of Mcm-41 Mesoporous Materials by Means of H-1-Nmr Spectroscopy, N-2 Adsorption, and Hrem - a Preliminary-Study. *Journal of the American Chemical Society,* 117**,** 4049-4056.

SCHREIBER, A., KETELSEN, I. & FINDENEGG, G. H. 2001. Melting and freezing of water in ordered mesoporous silica materials. *Physical Chemistry Chemical Physics,* 3**,** 1185-1195.

SEL, O., KUANG, D. B., THOMMES, M. & SMARSLY, B. 2006. Principles of hierarchical meso- and macropore architectures by liquid crystalline and polymer colloid templating. *Langmuir,* 22**,** 2311-2322.

SHCHIPUNOV, Y. & SHIPUNOVA, N. 2008. Regulation of silica morphology by proteins serving as a template for mineralization. *Colloids and Surfaces B-Biointerfaces,* 63**,** 7-11.

SIMINA, M., NECHIFOR, R. & ARDELEAN, I. 2011. Saturation-dependent nuclear magnetic resonance relaxation of fluids confined inside porous media withmicrometer-sized pores. *Magnetic Resonance in Chemistry,* 49**,** 314-319.

SING, K. S. W., EVERETT, D. H., HAUL, R. A. W., MOSCOU, L., PIEROTTI, R. A., ROUQUEROL, J. & SIEMIENIEWSKA, T. 1985. Reporting physisorption data for gas/solid systems with special

reference to the determination of surface area and porosity (Recommendations 1984). *Pure and applied chemistry,* 57**,** 603-619.

SNOEREN, T. H. M., VAN MARKWIJK, B. & VAN MONTFORT, R. 1980. Some physicochemical properties of bovine αs2-casein. *Biochimica et Biophysica Acta (BBA) - Protein Structure,* 622**,** 268-276.

SOLER-ILLIA, G. J. D. A. A., CREPALDI, E. L., GROSSO, D. & SANCHEZ, C. 2003. Block copolymer-templated mesoporous oxides. *Current Opinion in Colloid & Interface Science,* 8**,** 109-126.

SONG, C. X., LABHASETWAR, V., MURPHY, H., QU, X., HUMPHREY, W. R., SHEBUSKI, R. J. & LEVY, R. J. 1997. Formulation and characterization of biodegradable nanoparticles for intravascular local drug delivery. *Journal of Controlled Release,* 43**,** 197-212.

SONG, K. C., LEE, H. S., CHOUNG, I. Y., CHO, K. I., AHN, Y. & CHOI, E. J. 2006. The effect of type of organic phase solvents on the particle size of poly(d,l-lactide-co-glycolide) nanoparticles. *Colloids and Surfaces A: Physicochemical and Engineering Aspects,* 276**,** 162-167.

SONG, S. W., HIDAJAT, K. & KAWI, S. 2005. Functionalized SBA-15 Materials as Carriers for Controlled Drug Delivery: Influence of Surface Properties on Matrix−Drug Interactions. *Langmuir,* 21**,** 9568-9575.

SØRLAND, G. H., ANTHONSEN, H. W., ZICK, K., SJÖBLOM, J. & SIMON, S. 2011. A spoiler recovery method for rapid diffusion measurements. *Diffusion Fundamentals.org,* 15**,** 1-9.

SPRY, B. & SAWYER, W. H. Year. Configurational diffusion effects in catalytic demetallization of petrolium feedstocks. *In:* 68th AIChE Annual meeting, Los Angeles, 1975. paper 3C.

STAIT-GARDNER, T., KUMAR, P. G. A. & PRICE, W. S. 2008. Steady state effects in PGSE NMR diffusion experiments. *Chemical Physics Letters,* 462**,** 331-336.

STEJSKAL, E. O. & TANNER, J. E. 1965. Spin Diffusion Measurements: Spin Echoes in the Presence of a Time-Dependent Field Gradient. *Journal of Chemical Physics,* 42**,** 288-+.

STORCK, S., BRETINGER, H. & MAIER, W. F. 1998. Characterization of micro- and mesoporous solids by physisorption methods and pore-size analysis. *Applied Catalysis a-General,* 174**,** 137-146.

STRANGE, J. H., ALLEN, S. G., STEPHENSON, P. C. L. & MATVEEVA, N. P. 1996. Phase equilibria of absorbed liquids and the structure of porous media. *Magnetic Resonance Imaging,* 14**,** 963-965.

STRANGE, J. H., RAHMAN, M. & SMITH, E. G. 1993. Characterization of porous solids by NMR. *Physical Review Letters,* 71**,** 3589-3591.

STRØMME, M., BROHEDE, U., ATLURI, R. & GARCIA-BENNETT, A. E. 2009. Mesoporous silica-based nanomaterials for drug delivery: evaluation of structural properties associated with release rate. *Wiley Interdisciplinary Reviews: Nanomedicine and Nanobiotechnology,* 1**,** 140-148.

TEIXEIRA, C. V., AMENITSCH, H., LINTON, P., LINDEN, M. & ALFREDSSON, V. 2011. The Role Played by Salts in the Formation of SBA-15, an in Situ Small-Angle X-ray Scattering/Diffraction Study. *Langmuir,* 27**,** 7121-7131.

THOMAS, M. J. K., SLIPPER, I., WALUNJ, A., JAIN, A., FAVRETTO, M. E., KALLINTERI, P. & DOUROUMIS, D. 2010. Inclusion of poorly soluble drugs in highly ordered mesoporous silica nanoparticles. *International Journal of Pharmaceutics,* 387**,** 272-277.

THOMMES, M., SMARSLY, B., GROENEWOLT, M., RAVIKOVITCH, P. I. & NEIMARK, A. V. 2006. Adsorption hysteresis of nitrogen and argon in pore networks and characterization of novel micro- and mesoporous silicas. *Langmuir,* 22**,** 756-764.

THURN, A., BURCHARD, W. & NIKI, R. 1987. Structure of casein micelles II. α_{s1}-casein. *Colloid & Polymer Science,* 265**,** 897-902.

TOMPSETT, G. A., KROGH, L., GRIFFIN, D. W. & CONNER, W. C. 2005. Hysteresis and scanning behavior of mesoporous molecular sieves. *Langmuir,* 21**,** 8214-8225.

TROYER, W. E., HOLLY, R., PEEMOELLER, H. & PINTAR, M. M. 2005. Proton spin-spin relaxation study of hydration of a model nanopore. *Solid State Nuclear Magnetic Resonance,* 28**,** 238-243.

VALIULLIN, R., KARGER, J. & GLASER, R. 2009. Correlating phase behaviour and diffusion in mesopores: perspectives revealed by pulsed field gradient NMR. *Physical Chemistry Chemical Physics,* 11**,** 2833-2853.

VALLET-REǴI, M., DOADRIO, J. C., DOADRIO, A. L., IZQUIERDO-BARBA, I. & PÉREZ-PARIENTE, J. 2004. Hexagonal ordered mesoporous material as a matrix for the controlled release of amoxicillin. *Solid State Ionics,* 172**,** 435-439.

VAN DE WEERT, M., HENNINK, W. E. & JISKOOT, W. 2000. Protein instability in poly(lactic-co-glycolic acid) microparticles. *Pharmaceutical Research,* 17**,** 1159-1167.

VAN SPEYBROECK, M., BARILLARO, V., DO THI, T., MELLAERTS, R., MARTENS, J., VAN HUMBEECK, J., VERMANT, J., ANNAERT, P., VAN DEN MOOTER, G. & AUGUSTIJNS, P. 2009. Ordered Mesoporous Silica Material SBA-15: A Broad-Spectrum Formulation Platform for Poorly Soluble Drugs. *Journal of Pharmaceutical Sciences,* 98**,** 2648-2658.

VARGAS-FLORENCIA, D., FURO, I. & CORKERY, R. W. 2008. Pore morphology and interconnectivity in a mesoporous/macroporous polyhedral silica foam material. *Langmuir,* 24**,** 4827-4832.

VARGAS-FLORENCIA, D., PETROV, O. V. & FURO, I. 2007. NMR cryoporometry with octamethylcyclotetrasiloxane as a probe liquid. Accessing large pores. *Journal of Colloid and Interface Science,* 305**,** 280-285.

VAUTHIER, C. & BOUCHEMAL, K. 2009. Methods for the Preparation and Manufacture of Polymeric Nanoparticles. *Pharmaceutical Research,* 26**,** 1025-1058.

VEITH, S. R., HUGHES, E. & PRATSINIS, S. E. 2004. Restricted diffusion and release of aroma molecules from sol-gel-made porous silica particles. *Journal of Controlled Release,* 99**,** 315-327.

VREEMAN, H. J., BRINKHUIS, J. A. & VAN DER SPEK, C. A. 1981. Some association properties of bovine SH-k-casein. *Biophysical Chemistry,* 14**,** 185-193.

VYALIKH, A., EMMLER, T., GRUNBERG, B., XU, Y., SHENDEROVICH, I., FINDENEGG, G. H., LIMBACH, H. H. & BUNTKOWSKY, G. 2007. Hydrogen bonding of water confined in controlled-pore glass 10-75 studied by H-1-solid state NMR. *Zeitschrift Fur Physikalische Chemie-International Journal of Research in Physical Chemistry & Chemical Physics,* 221**,** 155-168.

W.H.O. 2000. *SIlicosis Fact Sheet N^{o} 238* [Online]. Available at http://www.who.int/peh/Occupational_health/OCHweb/OSHpages/OSHDocuments/Factsheets/Silicosis.htm. [Accessed October 2012].

WANG, H., ZHAO, Y., WU, Y., HU, Y.-L., NAN, K., NIE, G. & CHEN, H. 2011. Enhanced anti-tumor efficacy by co-delivery of doxorubicin and paclitaxel with amphiphilic methoxy PEG-PLGA copolymer nanoparticles. *Biomaterials,* 32**,** 8281-8290.

WANG, K. W., ZHOU, L. Z., SUN, Y., WU, G. J., GU, H. C., DUAN, Y. R., CHEN, F. & ZHU, Y. J. 2010. Calcium phosphate/PLGA-mPEG hybrid porous nanospheres: A promising vector with ultrahigh gene loading and transfection efficiency. *Journal of Materials Chemistry,* 20**,** 1161-1166.

WANG, Y. C., WU, Y. T., HUANG, H. Y. & YANG, C. S. 2009. Surfactant-free Formulation of Poly(Lactic/Glycolic) Acid Nanoparticles Encapsulating Functional Polypeptide: A Technical Note. *Aaps Pharmscitech,* 10**,** 1263-1267.

WEBBER, J. B. W. 2000. *Characterizing porous media.* Doctor of philosophy, University of Kent.

WEBBER, J. B. W., STRANGE, J. H. & DORE, J. C. 2001. An evaluation of NMR cryoporometry, density measurement and neutron scattering methods of pore characterisation. *Magnetic Resonance Imaging,* 19**,** 395-399.

WHITE, E., BIENEMANN, A., TAYLOR, H., HOPKINS, K., CAMERON, A. & GILL, S. 2012. A phase I trial of carboplatin administered by convection-enhanced delivery to patients with

recurrent/progressive glioblastoma multiforme. *Contemporary Clinical Trials,* 33**,** 320-331.

WHITMORE, L. & WALLACE, B. A. 2008. Protein secondary structure analyses from circular dichroism spectroscopy: Methods and reference databases. *Biopolymers,* 89**,** 392-400.

WITOON, T., CHAREONPANICH, M. & LIMTRAKUL, J. 2010. Size control of nanostructured silica using chitosan template and fractal geometry: effect of chitosan/silica ratio and aging temperature. *Journal of Sol-Gel Science and Technology,* 56**,** 270-277.

WOO, H. J., PORCHERON, F. & MONSON, P. A. 2004. Modeling desorption of fluids from disordered mesoporous materials. *Langmuir,* 20**,** 4743-4747.

WU, D. H., CHEN, A. D. & JOHNSON, C. S. 1995. An Improved Diffusion-Ordered Spectroscopy Experiment Incorporating Bipolar-Gradient Pulses. *Journal of Magnetic Resonance Series A,* 115**,** 260-264.

WU, Z. M., GUO, X. D., ZHANG, L. J., JIANG, W., LING, L., QIAN, Y. & CHEN, Y. 2012. Solvent mediated microstructures and release behavior of insulin from pH-sensitive nanoparticles. *Colloids and Surfaces B: Biointerfaces,* 94**,** 206-212.

XIE, X., TAO, Q., ZOU, Y., ZHANG, F., GUO, M., WANG, Y., WANG, H., ZHOU, Q. & YU, S. 2011. PLGA Nanoparticles Improve the Oral Bioavailability of Curcumin in Rats: Characterizations and Mechanisms. *Journal of Agricultural and Food Chemistry,* 59**,** 9280-9289.

XU, P. S., GULLOTTI, E., TONG, L., HIGHLEY, C. B., ERRABELLI, D. R., HASAN, T., CHENG, J. X., KOHANE, D. S. & YEO, Y. 2009. Intracellular Drug Delivery by Poly(lactic-co-glycolic acid) Nanoparticles, Revisited. *Molecular Pharmaceutics,* 6**,** 190-201.

YALLAPU, M. M., GUPTA, B. K., JAGGI, M. & CHAUHAN, S. C. 2010. Fabrication of curcumin encapsulated PLGA nanoparticles for improved therapeutic effects in metastatic cancer cells. *Journal of Colloid and Interface Science,* 351**,** 19-29.

YANG, B. & EDLER, K. J. 2009. Free-Standing Ordered Mesoporous Silica Films Synthesized with Surfactantâˆ'Polyelectrolyte Complexes at the Air/Water Interface. *Chemistry of Materials,* 21**,** 1221-1231.

YANG, H. 2010. Nanoparticle-Mediated Brain-Specific Drug Delivery, Imaging, and Diagnosis. *Pharmaceutical Research,* 27**,** 1759-1771.

YANG, Y.-Y., CHIA, H.-H. & CHUNG, T.-S. 2000. Effect of preparation temperature on the characteristics and release profiles of PLGA microspheres containing protein fabricated by double-emulsion solvent extraction/evaporation method. *Journal of Controlled Release,* 69**,** 81-96.

YIU, H. H. P., BOTTING, C. H., BOTTING, N. P. & WRIGHT, P. A. 2001. Size selective protein adsorption on thiol-functionalised SBA-15 mesoporous molecular sieve. *Physical Chemistry Chemical Physics,* 3**,** 2983-2985.

ZHANG, X., SUN, M., ZHENG, A., CAO, D., BI, Y. & SUN, J. 2012. Preparation and characterization of insulin-loaded bioadhesive PLGA nanoparticles for oral administration. *European Journal of Pharmaceutical Sciences,* 45**,** 632-638.

ZHANG, Y. & MILLER, D. W. 2005. Pathways for drug delivery to the central nervous system. *In:* WANG, B., SIAHAAN, T. & SOLTERO, R. (eds.) *Drug delivery-Principles and Applications.* John Wiley & Sons.

ZHANG, Z. P. & FENG, S. S. 2006. In vitro investigation on poly(lactide)-Tween 80 copolymer nanoparticles fabricated by dialysis method for chemotherapy. *Biomacromolecules,* 7**,** 1139-1146.

ZHAO, D. Y., HUO, Q. S., FENG, J. L., CHMELKA, B. F. & STUCKY, G. D. 1998a. Nonionic triblock and star diblock copolymer and oligomeric surfactant syntheses of highly ordered, hydrothermally stable, mesoporous silica structures. *Journal of the American Chemical Society,* 120**,** 6024-6036.

ZHAO, D. Y., YANG, P. D., HUO, Q. S., CHMELKA, B. F. & STUCKY, G. D. 1998b. Topological construction of mesoporous materials. *Current Opinion in Solid State & Materials Science,* 3**,** 111-121.

ZIJLSTRA, G. S., RIJKEBOER, M., VAN DROOGE, D. J., SUTTER, M., JISKOOT, W., VAN DE WEERT, M., HINRICHS, W. L. J. & FRIJLINK, H. W. 2007. Characterization of a cyclosporine solid dispersion for inhalation. *Aaps Journal,* 9**,** E190-E199.